Faculty of Engineering, University of Porto

U.PORTO
FEUP FACULDADE DE ENGENHARIA
UNIVERSIDADE DO PORTO

Innovative Methodology for Railway Tunnel Inspection

Behzad Vasheghani Farahani

Submitted for the degree of Doctor of Philosophy
in Mechanical Engineering

Supervisor: Pedro Miguel Guimarães Pires Moreira (PhD)
Co-supervisors: Paulo José da Silva Tavares (PhD)
Marcos Massao Futai (PhD)

September 2019

This thesis is dedicated to:

My beloved wife, Parisa;
My late father, Mohammad;
My loyal mother, Fatemeh;
and;
My brothers, Masoud and Mehrdad.

Abstract

Railway tunnels deteriorate due to ageing, environmental factors, loading increase, damage caused by human or natural factors, inadequate maintenance, and deferred repairs. The increased perception of those problems, led by advances in analysis techniques, further stresses the necessity to deploy fully automated systems for inspection and condition assessment.

In particular, the practical inspection of tunnels commonly relies on human based methods that entail inherent limitations. However, applications of laser technology are dramatically expanding, with diminished cost and greater accuracy. In the same way, significant advances in high-speed 3D imaging technology have been accomplished in the last decades leading to better solutions for automatic evaluation of the infrastructure condition at high-speed.

Presently, Structural Health Monitoring (SHM) on railway tunnels is turning from traditional measuring solutions to full-field image-based ones. Recent progress in full field image-based techniques such as Digital Image Correlation (DIC) has been directed at the analysis of defects in large structures, in tunnel locations signaled by 3D geometry changes, although some work remains to be done in order to bring these solutions to the field. Recent improvements in imaging techniques keep fueling the progress towards fully automated tunnel inspection systems to enable remote inspection without direct human intervention.

The relevance of adequate inspection methodologies to signal potential problems that demand focused attention is at the forefront of any monitoring systems for problems that may affect a tunnels' stability. Signaling these defects is crucial for efficient inspection at an early stage, verifying the tunnel status, and carrying out maintenance, where required.

This thesis aims at establishing a highly automated inspection methodology to monitor defects in railway tunnels. Although detect detection and monitoring has been increasingly dominated by systems automation, the author believes that stepping back to defining an inspection and monitoring methodology for both the geometrical and mechanical aspects is pertinent and may have a twofold important impact on quality standards and safety. To achieve an effective inspection system, railway tunnels and its defects are studied here. The present PhD research rests on 3D laser scanning to inspect a tunnel degradation, particularly its structural integrity, through the impact it conveys on the tunnel's geometry. Taking into account the system originality and to assess the applicability and accuracy of the deployed 3D laser system, the implementation of a model prototype is proposed for the laboratory experiments, including a scaled tunnel and an additive manufactured model of a real tunnel. Local defects and geometry changes can be signaled by comparing the obtained 3D profiles and thereby post-processing analysis brought-in to measure variables such as displacement and strain fields with an optical measuring tool based on 3D DIC. In conclusion, encouraging results are presented for evaluating a tunnel's condition and monitoring the tunnel profile in static scanning mode, and further DIC data is presented that shows the displacement field progress of an introduced structural defect.

In the real scale case, the methodology will be implemented by installing instruments on trains so that the tunnel interior wall is scanned when the trains pass through the tunnels during a certain period. The captured images are used to build the tunnel's 3D surface which can be monitored through time. Subsequently, a number of artificial defects and geometry changes were applied and accurately detected. Furthermore, advanced optical non-destructive monitoring techniques such as DIC and thermography were used to monitor and characterize the progression of structural defects.

The potential for a highly automated inspection methodology for SHM in railway tunnels is demonstrated in this thesis. It aims to serve as a stimulus for future development within this field, expanding the design applications and technology maturity levels.

Sumário

Os túneis de ferrovia deterioram-se com o envelhecimento, os factores ambientais, os carregamentos extraordinários, dano de origem humana ou natural, manutenção desadequada e reparações diferidas ou atrasadas. O aumento da percepção destes problemas, no essencial devido aos avanços nas técnicas de análise, acentua a necessidade para implementação de sistemas automáticos de inspecção e monitorização da condição da infraestrutura.

A inspecção destas infraestruturas apoia-se actualmente em metodologias baseadas na experiência, que possuem limitações inerentes à condição humana. No entanto, as aplicações das tecnologias laser têm vindo a expandir-se dramaticamente com custo reduzido e melhoria contínua de resolução. Da mesma forma, os avanços significativos em tecnologias 3D baseadas em imagem nas últimas décadas, têm progredido na direcção da obtenção de soluções superiores para a avaliação automática da condição da infraestrutura a alta-velocidade.

Actualmente, a evolução da Monitorização de Integridade Estrutural (SHM) de túneis ferroviários passa pela substituição das técnicas tradicionais de medição ponto-a-ponto para técnicas de campo inteiro baseadas em imagem. Os recentes progressos nestas técnicas, tais como a Correlação Digital de Imagem (DIC), têm sido dirigidos para a análise de defeitos em grandes estruturas, nas localizações sinalizadas por alterações da geometria 3D, embora várias questões continuem por resolver de forma a trazer estas soluções para o campo. A evolução recente em técnicas de imagem continua a alimentar o progresso na direcção do desenvolvimento dos sistemas de inspecção de túneis totalmente automáticos para suporte à inspecção remota sem intervenção humana directa.

A relevância das metodologias de inspecção adequadas para a sinalização atempada de problemas potenciais que requerem atenção focada encontra-se na vanguarda do desenvolvimento dos sistemas de monitorização para os problemas que afectam potencialmente a estabilidade de infraestrutura. A sinalização destes defeitos é crucial para a inspecção eficaz num estado inicial, verificando o estado da infraestrutura e indicando os locais onde a manutenção é necessária.

Esta dissertação foca-se no estabelecimento de uma metodologia de inspecção automática para monitorização de defeitos em túneis ferroviários. Apesar da detecção e monitorização de defeitos serem crescentemente dominadas pela automação de sistemas, é pertinente a definição de uma metodologia de inspecção e monitorização para ambos os aspectos relacionados com as alterações geométricas e os aspectos mecânicos da infraestrutura, com um importante impacto duplo nos padrões de qualidade e segurança. Para alcançar um sistema de inspecção eficaz, são estudados ambos as infraestruturas de túneis ferroviários e os defeitos a elas associados. O trabalho descrito nesta dissertação apoiou-se no varrimento laser 3D para inspeccionar a degradação do túnel, em particular a sua integridade estrutural, através do impacto que transmite à sua geometria. Tendo em vista a originalidade da metodologia proposta e por forma a avaliar a aplicabilidade e exactidão do sistema laser 3D desenvolvido, foi implementado um protótipo para validação experimental em laboratório, que inclui um túnel em escala reduzida e um modelo de um túnel real, também à escala, produzido por fabrico aditivo. Os defeitos locais e as alterações de geometria resultantes de um carregamento externo foram detectados e sinalizados com precisão por comparação dos perfis 3D obtidos e a análise em pós-processamento para a monitorização dos campos de deslocamento e deformação, a partir de uma ferramenta baseada em DIC 3D, realizada com sucesso. Em conclusão, são apresentados resultados encorajadores para a avaliação da condição da infraestrutura e monitorização do perfil 3D do túnel no modo de varrimento estático, sendo em seguida apresentados os resultados de DIC 3D que mostram o progresso do campo de deformações dos defeitos estruturais introduzidos artificialmente.

Numa aplicação real a metodologia será implementada instalando instrumentos nas composições para digitalizar a parede do túnel à medida que estas progridem ao longo do mesmo. As imagens capturadas serão utilizadas para reconstruir a superfície tridimensional do túnel e monitorizar alterações da geometria adquirida ao longo do tempo.

O potencial para o desenvolvimento de um sistema altamente automatizado de SHM para túneis de ferrovia fica assim sobejamente demonstrado neste trabalho que serve ainda como estímulo para desenvolvimentos futuros neste domínio, expandindo as aplicações do desenho proposto e o nível de maturidade da tecnologia.

Acknowledgements

I would like to express profound gratitude to my supervision group, Professor *Pedro Miguel Guimarães Pires Moreira,* Professor *Paulo José da Silva Tavares* from Institute of Science and Innovation in Mechanical and Industrial Engineering (INEGI) and Faculty of Engineering, University of Porto (FEUP) and Professor *Marcos Massao Futai* from University of São Paulo (USP) for their valuable support, encouragement, great supervision and useful recommendations throughout this PhD research work. Their countless aegis and continuous guidance enabled me to complete my work successfully.

In addition, I acknowledge the immense support received from i-Rail doctoral program coordinator, Professor *Rui Calçada*, for his dedication to organizing the PhD course. In this regard, The Fundação para Ciência e Tecnologia (FCT) funding through the scholarship PD/BD/114095/2015 is also sincerely acknowledged. I would like to thank Professor *José César de Sá*, senior scientist, (the chairman of Doctoral Program in Mechanical Engineering, FEUP) who has organized this PhD course effectively.

The support and collaboration of Eng. *Tiago M. C. Chaves* and Eng. *Alberto J. G. S. M. Baptista* at Tegopi Company are also acknowledged. I sincerely thank to my colleague from USP, Dr. *Pedro Pazzoto Cacciari* for his collaboration.

A very special thanks is also due to all the colleagues at Laboratory of Optics and Experimental Mechanics, LOME, who have indeed been supportive, Eng. *Francisco Barros*, Eng. *Pedro Sousa*, Dr. *Shayan Eslami*, Eng. *Mihai Popescu* and Eng. *Nuno Ramos* for their collaboration throughout the experimental tests and valuable assistance in the framework of the optical measurements. In addition, I would like to acknowledge the constant guidelines from Professor *Rui Carneiro de Barros*, Professor *Paulo Tavares de Castro*, Professor *Jorge Belinha* and Professor *Francisco José de Melo* for their guidelines in theoretical, numerical strategies and practical suggestions developed during this work.

I cannot ever express my appreciation to my parents and brothers for their moral, economical and heartfelt support throughout my PhD course and most importantly, what they have been doing for the past years of my life. I hope that I will pay up their favors in the near future, as they really deserve.

Last, but in no way least important, my wife, always behind me and extremely sympathetic. *Parisa* had to endure her share, and it was not a minor one. Absent nights, missed weekends and events, lack of attention, she has bravely taken all of that and much more. Simply put, this work would not have been possible without her courageous attitude, passion and incentive.

Contents

Chapter 1 : Introduction 1
1.1 Motivation 1
1.2 Problem statement and research questions 2
1.3 Research sites and industrial partners 4
1.4 Thesis outline 4
1.5 Academic publications 6

Chapter 2 : Railway Tunnels, Inspection and Proposed Solutions 11
2.1 Railway tunnels structure 11
2.2 Potential defects and deterioration in concrete tunnels 13
2.3 Real examples of damaged tunnels; evidence and solution 18
2.4 Inspection technologies 23
  2.4.1 Automated inspection-based image processing 25
2.5 Optical NDIs on SHM and defect monitoring 34
  2.5.1 Digital image correlation 35
  2.5.2 Thermography 38
2.6 Numerical simulations 39
2.7 Predictive maintenance 42
2.8 Chapter summary 46

Chapter 3 : Second-stage Inspection Techniques 49
3.1 DIC applications on SHM 50
3.2 Numerical damage analysis on concrete structures 79
3.3 Chapter summary 85

Chapter 4 : Deployed Inspection System 87
4.1 Mathematical formulations 88
  4.1.1 Camera model and calibration 88
4.2 Scaled tunnel: model definition and experiments 91
  4.2.1 Initial geometry 95
  4.2.2 Feature detection 97
  4.2.3 Loaded tunnel 100
  4.2.4 Tunnel containing notches 105
4.3 Real tunnel experiments on a scale model 115
  4.3.1 Geometry acquisition by the 3D LSS 116
  4.3.2 Deformation experiment by the LSS and DIC 121
4.4 Field application, Wind tower experiment 126
  4.4.1 Model Definition and system setup 126
  4.4.2 Experiments and results 129
4.5 Chapter summary 134

Chapter 5 : Conclusions 135
5.1 Concluding final remarks 135
5.2 Future works 137

Appendix A : Camera Calibration 143
Appendix B : Meshless Method 149
Appendix C : Damage Formulation 159
Appendix D : SIF Calculation 163
Appendix E : Gurson- Tvergaard- Needleman Damage Criterion 169
References 173

List of figures

Figure 1.1: Synopsis diagram. 5
Figure 2.1: Typical cracking defect examples in concrete: a) crack with efflorescence [26], b) spalling of lining extended to the opening [27], c) crown spalling [27], d) longitudinal cracks of crown [28], e) transverse crack [28] and f) inclined cracks of side wall [28].. 15
Figure 2.2: Deterioration on concrete tunnel [12]... 16
Figure 2.3: Steel reinforcement corrosion; a) mechanism and b) tunnel deterioration illustration [12]. 17
Figure 2.4: Examples on the leaks in tunnels at, a) cracks, b) segment joints and c) cold joint [12].. 17
Figure 2.5: Example of tunnel failure due to the ground movement [12]. 18
Figure 2.6: Spalling and collapse of concrete lining because of the seismic loading in the Tawarayama Tunnel, Japan. a) Concrete lining spalling along with inclined crack, b) large area vault collapse of crown; and c) concrete lining fallings [28]. 18
Figure 2.7: Typical damages in the Finnish railway tunnels; a) cracks on the interior wall surface and b) water intrusion leads to freezing in cold areas [31]. 19
Figure 2.8: a) Spalling and dense cracking of the liner inside the Longxi tunnel and b) inclined cracking at the sidewall with water leakage and spalling [35]..................... 19
Figure 2.9: Comparable results a) numerical analysis and b) in-situ damage investigation of the tunnel [35].. 20
Figure 2.10: A typical tunnel deformation due to ground stress [36]. 20
Figure 2.11: Damages on Amtrak's 104-year old Hudson River tunnels, New York, the USA [38]. 21
Figure 2.12: A long crack detected on the tunnel interior wall, Haflong, India [39]........... 21
Figure 2.13: Damage on Rossio Railway Tunnel; a) deformation and erosion of the masonry . 21
Figure 2.14: a) Compressive failure in the Tukayama tunnel, b) spalling Mechanism in the Rebunhama tunnel and c) Lining of the Rebunhama Tunnel after spalling, Japan [29]. . 22
Figure 2.15: a) image captured on the wall and b) extracted cracks. 26
Figure 2.16: a) A general view of the CSI inspection system, the tunnel surface scanned by the CSI system c) the extracted crack [74].. 27
Figure 2.17: a) Image acquisition equipment on Metro tunnel inspection, b) crack-only image, c) Leakage-only image, d) Two-defect-non-overlapping image and e) Two-defect-overlapping image [75].. 27
Figure 2.18: a) Obtained 3D point cloud of the tunnel scanned by TLS and b) water leakage detected by CCD camera [76].. 28
Figure 2.19: Developed inspection system; a) prototype of the tunnel inspection platform and b) normalized original, filtered and segmented images on the detected defect [68]. 28
Figure 2.20: a) Constructive aspects of the optical profilemeter, b) Measurement principle of the optical profilemeter and c) internal view of point cloud from the test surface, defect detection [79].. 29
Figure 2.21: a) A schematic perspective of the robotic platform for tunnel lining inspection, b) A slice from tunnel taken with the 3D LSS and c) a crack with water leakage reconstructed from the 3D LSS point cloud [84]................................ 30
Figure 2.22: Modelled tunnel and expanded profile of the train; a) Tunnel surface, b) expanded profile of the train, c) estimated clearances and failures and d) 1 m cross sections; the tunnel mesh is created from the scan data [85].............................. 31
Figure 2.23: a) LSS mounted on an all-terrain vehicle, b) Sensor deployments, c) resolution in terms of the inspection speed, d) Merged tunnel profile and e) detected moisture on tunnel wall [86].. 32
Figure 2.24: Point cloud dataset on the Xieziyan railway tunnel [87]. 33
Figure 2.25: a) the 3D point cloud data before surface flattening and b) 2D point cloud data after surface flattening [88]. 33

Figure 2.26: Tunnel inspection solution based on the laser scanning technology used in Finland; a) the mounted system, b) the system configuration and c) the detected defect and moisture on the tunnel interior wall [31]. 34
Figure 2.27: a) Tested masonry wall and b) horizontal displacement field [92]. 36
Figure 2.28: a) Sketching map of the cracks and b) maximum principal strain field [60]. 36
Figure 2.29: Contours of strain in x-direction at different applied load levels a) 100 kN b) 132 kN; c) 168 kN and d) 146 kN [96]. 37
Figure 2.30: The case study; a) performed four-point-bending test on a RC concrete beam and b) crack localization obtained by DIC for different applied load levels [97]. 38
Figure 2.31: Cracking repair on the tunnel-lining, a) manual maintenance and b) epoxy resins to repair the crack [12]. 42
Figure 2.32: Repair of deteriorating concrete (delamination, spalling, and steel corrosion) [12]. 43
Figure 2.33: The local maintenance performed on the frozen section of the tunnel lining by installation of the new membrane, Finland [140]. 43
Figure 2.34: Tunnel waterproofing approaches; a) crack seals, b) ground grouting, c) surface coatings, d) joints seals, e) membrane sand f) rerouting [12]. 44
Figure 2.35: Additional lining support installation on the tunnel lining [12]. 44
Figure 2.36: Tunnels reinforced by steel panels; a) basic structure, b) a reinforced railway tunnel and c) panel installation by the electric machine [144]. 45
Figure 3.1: AA5352 specimen manufactured according to ASTM E 8M-04, dimensions are in mm [157]. 50
Figure 3.2: DIC system standing in front of tested specimen with a working distance of 1000 mm, b) specimen mounted in the tensile machine, c) camera field of view and d) a facet field respecting speckle pattern. 51
Figure 3.3: Strain evolution obtained from DIC for AA5352 specimen, a) longitudinal strain, b) transverse strain and c) shear strain. 52
Figure 3.4: Reaction force response on point A in terms of the displacement variation, ΔvCB obtained from experimental uniaxial tensile test [157]. 53
Figure 3.5: Numerical model of AA5352 specimen; a) FE mesh and b) meshless nodal distribution [157]. 54
Figure 3.6: Reaction force response on point A correlated with the displacement variation ΔvCB obtained from all studies [157]. 55
Figure 3.7: Equivalent von Mises stress obtained for a) FEM-Abaqus, b) FEM-3n, c) RPIM, d) NNRPIMv1 and e) NNRPIMv2 [157]. 55
Figure 3.8: Standard bi-failure specimen: a) a general view, b) front view on the central section and c) side view of the central section, values are in mm. 56
Figure 3.9: Experimental setup of the bifailure specimen; a) the 3D DIC system standing in front of the specimen and b) specimen and grips [3]. 58
Figure 3.10: a) DIC domain and details on the notches presenting auxiliary points and b) detail on a facet field and speckle pattern [159]. 59
Figure 3.11: Computational AA6061-T6 elastoplastic model with the essential boundary condition illustration; a) FEM and b) RPIM meshless method. 60
Figure 3.12: Remote stress correlated with the longitudinal strain variation on; a) left side notch, and b) right side notch, obtained for all approaches [159]. 61
Figure 3.13: Strain distribution extracted at the end of the elastoplastic analysis: top row: DIC, middle row: FEM and bottom row: RPIM meshless study [159]. 62
Figure 3.14: Equivalent von Mises strain distribution obtained at the end of the elastoplastic analysis: a) DIC, b) FEM and c) RPIM [159]. 62
Figure 3.15: Force response vs. vertical displacement on AA6061-T6 w4 obtained for central sections, DIC and FEM [3]. 63
Figure 3.16: Modified bi-failure specimen, AA6061-T6 W1.5: a) a general view with geometrical dimension presentation and b) FEM model, dimensions are in mm. 64
Figure 3.17: Failure evolution; top row: AA6061-T6 W4 and bottom row:AA6061-T6 W1.5 [3]. 64
Figure 3.18: Force-displacement response on AA6061-T6 W1.5 [3]. 65
Figure 3.19: Numerical DP600 model with the essential boundary condition illustration; a) FEM and b) RPIM and NNRPIM meshless method [160]. 66
Figure 3.20: Load/displacement response for DP600 analysis captured on: a) left, b) central and c) right side notch [160]. 67

Figure 3.21: DP600 Analysis; Top: Logarithmic transverse strain and bottom: Logarithmic longitudinal strain profile derived from a) DIC, b) FEM, c) RPIM, d) NNRPIMv1 and e) NNRPIMv2 [160]. 68
Figure 3.22: Engineering stress/strain curves on DP600 analysis sorted for a) left side notch [P_2 and P_1], b) right side notch [P_6 and P_5] and c) central notch [P_4 and P_3] [160]. 69
Figure 3.23: Logarithmic strain profiles plotted with logarithmic contour intervals, a) longitudinal strain-DIC, b) longitudinal strain-GTN, c) ε-DIC and d) ε-GTN [160]. 70
Figure 3.24: TF in side notches; a) before first failure, b) after first failure, c) after second failure and d) TF vs. engineering strain in the loading direction, GTN analysis [160]. ... 71
Figure 3.25: Aluminium CT specimen used in the experimental test, a) geometry representation, b) before surface preparation and c) DIC speckle pattern [161]. 71
Figure 3.26: a) the 3D DIC system standing in front of the tested specimen, and b) travelling microscope to measure the crack size. 72
Figure 3.27: Crack propagation vs. fatigue cycles, read by travelling microscope, [161]. 72
Figure 3.28: Numerical CT model, essential and natural boundary conditions and intended region representation; (a) FE and (b) meshless model [161]. 73
Figure 3.29: Opening strain distribution [161]. 74
Figure 3.30: A general view of the tested polycarbonate central notch MT specimen, dimensions are in mm [163]. 75
Figure 3.31: a) the 2D DIC standing in front of the specimen and b) experimental setup [163]. 76
Figure 3.32: MT specimen; a) applied boundary conditions, b) detail on anticipated dead zone, c) FOV and d) a facet field with speckle size [163]. 77
Figure 3.33: Numerical model respecting applied boundary conditions a) FEM mesh and b) nodal discretization for meshless methods [163]. 77
Figure 3.34: Longitudinal strain profile; a) DIC, b) FEM, c) RPIM, d) NNRPIMv1 and e) NNRPIMv2 analyses [163]. 78
Figure 3.35: Longitudinal strain profile mapped on the dead zone for a) DIC, b) FEM, c) RPIM, d) NNRPIMv1 and e) NNRPIMv2 analyses [163]. 78
Figure 3.36: Concrete three-point-bending beam: a) geometry and b) RPIM nodal pattern [127]. 80
Figure 3.37: The final analysis results correspond to a) force response vs. deflection on point A and b) damage variation versus effective strain at the crack tip [164]. 81
Figure 3.38: Total damage evolution for concrete three-point-bending beam at different displacement impositions a) 1.2841E-01 mm, b)1.7526E-01 mm and c) 3.1581E-01 mm [164]. 81
Figure 3.39: Concrete CT specimen: a) geometry and b) RPIM nodal discretization [127]. 82
Figure 3.40: Load response versus mouth opening of the hole, Q , obtained for different nodal discretizations [127] compared to the experimental solution [168]. 83
Figure 3.41: Total damage distribution for different RPIM nodal discretizations; a) 259, b) 498, c) 1009 and d) 2165 nodes [127]. 84
Figure 3.42: a) Equivalent total von-Mises stress profile and b) Equivalent damaged von-Mises stress profile [127]. 84
Figure 3.43: Total damage in terms of effective strain [127]. 84
Figure 4.1: A general view of the developed inspection system. 88
Figure 4.2: The slider adopted for the developed 3D LSS. 92
Figure 4.3: Deployed 3D LSS; a) a general view of the system, b) top and c) side view. 93
Figure 4.4: a) A-9×8-checker board used for the calibration, laser light projection illustration, b) re-projection error in pixels acquired from calibration procedure and c) camera and laser position in the scaled tunnel experiment. 94
Figure 4.5: the 3D structured light scanning system experiment, reference solution, a) setup and b) Initial tunnel profile. 96
Figure 4.6: Initial tunnel experiment performed by the 3D LSS a) projected laser light on the scaled tunnel interior wall and b) obtained point cloud. 96
Figure 4.7: Objects used for feature detection experiments with the dimension illustration: a) object 1, plastic block, b) object 2, plastic block, c) object 3, adhesive tape, d) object 4, plastic wire and e) a general view of the objects attached to the interior wall. 98
Figure 4.8: Obtained results from feature detection LSS experiments: a) object 1, b) objects 1 and 2, c) objects 2, 3 and 4 and d) detail on all objects. 99

Figure 4.9: Loaded tunnel experiment a) mechanical setup and b) displacement imposition configuration. 100
Figure 4.10: a) Graphical representation of acquired point clouds and b) one frame point cloud corresponding to position where the displacement was imposed, notice that the tunnel was loaded on point P. 101
Figure 4.11: One frame extraction on tunnel mid-section where displacement imposed from exterior wall, inner diameter measurements. 102
Figure 4.12: The 3D DIC analysis: a) adopted DIC system, b) a schematic view of the system arrangement, c) cameras positioned in front of the interest region, d) calibration pattern, e) camera FOV with its dimensions and f) a facet field with the speckle pattern presentation. 103
Figure 4.13: Displacement field obtained from the DIC analysis. 104
Figure 4.14: Defects built in the tunnel's interior wall, arranged respecting z-direction, a) a general 2D view of the tunnel wall with the notches, b) horizontal, c) vertical and d) angled notch. 105
Figure 4.15: Tunnel containing notch experiments, a) horizontal notch, b) vertical notch, c) angled notch configurations. 106
Figure 4.16: a) Loading mechanism adopted for horizontal and angled notches, b) loading mechanism for vertical notch, c) DIC system for horizontal and angled notches and d) DIC adopted for the vertical notch. 107
Figure 4.17: DIC results for the vertical notch loading experiment for different displacements: top row: y-displacement perpendicular to the notch plane; middle row εxx, and; bottom row εzz. 108
Figure 4.18: DIC results obtained for the angled notch experiment measured for various displacement impositions, top row: x-displacement perpendicular to the notch plane; middle row εyy, and; bottom row εzz. 109
Figure 4.19: The LSS experiment extracted point cloud; a) profile with the detected horizontal defect and b) notch plane, points coordinates. 110
Figure 4.20: FE model of the horizontal notch study, a) a general view and b) displacement imposition illustration on the exterior wall adjacent to the notch plane. 111
Figure 4.21: Displacement profile in x-direction perpendicular to the notch plane, Top row extracted from the 3D DIC and bottom row derived from the FEM. 112
Figure 4.22: Strain profile, $\varepsilon yy,$ evolution on the notch plane. Top row shows the deformation fields obtained with the 3D DIC and the bottom row shows the FEM results. 112
Figure 4.23: Strain profile εxx evolution on the notch plane. Top row shows the deformation fields obtained with the 3D DIC and the bottom row shows the FEM results. 113
Figure 4.24: Notch plane of the horizontal defect case study respecting the auxiliary points, a) DIC and b) FE model. These points are used to validate obtained results. 114
Figure 4.25: Point cloud of Monte Seco tunnel scanned by the 3D TLS technique. 116
Figure 4.26: Generated 3D surface of the point cloud, Monte Seco tunnel. 117
Figure 4.27: Additive manufactured tunnel model, a) a general view of the tunnel and b) a side view with its real dimensions. 117
Figure 4.28: The developed 3D LSS for the real tunnel shape acquisition, a) a general view of the components, b) top view and c) side view of the system. 118
Figure 4.29: The LSS image acquisition, a) the tunnel marked with the corks, b) the obtained point clouds in status 1 and c) status 2. 119
Figure 4.30: a) The obtained point cloud of tunnel from the LSS with its geometrical properties and b) the reduced point cloud. 120
Figure 4.31: a) Compressive loading mechanism imposed by a displacement enforcement on point P and b) details on Point P. 121
Figure 4.32: a) A general view of deformation experiment respecting the LSS and DIC systems, b) a schematic view of DIC system, c) speckle pattern respecting a-21×21-pixel^2 facet field and d) the DIC system standing in front of interest region where loading is applied. 122
Figure 4.33: A 3D view of the reference and deformed profile of the tunnel obtained by the LSS, a) original and b) simplified point clouds. 123
Figure 4.34: X-displacement field obtained from DIC analysis for a) reference, b) deformed status; $u = 11.5\ \mathrm{mm}$. 124

Figure 4.35: One-frame-point-cloud extraction on different sections as described in the DIC analysis, a) section 1, b) section 2 and c) section 3. 125
Figure 4.36: A-9-meter-long cylindrical wind tower, field experiment; Tegopi Company. ...126
Figure 4.37: a) Adopted LSS for tower experiment and b) system mounted on the welding robot's arm. 127
Figure 4.38: a) A 9-by-8-square calibration pattern, b) laser projection on the calibration pattern, c) re-projection error and d) laser and camera positions. 128
Figure 4.39: A general view of the LSS experiment in the tower model. 129
Figure 4.40: Tower exterior wall with the roller presentation and b) the magnetic bases hold on the interior surface of the tower. 130
Figure 4.41: An individual RGB image captured by the camera over the image acquisition, a) Half_one experiment and b) Half_two experiment. 131
Figure 4.42: Image processing steps performed to convert the RGB into binary image, a) original RGB image, b) ROI, c) CIELAB a*, d) BG, e) CIELAB L* and f) TH2 conversion. .132
Figure 4.43: Binary image derived from image processing for; a) Half_one experiment and b) Half_two experiment. 133
Figure 4.44: a) A 3D view of the tower profile and b) a top view of the tower with its dimensions obtained by the LSS. 133
Figure 5.1: a) The Monte Seco railway tunnel detail and b) a schematic view on the designed system. 138
Figure B.1: A RPIM problem domain and its influence domain with regard to the interest point and an integration cell with 3×3 integration points in the discrete model illustration [157]. 150
Figure B.2: a) Voronoï Diagram, b) Natural neighbours, c) Sub-cells obtained by the overlap of a cell of the Voronoï diagram and the Delaunay tessellation of that cell, d) Application of the quadrature points (one in each sub-cell) following the Gauss-Legendre integration scheme and e) Mesh of the integration points [157]. 151
Figure B.3: a) a 7×4 regular nodal discretization, b) irregular arrangement with λ=2 and c) irregular arrangement with λ=5 [182]. 151
Figure B.4: The 3D thin plates and b) stress components in plane stress state [105]. 154
Figure B.5: Nonlinear K_{T0} algorithm, it is based on the incremental displacement imposition and stress returning mapping scheme [159]. 158
Figure C.1: Arrangement of the interest point and accepted neighbour points for non-local damage process [165]. 161
Figure C.2: Numerical algorithm of non-local damage model [165]. 162
Figure D.1: a) Ideal unloaded region, the red highlighted region depicts the stress dead zone, b) central notch MT specimen and c) dead zone characteristics [163]. 166

List of tables

Table 2.1: List of main in-service rail tunnels in Portugal. 12
Table 2.2: Classification of common defects in the concrete tunnels and respective severity scales [19]. 15
Table 3.1: Material properties and experimental configurations on bi-failure tests [3], [159], [160]. 57
Table 3.2: Main parameters in GTN model, FE analyses [3], [160]. 57
Table 3.3: The correctness degree of the DIC calibration [159]. 59
Table 3.4: DIC specifications for AA6061-T6 and DP600 experiments. 59
Table 3.5: Experimental test characteristics on Aluminium CT specimen [161]. 72
Table 3.6: $\Delta \mathrm{KI}\ \mathrm{MPa.mm0.5}$ obtained for various crack lengths on CT specimen [161]. 74
Table 3.7: Material characteristics of Polycarbonate, Optical Grade [163]. 75
Table 3.8: Mode I SIF obtained from all methods, values are in (MPa.mm^0.5) [163]. 77
Table 3.9: Dead zone characterizations [163]. 78
Table 3.10: Assessment on point B: RPIM [127], FEM [168] and experimental solution [167]. 83
Table 4.1: Properties of AlfaGAS, EN 1555 SDR 17, PE100 pipe, extracted from manual. 92
Table 4.2: Optical instruments technical specification adopted for the 3D LSS. 93
Table 4.3: Camera and laser calibration results, scaled tunnel experiments. 94
Table 4.4: Inner diameter measured by the 3D structured light (reference) and LSS. 97
Table 4.5: Geometrical characteristics of the objects in the feature detection experiments measured by LSS. 98
Table 4.6: Point cloud extracted from each experiment, loaded tunnel state. 102
Table 4.7: Point coordinates acquired for the loaded tunnel experiments. 102
Table 4.8: Key features of the webcam and the calibration solution adopted for the DIC analysis, loaded tunnel experiment. 104
Table 4.9: X-displacement variation obtained for distinct displacement impositions, the LSS and the DIC. 104
Table 4.10: Notch dimensions measured by LSS experiments compared to the real values. 107
Table 4.11: Horizontal notch coordinates obtained from the LSS. 110
Table 4.12: Assessment on acquired results from DIC and FEM, vertical notch experiment. 114
Table 4.13: Material properties of the PLA used for the 3D printing. 117
Table 4.14: Calibration results for the real (additive manufactured) tunnel example. 118
Table 4.15: Comparison on tunnel dimensions, real tunnel model. 120
Table 4.16: Correctness degree of DIC calibration, real additive manufactured tunnel. 123
Table 4.17: Points coordinate related to different sections defined on DIC problem domain. 124
Table 4.18: Comparison on the displacement variation obtained from DIC and LSS studies. 124
Table 4.19: Key features of camera and calibration results used in the tower experiment. 129
Table 4.20: Experimental test configurations, field experiment. 131
Table 5.1: Technical specifications of the designed system proposed for the future plan. 139
Table 5.2: Details of the designed LSS system for the future plan. 139
Table C.1: Weight function for non-local damage analysis [165]. 161

Abbreviations and Symbols

List of Abbreviations

1D	One-dimensional
2D	Two-dimensional
3D	Three-dimensional
ASTM	American Society for Testing and Materials
CCD	Charged Couple Device
CIELAB	International Commission on Illumination L*a*b*
CT	Compact Tension
DIC	Digital Image Correlation
ESPI	Electronic Speckle Pattern Interferometry
FE	Finite Element
FEA	Finite Element Analysis
FEM	Finite Element Method
FEUP	Faculty of Engineering of The University of Porto
FOV	Field of View
FRP	Fiber Reinforced Polymer
GFRP	Glass Fiber Reinforced Polymers
GTN	Gurson Tvergaard Needleman
INEGI	Institute of Science and Innovation in Mechanical and Industrial Engineering
LED	Light-Emitting Diode
LEDM	Linear Elastic Damage Mechanics
LEFM	Linear Elastic Fracture Mechanics
LOME	Laboratory of Optics and Experimental Mechanics
LSS	Laser Scanning System
MCSRD	Modified Cross-Section Racking Deformation
MLE	Maximum Likelihood Estimation
MRE	Mean Re-projection Error
MT	Middle Tension
NDI	Non-Destructive Inspection
NDT	Non-Destructive Tests
NNRPIM	Natural Neighbor Radial Point Interpolation Meshless Method
NNRPIMv1	The First-Degree Influence-Cell of NNRPIM
NNRPIMv2	The Second-Degree Influence-Cell of NNRPIM
PLA	Polylactic Acid
PP	Polypropylene
RBF	Radial Basis Function

RF	Reference Point
RGB	Red, Green and Blue light
ROI	Region of Interest
RPI	Radial Point Interpolator
RPIM	Radial Point Interpolation Meshless Method
SERR	Strain Energy Release Rate
SFRC	Steel Fibre Reinforced Concrete
SHM	Structural Health Monitoring
SIF	Stress Intensity Factor
TF	Stress Triaxiality factor
TLS	Terrestrial Laser Scanning
TRL	Technology Readiness Level
UTS	Ultimate Tensile Stress
USP	University of São Paulo
XFEM	Extended Finite Element Method

List of symbols

$\boldsymbol{A}$	Intrinsic matrix
A	Area
$A_{ef.}$	Effective Cross section
$\boldsymbol{a}$	Cone axis
a	Crack length
a_0	Initial notch
$\boldsymbol{B}$	Deformation matrix
b	Notch opening
$\boldsymbol{C_m}$	Material constitutive matrix
C	Compliance
D	Width
D_o	Outer diameter
D_i	Inner diameter
$D_i^{ref.}$	Reference diameter of the tube
D_i^{Real}	Real diameter of the tube
d	Damage
d_{iI}	Distance
d_{total}	Total damage
E	Young's modulus
E_{T0}	Tangent modulus
e	Thickness
e_{ii}	Deviatoric strains
F	Focal length
f	Frequency
f^*	Total effective VVF
f_0^+	Max. Uniaxial tensile strength
f_0^-	Max. Uniaxial compressive strength
f_c	Critical void volume fraction
f_f	Total VVF at total failure
f_N	Volume fraction of void nucleation
f_s	Camera framerate
G	Strain energy release rate
G_f	Fracture energy
H	Height
ΔK	SIF range
α	Intrinsic parameter

$\boldsymbol{K}$	Global stiffness matrix
k_i	Radial distortion coefficients
L	Length
l_0	Initial clip gauge length
N	Index of the current frame
n_i	Node
$\boldsymbol{O}_L$	The camera origin
P	Applied force
p_i	Tangential distortion coefficients
q_i	Material constants
$\boldsymbol{R}$	Rotation matrix
R_L	Load ratio
S_N	Standard deviation
S_Y	Yield strength
$\bar{v}$	Vertical displacement imposition
T	Temperature
$\boldsymbol{T}_L$	Cone vertex position
$\boldsymbol{t}$	Translation vector
$toler$	Tolerance
U	Total strain energy
UTS	Ultimate tensile stress
$\boldsymbol{u}$	Displacement vector
u_i	Horizontal displacement imposition
V_z	Constant linear velocity
W, w	Specimen width
$\boldsymbol{X}$	Space domain
$\boldsymbol{X}_C$	Camera's frame of reference
$\boldsymbol{X}_L$	Laser's frame of reference
$\boldsymbol{X}_w$	Point's world coordinates
$\boldsymbol{x}_h$	Homogeneous coordinates
$\boldsymbol{x}_{laser}$	Laser points
$\hat{\boldsymbol{x}}$	Checkerboard corner
$\mathcal{K}$	Thermoelastic coefficient
$\mathbb{N}$	Natural numbers
$\mathbb{R}$	Real numbers

β	Intrinsic parameter
β_{DIC}	Angle, DIC
ρ	Density
υ	Poisson’s ratio
$\boldsymbol{\varepsilon}$	Strain tensor
ε_{ii}	Normal strain
ε_p	Plastic strain
ε_N	Mean void nucleation strain
$\tilde{\varepsilon}$	Equivalent von Mises strain
$\dot{\varepsilon}$	Strain rate
$\bar{\dot{\boldsymbol{\varepsilon}}}^p$	Plastic strain rate tensor
ε_0^+	Max. Uniaxial tensile strain
ε_0^-	Max. Uniaxial compressive strain
$\bar{\varepsilon}^p$	Equivalent plastic strain
$\bar{\varepsilon}_f^p$	Critical equivalent plastic strain
F	Subset centre at the source in DIC
γ_{ii}	Shear strain
$\tilde{\sigma}$	Equivalent von Mises stress
σ_{ii}	Normal stress
τ_{ii}	Shear stress
σ_{amp}	Stress amplitude
Ω	Problem domain
λ	Irregularity parameter
$d\lambda$	Plastic strain rate multiplier
$d\boldsymbol{\varepsilon}_p$	Plastic strain rate
φ	Laser aperture
γ	Skewness
δ	Imposed vertical displacement
g	Target point in DIC
$\boldsymbol{\sigma}$	Stress tensor

Chapter 1 : Introduction

The present PhD research focused on railway tunnels inspection, addressing the geometry changes, and defect detection and monitoring. The proposed technological design followed an image-based technique and a demonstrator relying on the three-dimensional (3D) Laser Scanning System (LSS) was built. The inspection system has been primarily deployed and studied for a scaled railway tunnel for laboratory tests and implemented on a real tunnel manufactured by an additive technique. Having developed some degree of confidence in the laboratory scaled process and small sized tunnel experiments, the field application of the deployed LSS was carried out on the geometry acquisition of a wind tower section.

Relevant applications in structural integrity components of railway tunnels were also taken into account in this study that add to the innovation capacity of structural health monitoring (SHM) systems for railway structures.

Overall, the main objective in this research is the development of new design concepts and understanding effects of a new technology, considering the different aspects and safety implications during railway tunnels' life. In addition, the significance of the optical non-destructive inspection (NDI) tools, including the Digital Image Correlation (DIC) in the SHM of the engineering structures is also emphasized as the second-stage inspection technologies throughout studying several benchmark examples.

1.1 Motivation

The latest developments in automation science and laser technology that support the development of contemporary tunnel inspection systems, increasingly focus on the automation of these systems in comparison with the formerly operated systems. Additionally, the continuous decrease in system component cost stimulates the widespread increase in research and the number of structural monitoring applications. Therefore, SHM on railway tunnels relying on full-field image-based approaches is becoming widely applicable. Recent improvements in optical NDI techniques, such as DIC [1]-[4] and thermography [5]-[10], have been adopted to examine defects in structural components. Hence, these progresses in optical

NDI imaging techniques keep fuelling the advances towards fully automated tunnel inspection systems to enable full-field inspection with no direct human interventions.

The significance of commensurate inspection methodologies to address potential problems is at the forefront of monitoring systems for problems that may affect a tunnels' integrity. Detecting and characterising these defects is decisive for effective inspection, investigating the tunnel state, and rescheduling maintenance operations, if necessary. Commonly, most railway tunnels are made of concrete-based materials, and their walls may encompass isolations such as fibre polymers, composites or metallic panels. Therefore, the main defects typically found in a tunnel are cracks, spalling and efflorescence/leakage. The use of computer vision measuring techniques, such as DIC or thermography methods, may provide an appropriate response for the analysis of those defects and check whether a structure that has been functional for years is still operationally safe, once those defects have been detected and monitored.

Therefore, considering both mechanical and geometrical aspects of the tunnel inspection, a novel automated technological solution is proposed in this PhD research for laboratory studies (TRL 3) with the potential to be implemented in real scale railway tunnels for geometry change appraisal and defect characterisations (TRL 6/7).

1.2 Problem statement and research questions

Currently, civil infrastructures (railway tunnels) are progressively deteriorating and can be in prompt necessity of inspection, damage assessment and repair due to senescence, environmental factors, over loading, operation alterations as well as insufficient maintenance or deferred repairs. The declared requirements are more than deceptive in underground transportation tunnels including a number of tunnels operating for more than half centuries which already present large evidences of corrosion, and in some cases, structural collapse [11].

In this work, different tunnel models are studied in which a 3D shape acquisition is implemented. The project intends to fulfil an inspection requirement of real railway tunnels. The developed system has the potential to avoid the presently performed manual inspection by human workers in tunnel environments. On the other hand, this work enables the detection of defects, mainly cracks to suggest a repair solution for maintenance. Therefore, future systems might be capable of both inspection and maintenance with minimal human intervention without supervision. Much research is ongoing to devise more efficient systems, capable of performing more accurate and cost-effective inspection, maintenance and assessment of structural integrity components that revert in safer environments and smaller costs in repair operations [11]-[18].

However, the main question that the proposed thesis intends to answer is:

- ➢ Can a fully automated inspection system be adopted as a new technological alternative for railway tunnels examination?

Due to the broad nature of this research question, many multidisciplinary topics needs to be addressed. Since railway tunnels are demanding structures in terms of construction materials and reinforcements, a set of secondary research queries ought to be taken into account to facilitate the resolution of the main research question, as follows;

- How is it possible to comprehensively detect and measure geometrical changes and evaluate their interaction in the condition monitoring of railway tunnels infrastructure?
- How it is possible to adopt the optical non-destructive inspection (NDI) tools for the efficient and on-demand updating of tunnels' stability parameters in defect detection and assessment models?
- What are the efficient approaches based on the image processing techniques to assess the SHM of the related engineering components?
- How the numerical simulations assist to study defects and predict the structures' lifetime?

In summary, the requirements that the proposed new technologic design should reply to, are the following:

- ➢ High cost of modern tunnel constructions (necessity for inspection, assessment and repair of existing damages);
- ➢ Inspection and assessment should be immediate to minimize tunnel operation disruption;
- ➢ Engineering times on tunnel inspection and assessment are rigorously restricted;
- ➢ Presently tunnel inspections are mainly accomplished throughout scheduled, periodic, tunnel-wide visual observations by inspection personnel experienced in recognising structural defects and classifying them manually, which is a slow and labour expensive procedure;
- ➢ By means of computational analyses, the SHM of the civil and mechanical structures can be assessed.

However, this PhD project was carried out in the scope of *i-Rail* doctoral programme, *Innovation in Railway Systems and Technologies*, at FEUP respecting the research and innovation area as follows:

- Cost Efficient and Reliable High Capacity Infrastructure;
- TD 3.5 Cost effective Tunnel solutions.

The following concepts have been proposed in the initial proposal of this PhD course by the scientific council of *i-Rail*:

(i) Implement an automatic high-speed 3D shape acquisition with texture analysis;

(ii) Develop a proprietary image processing solution for automatic defect detection such as moisture stains;
(iii) Consecutive 3D shape differences beyond a certain threshold which signal defects such as geometry change or concrete cracks, will trigger on-site inspection;
(iv) Low-cost 3D Digital Image Correlation (DIC) supplied at signalled tunnel deformation sites.

1.3 Research sites and industrial partners

The multidisciplinary modality of the deployed model has been addressed through the collaboration amongst university, research institute and industrial partners. The major intervening entities in this research have been:

FEUP *Faculty of Engineering, University of Porto*, a public university located in Porto, Portugal focusing on the research and engineering science, which is the host of this PhD research work. Some experimental tests and numerical analyses have been performed here.

INEGI *Institute of Science and Innovation in Mechanical and Industrial Engineering*, a Research and Technology Organization linking the University with the Industry. INEGI focuses on the Applied Research and Development, Innovation and Technology Transfer activities for the industry. INEGI is located inside the FEUP. Research accomplishments have been carried out at its Laboratory of Optics and Experimental Mechanics (LOME), from system design, optical equipment to experimental testing and analyses. The Structural Health Monitoring (SHM) analyses on the metallic structures and polymers have been performed here.

TEGOPI, a private company located in Vila Nova de Gaia, Portugal, with an important export volume in mechanized chassis, container-handling equipment, and structures for wind generation, electrical equipment modules. The field application test has been performed here on the manufactured wind towers, acquiring the inner geometry of wind turbine towers by the developed inspection system.

EPUSP *Polytechnic School of the University of São Paulo*, an engineering school in the University of São Paulo located in São Paulo state, Brazil. A part of research has been carried out at EPUSP with collaboration with Professor Marcos M. Futai and his research team and the obtained results have been exploited in the analysis of the real experiment.

1.4 Thesis outline

The investigation conducted in this PhD dissertation aimed at clarifying the queries indicated in this chapter and comprised in the field of technological progress for railway infrastructures applications. Figure 1.1 presents an overview on the accompanied study.

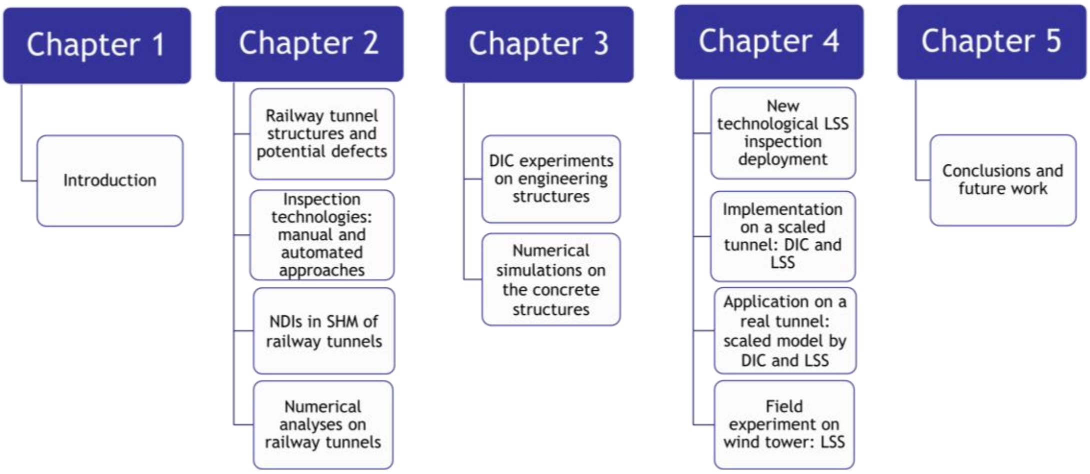

Figure 1.1: Synopsis diagram.

This Dissertation is structured in five chapters from the introduction to conclusions. This first chapter focuses on the work developed in the thesis framework in which the following aspects are taken into account; motivation, problem statement, potential research queries, involved institutions and academic publications.

Chapter 2 presents an overview on the railway tunnel structures and also reviews the innovation and adoption of new technologies to this end. A considerable attention is given to technologies that will integrate the solution to be developed, i.e., geometrical changes in the tunnels and defect characterization. It thereby includes the proposed solutions on the tunnel maintenance. This review sets the state-of-the-art in relation to the inspection system technologies and NDI tools on the SHM; discusses their limitations and potential advantages for defined experimental activities that are later described in following chapters.

Chapter 3 concentrates on the applications of the proposed NDIs as the second-stage inspection technologies. In essence, the SHM investigations on engineering structures related to the railway components are offered. The presented benchmarks are mainly experimentally performed and validated numerical simulations, over the PhD research, in concrete, steel, aluminum alloys and polymers structures. In summary, the influence of the implementation of the image processing method development on the structural integrity components are evaluated in this chapter.

In chapter 4, the technological inspection system deployment based on the 3D LSS for the railway tunnels is presented. As a preliminary study, a scaled tunnel model is taken into account for the laboratory tests including the experimental activities and numerical modeling steps. The system components comprising optical and mechanical instruments are described in this chapter. Moreover, mathematical formulations of the adopted optical system are elaborated here. The performed experimental tests on different tunnel states are thereby demonstrated. To monitor the defects, a contactless measuring system is developed based on the 3D DIC leading to validate the obtained LSS solution. The model is thereby numerically solved, and the obtained mechanical behavior of the tunnel was validated by experimental results, to serve as future design tools. Next stage, an additive manufactured model of a real tunnel, known as *Monte Seco tunnel*, is considered to implement the deployed 3D LSS led to document its geometry. Similar to the scaled tunnel experiment, this tunnel is also loaded, and the deformation is captured by the 3D LSS and the developed 3D DIC and a comparison is drawn amongst the obtained results. Moreover, a field application is also considered by conducting an experiment on a wind tower section to acquire its profile.

Chapter 5 includes the inclusive final remarks of the accomplished work in addition to proposal of some potential future expansions and research approaches within the topics oriented through this dissertation.

1.5 Academic publications

The investigation presented in this dissertation has already been published by the author in scientific journals and conferences. Part of the results represented in this document may, among others, be found also in the references listed below:

Chapter 2: B. V. Farahani, P. J. Sousa, F. Barros, P. J. Tavares, and P. M. G. P. Moreira, "Advanced image based methods for structural integrity monitoring: Review and prospects," in AIP Conference Proceedings, 2018, vol. 1932. https://doi.org/10.1063/1.5024176.

Chapter 2: S. Eslami, B. V. Farahani, P. J. Tavares, and P. M. G. P. Moreira, "Fatigue behaviour evaluation of dissimilar polymer joints: Friction stir welded, single and double-rivets," International Journal of Fatigue, vol. 113, pp. 351-358, 2018. https://doi.org/10.1016/j.ijfatigue.2018.04.024.

Chapter 2: B. V. Farahani, J. Berardo, J. Belinha, A. J. M. Ferreira, P. J. Tavares, and P. Moreira, "An Optimized RBF Analysis of an Isotropic Mindlin Plate in Bending," Procedia Structural Integrity, vol. 5, pp. 584–591, 2017. https://doi.org/10.1016/j.prostr.2017.07.018.

Chapter 2: B. V. Farahani, J. Berardo, J. Belinha, A. J. M. Ferreira, P. J. Tavares, and P. M. G. P. Moreira, "On the optimal shape parameters of distinct versions of RBF meshless methods for the bending analysis of plates," Engineering Analysis with Boundary Elements, vol. 84, pp. 77–86, 2017. https://doi.org/10.1016/j.enganabound.2017.08.010.

Chapter 2: B. V. Farahani, P. J. Tavares, P. M. G. P. Moreira, and J. Belinha, "Stress intensity factor calculation through thermoelastic stress analysis, finite element and RPIM meshless method," Engineering Fracture Mechanics, vol. 183, pp. 66–78, 2017. https://doi.org/10.1016/j.engfracmech.2017.04.027.

Chapter 2: B. V. Farahani, P. J. Tavares, and P. M. G. P. Moreira, “SIF Determination with Thermoelastic Stress Analysis,” in Procedia Structural Integrity, 2016, vol. 2, pp. 2148-2155. https://doi.org/10.1016/j.prostr.2016.06.269.

Chapter 3: B. V. Farahani, R. Amaral, P. J. Tavares, P. M. G. P. Moreira and A. dos Santos “Material Characterization and Failure Assessment on AA5352 Aluminum Alloys Using Digital Image Correlation,” The Journal of Strain Analysis for Engineering Design, June 2019, Peer Review in Process.

Chapter 3: B. V. Farahani, S. Eslami, F. Q. de Melo, P. J. Tavares, P. M. G. P. Moreira, “Concept of Stress Dead Zone in Cracked Plates: Theoretical, Experimental and Computational Studies,” Fatigue & Fracture of Engineering Materials & Structures, 2019, In Press. https://doi.org/10.1111/ffe.12988.

Chapter 3: B. V. Farahani, J. Belinha, R. Amaral, P. J. Tavares, and P. M. P. G. Moreira, “Extending radial point interpolating meshless methods to the elasto-plastic analysis of aluminium alloys,” Engineering Analysis with Boundary Elements, vol. 100, pp. 101-117, 2019. https://doi.org/10.1016/j.enganabound.2018.02.008.

Chapter 3: B. V. Farahani, J. Belinha, P. J. Tavares, and P. M. G. P. Moreira, “Elastoplastic response and failure assessment of steel alloys: Empirical and computational analyses,” Fatigue & Fracture of Engineering Materials & Structures, vol. 42, no. 6, pp. 1247-1261, 2018. https://doi.org/10.1111/ffe.12914.

Chapter 3: B. V Farahani, J. Belinha, P. J. Tavares, and P. M. Moreira, “A nonlinear simulation of a bi-failure specimen through improved discretisation methods: A validation study,” The Journal of Strain Analysis for Engineering Design, vol. 53, no. 8, pp. 616-629, 2018. https://doi.org/10.1177/0309324718795055.

Chapter 3: B. V. Farahani, J. Belinha, R. Amaral, P. J. Tavares, and P. Moreira, “A digital image correlation analysis on a sheet AA6061-T6 bi-failure specimen to predict static failure,” Engineering Failure Analysis, vol. 90, pp. 179-196, 2018. https://doi.org/10.1016/j.engfailanal.2018.03.011.

Chapter 3: B. V. Farahani, P. J. Tavares, J. Belinha, and P. Moreira, “Compact tension fracture specimen: Experimental and computational implementations on stress intensity factor,” The

Journal of Strain Analysis for Engineering Design, vol. 53, no. 8, pp. 630–647, 2018. https://doi.org/10.1177/0309324718763189.

Chapter 3: B. V. Farahani, J. Belinha, P. J. Tavares, and P. M. G. P. Moreira, “An Elasto-plastic Analysis of a DP600 Bi-Failure Specimen: Digital Image Correlation, Finite Element and Meshless Methods,” Procedia Structural Integrity, vol. 5, pp. 1237–1244, 2017. https://doi.org/10.1016/j.prostr.2017.07.092.

Chapter 3: B. V. Farahani, J. Belinha, P. J. Tavares, and P. M. G. P. Moreira, “On the Nonlinear Elasto-Plastic Behavior of AA6061-T6: Experimental and Numerical Implementations,” Procedia Structural Integrity, vol. 5, pp. 468–475, 2017. https://doi.org/10.1016/j.prostr.2017.07.145.

Chapter 3: B. V. Farahani, P. J. Tavares, J. Belinha, and P. M. G. P. Moreira, “A Fracture Mechanics Study of a Compact Tension Specimen: Digital Image Correlation, Finite Element and Meshless Methods,” Procedia Structural Integrity, vol. 5, pp. 920–927, 2017. https://doi.org/10.1016/j.prostr.2017.07.113.

Chapter 3: B. V. Farahani, R. Amaral, J. Belinha, P. J. Tavares, and P. Moreira, “A GTN Failure Analysis of an AA6061-T6 Bi-Failure Specimen,” Procedia Structural Integrity, vol. 5, pp. 981–988, 2017. https://doi.org/10.1016/j.prostr.2017.07.147.

Chapter 3: B. V. Farahani, J. Belinha, F. M. Andrade Pires, and P. M. G. P. Moreira, “The Simulation of Concrete Materials Using a Damage Model Combined with an Advanced Discretization Meshless Technique,” in Material Modelling: Applications, Challenges and Research; Series in Mechanical Engineering Theory and Applications, 1st ed., André Ferreira Costa Vieira, Ed. New York: Nova Science Publishers, Inc, 2017, pp. 249-303.

Chapter 3: B. V. Farahani, J. Belinha, F. M. A. Pires, A. J. M. Ferreira, and P. M. G. P. Moreira, “A meshless approach to non-local damage modelling of concrete,” Engineering Analysis with Boundary Elements, vol. 79, pp. 62–74, 2017. https://doi.org/10.1016/j.enganabound.2017.04.002.

Chapter 3: B. V. Farahani, J. Belinha, F. M. Andrade Pires, A. J. M. Ferreira, and P. M. G. P. Moreira, “Extending a radial point interpolation meshless method to non-local constitutive damage models,” Theoretical and Applied Fracture Mechanics, vol. 85, no. Part (A), pp. 84–98, 2016. https://doi.org/10.1016/j.tafmec.2016.08.008.

Chapter 3: B. V. Farahani, F. M. Andrade Pires, P. M. G. P. Moreira, and J. Belinha, "A meshless method in the non-local constitutive damage models," in Procedia Structural Integrity, 2016, vol. 1, pp. 226–233. https://doi.org/10.1016/j.prostr.2016.02.031.

Chapter 4: B. V. Farahani, F. Barros, P. J. Sousa, P. Cacciari, P. J. Tavares, M. M. Futai, and P. M. G. P. Moreira, "A Coupled 3D Laser Scanning and Digital Image Correlation System for Geometry Acquisition and Deformation Monitoring of a Railway Tunnel," International Journal of Tunnelling and Underground Space Technology, vol. 91, p. 102995, 2019 https://doi.org/10.1016/j.tust.2019.102995.

Chapter 4: B. V. Farahani, F. Barros, P. J. Sousa, P. J. Tavares, and P. M. G. P. Moreira, "A Railway Tunnel Structural Monitoring Methodology Proposal for Predictive Maintenance," International Journal of Structural Control and Health Monitoring, Wiley, June 2019, Peer review in Process.

Chapter 4: B. V. Farahani, F. Barros, M. A. Popescu, P. J. Sousa, P. J. Tavares and P. M. G. P. Moreira, "Geometry Acquisition and 3D Modelling of a Wind Tower using a 3D Laser Scanning Technology", in Procedia Structural Integrity, 2019, vol. 17, pp. 712-717. https://doi.org/10.1016/j.prostr.2019.08.095 .

Chapter 2 : Railway Tunnels, Inspection and Proposed Solutions

An underground tunnel is a structure which bears several aspects that depart heavily from aboveground civil structures. In the context of railway tunnel inspection, the structure characteristics, loading and environmental conditions and deterioration outline should be considered. Furthermore, the maintenance of a tunnel involves inspection facilities, management strategy, related technologies of inspection and repair or rehabilitation [19]. Generally, preventive maintenance operations are considered with respect to safe operation.

This chapter concentrates on fundamentals of railway tunnel constructions and proposed inspection and predictive maintenance methodologies. Hence, a brief introduction is firstly given on the concrete tunnel structures. Then, a general overview is provided concerning in-service railway tunnels, in Portugal. Afterwards, the potential defects and real examples on tunnel deterioration are taken into account. This chapter also covers the inspection technologies and the importance of the automated approaches based on the computer vision methodologies. It emphasizes SHM on the tunnels' inspection throughout, presenting the relevant works on LSS and pure image processing technologies. The role of optical NDI tools in the assessment of the structural integrity of components involved in the railway constructions are also studied, categorised as DIC, thermography and numerical simulations. The proposed research work impact in inspection, preservation and repair methodologies for railway tunnels is reviewed in this chapter.

2.1 Railway tunnels structure

Railway tunnel construction is progressively developing in support of high-speed trains and long-distance railway journeys. Numerous aspects such as geology and cost are involved in tunnel construction.

Materials used in tunnels differ with the design and construction methods chosen for each project. In fact, the most common modern lining material is concrete reinforced by either steel or fibre, which may be sprayed on, cast in place, or prefabricated in panels.

A tunnel support system is complex; it may be the surrounding ground itself, a lining system, or a composite structure. For tunnel maintenance, the support systems of the tunnel should be analysed first. Tunnel lining is mainly considered as composite lining or integral lining. Composite lining comprises multiple supports during the construction. The flexible preliminary support enables surrounding ground to deform and self-sustain. The secondary liner is mainly for waterproofing, decoration, and enhancing structural safety. In contrast, integral lining has only one layer of liner. Most contemporary tunnels were constructed with composite lining while integral concrete lining is mostly found in old tunnels [20].

Most worldwide railway tunnels were built many decades ago, with some dating back to the mid-nineteenth century. Hence, the stability examination of technical structures is a challenging task, already being addressed for a long time in literature [21].

Railway tunnels in Portugal

As a potential case study of the railway tunnel inspection, it was opted to provide information on the railway tunnels based in Portugal. Portuguese railway network includes around 120 tunnels with the majority of these over a hundred years in age. Some of the in-service tunnels are listed in Table 2.1. They were constructed mainly in the 19th and beginning of 20th century [22]. The age of such structures is related to their degradation and therefore their stability conditions have been compromised leading to cause safety concerns in the underground structures. The defects detection, by a technological inspection system, can improve the stability of old railway tunnels. Systematic inspection remains as a fundamental operation to monitor tunnel state and guarantee enough safety levels in Portuguese railway.

Table 2.1: List of main in-service rail tunnels in Portugal.

No.	Tunnel name	Location	Length (m)	Construction year
1	Alcântara	Lisbon	550	1887
2	Cabaço	Lisbon	74	1887
3	Caíde/Tapada	Lousada	1086	1878
4	Certã	Lisbon	328	1882
5	Grande Salgueiral	Beira Alta	1096	1882
6	J	Porto	274	2003
7	Juncal	Juncal	1621	1879
8	Lapa	Porto	494	1938
9	Outeiro Grande	Gavião	213	1891
10	Outeiro Pequeno	Gavião	102	1891
11	Pragal	Pragal	282	1998
12	Rossio	Lisbon	2613	1891
13	São Bento	Porto	753	1896

As reported in [22], the majority of the detected defects in Portuguese tunnels are concomitant with the construction process, as follows:

Rock masses – Represented by a certain decompression around the cavity, which is accompanying by successive deconsolidation due to the construction scheme. Substantial voids could befall having high negative impacts on the underground structures' stability.

Supports – Defects on the crown and in the extrados of the support in addition to the occurrence of hollow joints, deficiency in springing, defective drainage and waterproofing. The supports deterioration with resistance reduction is mostly linked to the presence of water, the erosive action of the wind caused by the passage of trains, the mechanical actions deriving from the envelope rock mass, significant deformations, cracks, etc.

There are some research studies focusing on the maintenance, inspection and condition monitoring of the Portuguese railway tunnels in the literature, e.g. [23]-[25].

2.2 Potential defects and deterioration in concrete tunnels

Railway tunnels concrete structures are often reinforced with metallic panels manufactured from steel or aluminium alloys and fibre polymers or composites can be used to isolate them from the seismic loading. These tunnels are known to degrade over time by way of leakages, deformation and concrete deterioration, owing to initial defects, material aging, aggressive operation condition, extreme loads due to earthquakes etc. [17]. According to [19], the main potential damage in the tunnels could be classified as follows:

Scaling: It remains as the steady and on-going loss of surface mortar and aggregate over an area.

Cracking: A crack is a linear fracture in the concrete structure standing by tension beyond the concrete’s tensile strength. Cracking can take place over curing (non-structural shrinkage cracks) or thereafter from external force, which are structural cracks. They might extend partially or completely through the concrete membranes. Due to the brittle material behaviour of the concrete, the cracked construction might lead to a precipitate rupture. In general, cracks can be classified as follows:

- ✓ **Transverse/Longitudinal Cracks**: These straight cracks are approximately perpendicular to the span direction of the concrete member. They vary in geometrical dimensions. These cracks possibly propagate through the entire slab or beam as well as through curbs and walls supporting the safety tunnel walk.

- ✓ **Horizontal Cracks**: They normally exist on the walls but would appear on beam sides as well, where encased either flanges or reinforcement steel panels have rusted. In nature, they are analogous to transverse/longitudinal cracks.

- ✓ **Vertical Cracks**: usually occur in the walls like transverse/longitudinal cracks in slabs and beams.

- ✓ **Diagonal Cracks**: These cracks are mostly parallel to each other in slabs skewed relative to the structure centreline. They are commonly shallow and varying in dimensions. If they are found in the vertical faces of beams, a potentially serious problem occurs.

- ✓ **Pattern or Map Cracks**: They are interconnected cracks which differ in size and form grids, equivalent to that of sun cracking observed in dry areas. They possess dissimilar shapes by barely visible, fine cracks to well-defined openings. Map cracks may be found in both slabs and walls.

- ✓ **D-Cracks**: a series of fine cracks at slightly close intervals with random patterns.

- ✓ **Random Cracks**: These cracks meander irregular ones which appear on the concrete surface. They possess no specific shape and do not reasonably fall into any of the categorisations described above.

Notice that the map, random, and D-cracks are mainly categorised as complex cracks.

Spalling: It is an almost circular or oval depression in the concrete produced by the separation and removal of a portion on the surface. It reveals a fracture phenomenon, which can be parallel or somewhat inclined to the surface. Typically, a portion of the depression rim remains perpendicular to the surface. Frequently, the reinforcement steel panel is exposed.

Leakage: It may take place on a region of the concrete surface where water is penetrating throughout the concrete.

Honeycomb: It may appear as a region on the surface, which has not been absolutely filled with concrete over the preliminary construction. Hence, the aggregate can be visible providing a defect with a honeycomb appearance.

Staining: It is a discoloration of the surface due to passing dissolved materials through the cracks and deposited on the surface if the water emerges and evaporates. Staining can appear in any colour although brown staining may signify corrosion of underlying reinforcement steel.

Table 2.2 reports the classification of the cracking and spalling in the concrete lining based on [19]. Figure 2.1 shows an example of spalling and cracking took place in the tunnels [26], [27].

a) b) c) d) e) f)

Figure 2.1: Typical cracking defect examples in concrete: a) crack with efflorescence [26], b) spalling of lining extended to the opening [27], c) crown spalling [27], d) longitudinal cracks of crown [28], e) transverse crack [28] and f) inclined cracks of side wall [28].

Table 2.2: Classification of common defects in the concrete tunnels and respective severity scales [19].

Defect type/severity	Minor	Moderate	Severe
Cracking (in width)	< 0.8 mm	0.8 - 3.2 mm, or < 0.1 mm (pre-stressed member)	> 3.2 mm or > 0.1 mm (pre-stressed member)
Scaling (in depth)	< 6.0 mm	6.0 -25.0 mm	> 25.0 mm
Spalling/joint spall (in diameter) (in depth)	 75.0 – 150.0 mm < 12.0 mm	 ≈ 150.0 mm 12.0-25.0 mm	 > 150.0 mm > 25.0 mm
Pop-outs (holes) (in diameter)	< 10.0 mm	10.0 – 50.0 mm	50.0-75.0 mm > 75.0 mm are spalls
Leakage	Wet surface, no drops	Active flow at volume < 30.0 drips per minute	Active flow at volume >30.0 drips per minute

The initial defects, often shaped by inappropriate construction practices, frequently commence the concrete deterioration. The aggressive operation condition simply encourages the serious deterioration of tunnels. An extraordinary event involving traffic, fires or earthquakes can seriously degrade a tunnel with excessive deformation, leakage, concrete deterioration, and even a structural rupture [17], [29], [30]. Generally, tunnel degradation causes aesthetic, serviceable or structural problems, sometimes may lead to the facility closure if proper repairs are not made. Figure 2.2 shows a typical deterioration in concrete tunnels.

As mentioned before, concrete structures deteriorate in forms of cracking, spalling, scaling, honeycombing, leakage, etc., although concrete material is typically expected to be durable [13], [18]. The influence of a defect on tunnel integrity varies, depending on its activity characteristics, location and dimensions. An active crack should be signalled as an important sign of the structural degradation of a tunnel; its propagation in length, width, or depth must be monitored for urgent measurements. On the other hand, a dormant crack might be assumed to have been caused by improper construction or material shrinkage, but a primary maintenance operation should be performed to avoid further deterioration. Moreover, delamination often occurs during concrete curing, as water and air trapped below the surface form subsurface voids. Thus, the reaction of coarse aggregate or steel corrosion may also cause concrete delamination. Concrete spalling often occurs because of delamination when the delaminated surface layer totally detaches. These must be presumed as a deterioration in structural integrity, in terms of the reduction of the cross-sectional area and also because the exposed steel is not working to distribute load any further. Furthermore, the steel reinforcement's corrosion can significantly decline the structural integrity of reinforced tunnels. Figure 2.3 shows the mechanism of the steel reinforcement corrosion [12].

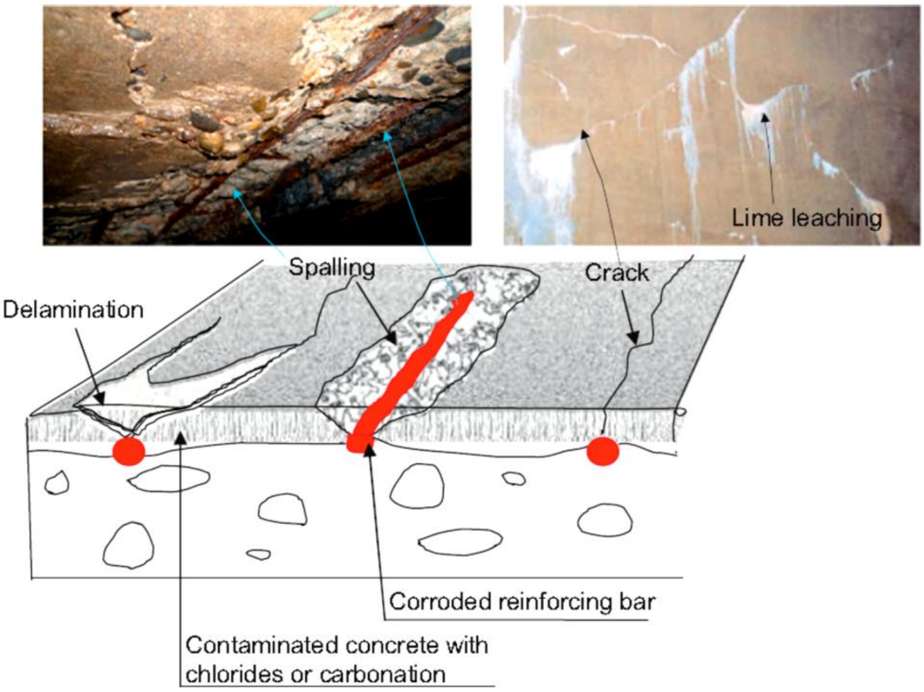

Figure 2.2: Deterioration on concrete tunnel [12].

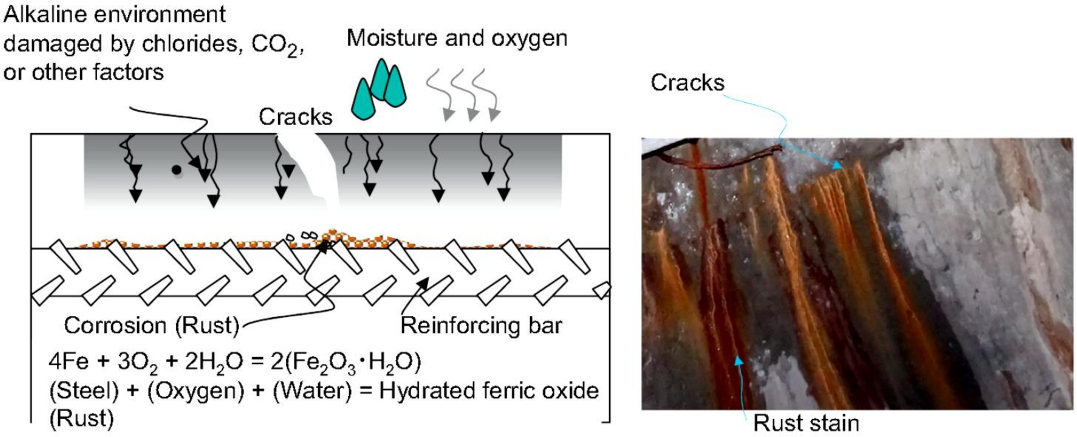

a) b)

Figure 2.3: Steel reinforcement corrosion; a) mechanism and b) tunnel deterioration illustration [12].

For many tunnels, leakage—as one of the most common and troubling problems—takes place with water infiltration in areas with penetrating cracks or joints as shown in Figure 2.4. Water infiltration imposes a direct impact on the structural integrity of tunnels, leads to problems with mechanical and electrical equipment, and promotes concrete deterioration. The representative problems on tunnels due to water leakage comprise:

a. Steel or reinforcement corrosion, especially when the groundwater is acidic;
b. Concrete cracking, spalling, and delamination;
c. Freeze thaw damage in colder climates;
d. The deterioration of protective finishes and coatings;
e. Ground loosening or voids around a tunnel;
f. The drainage system clogging.

Therefore, leakage must be assumed as one of the indispensable factors leading to degrade tunnels. Likewise, the rainwater intrusion or snow from the opening should be taken into account since it may have the same effects as leakage [12].

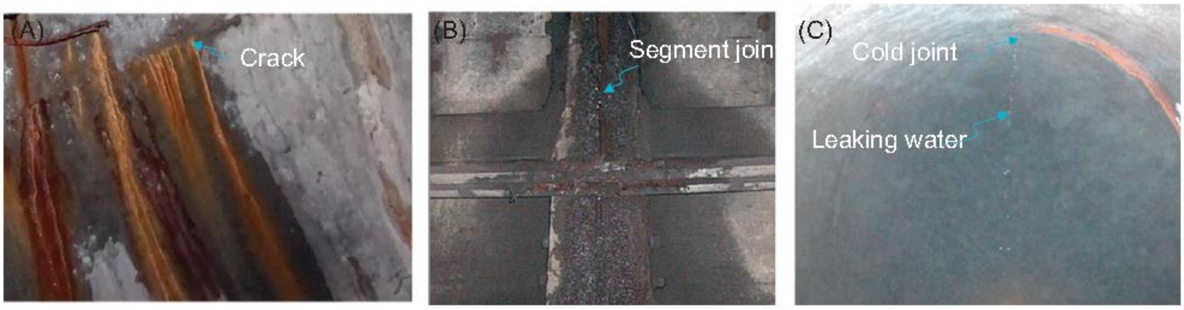

Figure 2.4: Examples on the leaks in tunnels at, a) cracks, b) segment joints and c) cold joint [12].

Besides, the structural degradation caused by ground movement could appear as transverse or longitudinal cracks and crushing at the inside surface of a tunnel, as well as sudden leakage, Figure 2.5 clarifies [12].

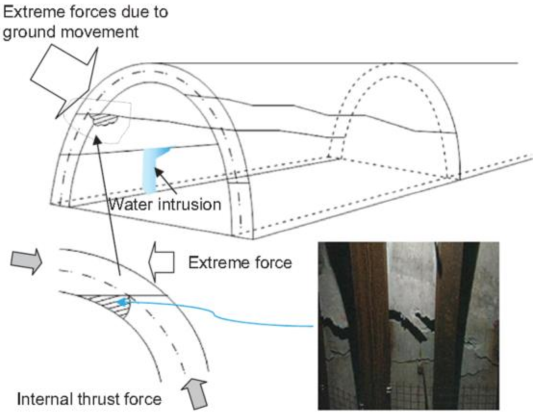

Figure 2.5: Example of tunnel failure due to the ground movement [12].

Hence, cracking and leakage phenomena stand for the most potential defects leading to degrade the tunnels, notwithstanding, the workmanship can affect concrete deterioration; the poor concrete and the inherent defects may be due to the improper placement of reinforcement steel, insufficient vibration to consolidate the concrete, or unsuitable concrete curing. Accordingly, preventative maintenance mostly adopted for infrastructure tunnels involves activities of periodic inspection, performance evaluation, and repair, discussed later.

In the next section, some real examples of damaged tunnels are presented in addition to the proposed solutions.

2.3 Real examples of damaged tunnels; evidence and solution

As mentioned before, the main reasons of tunnel degradation can be associated to the external/internal aspects including defects and natural ground deformation and in some cases seismic loading caused by earthquakes, Figure 2.6 shows a tunnel lining degradation due to the seismic loading in Japan [28]. Furthermore, Figure 2.7 demonstrates some examples of the cracking and spalling occurred on in-service railway tunnels in Finland [31].

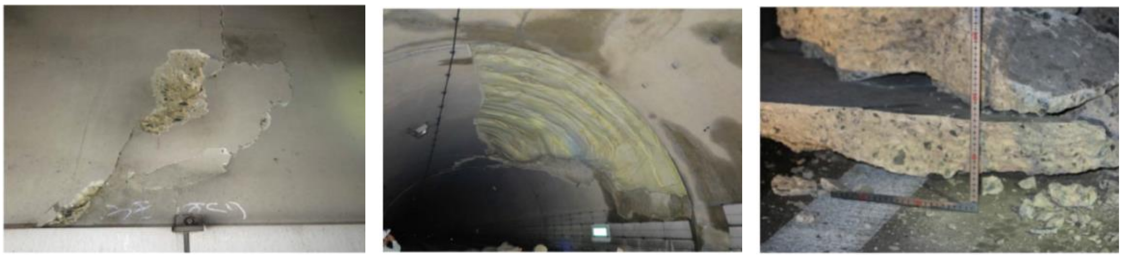

a) b) c)

Figure 2.6: Spalling and collapse of concrete lining because of the seismic loading in the Tawarayama Tunnel, Japan. a) Concrete lining spalling along with inclined crack, b) large area vault collapse of crown; and c) concrete lining fallings [28].

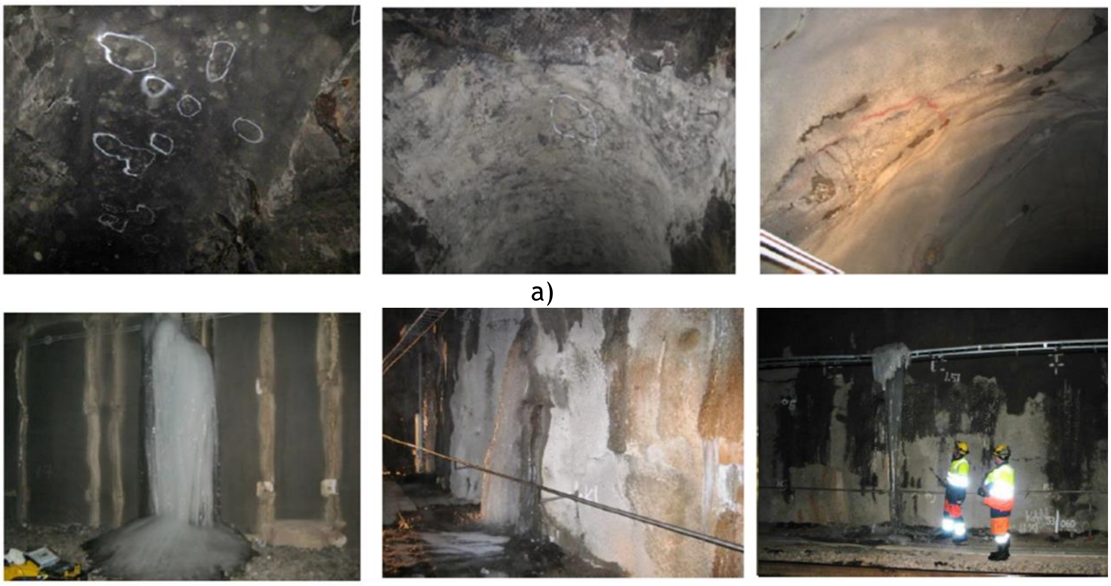

a)

b)

Figure 2.7: Typical damages in the Finnish railway tunnels; a) cracks on the interior wall surface and b) water intrusion leads to freezing in cold areas [31].

A number of researchers has investigated the structural behaviour of tunnels over a seismic loading [32]-[34]. More recently, in 2016, Yu et al. [35] carried out a study on one of the most damaged tunnels (Longxi tunnel) during an earthquake occurred in 2008 in China. The tunnel interior received substantial damage due to the formation of heavy cracking and spalling at the crown, see Figure 2.8.

a) b)

Figure 2.8: a) Spalling and dense cracking of the liner inside the Longxi tunnel and b) inclined cracking at the sidewall with water leakage and spalling [35].

Based on the finite element method, FEM, formulations, a seismic damage analysis has been numerically simulated in ABAQUS© from small to huge cracking phenomenon inside the tunnel and portals. Figure 2.9 shows a comparison between predictions from the model and field observations on a tunnel section. In conclusion, the tunnel has been rehabilitated and the steel reinforcement was repaired in many places after rehabilitation.

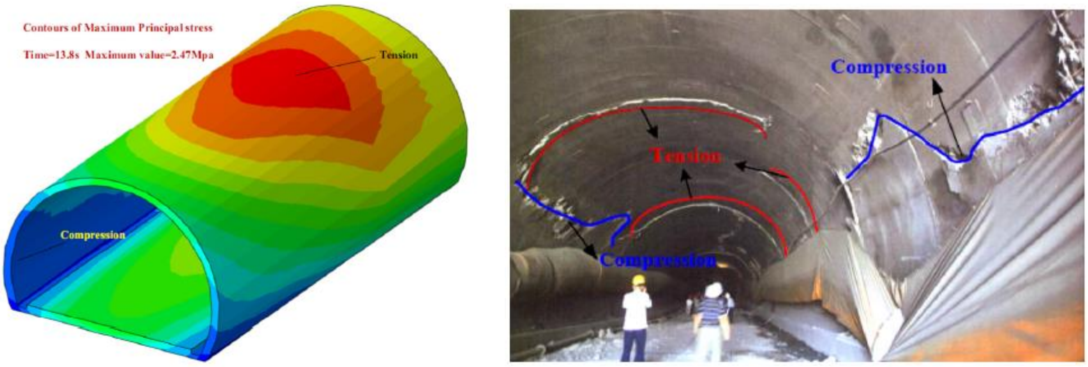

a) b)

Figure 2.9: Comparable results a) numerical analysis and b) in-situ damage investigation of the tunnel [35].

The ground stresses can cause severe deformations, as an illustration, Figure 2.10 shows the damage on the tunnel's lining and its support [36].

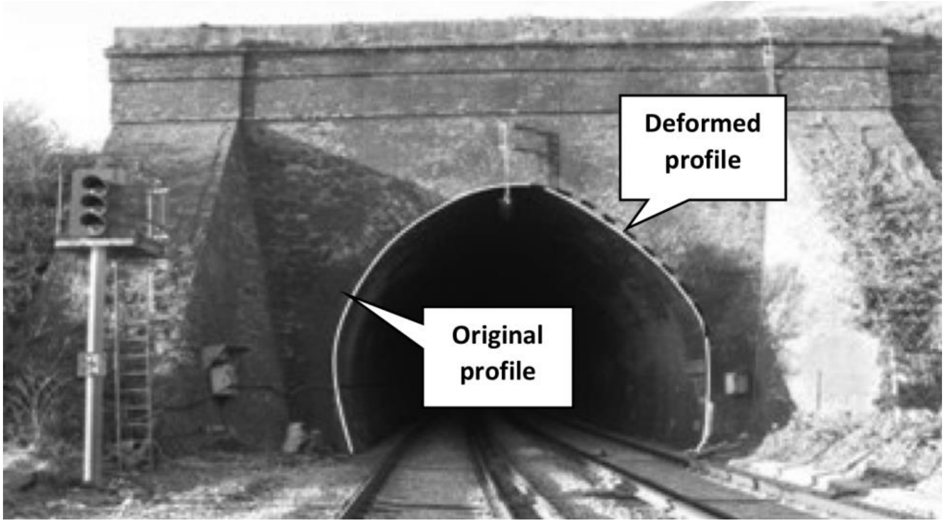

Figure 2.10: A typical tunnel deformation due to ground stress [36].

As another illustration, the Hudson River Tunnel in the USA was shut down for a long time due to the presence of macro cracks on the tunnel wall. The damage was a consequence of Hurricane Sandy flooding in 2012. The water level was high to reduce the resistance of the concrete material on the wall (see Figure 2.11). To strengthen the tunnel against the possible damage, the New York State Bridge Authority has planned to rehabilitate the tunnels to repair the destroyed components. It will be starting in service in late 2026 and extending to early 2030 when the rehabilitation would be complete, and service using the North River Tunnel would be fully renovated [37].

Figure 2.11: Damages on Amtrak's 104-year old Hudson River tunnels, New York, the USA [38].

Furthermore, in April 2016, a 30-40 meter-long crack was spotted on the interior wall of a railway tunnel in Haflong, India [39]. It happened due to the heavy rainfall for over two weeks that resulted in cancellation of all trains along the corresponding route, referring to Figure 2.12.

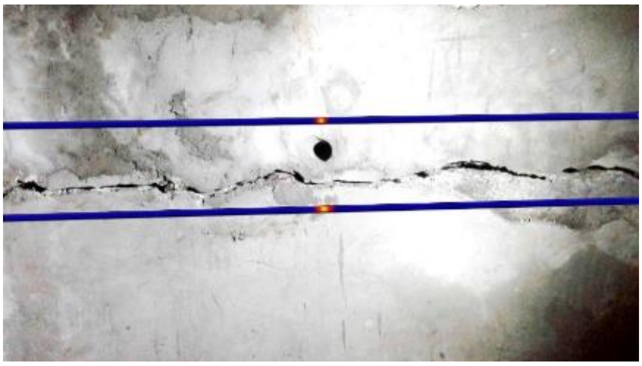

Figure 2.12: A long crack detected on the tunnel interior wall, Haflong, India [39].

Moreover, as reported in Table 2.1, Lisbon's Rossio Railway Tunnel opened in May 1891 and it is 2600-meter long. The station was closed to rail services from October 2004 until February 2008 due to tunnel renewal work when cracks were discovered in the walls, threatening its imminent collapse, Figure 2.13. Rossio tunnel has been renovated to permit the safe and functional operations for the railway transportation.

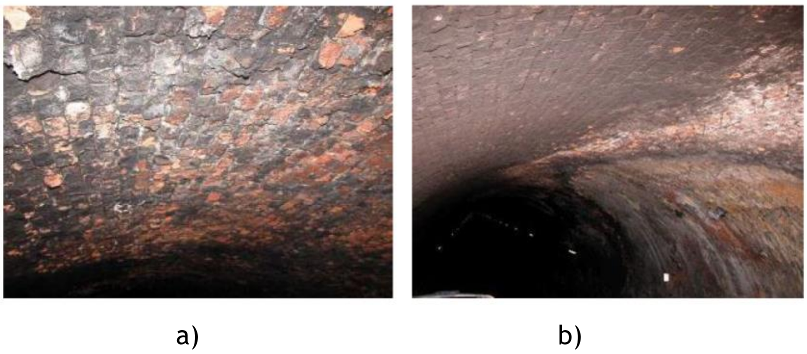

a) b)

Figure 2.13: Damage on Rossio Railway Tunnel; a) deformation and erosion of the masonry on the vault surface and b) deformation on vault section [39].

As reported in [29], Japanese Tsukayama Tunnel as a double-track railway tunnel with a total length of 1766 m was constructed in 1967. After completion, the tunnel deformed in such a way that both sidewalls were pushed into the tunnel space accompanied by mud-pumping at the tracks and lifting at the base. The arch crown was pushed upwards and failed in a bending and compressive manner, see Figure 2.14-a). The Japanese Rebunhama Tunnel, with a total length of 1232 m, has been in-service since 1975. In 1999, a freight train spotted something strange on the tracks and the train hit it and derailed. From the examination, it was found that five pieces of concrete blocks, as large as several tens of centimetres, laid on the track where they had fallen from the tunnel arch. It was reported that most of the surface which ruptured due to the shear failure, they were therefore carbonized, see Figure 2.14-b). After replacement of lining concrete, the rock above the lining became loosen over a short time, and a protruding rock block near the arch crown exerted pressure onto the lining. Due to this pressure, cracks developed radially from the protruded rock block and punching shear failure then took place forming the ruptured surface. Train vibrations and cycles of freezing and thawing caused the cracks to gradually propagate toward the tip of the ruptured surface. Finally, the self-weight brought a new ruptured surface to the portion sustaining the spalled block; the entire portion then dropped [29], as shown in Figure 2.14-b).

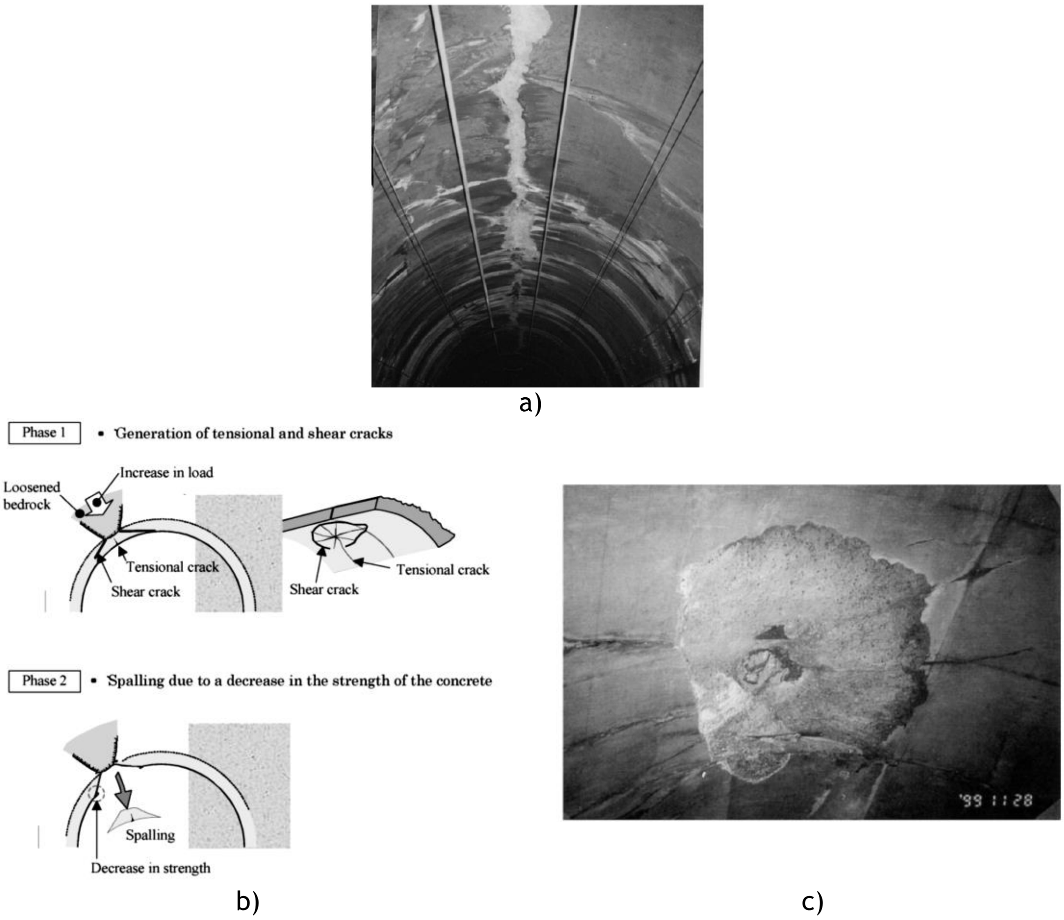

a)

b)

c)

Figure 2.14: a) Compressive failure in the Tukayama tunnel, b) spalling Mechanism in the Rebunhama tunnel and c) Lining of the Rebunhama Tunnel after spalling, Japan [29].

However, owing to the presented real examples on the damaged railway tunnels, the significance of tunnel inspection accounted for the primary stage to prevent the degradation and guarantee the tunnel security. In the next section, the inspection technologies applicable on SHM of railway tunnels are presented.

2.4 Inspection technologies

In general, tunnel inspection aimed at checking whether a structure which has been in-service for years is still safe or not. So, it is necessary to perform accurate inspection without creating any destructive effect on the tunnel structure. With the technological advances, non-destructive inspection (NDI) tools are proving to be accurate and efficient and the item remains as intact and undamaged at the end of testing. According to [40], proposed inspection approaches applicable on concrete tunnels are described with detail as follows:

✓ **Visual methods**

Visual testing remains as the most important method amongst all NDI tools. Typically, it can deliver valuable facts to the well-trained eye. Besides, visual features may be associated with workmanship, structural serviceability, and material deterioration. Thus, it can be particularly important for the engineers to be able to differentiate between the various signs of distress that may be encountered. Therefore, statistics may be collected on visual inspection results to provide a preliminary indication of the structure status and enable formulation of a subsequent testing program.

✓ **Strength based methods**

Rebound and penetration examinations can measure the materials surface’s hardness to deliver an estimation of surface compressive strength, uniformity and quality of the constructions. Examples include the Schmidt Hammer [41], [42] (rebound), the Windsor Probe [41], [43] (penetrating), Flat Jack Testing [44], [45](applied to masonry), or methods without contact [46].

✓ **Sonic and ultrasonic methods**

These methods are known as impact-echo tests in which hammer blows generate impulses and the travel period of these sonic pulses is measured with pickups placed on the wall [47]-[49]. The travel time is associated to the elasticity modulus which is related to the material strength. In the same way, ultrasonic devices are usually adopted to measure the velocity in the material of a pulse generated by a piezoelectric transducer [50]-[52]. The pulse velocity depends on the composition and maturity of the material and its elastic characteristics [53].

Ultrasonic inspection is conducted principally for the detection of discontinuities. Bonds produced by welding, brazing, soldering, and adhesion also can be ultrasonically inspected.

- ✓ **Magnetic methods**

Magnetic methods aim at determining the reinforcement's position. They are not indicated for defect detection or deterioration direct measurement. Examples of magnetic methods are the Magnetic Flux Leakage method [54], [55] or Magnetic Field Disturbance method [26]. Magnetic methods can be applied to a part to identify a leak, ferrous particles, either dry or in a wet suspension. These are attracted to an area of flux leakage and form what is known as an indication, which is evaluated to determine its nature, cause, and course of action, if any.

- ✓ **Electrical methods**

These approaches are adopted to inspect tunnel components comprising resistance and potential measurements [56]-[59]. Therefore, electrical resistance has been used to measure the permeability of deck seal coats and involves measuring the resistance between reinforcing steel and surface, while electrical potential alterations are caused by reinforcement corrosion.

- ✓ **Thermography Methods**

Thermography techniques intend to measure the thermal radiation emitted by tunnel's walls. Infrared-based techniques contribute to the graphical representation of the temperature distribution on the surface [10], [17], [60]. It describes the thermal flow throughout the surface, which in turn is influenced by the mechanical and/or hydraulic discontinuities of the structure and the related change in water content due to these defects as water evaporation causes visible difference in temperature readings. As a result, thermal discontinuities on tunnel surfaces reflect abnormalities within the underlying structure. When compared with other techniques such as ultrasonic or radiographic testing, thermographic inspection is safe, nonintrusive and noncontact allowing the detection of relatively subsurface defects. The defects locations can then be detected by thermography cameras through the process of mapping temperature distribution on the surface of the object.

- ✓ **Radar methods**

These techniques have been extensively used to detect defects in railway tunnels and other infrastructures. The most used is the Ground-Penetrating Radar [61]-[63]. It is the electromagnetic analogue of sonic and ultrasonic pulse echo methods, which is based on the electromagnetic energy propagation through materials of diverse dielectric constants. The greater the difference between dielectric constants at an interface amongst two materials, the greater the amount of electromagnetic energy reflected at the interface. These methods can be used to detect subsurface objects, changes in material properties, and voids and cracks by the reflected signals from subsurface structures.

- ✓ **Radiography Methods**

In these methods, X-rays, gamma radiation or neutron rays can penetrate structural materials and therefore might be adopted for inspection purposes [64], [65]. The amount of radiation absorbed by the material is dependent on its density and thickness. This radiation can be detected on sensitized paper being visible on a fluorescent screen or by electronic sensing equipment. Within this method, limitations are imposed by accessibility to both sides of object, long exposure times, and safety precautions required to protect both operators and public. These methods would assist to verify the structural integrity of the components.

- ✓ **Endoscopy Methods**

Generally, endoscopes or videoscopes comprise of rigid or flexible viewing tubes that can be inserted into predrilled boreholes of an element under examination to inspect its conditions [66], [67]. These scopes allow close examination of parts of the structure that could not be otherwise viewed. Although this is a viewing instrument, some destruction of material is necessary for its proper use.

Even with the prodigious diversity of inspection techniques rendered above, current structural tunnel inspection is predominantly performed throughout scheduled, periodic, tunnel-wide visual observations by inspectors who identify structural defects and characterise them. This process stands as slow, labour intensive and subjective, working in an unpleasant environment due to dust, absence of natural light, uncomfortable conditions or even toxic substances such as lead and asbestos.

Nevertheless, technological design relying on computer vision is a rapidly growing field concentrating on processing and modifying the high-level understanding of images.

In the next section, automated inspection relying on computer vision is discussed.

2.4.1 Automated inspection-based image processing

Previously mentioned manual and visual tunnel inspections techniques may demand personnel to access hazardous environments soliciting the necessity for automatic operations to minimize human intervention. Generally, the automated inspection system on railway tunnels involves three main phases: image acquisition, processing, and result exploitation [68]. The use of automation in the inspection field was indicated by several studies [11], [69], [70] reviewing the advantages of autonomous platforms in railway tunnels. These systems have the potential to fulfil the inspection process with objective outcomes and high proficiency. They also enhance safety by performing inspection in dangerous environments [40]. Consequently, manual and visual inspections are being gradually substituted with more precise systems using mechanical, electronic and robotic components and processing data provided by cameras, laser, sensors, etc. [71].

In the next section, automated systems applicable on the tunnel examination based on the pure image processing and the 3D laser scanning technologies are discussed and reviewed in detail.

2.4.1.1 Pure image processing

In the framework of the automated inspection technology, pure image-based processing approaches stand as a merit key to perform the inspection tasks and detect the defects. The literature presents several investigations to automatically examine the tunnel status and monitor the defects following pure image processing techniques.

Mohan and Poobal [72] reviewed crack detection methodologies based on the pure image processing approaches for concrete structures including railway tunnels. The communication concluded that the majority of researchers adopt camera-based image techniques for the analysis with segmentation algorithms such as the threshold technique and reconstructable feature extraction technique for a comprehensive damage analysis. Yu et al. [73] proposed an automated vision system relying on a mobile robot to detect cracks in concrete tunnels. It was controlled to maintain a constant distance from walls while acquiring image with a Charged Couple Device (CCD) camera. The system was validated on a subway tunnel. Figure 2.15 reveals an acquired image on the tunnel wall and the extracted cracks by the deployed system.

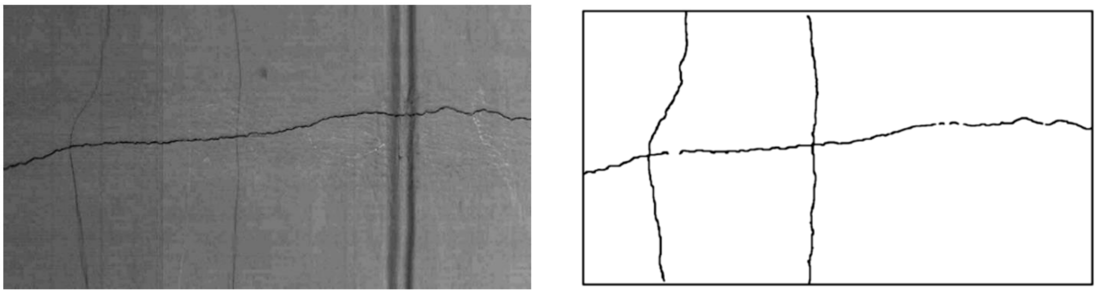

a) b)

Figure 2.15: a) image captured on the wall and b) extracted cracks.

Ukai [74] developed a system relying on continuously scanning image process to detect the wall deformation. The designed system consists of a one-dimensional (1D) line sensor camera and an image processing database as a diagnosing tool for the tunnel condition by image processing. Images have been taken on the interior tunnel wall and stitched in order to build a full surface. Then, an automated image-processing algorithm was adopted to extract the defects, mainly cracks, and structural objects such as joints, Figure 2.16.

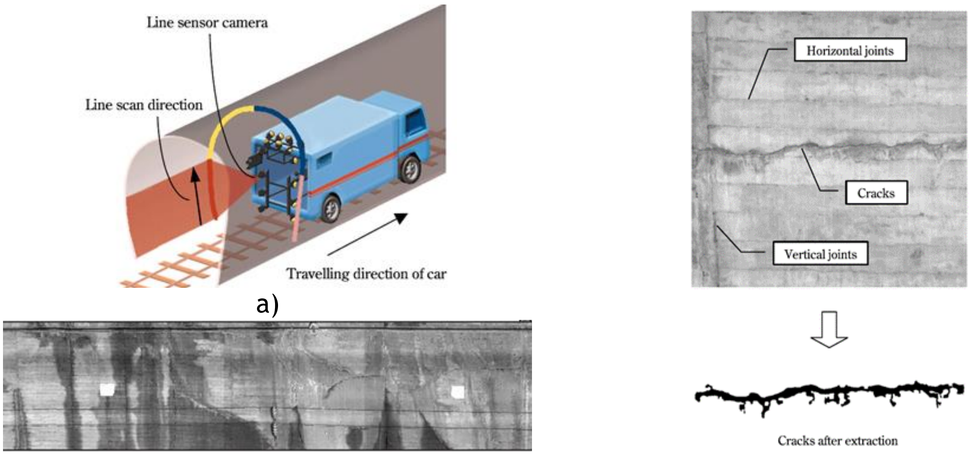

a)

b)

c)

Figure 2.16: a) A general view of the CSI inspection system, the tunnel surface scanned by the CSI system c) the extracted crack [74].

Huang et al. [75] proposed a pioneering image recognition methodology on semantic segmentation of crack and leakage defects of metro shield tunnel using hierarchies of features extracted by a fully convolutional network. As shown in Figure 2.17-a), the inspection equipment continuously scans the inner surface of metro shield tunnel lining, Figure 2.17- b) to e).

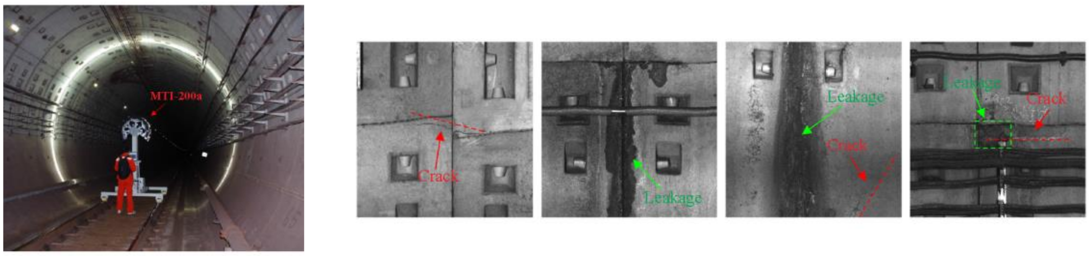

a) b) c) d) e)

Figure 2.17: a) Image acquisition equipment on Metro tunnel inspection, b) crack-only image, c) Leakage-only image, d) Two-defect-non-overlapping image and e) Two-defect-overlapping image [75].

A new methodology has been proposed by Xu et al. [76] for water leakage detection in tunnels using the 3D point cloud obtained by a terrestrial laser scanner, TLS. For the field experiment, an underground tunnel at Fengtai District, Beijing, China has been scanned by the system and its 3D point cloud data and intensity data of the tunnel have been obtained. Figure 2.18–a) presents the obtained point cloud of the underground tunnel. A section on the tunnel profile marked as red box in Figure 2.18-a) was examined for water leakage regions, as seen in Figure 2.18-b).

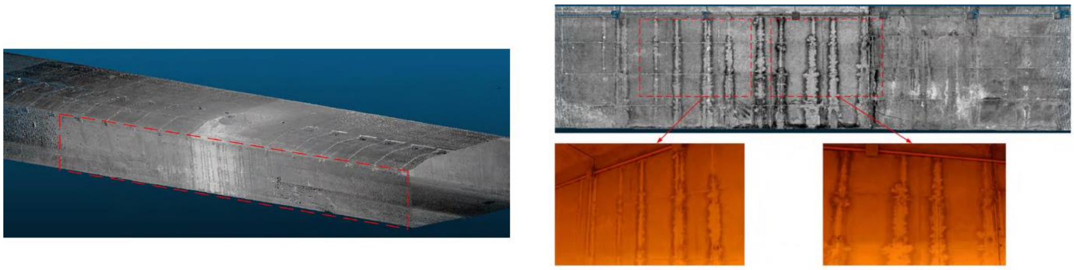

Figure 2.18: a) Obtained 3D point cloud of the tunnel scanned by TLS and b) water leakage detected by CCD camera [76].

Another computer vision–based methodology based on image sensors for the inspection of fissures and cracks has been proposed by Medina et al. [68]. In the developed system, the camera sensors resolution and the number of cameras were dependent on the crack size and the tunnel type. The acquired images were analysed using a modified genetic algorithm based on the differential evolution optimization method. A mobile platform traveling through the railroad track (as illustrated in Figure 2.19-a) has been developed to assess the feasibility of the proposed scheme. Figure 2.19-b) reveals the application of the inspection system to defect detection. Consequently, the use of linear cameras has been recommended in order to simplify lighting and ulterior data processing.

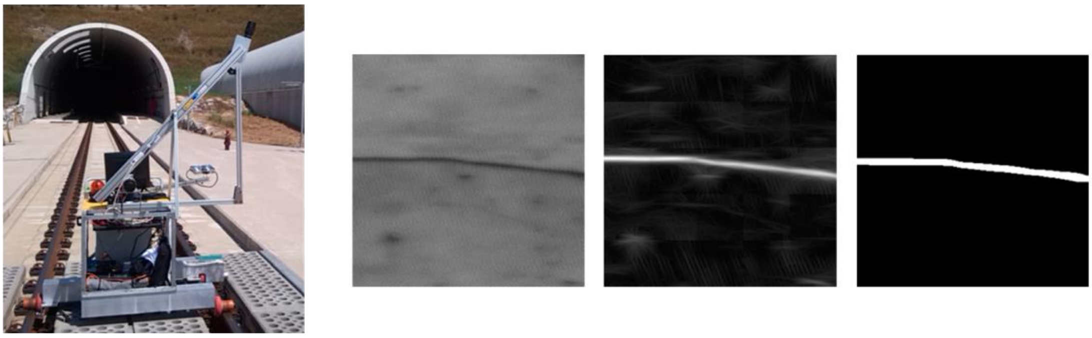

Figure 2.19: Developed inspection system; a) prototype of the tunnel inspection platform and b) normalized original, filtered and segmented images on the detected defect [68].

However, in the framework of the automated inspection of railway tunnels, there is a robust technologic solution proposal that relies on the laser scanning technology to examine railway tunnels. Since the laser scanner can scan underground tunnels without illumination equipment, it offers significant advantages on SHM of tunnels. In order to acquire, process and analyse images, the computational vision field produces adequate data for both experimental validation and numerical solution [77].

Within the concept of the tunnel examination, maintenance of pipelines would be a relevant topic in the interdependent areas. Thus, in the next section, inspection methods in pipelines are described first prior to railway tunnel inspection.

2.4.1.2 Laser scanning technology

Laser triangulation-based devices are a more appropriate approach for internal inspection of pipes. A comprehensive study has been thereby carried out on pipeline inspection by Albertazzi et al. [78]-[82]. They have designed a 3D laser scanner to obtain the pipe profile in order to monitor defects inside the tube, such as protrusions. Inner geometry inspection regarding pipelines was performed by optical methods [79]. For this purpose, a scanner so-called “*profilemeter*” was built, as seen in Figure 2.20. The profilemeter was set to travel inside a pipe and scan the inner surface. It is possible to obtain point clouds in the region of welded joints. A set of regularly spaced sections was measured while the profilemeter moved along the pipe using a self-centring mechanical structure. A graphical representation of the obtained result is demonstrated in Figure 2.20-c).

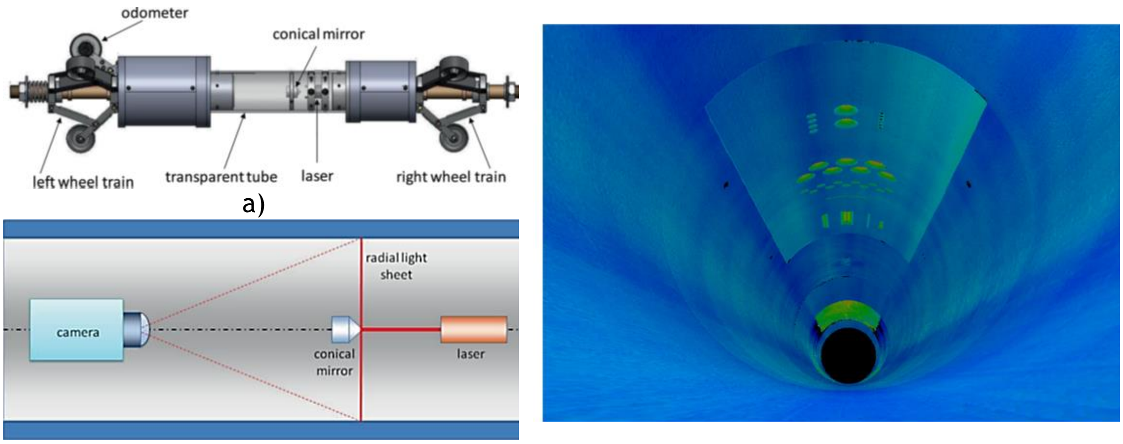

a)

b)

c)

Figure 2.20: a) Constructive aspects of the optical profilemeter, b) Measurement principle of the optical profilemeter and c) internal view of point cloud from the test surface, defect detection [79].

As shown by the pipeline inspection, the technology of the 3D LSS enables the possibility of contactless, direct and automated 3D measurements on pipes. The applications of LSS are also exponentially expanding in the civil engineering domain in railway structures.

As an illustration, Fekete et al. [83] have been successful in the implementation of the static LSS at four sites near Oslo, Norway, including two active tunnelling operations. Stentoumis et al. [84] proposed a system equipped with a 3D LSS which can detect, recognize and document existing defects on the tunnel lining in a single pass, both visually and geometrically. The experiments were performed on real data from European tunnels. As Figure 2.21-a) illustrates, the proposed system consists of two individual stations: a camera and a laser being adopted to scan the tunnel surface and if defects have been detected, the other station named as stereo vision system rig was responsible to capture digital images from the suspected regions and then the images were analysed to detect and measure the defects. The robot inspector has scanned a slice of the tunnel where a defect was identified and, after removing the noise, the tunnel profile was reconstructed as shown in Figure 2.21-b). The defect distinguished by the system is shown in Figure 2.21-c).

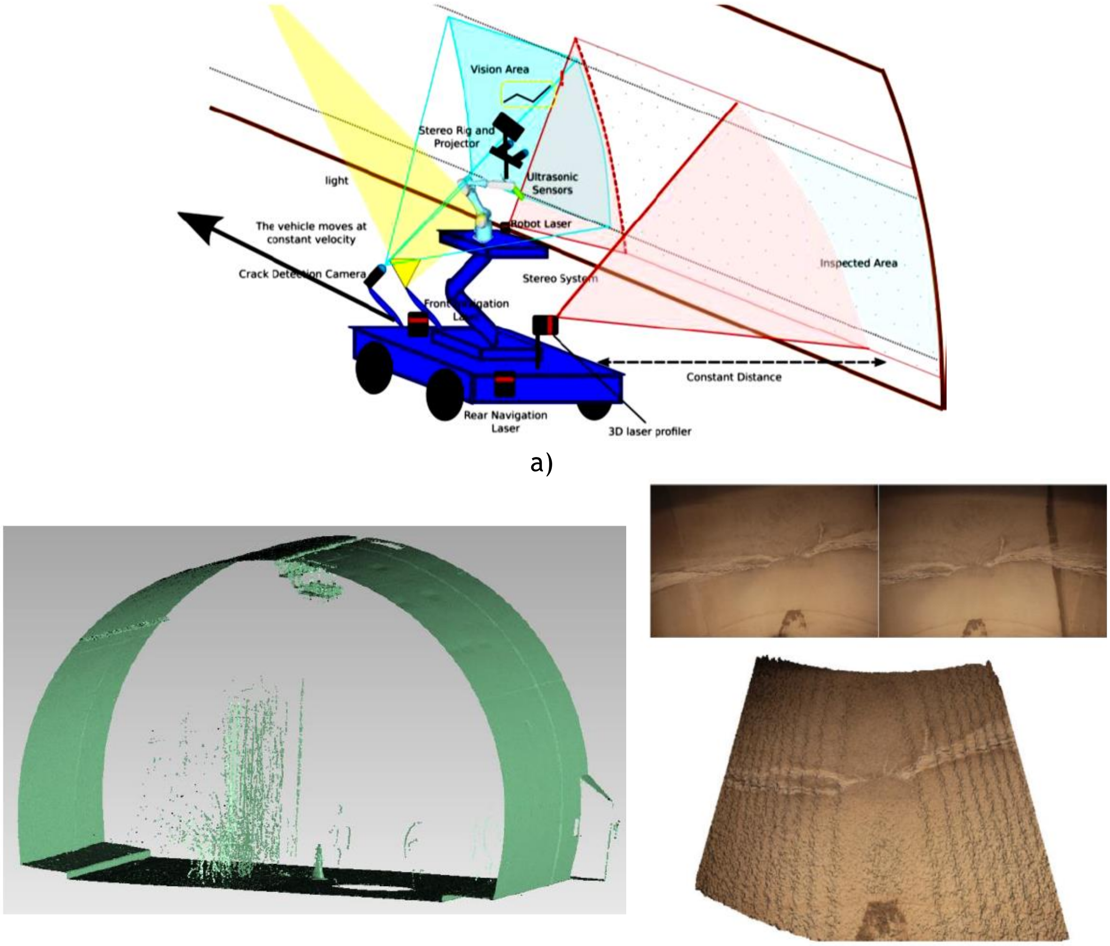

a)

b)

c)

Figure 2.21: a) A schematic perspective of the robotic platform for tunnel lining inspection, b) A slice from tunnel taken with the 3D LSS and c) a crack with water leakage reconstructed from the 3D LSS point cloud [84].

Pejic´ [85] designed and optimised a LSS for tunnels geometrical inspection. Based on a subjective survey on rail tunnels, some essential points were considered inside a tunnel to demonstrate the failure phenomenon and defects. It was reported that there are some factors having most influence on scanning parameters consisting of the shape and dimension of the tunnel and the scanner parameters. In addition, requested positional accuracy of the tunnel point cloud should be obtained through careful planning and adequate control of the measurement results, Figure 2.22. The expanded profile of the train is modelled in respect to the surveyed positions of the rails.

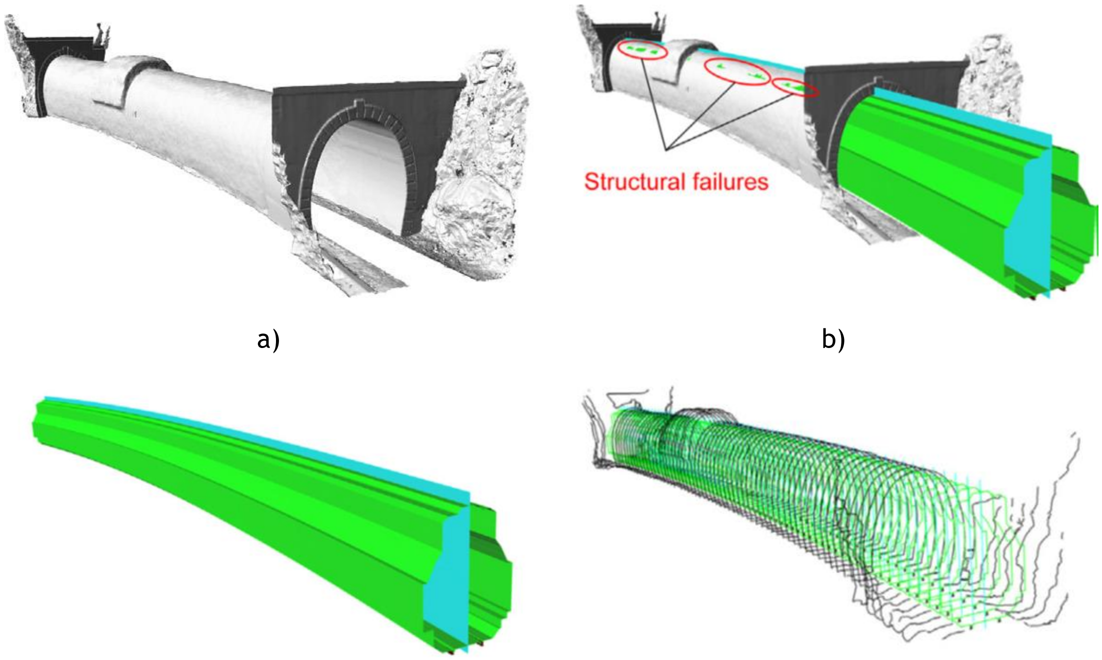

a) b)

c) d)

Figure 2.22: Modelled tunnel and expanded profile of the train; a) Tunnel surface, b) expanded profile of the train, c) estimated clearances and failures and d) 1 m cross sections; the tunnel mesh is created from the scan data [85].

Another research work was thereby carried out to explore the application of the 3D LSS to the function of tunnel inspection in Europe and Asia [86]. So, high-speed cameras, custom optics and laser line projectors were used to acquire both two-dimensional (2D) images and the high-resolution 3D profiles of infrastructure surfaces at speeds up to 100 km/h. The built system could be mount on any kind of terrain vehicles such as trains, trucks etc., (Figure 2.23-a). Besides, laser lines can be projected at high frequencies -up to 11200 Hz- in order to ensure a high resolution. Figure 2.23-b) and –c) show a general view of the assembled system with the sensors and the resolution correlated with different inspection velocities. As a result, the crack, moisture and poor panel alignment detection were accomplished in addition to the 3D model tunnel construction (c.f. Figure 2.23-d) and –e).

Qiu and Cheng [87] proposed an innovative clearance inspection method to produce high-resolution digital elevation model on railway tunnel surfaces, mainly bare lining, from LSS data. Based on the tunnel point clouds projection, an automated extraction of the horizontal and vertical alignments was implemented in addition to a new technique to unwrap a tunnel surface. The developed system possesses a high-accuracy interpolation and filtering numerical algorithm for generating bare-lining models with no restrictions on tunnel cross-sectional shapes. The deployed system has been applied on a point cloud dataset on the Xieziyan railway tunnel with a total length of 532 m located in Sichuan, China; see Figure 2.24.

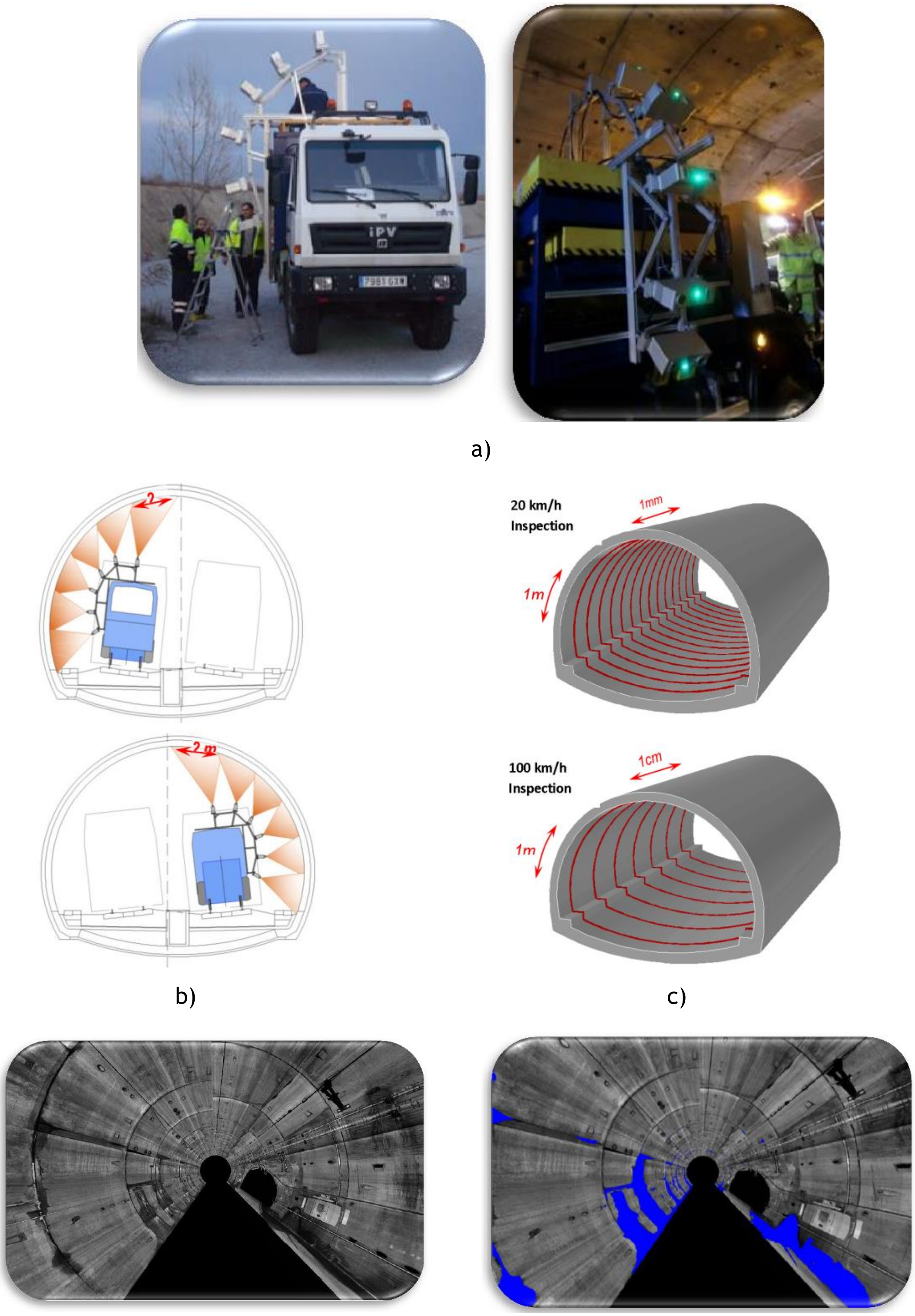

a)

b)

c)

d)

e)

Figure 2.23: a) LSS mounted on an all-terrain vehicle, b) Sensor deployments, c) resolution in terms of the inspection speed, d) Merged tunnel profile and e) detected moisture on tunnel wall [86].

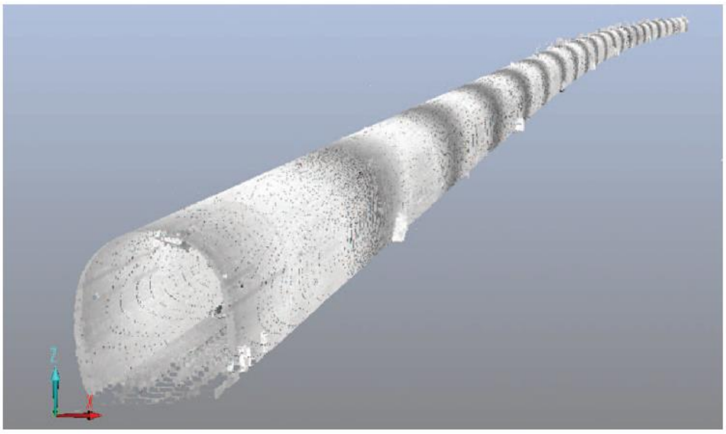

Figure 2.24: Point cloud dataset on the Xieziyan railway tunnel [87].

Xiao et al. [88] adopted a surface flattening algorithm. It contributed to extract the 3D point cloud data derived from the LSS. It intended to reconstruct the triangular mesh surface from the point cloud data. Afterwards, the surface flattening based on geometrical method is conducted to form a 2D plane. The damage or deteriorations on the interior wall of tunnels can be detected from the acquired point cloud. The field experiment has been carried out on the Shanghai Metro Line tunnel, as seen Figure 2.25-a). The tunnel profile has been acquired by the 3D point cloud data attained from the LSS system as shown in Figure 2.25-b).

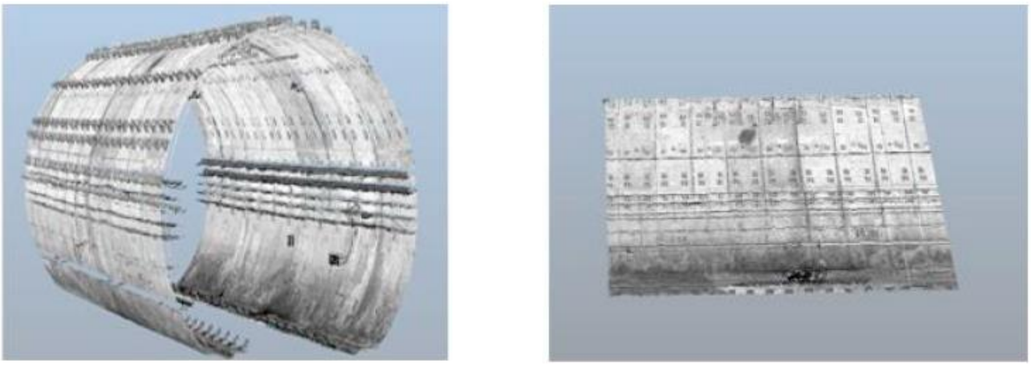

a) b)

Figure 2.25: a) the 3D point cloud data before surface flattening and b) 2D point cloud data after surface flattening [88].

Laser scanning projects [31] in Finland have been carried out to obtain the tunnel interior wall and the rails by developed inspection technology as shown in Figure 2.26-a). The system was capable to perform damage analysis from the scanned profiles to assess the tunnel conditions. The system operates with a 360° viewing angle with a rotation at 300 Hz combining the single measurements to an image, see Figure 2.26-b). It aimed at determining the visible surface and its conditions and in parallel, defect detection in addition to the moisture, water intrusion and warm anomalies by thermal variations, as shown in Figure 2.26-c).

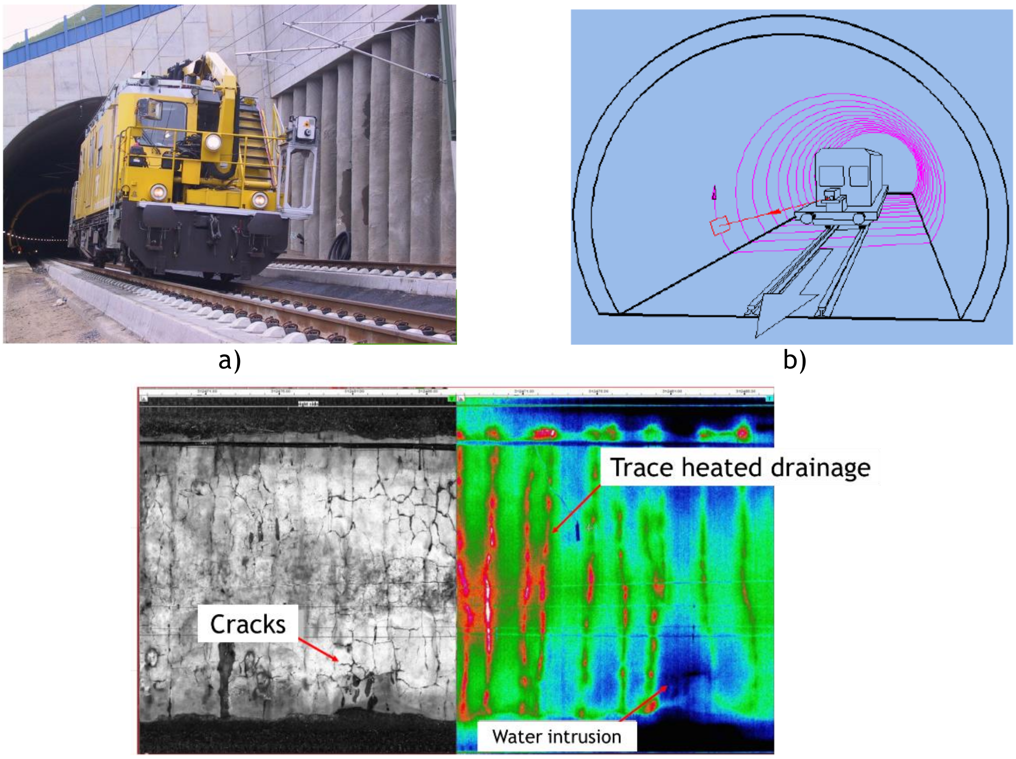

a) b)

c)

Figure 2.26: Tunnel inspection solution based on the laser scanning technology used in Finland; a) the mounted system, b) the system configuration and c) the detected defect and moisture on the tunnel interior wall [31].

The 3D LSS in the railway tunnel examination has been reviewed so far. The next section describes the optical NDI application on SHM of railway tunnels, considered as the second-stage inspection technologies.

2.5 Optical NDIs on SHM and defect monitoring

Tunnel inspection embraces not only the evaluation of the internal state of a tunnel lining but also its defects characterization. Generally, the geometrical properties of a tunnel is relevant to traversed material, the tunnel depth and its construction method. Besides, tunnel's deformation with time could lower its clearance.

As the second-stage inspection technology, automated systems based on optical NDI tools received admissible feedback from the field applications.

Haack et al. [89] presented a review of NDI methods, where advantages and disadvantages of mechanical, radiation, electric and optical techniques are discussed. Farahani et al. [90] presented a review paper describing advanced image based methods for structural integrity monitoring. Interferometric methods including Electronic Speckle Pattern Interferometry (ESPI) and shearography were thereby reviewed in addition to their applications in the engineering areas particularly solid mechanics and aeronautics. Moreover, DIC approach was also surveyed and it is notable that DIC permits to acquire the deformation variation on the structural components under various loading conditions. It also enables to experimentally characterize essential material behaviours such as fracture and damage parameters. Justifying the DIC applications, this technique is widely used in health monitoring manners contributing to anticipate the structures' lifetime. Additionally, a thermography method relying on the temperature variations on materials was discussed in details. It is indeed classified as a non-contact technique in experimental mechanics allowing to measure a stress field function resulting from thermal effects on a variety of material behaviours consisting of concrete, metals, cellular tissues, polymers and composite constructions. It plays a significant role in the condition health monitoring since it has the potential to distinguish any fluid leakages, moisture and temperature variation on the structural integrity components especially on bridges and tunnels. Besides, this thermography method is reliable for the evaluation of fracture and fatigue behaviour of the material leading to the identification of the components' lifetime. Overall, the presented optical techniques are feasible and efficient to analyse and experimentally determine distinct material behaviours able to validate the similar computational solutions with a high accuracy.

In order to signify the capability of advanced image-based methods in the SHM, the following queries must be addressed:

a) What are the typical manual procedures to track defects?
b) What are the limitations of manual defect monitor?
c) How are the defects characterised?
d) What tools and metrics are used to evaluate the condition of each infrastructure element?

Owing to the NDIs, apart from detecting defects, it is crucial to evaluate if defects in tunnels are changing over time and how fast they do so. This information aids determining the deterioration rate of the structural tunnel components. Hence, amongst all of SHM approaches on the computer vision and image processing-based condition assessment, DIC is the interest of this PhD thesis content. In this respect, this section describes the categorization of several state-of-the-art on the mentioned NDI methodologies, which are adopted to automate the process of defect monitoring and damage characterisation on the concrete structures.

2.5.1 Digital image correlation

Digital Image Correlation (DIC) has been deeply developed and successfully applied in experimental mechanics amongst all kinds of non-contacting optical methods as it was firstly proposed in 1983 [91]. The key merits of DIC over other non-contact optical techniques include: (1) the setup of test equipment is convenient, and suitable grey intensity distribution can be obtained by spraying paints onto the measured surface to create random speckles; (2) there are no strict limitations on illumination if a white light source or nature light can be provided;

(3) high spatial-resolution digital image acquisition devices are available everywhere to meet the required measurement sensitivity and resolution. It also possesses the potential to measure the structure deflection and mechanically characterise defects. Building on this concept, some of existing relevant works on concrete infrastructures are reviewed and discussed here.

Ramos et al. [92] used the 2D and the 3D DIC on large masonry specimens in order to study the SHM. Hence, the rigid body motion has been characterized, displacement and strain fields have been measured in in-plane and out-of-plane load applications, see Figure 2.27.

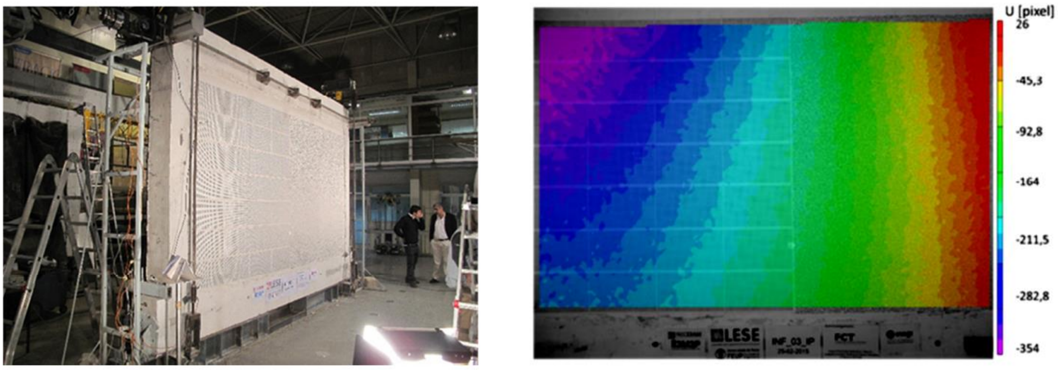

a) b)

Figure 2.27: a) Tested masonry wall and b) horizontal displacement field [92].

Areias et al. [93] performed a set of experimental tests on cylindrical concrete buffers to monitor surface cracking by means of the DIC. Hence, the crack evolution has been monitored over a period representing the deformation field on the corresponding surface.

The application of the 2D DIC technique was considered to determinate the actual mechanical behaviour, (i.e. cracking, curvature and deflection), of a full-scale reinforced concrete beam after 25 years of service in a severe industrial environment. It included the analysis of cracks and deformation measurement [94]. The beam was tested in a four-point-bending loading condition, concrete cracks were identified near the steel reinforcement and their dimensions were measured over five loading cycles in tensile zone of the beam.

Salmanpour and Mojsilović [4] had used the 2D DIC in large confined masonry walls in order to detect and trace accurate crack maps in a shear stress solicitation experiment. Zhu et al. [60] employed the 3D DIC technique to monitor the cracking behaviour on a concrete lining over prototype loading experiments of a special-shape tunnel. Based on the displacement variation, the onset of cracking and the crack width were determined as shown in Figure 2.28.

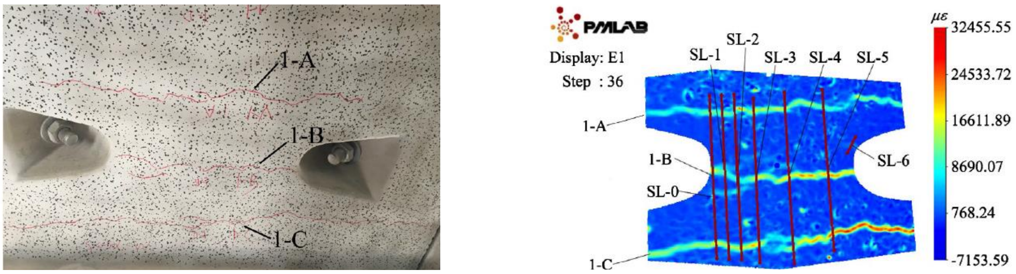

a) b)

Figure 2.28: a) Sketching map of the cracks and b) maximum principal strain field [60].

Lei et al. [95] performed an experimental study on impact damage on a concrete structure by means of the 3D DIC. The study relied on a horizontal impact load applying on the upper part of the concrete structure by a hammer striking. The local significant damage has been detected by using this technique. After applying several impact loads, the structure has been ruptured on the position where substantial damage was identified originally through DIC. The experimental results proved that adopted procedure is accurate to predict the damage location. Gali et al. [96] investigated the mechanical behaviour of cracks in the shear response of Steel Fibre Reinforced Concrete (SFRC) structures. The cracking has been assessed by surface displacements acquired from a 2D DIC system. Based on the acquired results, the crack patterns on the side of the structure without shear stirrups are shown in Figure 2.29. It was concluded that the adopted methodology delivers full-field displacement measurements offering the advantage of posterior evaluation of cracks. Besides, it was able to evaluate displacement variations after the crack's formation.

Rimkus et al. [97] also adapted the DIC for the crack localization in reinforced concrete elements. An algorithm has been proposed permitting to evaluate crack coordinates and forward resulting data throughout a numerical procedure of crack spacing determination. It aimed at realization of an automated crack detection system, which allows eliminating subjective judgment characteristics of the traditional expertise. The cracking behaviour in the pure bending zone of a reinforced concrete beam has been assessed under a four-point-bending scheme, as seen in Figure 2.30-a). By means of DIC, the crack localization has been delineated over several loading conditions as illustrated in Figure 2.30-b).

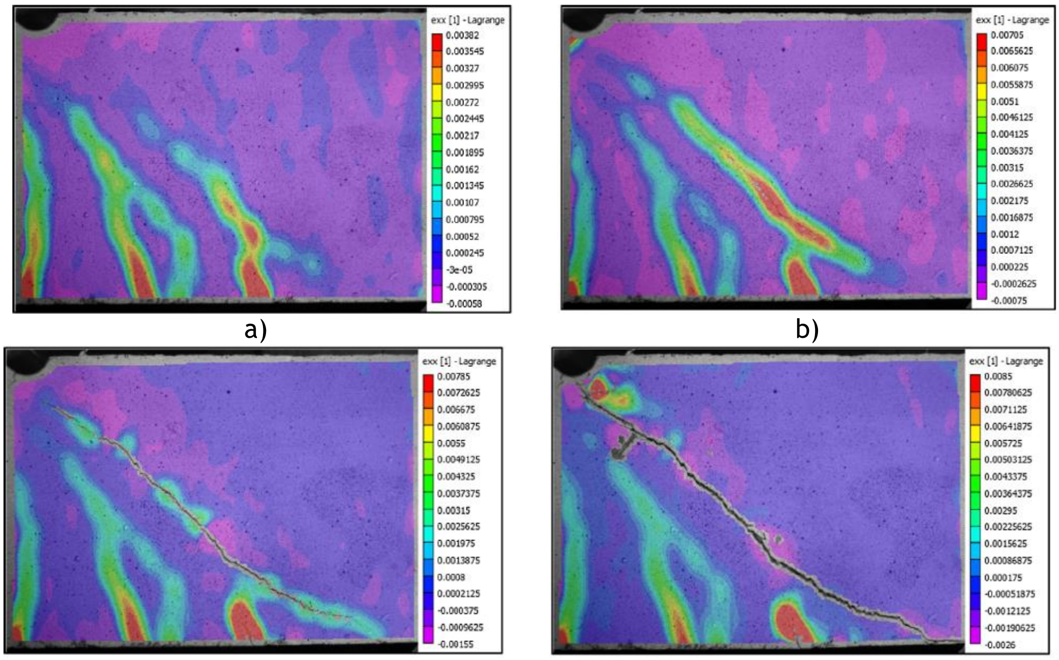

a) b)

c) d)

Figure 2.29: Contours of strain in x-direction at different applied load levels a) 100 kN b) 132 kN; c) 168 kN and d) 146 kN [96].

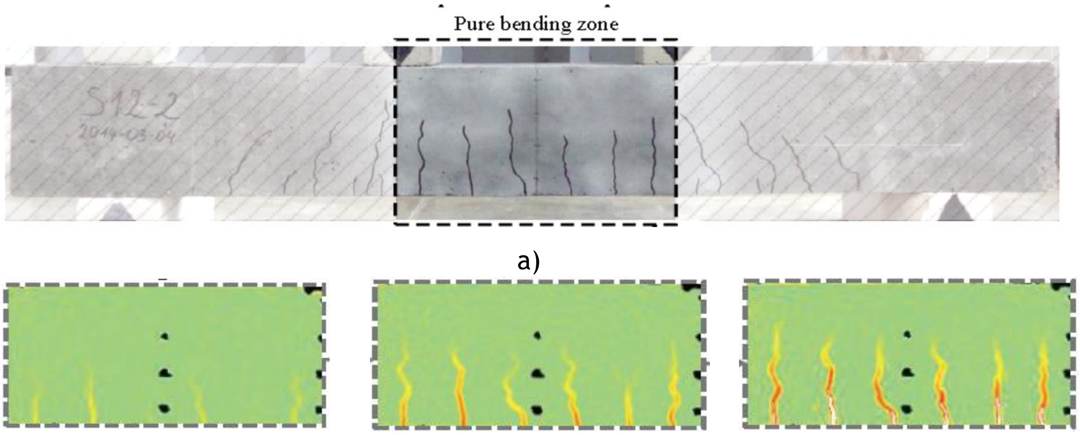

a)

b)

Figure 2.30: The case study; a) performed four-point-bending test on a RC concrete beam and b) crack localization obtained by DIC for different applied load levels [97].

2.5.2 Thermography

The use of thermography methods as a NDI for the SHM has slightly increased recently, due in large part to the advancement of infrared cameras and the considerable reduction in their cost. The slow growth of thermography applications on concretes is because, unlike metals concrete is an extremely inhomogeneous composite material on a macroscopic level with varying composition and dissimilar raw materials. Besides, compared to metals, concrete possesses low thermal conductivity which means that it takes a lot of energy to manipulate its temperature change [98], [99]. Farahani et al. [100]–[102] adopted thermography to study the mechanical behaviour of metal and polymer structures subjected to fatigue loading conditions. It was proved that thermography is capable to monitor the structural behaviour based on the thermal variations.

As reported in [16], water/moisture leakage is an issue in any tunnel. This causes problems during excavation and support of the ground, and later it can lead expand to linings. It is accounted for the most common maintenance hazard, causing difficulties during tunnels' working life, not only to the tunnel lining, but also to the fittings within the tunnel. Problems are commonly encountered with incoming water in tunnels in conjunction with frost, giving rise to

- Reduction of the size of the tunnel opening by the formation of ice barriers;
- Obstruction of ventilation and other service ducts and shafts;
- Hazards from icicles forming in the tunnel roof.

Considering tunnels with unreinforced/reinforced concrete linings or tunnels with segmental concrete linings, water leakage is the most commonly cause of giving rise to transportation of fines, the formation of voids, settlement of ground, and eventually eccentric loading and distress of the lining. Inadequate sealing of the joints between concrete segments and poorly constructed joints in cast in situ concrete linings can lead to water leakage. Therefore, thermography is mainly able to identify [16]:

- ✓ Water circulating at a different temperature from that of the lining or surrounding rock;
- ✓ Changes in the geological conditions behind the lining;
- ✓ Defects in the lining;
- ✓ Voids.

There are the following limitations in its use:

- ➢ A stable thermal flow through the tunnel wall remains as essential. This should be steady over the measurement period to assess variations in conditions and the gradient between the rock and the lining surface should be at least 2 to 4°C, dependent on the accuracy of the thermography camera;
- ➢ The tunnel lining should have no coating or installation preventing thermal radiation penetration and, as a result of the insulating effect of the coating, alter the thermal flow through the material;
- ➢ Variations in water content over time will cause disturbance in the results;
- ➢ It is not easy to assess the depth and shape of an abnormality based on thermography alone.

Former research works [103], [104] demonstrate that thermography is capable to detect the water leakage and moisture in the tunnels' interior surface. On the other hand, it cannot be adopted to study the stress/strain fields on tunnels nor to monitor the crack existing on the interior wall.

Overall, owing to objectives of the present PhD research study, it can be concluded that the application of optical NDI methods on SHM of railway tunnels is an adequate task for to DIC, which will be discussed in Chapter 3 and Chapter 4.

2.6 Numerical simulations

This section reviews computational analyses on damage and fracture characterization of the railway tunnels which have been received damages due to the presence of defects.

Concrete is known to be a brittle material [105]. Typical to these materials, it has much lower strength in tension, than in compression. Cracks might appear in concrete elements when the structure is submitted to a load. Physical phenomena such as micro-crack appearance and growth and possibly their coalescence, modify the mechanical characteristics of the material. Hence, the damage and fracture mechanics can deduct this evolution using internal state variables, scalar or tensor according to objective when numerical modelling is applicable.

Numerous challenging fields in computational mechanics involve the study of the numerical nonlinear damage solution of concrete materials using FEM formulations [106]-[113]. Distinct aspects of the continuum damage mechanics field have been investigated by researchers to capture the concrete behaviour [114], [115]. Amongst all, there exist research works reporting the behaviour of concrete materials, such as softening response of concrete under monotonic uniaxial tension test [116], the behaviour of concrete under compressive enforced displacement [117], the response of concrete under biaxial stress states [118] and the three-point-bending tests on single-edge notched beams [119].

Various demanding isotropic nonlinear damage models for concrete structures were analysed with the FEM formulations, such as linear elastic models [114], [120]-[124], rate-dependent models [108] [110], viscous-damage models [107] and, more recently, elastoplastic damage models for crack propagation using Extended Finite Element Method (XFEM) formulations [125].

Within the scope of the present PhD research work, Farahani et al. [105], [126], [127] studied the damage and fracture behaviour of the concrete structures using FEM and Meshless methods. A numerical algorithm programmed in MATALB© was adopted to extend the Meshless method formulations to the nonlinear elastostatic damage mechanics. The developed formalism has been validated throughout several examples. Moreover, the nonlocal damage phenomenon in the presence of the micro-cracks in the concrete structures was also investigated by smoothing the strain field distributed on the surrounding nodes. Kamel et al. [128] proposed a methodology to acquire a state of deterioration of infrastructures and their evolution over time by integrating different parameters into the tunnels geometry and mechanical parameters of the tunnel components and the ground. Hence, a FE model, relying on parameters derived from the proposed procedure for auscultation, has been adopted to highlight the most damaged areas, which can disrupt the stability of the structure. The accomplished results proved that this numerical scheme combined with the diagnostic methodology for monitoring remained as the first step assisting managers to better assess the residual potential of their network and consequently improved repairs.

In the case of seismic analyses, Kampas et al. [129] carried out a Finite Element Analysis, FEA, to pursue the influence of tunnel lining modelling methods on the seismic response of concrete tunnels, demonstrating where the maximum circumferential forces took place. Bending moments have been analysed in the arch section on the tunnel led to identifying locations for strengthening as motions become more intense. It meant that a reinforced concrete tunnel augmented itself where the location of maximum circumferential force becomes coincident with the region of maximum bending moment. Kiryu et al. [130] numerically analyse the seismic retrofitting on cut-and-cover railway tunnels. A polymer isolation method has been established in which thin walls manufactured from polymers, so-called “isolation walls”, are appended between the ground and the tunnel’ sidewalls. The efficiency of the projected technique in seismic response reduction of tunnels has been evaluated by using computational simulations. It was concluded that the applicability of the polymer isolation method to the seismic retrofits design is robust and reliable. The structures safety has been also verified under the static conditions. Chen et al. [131] numerically studied the influence of the tunnel depth on its seismic damage using finite element, FE, simulations. The obtained results from the presented investigation can be simplified into convenient charts, which with reference to the uniaxial compressive strength of the rock and the rock mass rating would be used to estimate the potential damage to tunnel lining over an earthquake.

From the field experiments, Ferreira et al. [22] carried out a research study on the defects and deteriorations of the old railway tunnels, in particular Lapa metro tunnel located in Porto, Portugal. The rehabilitation works on the mentioned tunnel were discussed throughout numerical analyses. Diverse tunnel's sections, which received damage, have been studied using FEM formulations and internal variational fields were thereby evaluated and documented. Most recently, Lu and Hwang [132] conducted a computational research on the vulnerability and deformation associated to Sanyi railway tunnel under Chi-Chi earthquake in 1999 subjected to strong ground motions. Hence, a method based on the modified cross-section racking deformation (MCSRD) was adopted to assess the seismic performance of the corresponding railway tunnel. In addition, the strengthening influence of the secondary lining has been surveyed upon a reinforcement benchmark. It was recommended that the structure resists against earthquake loading if it is properly reinforced with steel bars. Besides, Yang and Wang [133] conducted a research study on Chinese Xian-nvyan tunnel of Xicheng high-speed railway to establish a 3D computational model. The deformation mechanism and the displacement of surrounding rock and the plastic failure were analysed by a combination of the geological forecast, computational simulation and field monitoring measurement.

Saloustros et al. [134] presented a review of FE approaches to cracking phenomenon in concrete structures focusing on the development and use of tracking algorithms. Several recognised challenges to model cracking with tracking algorithms have been addressed throughout the presentation of a local tracking algorithm. Strategies for modelling arbitrary internal and boundary cracking, crack-path continuity, crack intersection, crack opening and closure, as well as multi-directional cracking were described in detail.

However, the state-of-the-art included more numerical analyses on the concrete structures in which the damage and fracture phenomena had been studied to fulfil the numerical SHM; i.e. Numerical modelling of a tunnel in jointed rocks subjected to seismic loading [135]; Seismic distortions of a deep circular tunnel in elastic slightly anisotropic ground [136]; Simulation of tunnel response under spatially varying ground motion [137]; Test and finite element analysis, FEA, of gravity load designed precast concrete wall under reversed cyclic loads [138]; Prediction of the seismic behaviour of an underground railway station and a tunnel in Napoli (Italy) [139].

2.7 Predictive maintenance

According to [19], [26], for most civil tunnels with concrete linings, repairs can be carried out for mainly remedying concrete cracking, spalling, leakage and steel reinforcement corrosion. In the case of dry tunnels, no leakage faced, concrete repair methods may be applicable; nevertheless, for leaking tunnels, the additional countermeasures, e.g., water rerouting and ground grouting is crucial to operate. Besides, concrete tunnels are commonly finished with a decorative or anticorrosive material, e.g., ceramic tile or composites, and therefore the tunnel investigation requires a special consideration of these aspects too. In this section, some of the potential maintenance proposals are exhibited and discussed.

The repair method should be designated after clarifying the foundation of the concrete deterioration. It is possible to perform some manual crack repair by workmanship as illustrated in Figure 2.31-a). Additionally, it can be performed by using epoxy resins to fill dry cracks and delay or stop their active propagation. Since the cracks in a tunnel are commonly directional, crack repair uses syringes to inject resin into the crack, after sealing the surface of the crack with a paste gel or seal sheet, as depicted in Figure 2.31-b). For active cracks, a structural retrofit should primarily be implemented, to prevent a subsequent crack occurring along or near the original one. In addition, for the cracks under leakage, waterproofing should be performed in advance, discussed later.

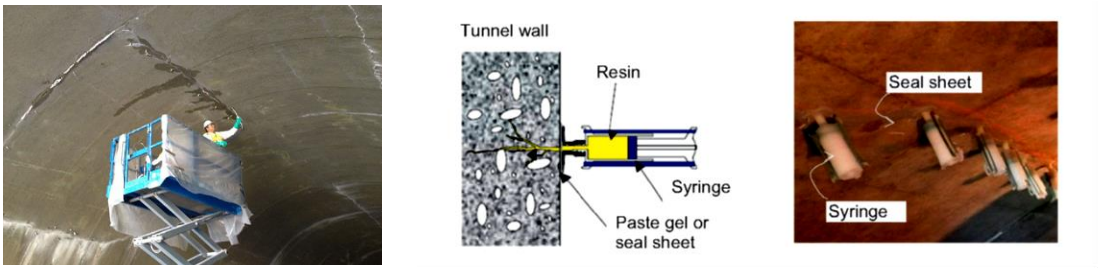

a) b)

Figure 2.31: Cracking repair on the tunnel-lining, a) manual maintenance and b) epoxy resins to repair the crack [12].

As mentioned before, delamination and spalls commonly happen with irregular shapes, which fluctuate hinging on whether the concrete has been reinforced or not. For reinforced structures, delamination typically takes place along reinforcement bars and results in the spalling of the concrete cover. The delaminated part must be removed straightaway when it is recognised as spalled. Spall repair depends on the size and effects; a deep spall must be repaired early, while a shallow one may be repaired later for aesthetic reasons. In consideration of the durability and structural integrity of the tunnel lining, delamination and spalling should be repaired by completely removing the deteriorating concrete and replacing the corroded steel. The repair procedure is demonstrated in Figure 2.32.

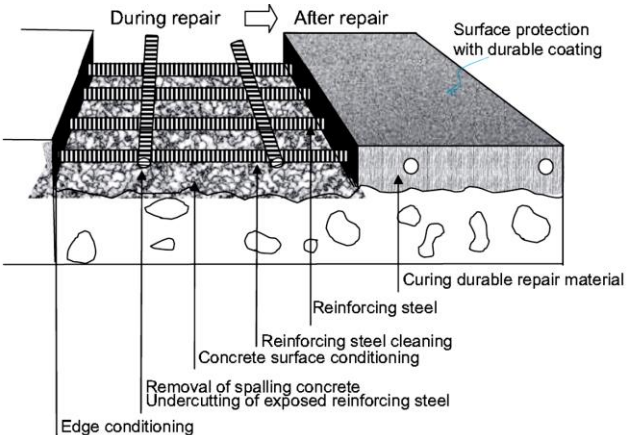

Figure 2.32: Repair of deteriorating concrete (delamination, spalling, and steel corrosion) [12].

In practice in Finland, in accordance with [140], if a tunnel received damages due to the crack presence or mainly water intrusion, the basic maintenance normally include local hammering of lose shotcrete, local repair of lining structures, ice removal, installation of local water controlling system and cleaning of drainage systems. The structures might be broken due to the pressure loads from traffic or ice formation behind the lining. Hence, several various techniques for local maintenance are necessary. As a solution, a new membrane structure on top of the old lining must be installed as seen in Figure 2.33.

Figure 2.33: The local maintenance performed on the frozen section of the tunnel lining by installation of the new membrane, Finland [140].

More about water leakage, it frequently befalls at a concrete crack or joints. The waterproofing method can be performed relying on the water intrusion passage and volume [141]. Figure 2.34 reveals several waterproofing approaches. These methods could be categorised into crack or joint sealing, based on the passage of water infiltration. Crack sealing and coating are beneficial for repairing a slight leak at a crack but are not appropriate for a torrential leak. In the case of a leak throughout a joint, a joint sealing approach should be taken into account. Furthermore, for shield tunnels, repacking the joint with a new gasket and new bolts might be necessary, depending on the deterioration condition. The final waterproofing adequate countermeasure should be determined in terms of cost, service life, aesthetics, functional effects, and constructability [12].

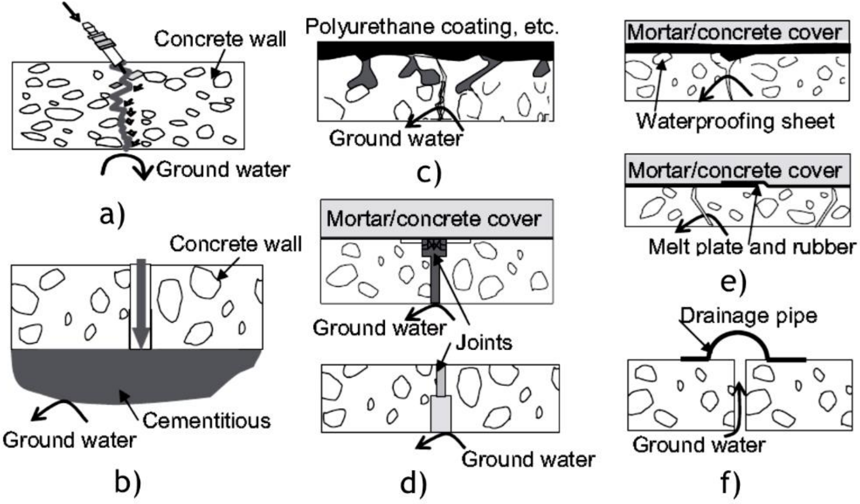

Figure 2.34: Tunnel waterproofing approaches; a) crack seals, b) ground grouting, c) surface coatings, d) joints seals, e) membrane sand f) rerouting [12].

On the other hand, if the structural integrity of a tunnel has substantially declined, tunnel rehabilitation may be considered. Many rehabilitation technologies have been developed in recent years, e.g., additional lining method for a large tunnel by a new structural lining installed inside [12]. Thus, if a local area or a member encounters severe degradation, a local reinforcement should be adopted by insertion an additional strengthening sheet, e.g., polymeric glass fibre sheet or composites, as schematically shown in Figure 2.35. Such reinforcements could improve the structural strength, but not the stiffness, and the effects greatly depend on the fibre sheets placement, which must be placed in the transverse and longitudinal layers with a high strength adhesive.

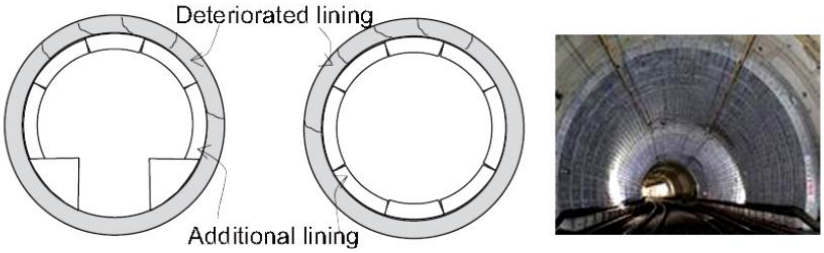

Figure 2.35: Additional lining support installation on the tunnel lining [12].

Owing to growing popularity of contemporary tunnels, modelling and monitoring composite-based tunnel structures is of excessive implication. It considers the development of composites in tunnel construction. Thus, the methodology to competently analyse the deformation and bending response of composite structures with its expanding application is standing an important topic. Several researchers compared the behaviour of traditional steel reinforced tunnels with new composite materials and thereby studied the tunnel structures' deformation [12], [142], [143].

Amongst all, Kiriyama et al. [144] proposed a tunnel reinforcement method using thin steel panels. Hence, this reinforcement method could be adopted to avoid exfoliation of concrete lining and restrain ground disturbance. Figure 2.36 demonstrates a structure of the reinforced tunnel with the railway tunnel presentation and the steel panel instalment. Therefore, because of the mentioned practical work, it would be feasible to establish a new, permanent measure to rehabilitate tunnel structures.

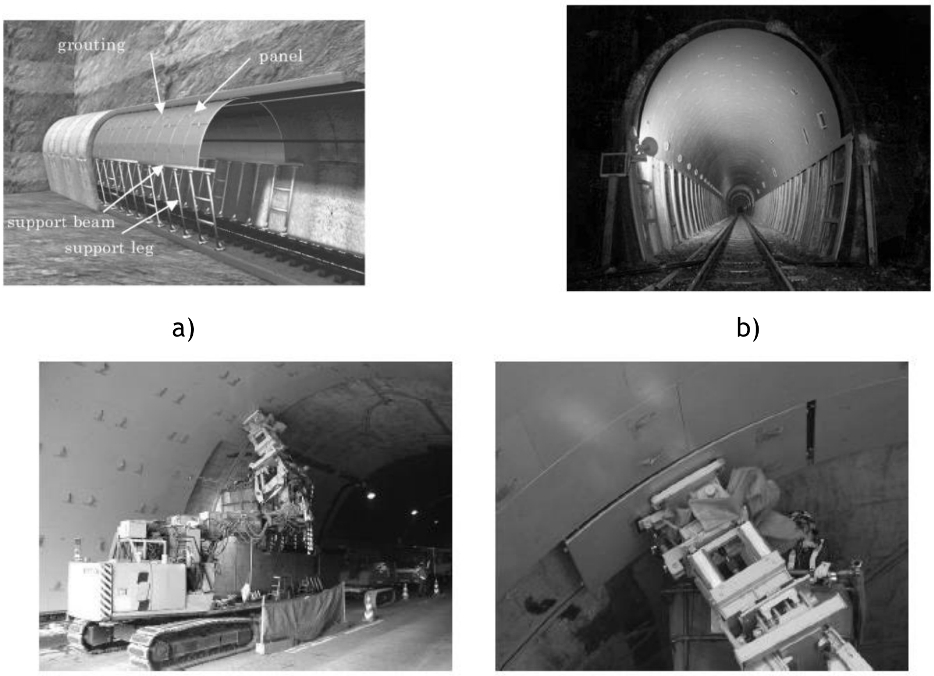

a)

b)

c)

Figure 2.36: Tunnels reinforced by steel panels; a) basic structure, b) a reinforced railway tunnel and c) panel installation by the electric machine [144].

Additionally, Wu et al. [145] studied the peeling and spalling strength of unidirectional Fibre Reinforced Polymer (FRP) sheets which have been externally bonded to the concrete surfaces throughout a series of peeling tests. Diverse factors were involved to provide the tested specimens such as fibres and adhesives sorts, process of surface treatment and the concrete strength.

Moreover, a robust method based on the optimal surface modelling has been developed by Yang et al. [146]. It aimed at optimizing the B-spline approximation for the typical composite tunnel structures in which profiles with various noises were considered. Experimentally, Caratelli et al. [147] studied the possibility of substituting the traditional steel reinforcement with Glass Fibre Reinforced Polymers (GFRP) in concrete tunnel segmental lining on metro infrastructures. This concept has envisaged cumulative interest for several applications in concrete components.

Regarding the composite sheets, that can be adopted as a solution of reinforcement on the tunnel lining, Farahani et al. [148], [149] computationally studied the response of the single layer composite structures subjected to bending loads. In the presented research, following FE and meshless methods, the mathematical equations respecting Radial Basis Function (RBF) formulation have been addressed with detail leading to optimise the shape parameter. The numerical analysis of a square Mindlin plate for the simply supported condition has been accomplished, which is of interest of the tunnel lining's reinforcement as well. Thus, a single-layered isotropic plate under a uniform distributed load has been analysed assuming both thick and thin conditions. The results derived from the presented study may assist to the production procedure of the composite applications to reinforce the tunnel linings.

2.8 Chapter summary

A literature review on inspection technologies for railway tunnels was presented in this chapter. Emphasis was put on the developed technologies and joining techniques associated to the ones surveyed in this PhD investigation. Railway tunnel structures and potential defects have been discussed and a series of the real damage railway tunnels were represented. A substantial variety of published research studies on the automated inspection technology were found, providing the application in the condition assessment and defect detection on railway tunnels. In addition, the adaptation of the laser scanning technology as a potential methodology of the automated inspection system has been highlighted.

Moreover, the optical non-destructive techniques, assisting to evaluate structural health monitoring of the civil infrastructure with a special attraction on the railway tunnels, have been reviewed by presenting their applications, advantages and disadvantages in defect monitoring. It was concluded that the structural cracks can be monitored and characterized by means of the digital image correlation analyses while the water leakage and moisture can be identified by the thermography methods. The repair proposals to tackle tunnels' disturbance preventing its collapse have been also reviewed. The combined application of the automated tunnel inspection and the defects monitoring is not commonly found in the literature, but field experiment requirements proved industrial interest and application case of combined automated inspection and defect characterization.

The research carried out during this PhD, which is stated in the following chapters intends to contribute to the-state-of-the-art, by deploying an automated inspection technique, building a laboratory scale demonstrator based on the 3D LSS, as well as monitor the geometrical changes and defects monitoring by means of the developed 3D DIC system.

As demonstrated in this chapter, the-state-of-the-art lacks a comprehensive study on the automated inspection system in the railway tunnels and simultaneously their SHM assessment. This thesis proposes to fill this gap in the literature, by not only developing and benchmarking the tunnel conditional assessment, but also studying its application to the real scale projects.

Chapter 3 : Second-stage Inspection Techniques

Given the development of the optical NDI techniques for the SHM of railway infrastructures, presented in the previous chapter, this chapter will study their implementation in engineering structures. The emphasis is on the application of optical NDI tools to monitor defects and assess the material's structural behaviour. For this purpose, different benchmarks associated with concrete, polymers, aluminium and steel alloys were studied by experimental tests and computational simulations.

All structural components deteriorate during service due to several factors including fatigue loading, and environmental circumstances. Therefore, the interest in SHM systems for these structures has progressively increased in the recent decades. This chapter highlights the structural analyses on different engineering benchmarks to fulfil the objectives of the second-stage inspection techniques such as the DIC.

Railway tunnels are commonly made of concrete and reinforced with steel, aluminium alloys and covered by fibre polymers and composites. Considering this, mechanical behaviour of the railway tunnel's components must be assessed in accordance with solid and fracture mechanic fundamentals. This structural analysis would be accompanied with the experimental tests performed with support of optical NDI techniques. Numerically, the presented examples are resolved using FE and Meshless methods. Thus, the accomplished results by the optical NDI tools on structural analyses of the engineering components validated the numerical methods, pointed out in this chapter.

Amongst optical NDI tools, DIC is of interest in this PhD research study. As demonstrated in the previous chapter, DIC has the potential to monitor the strain field and characterize the crack growth during mechanical testing, which is the orientation of the developed inspection technology on the railway tunnel, proposed in this PhD thesis.

Overall, mechanical testing supported by DIC analysis enables the acquisition of the required deep knowledge about the fundamentals of DIC potential in SHM, later proposed for tunnel inspection.

3.1 DIC applications on SHM

DIC principles rely on the image acquisition over a mechanical testing procedure. Image correlation fundamentals for practical applications have been extensively described in the literature [150] as a reference for academic and industry-based researchers and engineers. DIC has been widely implemented in the scope of elasto-plasticity, damage, fracture and fatigue mechanics of various material behaviours [151]-[155].

This section presents several benchmarks analysed by means of the 2D and the 3D DIC. The performed experiments focused on the elastoplastic, fracture, and fatigue and damage behaviour of different materials. It intended to prove the capability and accuracy of the DIC on the SHM.

In the presented examples, the diverse mechanical behaviours are experimentally characterized relying on DIC. The force in terms of displacement, stress intensity factor (SIF) and stress/strain distributions are obtained. Numerically, all benchmarks are resolved using FE and Meshless methods. Owing to acquired results, the structural behaviour under different loading conditions is assessed.

3.1.1 Aluminium AA5352 specimen

This study is a nonlinear elastoplastic failure analysis performed on an Aluminium alloy AA5352 specimen manufactured according to ASTM E 8M-04 [156], as published in [157]. A general view of the specimen with its geometrical dimensions is presented in Figure 3.1. The specimen thickness is $e = 0.28\ \mathrm{mm}$. The experimental test was performed by a servo-hydraulic material test system, $10\ kN\ MTS - 812$ using a crosshead speed of $V = 5.00\ \mathrm{mm/min}$ with a total displacement enforcement of $\bar{v}(x,y) = 7.50\ \mathrm{mm}$ on point A, see Figure 3.1. The force/displacement variation was obtained by the 3D DIC [157].

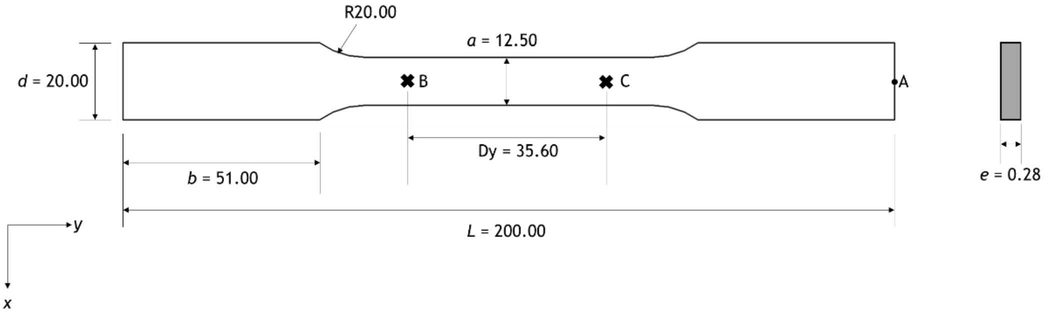

Figure 3.1: AA5352 specimen manufactured according to ASTM E 8M-04, dimensions are in mm [157].

The 3D DIC system was positioned in front of the tested specimen as presented in Figure 3.2-a). Regarding the setup, two 4.1 mega pixel cameras with a resolution of $2048.0 \times 2048.0\ \mathrm{pixel}^2$ were used. To illuminate the specimen's surface, a $150.0\ \mathrm{W}$ halogen lamp was used. The mounted specimen considering its gripping setup and reduced section is also shown in Figure 3.2-b). The field of view (FOV) of the DIC image acquisition in the sensor format and the Cartesian coordinate system are depicted in Figure 3.2-c). The investigated area was gridded with a subset of $29\ \text{pixel}$ and step size of $6\ \text{pixel}$. A facet field respecting a $29 \times 29 - \text{pixel area}\ (0.71 \times 0.71\ \text{mm}^2)$ is presented in Figure 3.2-d). The speckle pattern was characterized with a stable black and white pigmentation with dot size varying between 2 and $5\ \text{pixel}\ (0.05 - 0.13\ \text{mm})$. Camera calibration was performed by a 12-by-9 dot 0checkerboard spaced by $2.50\ \text{mm}$.

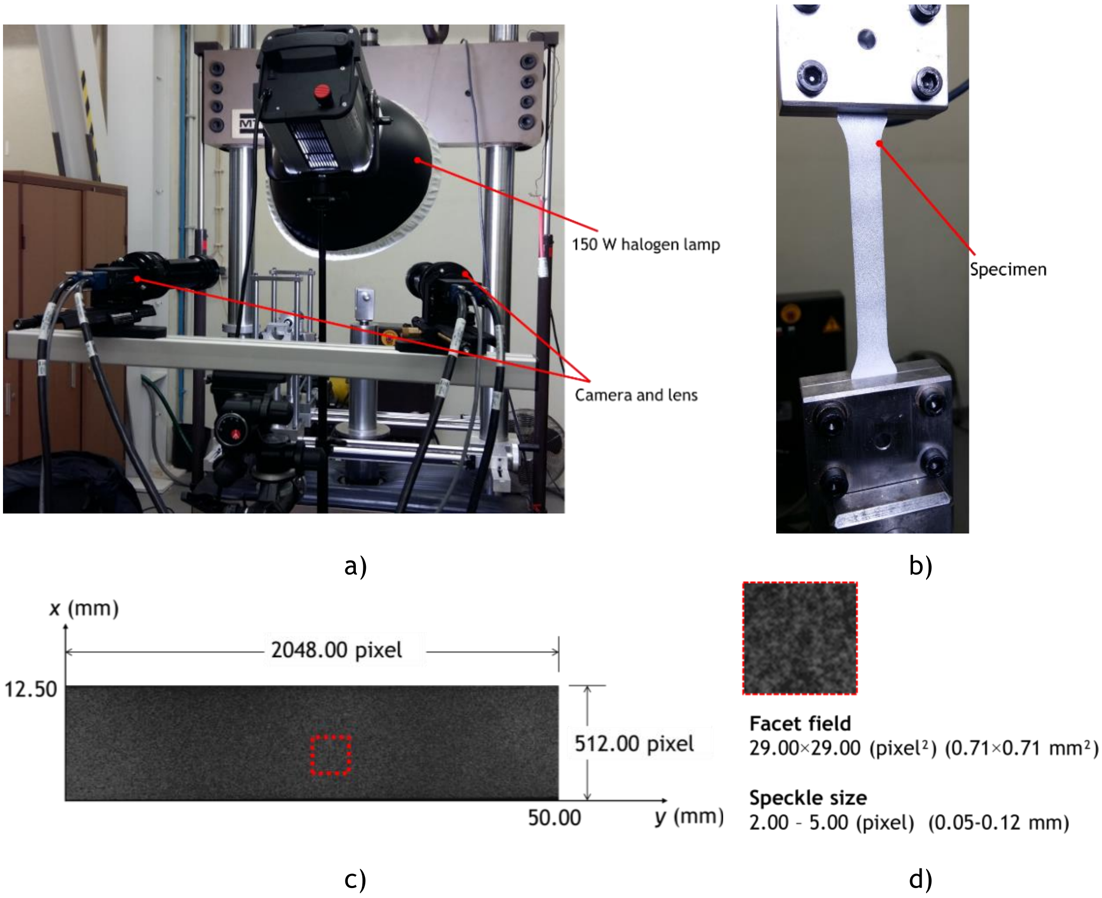

a) b)

c) d)

Figure 3.2: DIC system standing in front of tested specimen with a working distance of 1000 mm, b) specimen mounted in the tensile machine, c) camera field of view and d) a facet field respecting speckle pattern.

Figure 3.3 presents the evolution of longitudinal, transverse and shear strain profiles, ε_{xx}, ε_{xy} and τ_{xy}, during the experimental test captured by DIC. To characterise the material properties, the following procedure was considered. Two points (B and C), with a vertical clip gage length of $35.65\ \text{mm}$, were selected on the specimen and then their displacement field were evaluated. Therefore, load correlated with the displacement variation between point B and point C, $[\Delta v(x, y)]$, was experimentally obtained, as shown in Figure 3.4. Notice that, the presented force/displacement response is associated to the elastoplastic analysis before the failure occurrence.

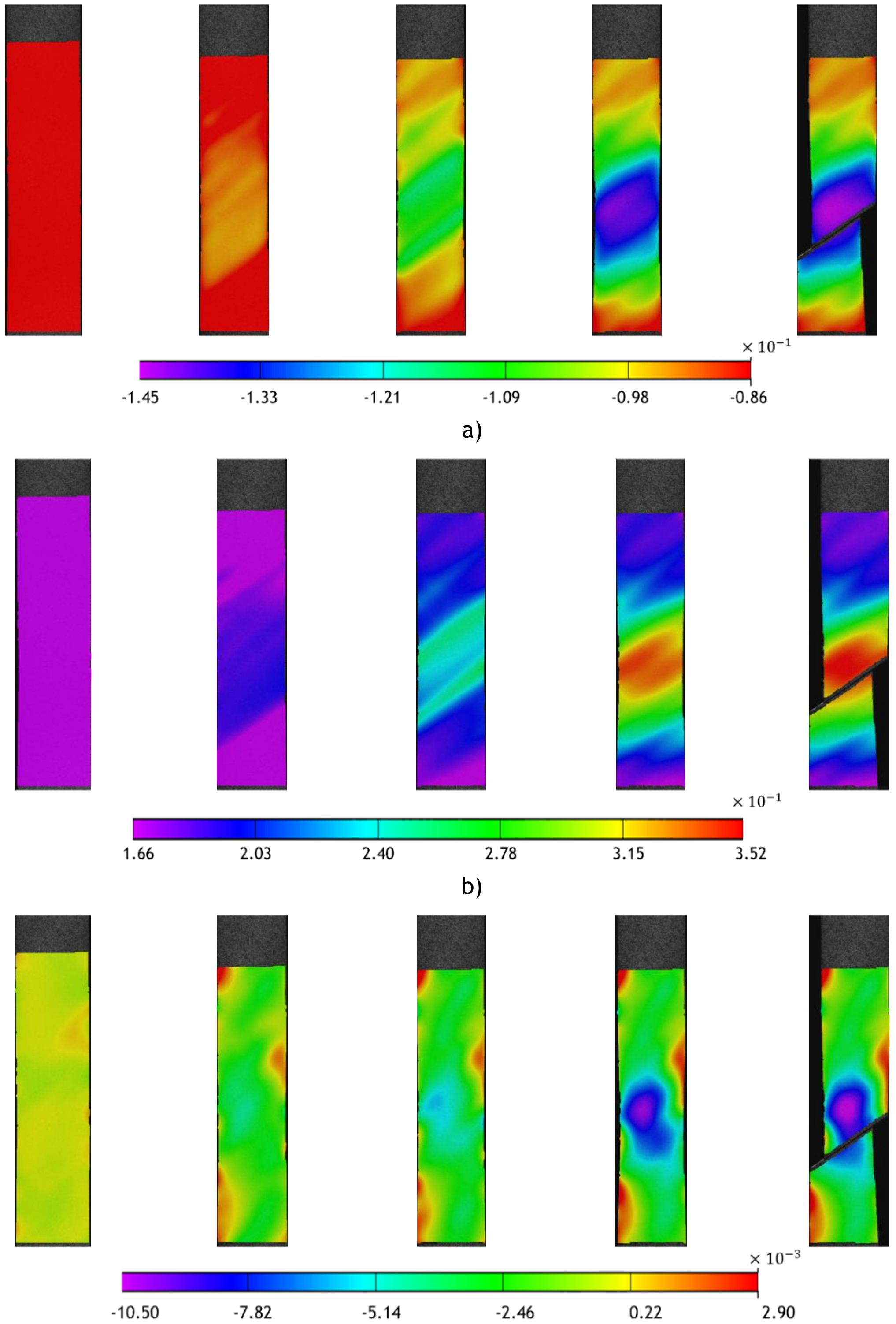

a)

b)

c)

Figure 3.3: Strain evolution obtained from DIC for AA5352 specimen, a) longitudinal strain, b) transverse strain and c) shear strain.

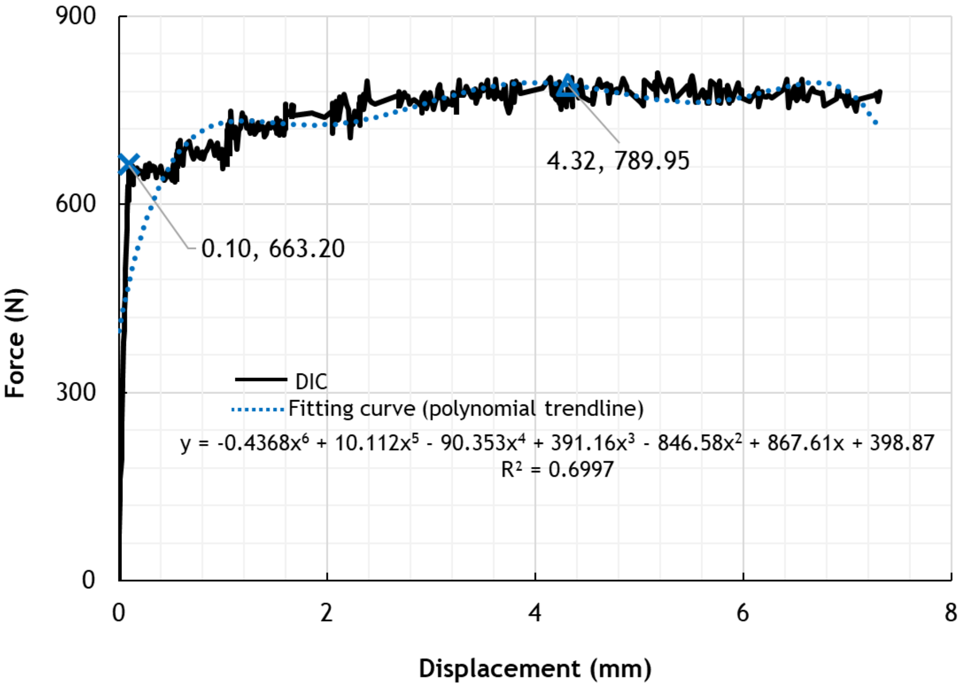

Figure 3.4: Reaction force response on point A in terms of the displacement variation, $\Delta \boldsymbol{v}_{\boldsymbol{CB}}$ obtained from experimental uniaxial tensile test [157].

To determine Young's modulus, E, the elastic limit of the material behaviour was identified on the force/displacement response as $\{v_0 = 0.10\ \mathrm{mm}\,, F_{el.} = 663.20\ \mathrm{N}\}$, as shown in Figure 3.4. Considering the effective cross section as $A_{ef.} = d \times e = 3.49\ \mathrm{mm}^2$, the yield strength of the material was computed as $S_Y = F_{el.}/A_{ef.} = 190.03\ \mathrm{MPa}$. Regarding the strain value at the elastic limit, it was calculated as $\varepsilon_0 = v_0/\Delta y = 2.80 \times 10^{-3}$. Within a simple calculation based on Hooke's Law, it was possible to evaluate the Young's modulus as $E = S_Y/\varepsilon_0 = 68.49\ \mathrm{MPa}$.

To calculate the tangent modulus, another point of the force/displacement response was chosen having a dimension of $\{v_1 = 4.32\ \mathrm{mm}\,, F_1 = 789.95\ \mathrm{N}\}$, see Figure 3.4. Afterwards, to obtain the engineering stress and strain components, the similar calculation was done leading to $\sigma_1 = 241.99\ \mathrm{MPa}$ and $\varepsilon_1 = 0.12$. Finally, the tangent modulus was derived as $E_{T0} = \Delta\sigma/\Delta\varepsilon = (\sigma_1 - S_Y)/(\varepsilon_1 - \varepsilon_0)$, leading to $E_{T0} = 238.26\ \mathrm{MPa}$. Regarding the Poisson's coefficient, it was considered as the typical value for the Aluminium alloys: $\upsilon = 0.33$.

Therefore, the essential material properties of aluminium alloy AA5352 have been determined using experimental data obtained by DIC.

Considering the standard elasto-plastic formulation, the model was solved using FEM, in ABAQUS©. Therefore, an explicit model was considered where a 2D plane stress shell formulation was assumed. Moreover, 3-node triangular general-purpose shell elements (S3) were used to construct the FE mesh. The FE mesh includes 5050 nodes and 9656 elements. Figure 3.5-a shows the mesh respecting the applied boundary conditions. Two reference points (RF_1, RF_2) have been assigned to the model kinematically coupled to the corresponding surface for the boundary condition definition. To analyse the model, an isotropic hardening behaviour of aluminium alloy AA5352 relying on Voce's law [158] was considered in FEA as follows:

$$S_Y = A - Bexp(-C \times \varepsilon_p) \tag{3.1}$$

where $A = 285.40\text{MPa}$, $B = 91.90\ \text{MPa}$ and $C = 15.53$ [157].

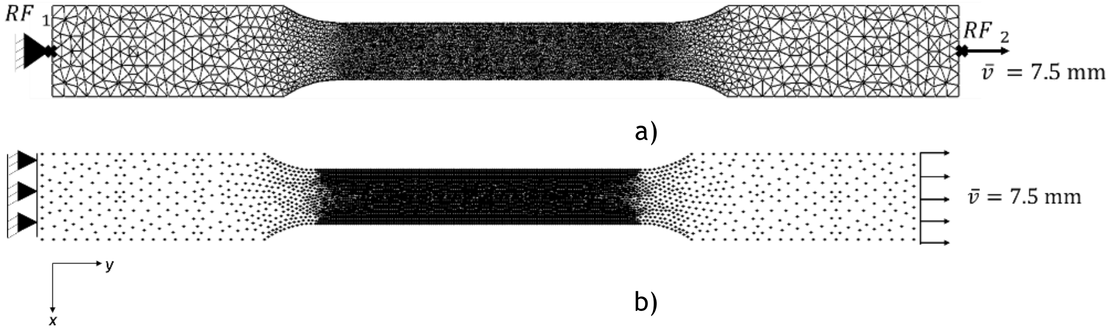

Figure 3.5: Numerical model of AA5352 specimen; a) FE mesh and b) meshless nodal distribution [157].

The model has been also solved using radial point interpolation meshless method, RPIM, and its natural neighbour version, NNRPIM, formulations (as extensively described in Appendix B) considering a nonlinear elastoplastic formulation (see Appendix B.6 for details). The material properties have been used as obtained by the DIC analysis. Figure 3.5-b) illustrates the meshless nodal discretization consisting of 5050 nodes while 28968 and 28876 integration points were considered in RPIM and NNRPIM, respectively. Owing to the nonlinearity, a nonlinear Newton-Raphson algorithm [157], was adopted to obtain the nonlinear converged solution. Therefore, a tolerance of $toler = 1 \times 10^{-6}$ was considered while displacement imposition was incrementally enforced during a total number of 30 increments in the nonlinear elastoplastic mechanism. Regarding NNRPIM analysis, both the first and the second degree influence-cell formulations (the concept of NNRPIM influence-cell was extensively explained in Appendix Appendix BB.1) are taken into account (NNRPIMv1 and NNRPIMv2, respectively).

Owing to the performed elastoplastic analyses, the reaction force response on point A correlated with the displacement variation ($\Delta \boldsymbol{v_{CB}}$), extracted from all experimental and numerical studies, is presented in Figure 3.6. This figure also comprises a trend associated with the FEM code based on the standard 2D constant strain triangle elements. The corresponding curve is identified as FEM-3n. Numerically, the equivalent von Mises stress ($\tilde{\sigma}$) distribution along the problem domain at the end of the elastoplastic analysis is shown in Figure 3.7.

The graphs reveal that the NNRPIMv2 solution is closer to the DIC and FEM solutions, allowing to infer that higher degree influence-cells permit to achieve more accurate results. Nevertheless, when the three formulations are compared considering even conditions, the results are not so different. The full analyses respecting different meshes and nodal discretization with the presented results on force/displacement, equivalent plastic strain and equivalent von Mises stress could be found in the published article [157].

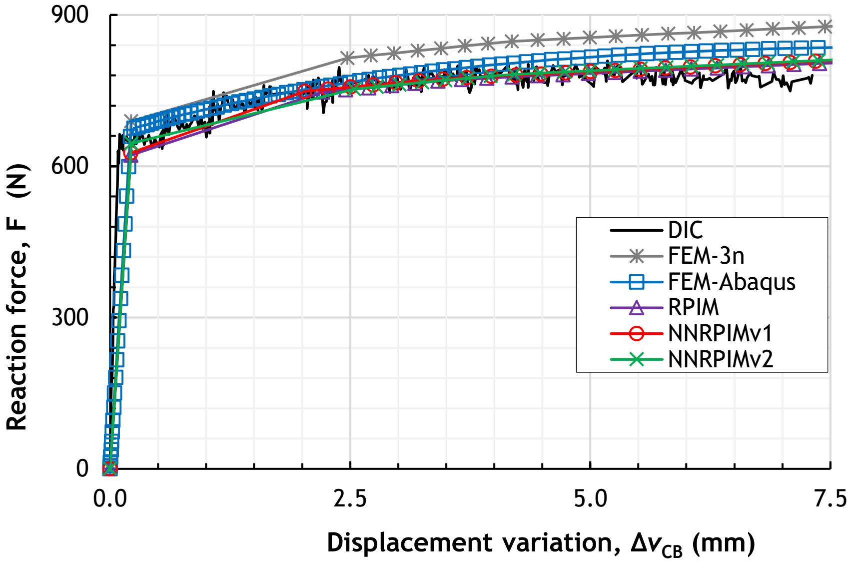

Figure 3.6: Reaction force response on point A correlated with the displacement variation (Δv_{CB}) obtained from all studies [157].

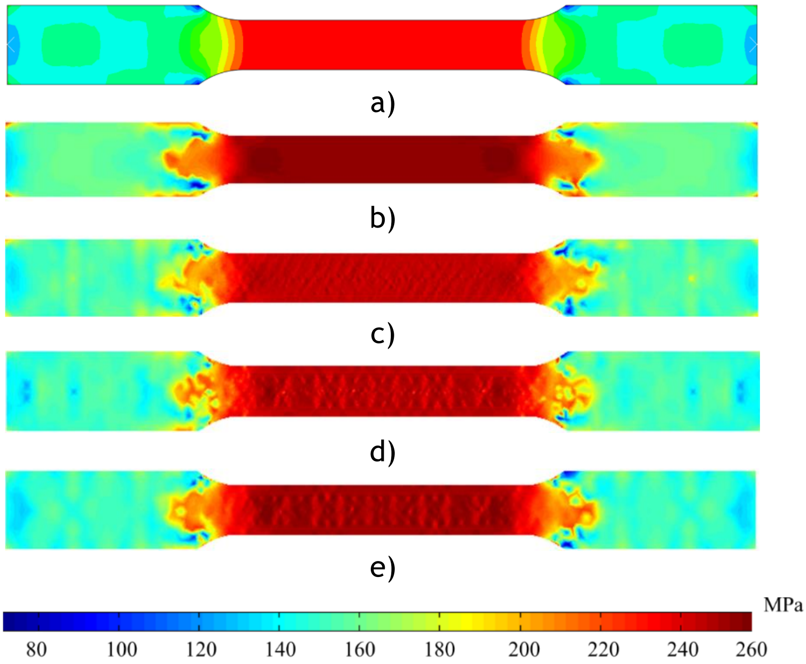

Figure 3.7: Equivalent von Mises stress obtained for a) FEM-Abaqus, b) FEM-3n, c) RPIM, d) NNRPIMv1 and e) NNRPIMv2 [157].

3.1.2 Bi-failure tests

In this part, bi-failure specimens manufactured from aluminium alloy AA6061-T6 and steel alloy DP600 have been mechanically tested using the 3D DIC [3], [159], [160]. It intended to capture the elastoplastic behaviour subjected to a uniaxial tensile test condition. Then, it aimed at determining the failure mechanism of materials due to the plasticity. The experiments have been performed using a servo-hydraulic $MTS - 812\ 100\,\mathrm{kN}$ tensile machine. The experiments were carried out with a crosshead rate of $V = 1.0\ \mathrm{mm.min^{-1}}$. To calculate strain rate, the following expression is applicable:

$$\dot{\varepsilon} = d\varepsilon/dt = [d\,(l - l_0)/l_0]/dt = V/l_0 \tag{3.2}$$

If the initial clip gage length, $l_0 = 50.0\ \mathrm{mm}$, was considered in Equation (3.2), the strain rate took the following value; $\dot{\varepsilon} = 3.3 \times 10^{-4}\ \mathrm{s^{-1}}$. The material properties of AA6061-T6 and DP600 in addition to the experimental test conditions are reported in Table 3.1. The standard bi-failure samples were designed according to ASTM E 8M-04 [156], as seen in Figure 3.8.

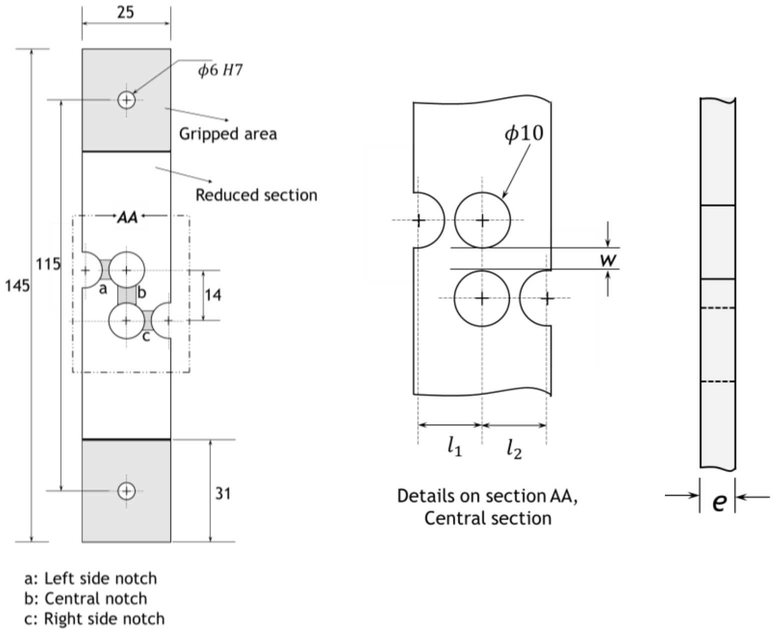

a) b) c)

Figure 3.8: Standard bi-failure specimen: a) a general view, b) front view on the central section and c) side view of the central section, values are in mm.

In general, the bi-failure experiments on AA6061-T6 and DP600 samples subjected to a uniaxial tensile condition are divided into two main categories:

a) Elastoplastic response of the intended materials in which the experimental data was evaluated by DIC and verified by numerical simulations respecting FE and meshless methods;

b) The damage and failure behaviour of the materials captured by DIC and computationally analysed using FEM formulation extended to Gurson Tvergaard Needleman, GTN, coupled damage criterion.

In the former bi-failure experiment, the meshless method analysis followed the nonlinear elastoplastic routine described in Appendix B.6 and the obtained results are compared to the standard FEA simulated in ABAQUS©. Owing to the presented results on the force/displacement diagrams and the internal variational fields, the elastoplastic response of the corresponding materials is assessed and documented. The latter one aims at determining the failure mechanism of the presented materials. The empirical results rely on DIC and then, FE damage model is resolved using GTN criterion, as its principles formulation explained in Appendix E. As a result, the engineering stress/strain curves are reported. Comparisons are made between DIC and GTN damage model. Promising computational results are verified by DIC results implying that supportive strategy is proficient. Table 3.2 presents the main parameters for both AA6061-T6 and DP600 materials used in the GTN analyses in FEM model.

Table 3.1: Material properties and experimental configurations on bi-failure tests [3], [159], [160].

Material Properties

		AA6061-T6	**DP600**
Young's modulus, E		$68.90\ \mathrm{GPa}$	$210.00\ \mathrm{GPa}$
Poisson's coefficient, ν		0.33	0.30
Density, ρ		$2.70 \times 10^{-9}\ \mathrm{ton/mm^3}$	$7.80 \times 10^{-9}\ \mathrm{ton/mm^3}$
Thickness, e		$1.00\ \mathrm{mm}$	$0.80\ \mathrm{mm}$
Yield stress, S_Y		$297.60\ \mathrm{MPa}$	$416.10\ \mathrm{MPa}$
Ultimate tensile stress, UTS		$333.80\ \mathrm{MPa}$	$630.90\ \mathrm{MPa}$
Tangent modulus, E_{T0}		$69.00\ \mathrm{MPa}$	$210.00\ \mathrm{MPa}$
Strain hardening, Voce's law	A	$149.00\ \mathrm{MPa}$	$746.00\ \mathrm{MPa}$
	B	$208.70\ \mathrm{MPa}$	$30.10\ \mathrm{MPa}$
	C	12.10	17.55

Experimental test conditions

Testing direction	RD
Crosshead motion rate, V	1.00 $\mathrm{mm/min}$
Frequency acquisition, f	5.00 Hz
Room temperature, T	20.00 $^{\circ}\mathrm{C}$

Table 3.2: Main parameters in GTN model, FE analyses [3], [160].

Material	**Porous metal plasticity**			**Void nucleation**			**Porous failure criteria**	
	q_1	q_2	q_3	S_N	f_N	ε_N	f_c	f_f
AA6061-T6	1.50	1.00	2.25	0.10	$0.80e^{-3}$	0.30	$1.30e^{-1}$	$0.40e^{-1}$
DP600	1.50	1.00	2.25	0.20	$0.20e^{-1}$	0.10	$1.80e^{-1}$	$0.45e^{-1}$

To carry out the 3D DIC analyses, two synchronised cameras (resolution of $2048 \times 2048\ \mathrm{pixel}^2$) were adopted considering an operational distance of $1000\ \mathrm{mm}$ to the specimens' surface. Camera lenses were configured based on work objectives, C-Mount Rodagon 80 mm f/4 lenses were thus designated to acquire correlated images. A $150\ \mathrm{W}$ halogen lamp was also used to illuminate the specimen surface, see Figure 3.9. To exclude lens distortions, cameras have been calibrated by means of a 12-by-9 checkerboard spaced as 4 mm, by means of the bundle adjustment, the correctness degree of the calibration is reported in Table 3.3. Moreover, the bare specimen was coated with a white ink sprinkled with black spots to generate a random pattern, as presented in Figure 3.10-b). Therefore, the generated arbitrary patterns on the surface were recorded during testing.

The captured images were processed in VIC-3D 2012© vision software. The examined region was meshed respecting a subset and step size presented in Table 3.4 for each test experiment. The camera field of view, FOV, dimensioned as $25 \times 53\ \mathrm{mm}^2$ with a sensor resolution of $965 \times 2048\ \mathrm{pixel}^2$, as Figure 3.10-a) indicates. It aimed at determining the force/displacement response on diverse sections on the specimen. As shown in Figure 3.10-a), six auxiliary points were selected on the problem domain with the defined initial length (gauge) correspond to each notch (left, right and central side).

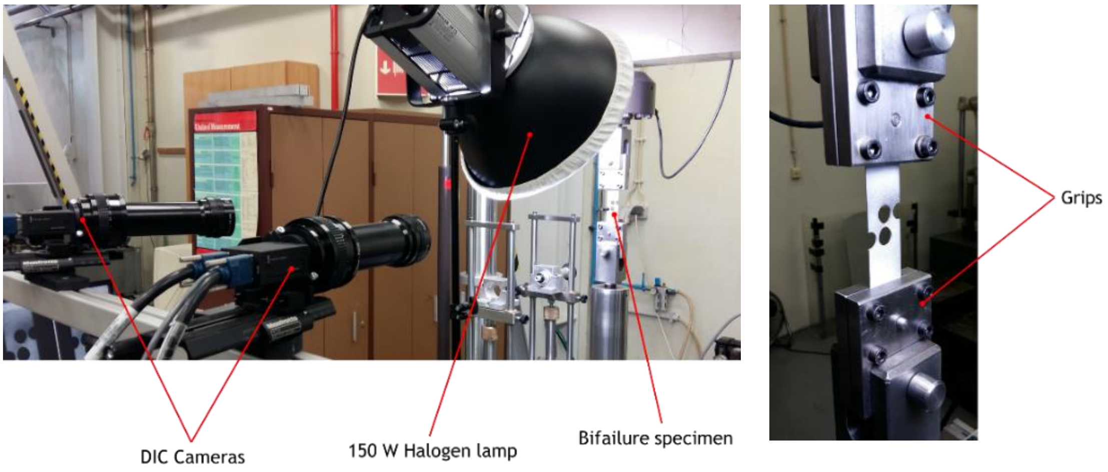

a) b)

Figure 3.9: Experimental setup of the bifailure specimen; a) the 3D DIC system standing in front of the specimen and b) specimen and grips [3].

Moreover, Figure 3.10-b) presents a facet field including an area of $29.00 \times 29.00\ \mathrm{pixel}^2$ with a dimension of $0.75 \times 0.75\ \mathrm{mm}^2$ in the interest region related to the AA6061-T6 bi-failure experiment. It denoted that a $29.00 \times 29.00\ \mathrm{pixel}^2$ region per $6.00 - \mathrm{pixel}$ was chased where the total smoothing space is $174.00\ \mathrm{pixel}$. Concerning its speckle pattern characterization, the spot size ranged from 2.00 to $5.00\ \mathrm{pixel}$ or $0.05\text{–}\ 0.13\ \mathrm{mm}$ contributing to construct a steady black and white colour distribution.

In order to evaluate the expected accuracy to compute the uncertainty of the measurements, some calculations are required. To estimate the spatial resolution or data-point spacing, the FOV in (mm) must be divided by its sensor format and then it must be multiplied by the step size. In this study, the spatial resolution accounted for a value of 0.16 (mm).

Moreover, since the available camera resolution permits to estimate the correlation accuracy equals to $1/50^{th}$ of a pixel for a controlled laboratory environment, the measurement accuracy could be calculated as $0.52\ \mu\mathrm{m}$.

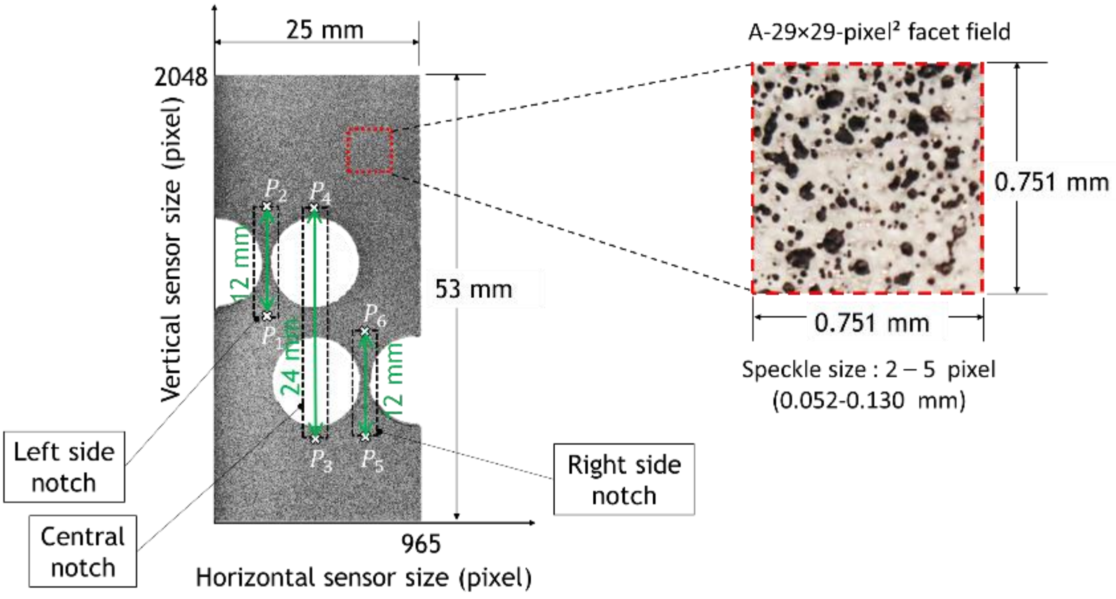

a) b)

Figure 3.10: a) DIC domain and details on the notches presenting auxiliary points and b) detail on a facet field and speckle pattern [159].

Table 3.3: The correctness degree of the DIC calibration [159].

Calibration result	Camera 1	Camera 2
k_1	-5.78×10^{-3}	2.11×10^{-2}
K_2	-6.08×10^{0}	1.57×10^{1}
γ	-7.59×10^{-1}	2.87×10^{-1}

Table 3.4: DIC specifications for AA6061-T6 and DP600 experiments.

Test	Subset size	Step size	Speckle size
AA6061-T6	29×29 pixel^2 0.751×0.751 mm^2	6 pixels	2- 5 pixels 0.052 - 0.130 mm
DP600	30×30 pixel^2 0.780×0.780 mm^2	7 pixels	3- 6 pixels 0.078 - 0.155 mm

Elastoplastic analysis on AA6061-T6 bi-failure specimen

The experiments begin with the elastoplastic analysis of the AA6061-T6 specimen and it completed with the GTN damage analysis. The geometry has been considered as shown in Figure 3.8 in which $w = 4.0\ \mathrm{mm}$, $l_1 = l_2 = 11.6\ \mathrm{mm}$ and the specimen thickness defined as $e = 1.0\ \mathrm{mm}$. The material properties have been adopted as reported in Table 3.1.

The elastoplastic experiment was carried out in displacement-control regime with a total magnitude of $\bar{v}(x, y) = 1.0\ \mathrm{mm}$ enforced on the upper grip (see Figure 3.8-a).

A FEA was carried out to evaluate the elastoplastic behaviour of the proposed model. Hence, the FEM model was explicitly simulated considering a 2D plane stress shell formula. Regarding the mesh, 3-node triangular shell elements (S3) respecting finite membrane strains were used to build the mesh, as Figure 3.11-a) illustrates. More elements were built on the interest region where the elastoplastic response was anticipated. The mesh included 3728 nodes and 7060 elements. Regarding the boundary conditions, a displacement of $\bar{v} = 1.0\ \text{mm}$ was imposed in y-direction over the uniaxial tensile analysis. To meet the experimental setup, the lower edge was fixed, Figure 3.11-a). Besides, an isotropic hardening behaviour depending on Voce's law [158] has been adopted following Equation (3.1), and the strain hardening constants were used as presented in in Table 3.1.

RPIM meshless formulation extended to nonlinear elastoplastic analysis was used to resolve the proposed problem, see Appendix B for the governing formulations. The solid domain has been discretised respecting 3726 nodes and 21174 integration points, as seen in Figure 3.11-b). The nodal discretization pattern and boundary conditions followed the similar FEM analysis. For the nonlinear solution algorithm (as described in Appendix B.6), the tangent modulus has been chosen as $E_{T0} = 69\ \text{MPa}$. A nonlinear Newton-Raphson algorithm was adapted to provide the nonlinear converged outcome. Consequently, a tolerance of $toler = 1 \times 10^{-6}$ was defined allowing for an incrementally imposed displacement with 30 increments in the nonlinear elastoplastic scheme. Owing to the complex nodal distribution on the interest section, to evaluate the effect of the influence domain in the RPIM analyses, a preliminary study has been performed in which the quantity of nodes inside any influence-domain increased from 13 to 19. It may contribute to obtain slightly more accurate results if a denser influence domain is applicable, on the other hand, it leads to increase the computational costs.

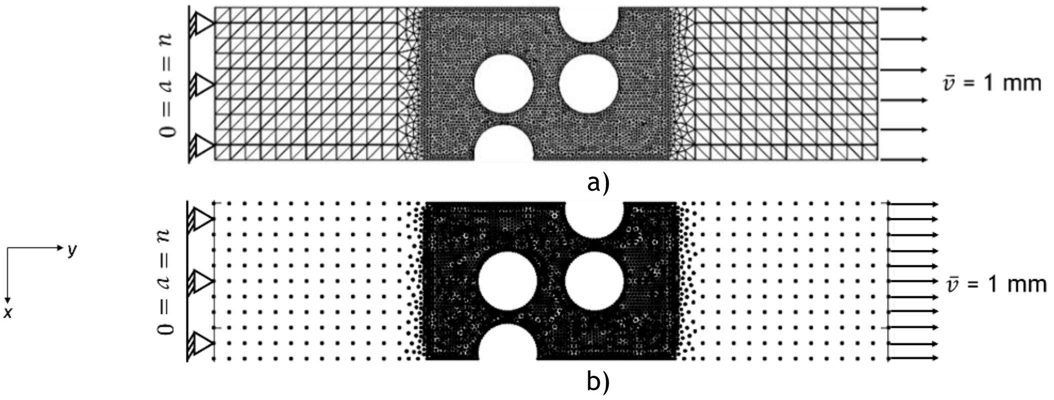

a)

b)

Figure 3.11: Computational AA6061-T6 elastoplastic model with the essential boundary condition illustration; a) FEM and b) RPIM meshless method.

The obtained results of the remote stress/longitudinal strain on the side notches extracted from all analyses are presented in Figure 3.12. Different RPIM studies are identifying as "RPIM_ID_13", "RPIM_ID_16" and "RPIM_ID_19" if each influence domain included 13, 16 and 19 nodes, respectively. From the presented diagrams, it can be inferred that although the nodal intensity increases inside influence domains lead to improve the solution accuracy, the amplification of the influence-domain size contributes to higher computational costs. Nonetheless, since there is no significant alteration amongst all RPIM analyses, a medium influence domain "RPIM_ID_16" case could be considered as the main RPIM study and the rest of results are correlated in accordance with this model.

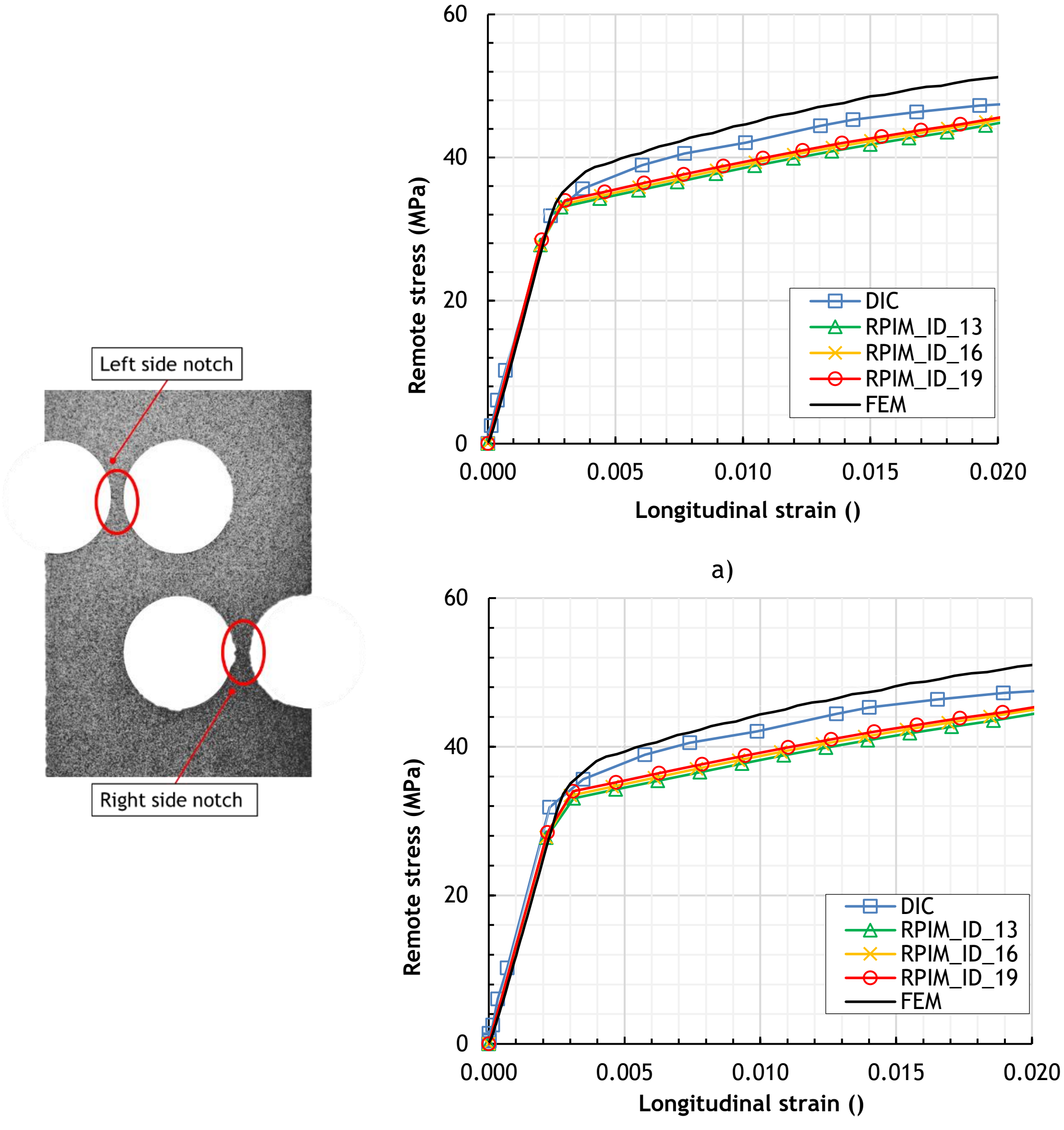

a)

b)

Figure 3.12: Remote stress correlated with the longitudinal strain variation on; a) left side notch, and b) right side notch, obtained for all approaches [159].

Figure 3.13 illustrates longitudinal, transverse and shear strain profiles obtained from DIC and FEM analyses, ε_{xx}, ε_{yy} and γ_{xy}. The profiles reveal a smooth shape anticipating the elastoplastic phenomenon in the specimen's middle section. In addition, the central notch underwent a high shear strain as the profile reveals. Figure 3.14 depicts the von Mises strain field from all analyses.

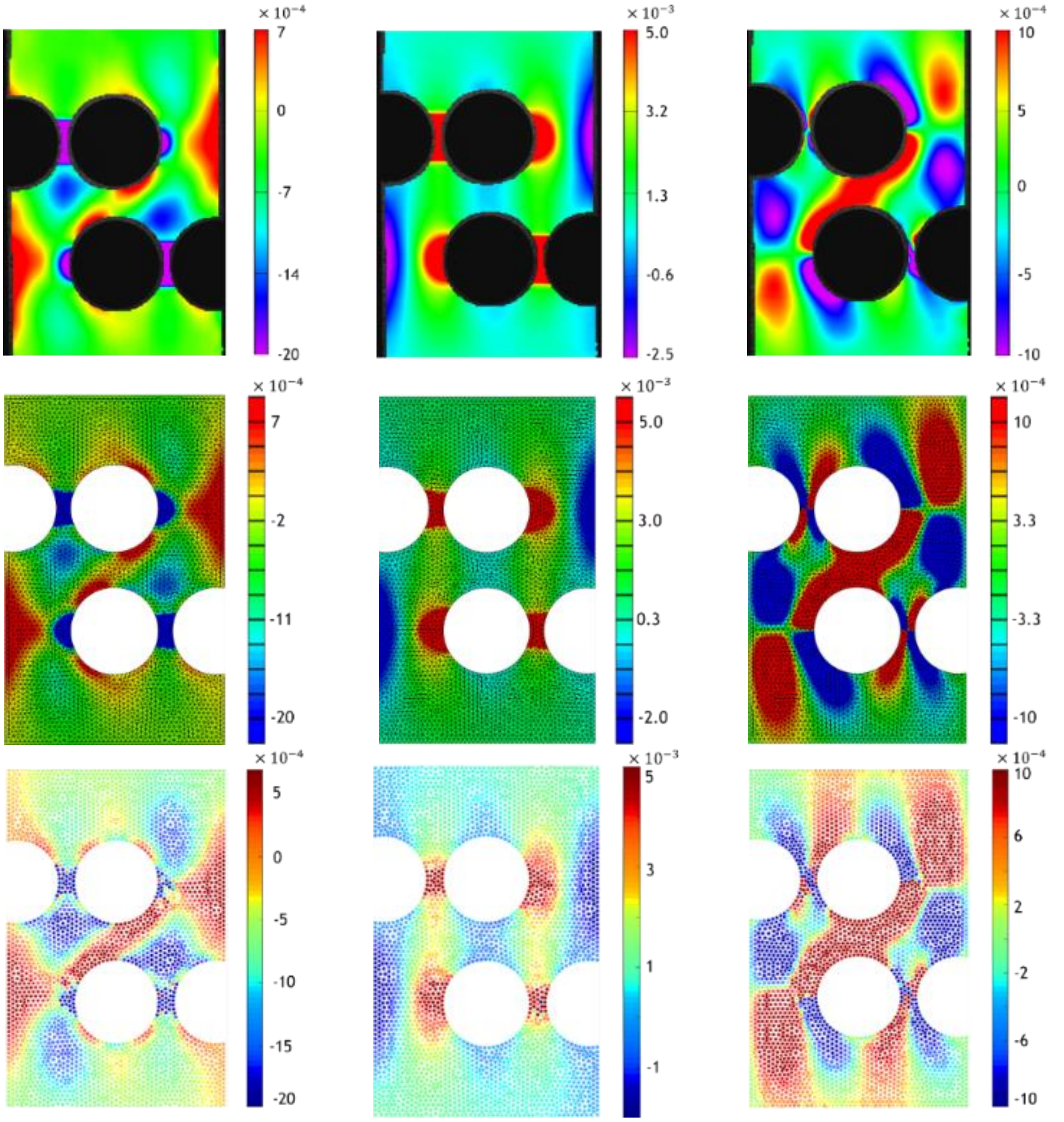

a) ε_{xx} b) ε_{yy} c) τ_{xy}

Figure 3.13: Strain distribution extracted at the end of the elastoplastic analysis: top row: DIC, middle row: FEM and bottom row: RPIM meshless study [159].

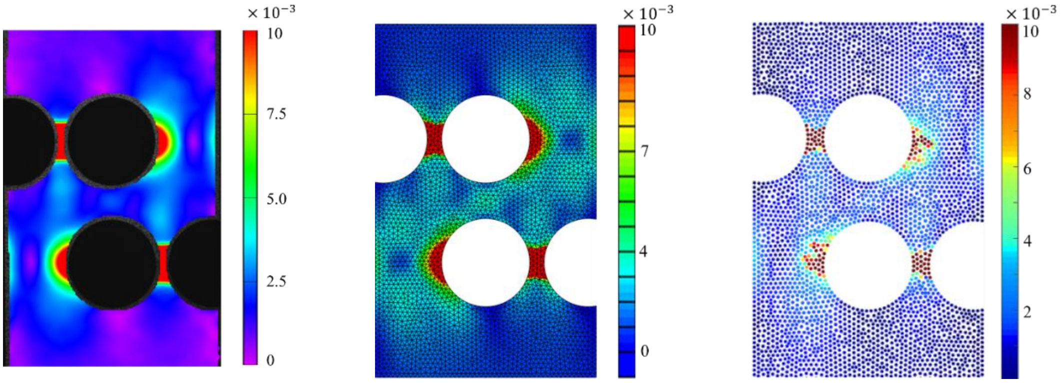

a) b) c)

Figure 3.14: Equivalent von Mises strain distribution obtained at the end of the elastoplastic analysis: a) DIC, b) FEM and c) RPIM [159].

GTN Damage analysis on AA6061-T6 bi-failure specimen

Considering a remote displacement of $\bar{v}(x,y) = 4\,\mathrm{mm}$, Figure 3.8-a), the failure has been completed on the bi-failure specimen AA6061-T6 where $w = 4\,\mathrm{mm}$. The failure model has been also resolved using FEM formulation extended to GTN damage criterion, as described in Appendix E. The material and GTN properties were used, as reported in Table 3.1 and Table 3.2. The reaction force correlated with the vertical displacement on the central section was acquired, Figure 3.15. The images obtained for various stages of the imposed displacement are shown in Figure 3.17, top profiles.

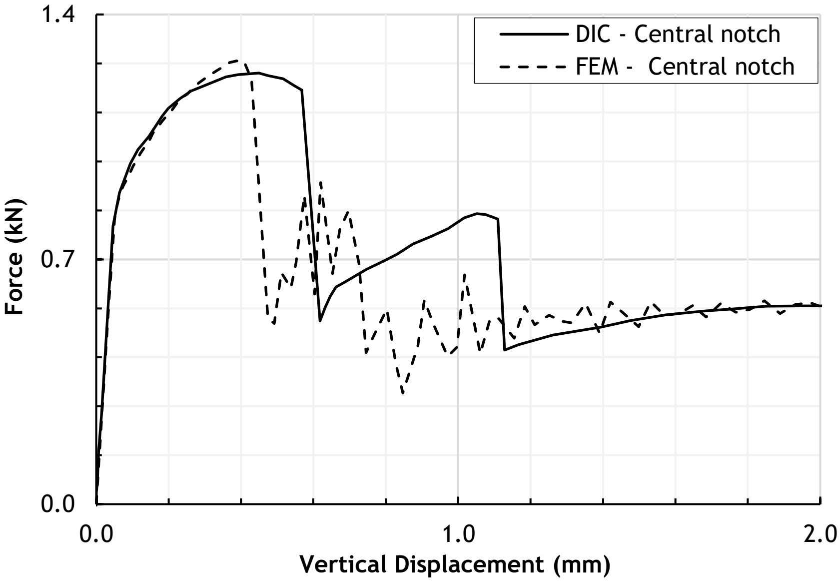

Figure 3.15: Force response vs. vertical displacement on AA6061-T6 w4 obtained for central sections, DIC and FEM [3].

The obtained results indicate that the failure of side notches never takes place simultaneously and therefore the failure of the final notch was not due to a pure shear stress. In turn, this likewise implies that the material underwent torsion along the axis defined by the loading direction, leading to a tear phenomenon on the left side of the specimen (see Figure 3.17-d). This might be a matter of the model complexity. Hence, as a solution, a modified model was proposed to promote failure phenomenon in the central section. Therefore, the corresponding width has been reduced to $w = 1.5\,\mathrm{mm}$ and then the influence of geometry refinement was surveyed, see Figure 3.16 for the modified geometry.

The analysis has been carried out on the modified bi-failure specimen and it was monitored by DIC. Figure 3.17 reveals the step-by-step images captured by DIC along the experimental test. The force/displacement response in the central section is shown in Figure 3.18.

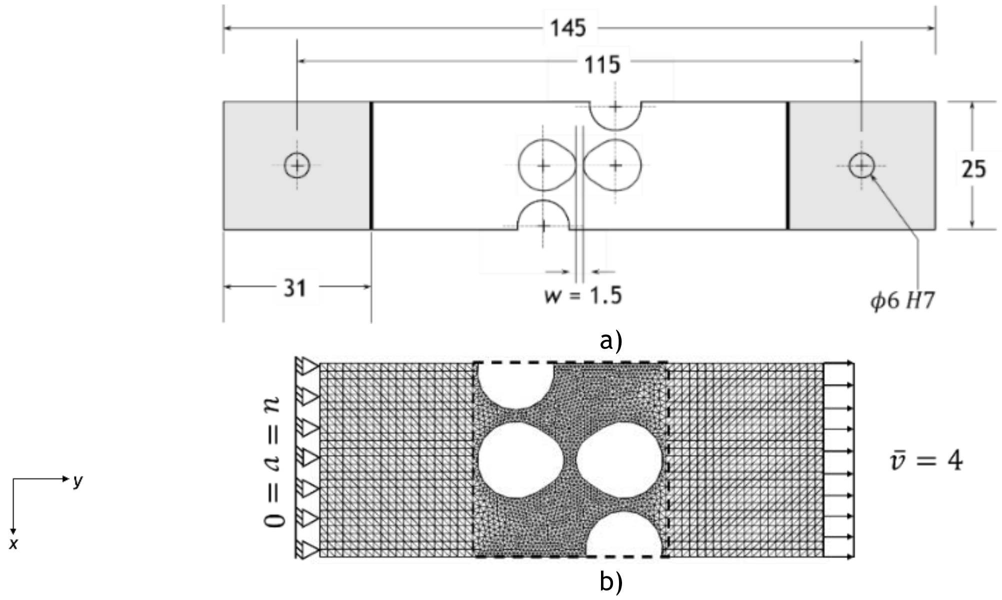

Figure 3.16: Modified bi-failure specimen, AA6061-T6 W1.5: a) a general view with geometrical dimension presentation and b) FEM model, dimensions are in mm.

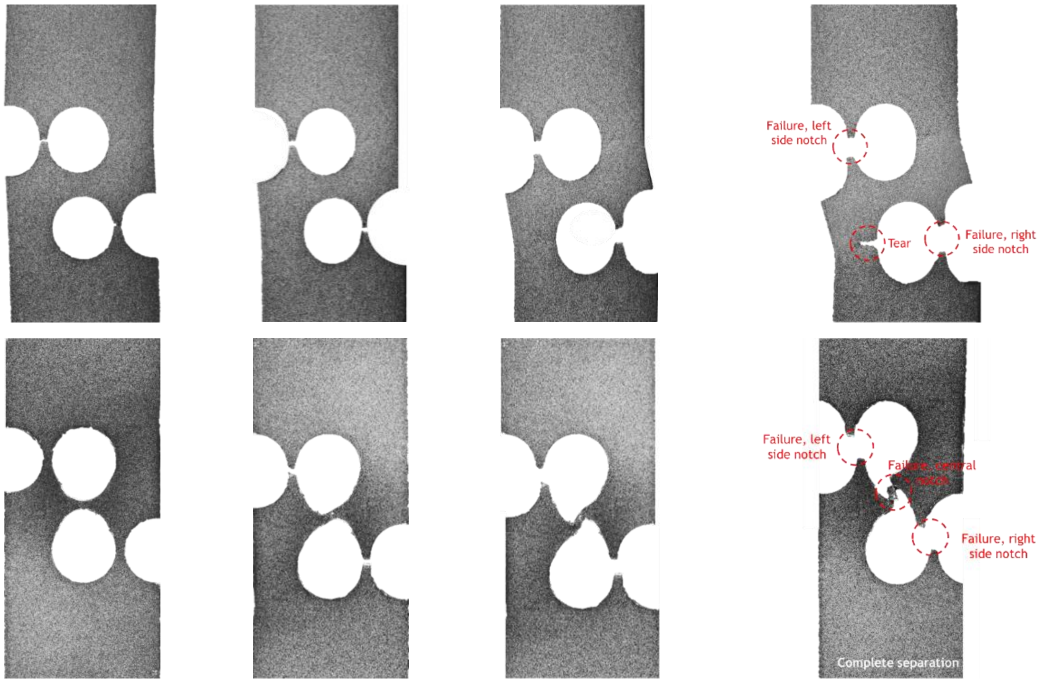

a) $u_{y,1} = 1$ mm b) $u_{y,2} = 2$ mm c) $u_{y,3} = 3$ mm d) $u_{y,4} = 4$ mm

Figure 3.17: Failure evolution; top row: AA6061-T6 W4 and bottom row:AA6061-T6 W1.5 [3].

The presented results prove that proposed modification was properly feasible so that the material experienced the first failure in the side notches simultaneously due to the high stress triaxiality state and then because of the pure shear; it suffered its final failure in the central section leading to the material collapse. More results obtained from the experimental and numerical analyses can be found in the published paper [3].

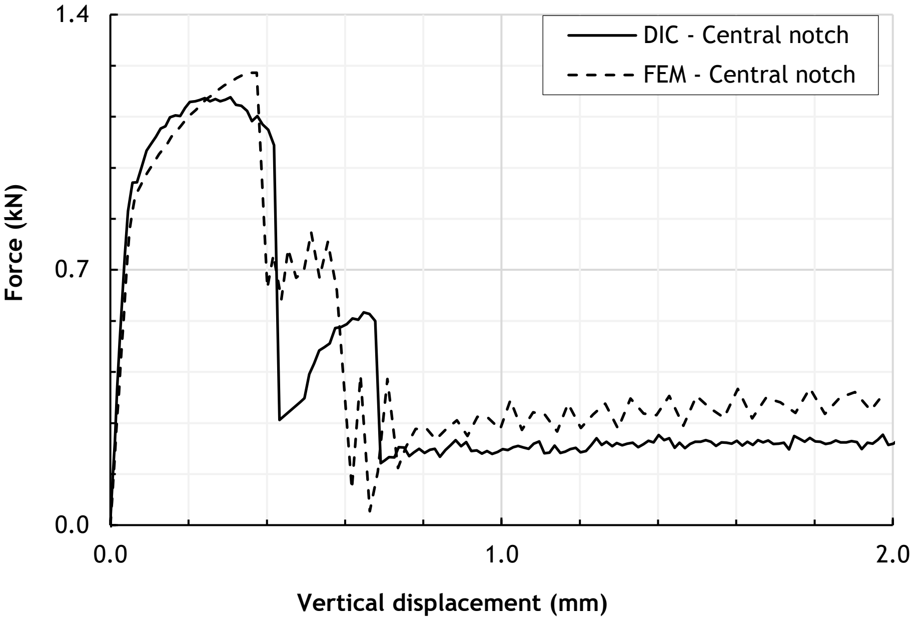

Figure 3.18: Force-displacement response on AA6061-T6 W1.5 [3].

Elastoplastic and damage analysis on DP600 bi-failure specimen

In this example, a bi-failure specimen made of a dual phase steel DP600 was designated; the specimen geometry is shown in Figure 3.8, where $w = 4.00\ \mathrm{mm}$, $e = 0.80\ \mathrm{mm}$, $l_1 = 12.00\ \mathrm{mm}$ and $l_2 = 12.25\ \mathrm{mm}$. The material properties are reported in Table 3.1. Like the experiment of aluminium bifailure specimen, the 3D DIC was used to assess the experimental data and the obtained results denoted as the empirical key. The experimental DIC setup used is shown in Figure 3.9. The DIC FOV and specimen's notches were the same as those presented in Figure 3.10. The DIC calibration solution and its problem domain properties are reported in Table 3.3 and Table 3.4.

The bi-failure specimen comprises three main areas, in which the material first tolerates plasticity and thereupon endures damage phenomenon leading to material rupture. Two of these regions are assumed to be affected by high stress triaxiality, left and right-side notches, when it is loaded under tension. Furthermore, there is a third region that suffers shear effect/low triaxiality, central notch.

To achieve a standard numerical solution, the elastoplastic model was solved within the FEM formulation in ABAQUS© respecting an isotropic hardening, introduced in Equation (3.1). Strain hardening coefficients based on the Voce's law were adopted as reported in Table 3.1. The FE mesh was constructed with 5629 linear shell elements of type S3 and 3009 nodes. Figure 3.19-a) presents the FE mesh and boundary conditions.

Furthermore, RPIM and NNRPIM meshless method formulations extended to the nonlinear elastoplasticity were adapted to solve the proposed model. As Figure 3.19-a) depicts, the problem domain was discretized with a nodal distribution including 3739 nodes where the RPIM and NNRPIM problem domain required 21138 and 25096 integration points, respectively. Regarding the elastoplastic scheme, as it is described in Appendix B.6, a nonlinear Newton-Raphson routine was considered with a tolerance of $toler = 10^{-6}$ where 40 increments were assigned [160]. Additionally, an initial tangent modulus has been assumed as presented in Table 3.1.

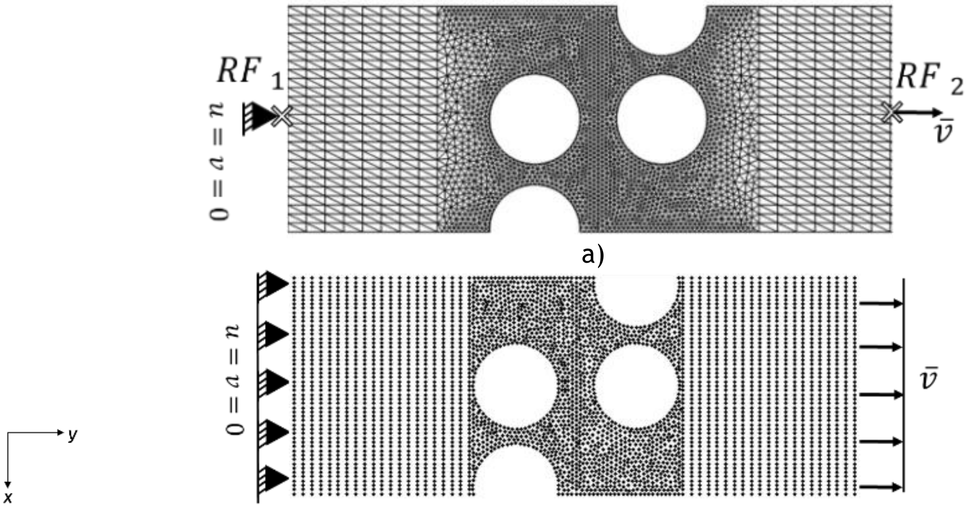

Figure 3.19: Numerical DP600 model with the essential boundary condition illustration; a) FEM and b) RPIM and NNRPIM meshless method [160].

These computational studies contribute to verify the numerical methodologies by comparing their results with DIC analysis output. The load in terms of the longitudinal displacement on three notch sections (by auxiliary points) was obtained for all analyses at the end of elastoplastic regime, as illustrated in Figure 3.20. It could be predicted that material had been already entered plasticity and that total amount of displacement imposed on upper jar of grip has been measured as $\bar{v}(x, y) = 0.2\ \text{mm}$.

Both lower and higher nodal connectivity schemes were considered to assess the efficiency of diverse NNRPIM constructions where plasticity is valid. Henceforward, '*NNRPIMv1*' and '*NNRPIMv2*' are associated with results of the first- and second-degree influence cell. It can be inferred that the NNRPIMv2 solution is a bit closer to DIC and FEM results [160].

The deformation field was monitored. Logarithmic transverse and longitudinal strain variations were extracted at the end of elastoplastic analysis, Figure 3.21.

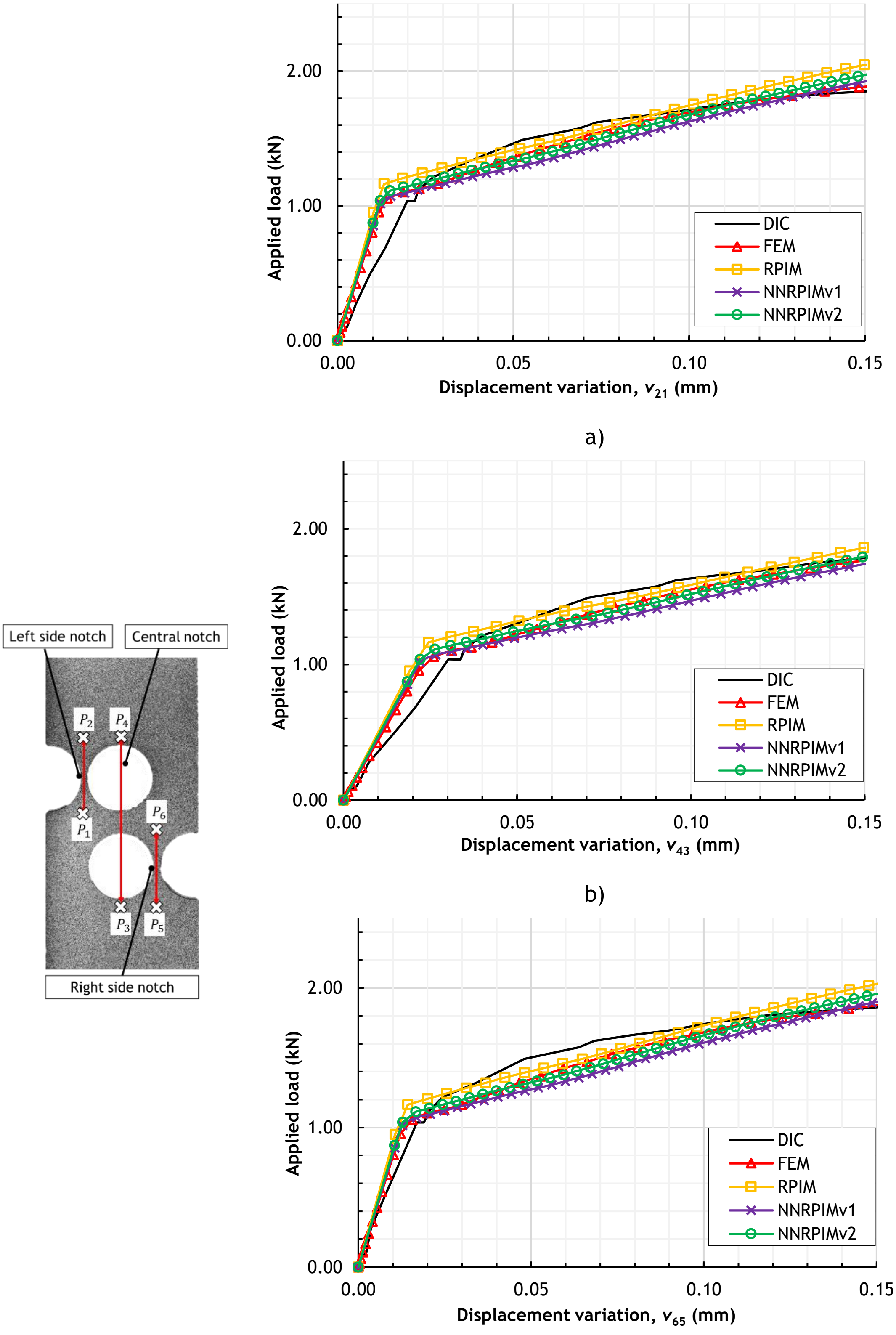

Figure 3.20: Load/displacement response for DP600 analysis captured on: a) left, b) central and c) right side notch [160].

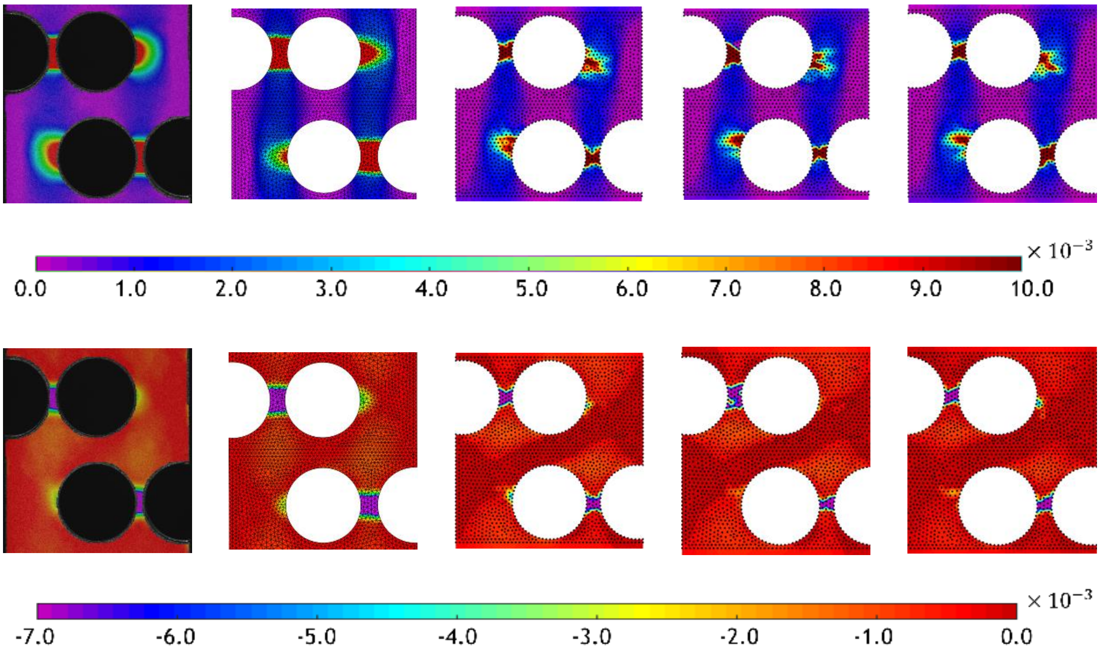

a) b) c) d) e)

Figure 3.21: DP600 Analysis; Top: Logarithmic transverse strain and bottom: Logarithmic longitudinal strain profile derived from a) DIC, b) FEM, c) RPIM, d) NNRPIMv1 and e) NNRPIMv2 [160].

A further study has been conducted on the DP600 bi-failure specimen to evaluate the failure behaviour due to the plasticity. Considering a total displacement of $\bar{v}(x,y) = 2\,\mathrm{mm}$, the material underwent its failure on the side notches as captured by the DIC analysis. Figure 3.22 presents the engineering stress/strain diagrams on the failure analysis.

Numerically, the model has been solved throughout GTN damage criterion (see Appendix E for the governing formulations) relying on the FEM simulated in ABAQUS©. The governing parameters used in the GTN damage simulation are reported in Table 3.1. The FE model was the same as presented in Figure 3.19-a) where $\bar{v}(x,y) = 2\,\mathrm{mm}$.

The engineering stress/strain curves obtained from GTN damage model were compared with the experimental DIC analysis for diverse specimen's sections, as shown in Figure 3.22. The failure phases were marked where the curves suffered sudden drops in the different sections.

Overall, an acceptable agreement was achieved with the numerical solution. Figure 3.23 reveals the logarithmic longitudinal strain profiles captured at the end of the failure mechanism for both experimental and GTN models. Logarithmic equivalent von Mises strain ($\tilde{\varepsilon}$) was also computed, for both analyses as accordingly depicted in the presented figure.

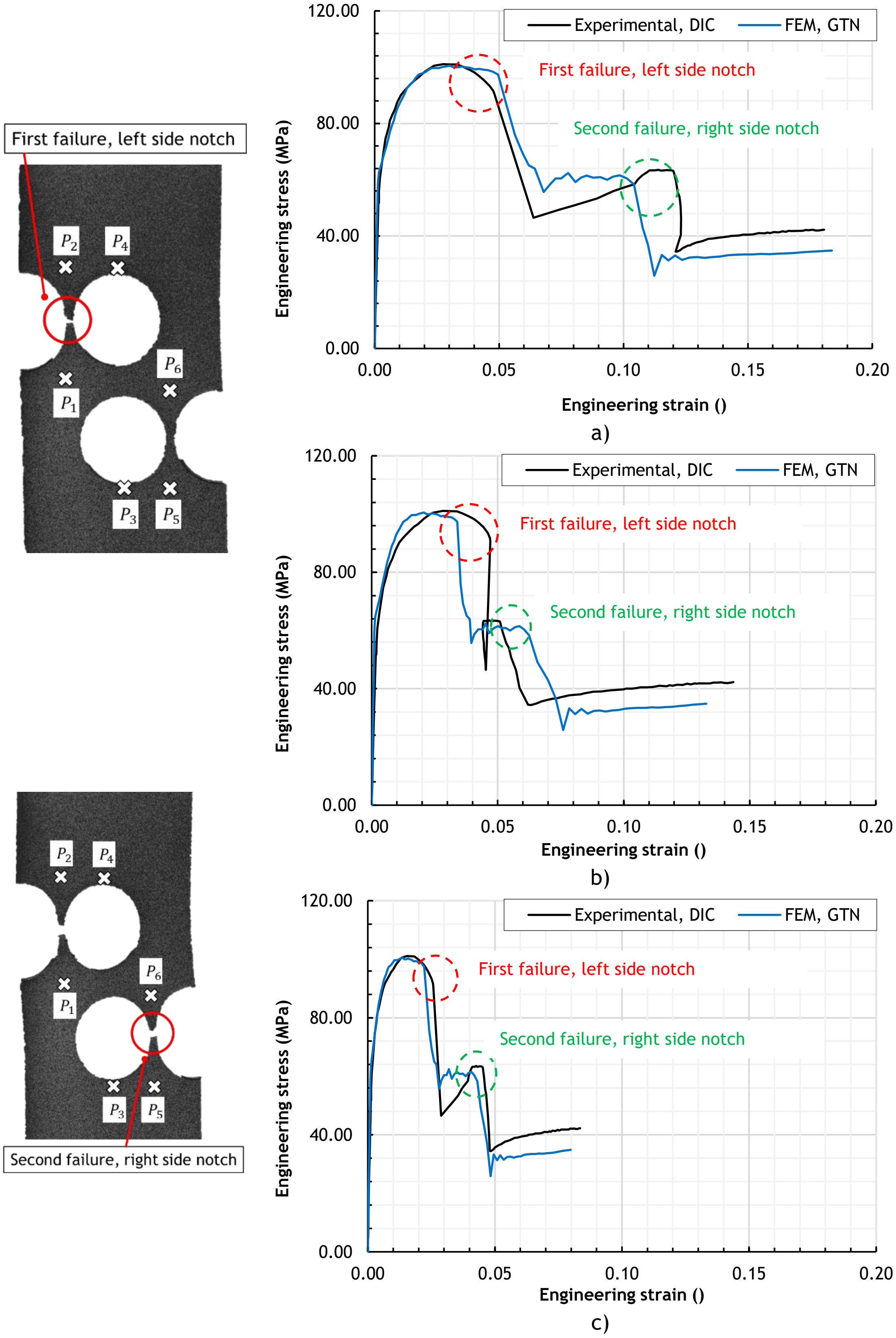

Figure 3.22: Engineering stress/strain curves on DP600 analysis sorted for a) left side notch [P_2 and P_1], b) right side notch [P_6 and P_5] and c) central notch [P_4 and P_3] [160].

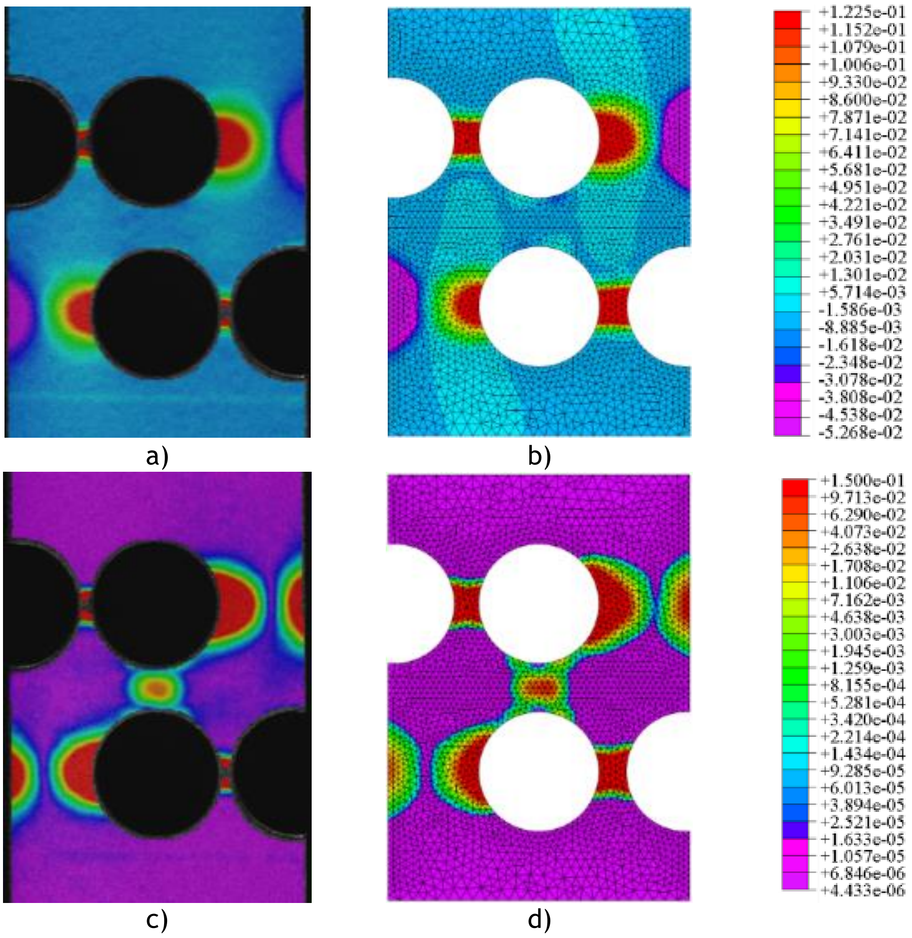

Figure 3.23: Logarithmic strain profiles plotted with logarithmic contour intervals, a) longitudinal strain-DIC, b) longitudinal strain-GTN, c) $\tilde{\varepsilon}$-DIC and d) $\tilde{\varepsilon}$-GTN [160].

The failure behaviour of the bi-failure specimen can be justified by the damage characteristics, such as the stress triaxiality factor, TF. Thus, the TF evolution, referring to Equation (E.8) in Appendix E, for different failure phases obtained from the numerical simulation is shown in Figure 3.24. Besides, TF variation, which was captured on the points P_L and P_R accordingly located on the left and right side notch, in terms of the engineering strain is demonstrated in Figure 3.24-d).

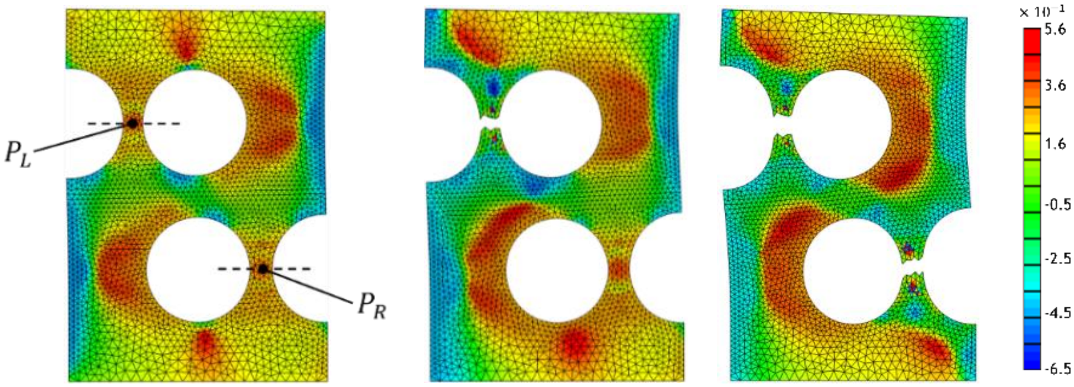

a) $\bar{v} = 0.3$ mm
b) $\bar{v} = 0.8$ mm
c) $\bar{v} = 2.0$ mm

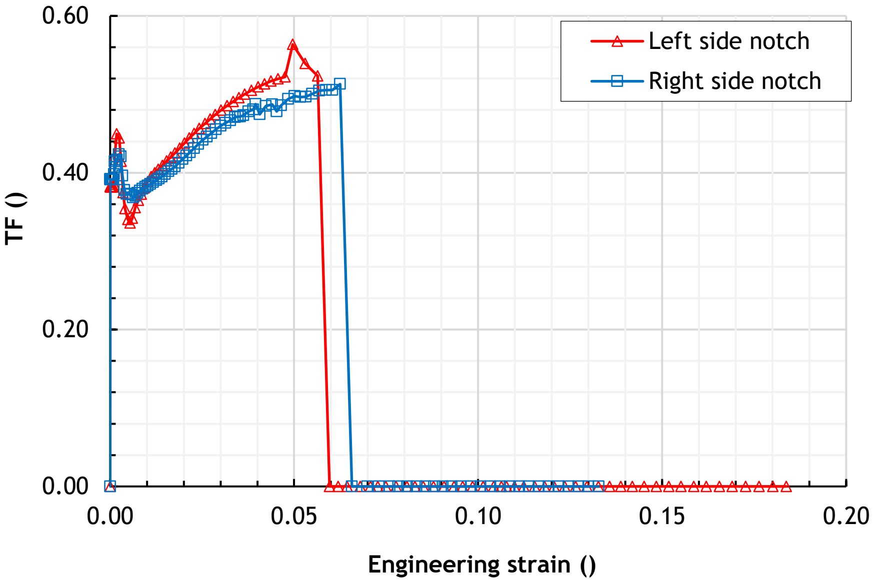

d)

Figure 3.24: TF in side notches; a) before first failure, b) after first failure, c) after second failure and d) TF vs. engineering strain in the loading direction, GTN analysis [160].

Further results can be found in the published manuscript [160].

3.1.3 *Aluminium compact tension fracture specimen*

An aluminium alloy AA6082-T6 pre-cracked Compact Tension, CT, specimen, with dimensions, $W = 40.00\ \mathrm{mm}$, thickness $e = W/20 = 2.00\ \mathrm{mm}$ and $a_n = 8.46\ \mathrm{mm}$, was tested [161]. The material properties are: Young's modulus $E = 70.00\ \mathrm{GPa}$ and Poisson's ratio $\nu = 0.33$. A standard drawing of a CT specimen with its geometric characteristics is illustrated in Figure 3.25-a). Moreover, ΔP denotes the applied load. To perform the test, the 3D DIC was employed to acquire the deformation field on the crack. The bare CT specimen and speckled pattern are illustrated in Figure 3.25-b) and -c).

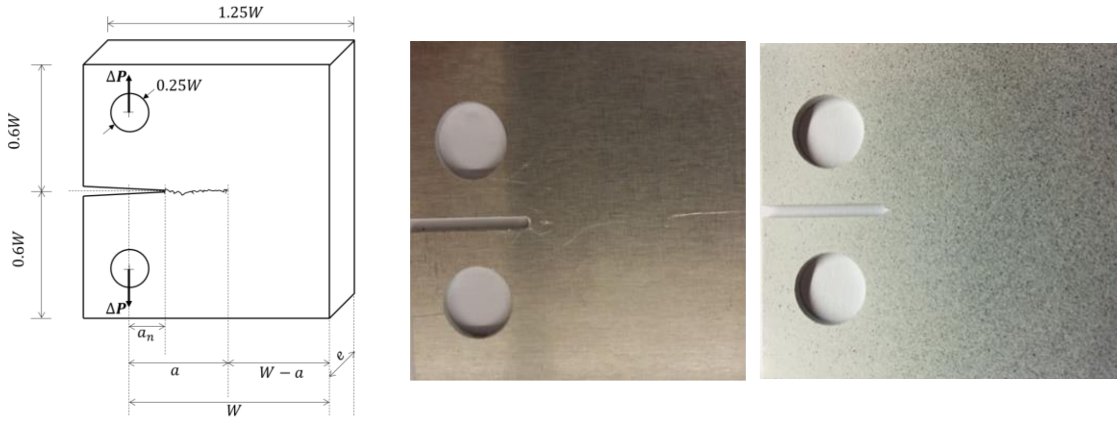

a) b) c)

Figure 3.25: Aluminium CT specimen used in the experimental test, a) geometry representation, b) before surface preparation and c) DIC speckle pattern [161].

The DIC setup used is demonstrated in Figure 3.26-a) and described in detail in [161], the specimen was loaded as reported in Table 3.5. As a result, the crack growth evolution $(a - a_n)$ (which was read by the travelling microscope moving parallel to the specimen as shown in Figure 3.26-b) correlated with the fatigue cycles is presented in Figure 3.27.

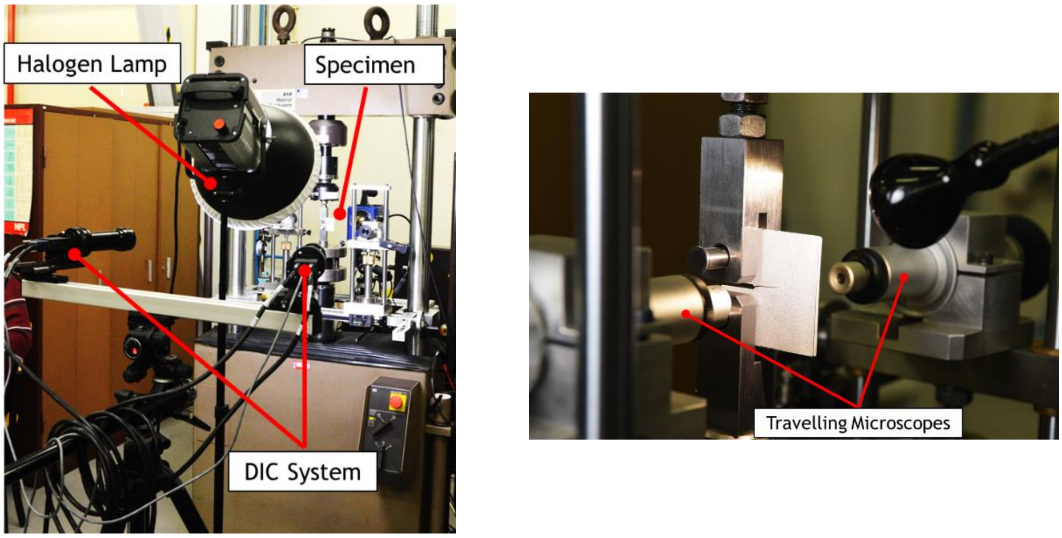

a) b)

Figure 3.26: a) the 3D DIC system standing in front of the tested specimen, and b) travelling microscope to measure the crack size.

Table 3.5: Experimental test characteristics on Aluminium CT specimen [161].

P_{max}	P_{min}	R	$P_{amplitude}$	P_{mean}	f
670 N	67 N	0.1	302 N	380 N	15 Hz

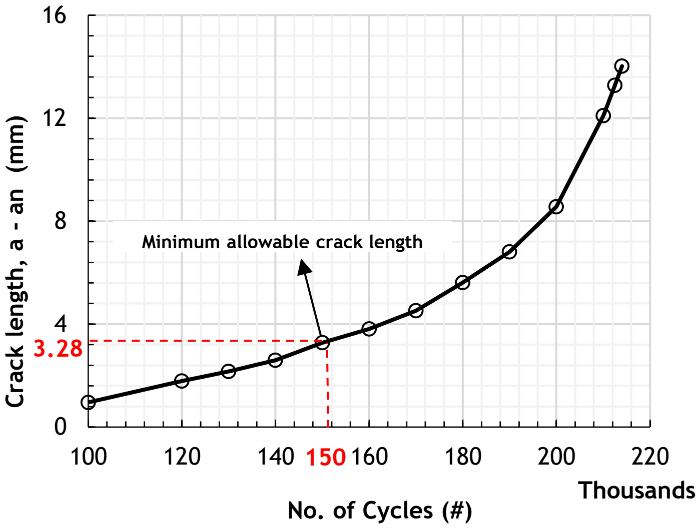

Figure 3.27: Crack propagation vs. fatigue cycles, read by travelling microscope, [161].

Numerically, the cracked model has been solved using the elastostatic FE formulation simulated in ABAQUS©. An explicit FE model with a 2D plane stress shell was considered. Standard 4-node bilinear plane stress quadrilateral elements (CPS4R) were used with a total number of 4238 and 4061 elements and nodes, respectively, Figure 3.28-a). The crack was created with the contour integral model and SIF ranges were obtained in accordance with the maximum strain energy release rate, SERR, criterion.

Moreover, based on the RPIM meshless method formulation, the model has been solved to obtain comparable solutions on the SIF ranges and internal fields. Figure 3.28-b) presents the meshless method model comprising 4861 nodes and 28155 and 35906 integration points for RPIM and NNRPIM studies. Taking advantage of the symmetry, only half of the problem domain was analysed. Regarding the SIF, the Williams series expansion involving seven terms was used. Therefore, ΔK_I was calculated together with a nonlinear overdeterministic algorithm described in Appendix D.2 and Appendix D.3.

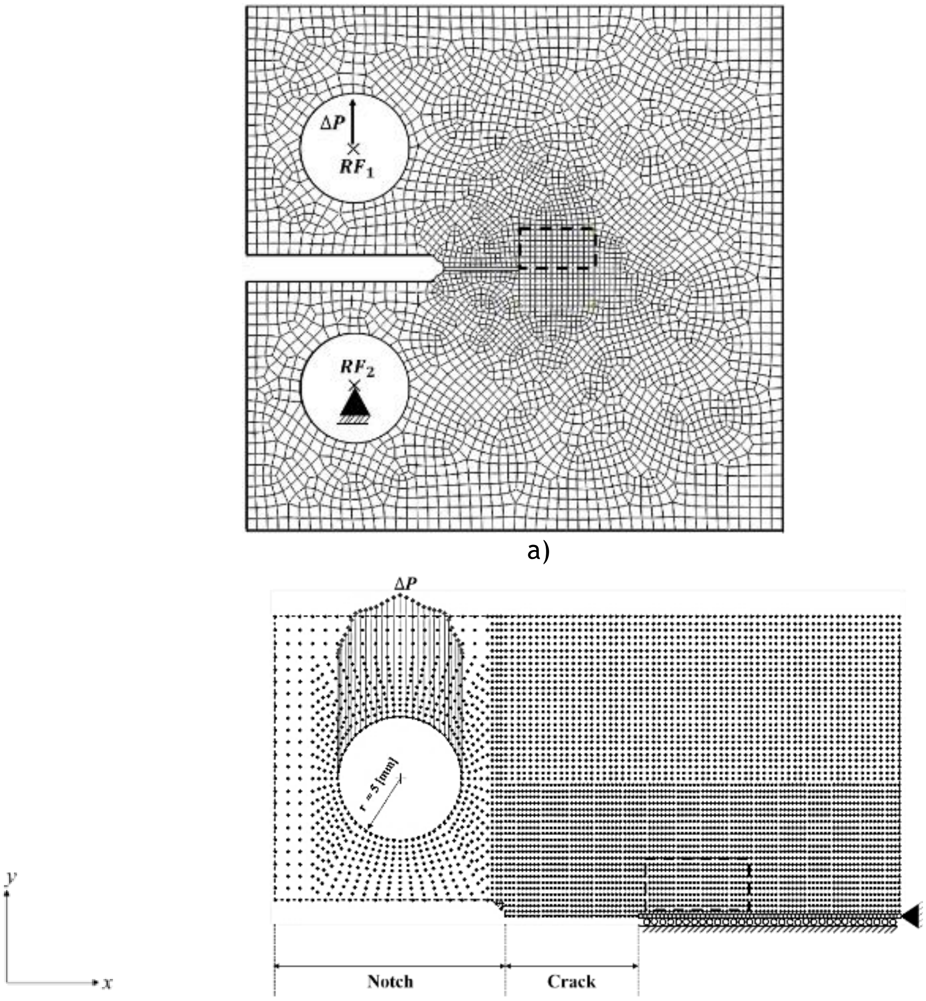

a)

b)

Figure 3.28: Numerical CT model, essential and natural boundary conditions and intended region representation; (a) FE and (b) meshless model [161].

Table 3.6 reports the SIF results obtained for different crack measurements captured on seven fatigue cycle quantities. ΔK_{ASTM} has been calculated following the proposed relationship by ASTM E647-15 [162], see Appendix D.1. Moreover, ΔK_{DIC} was thereby calculated from the obtained strain field using Williams expansion series together with overdeterministic algorithm as described in Appendix D.2 and Appendix D.3.

Table 3.6: ΔK_I $(\mathrm{MPa.mm^{0.5}})$ obtained for various crack lengths on CT specimen [161].

No Cycles	*a* (mm)	ΔK_{ASTM}	ΔK_{DIC}	ΔK_{FEM}	ΔK_{RPIM}	ΔK_{NNRPIM}
170000	12.98	285.41	277.17	286.53	282.42	281.42
180000	14.07	306.08	301.20	304.21	301.14	286.41
190000	15.26	330.55	323.12	326.25	324.94	328.51
200000	17.01	371.27	347.40	363.18	360.36	348.07
210000	20.56	481.04	483.57	466.36	467.93	473.50
212500	21.74	529.85	519.10	514.53	522.03	516.56
214000	22.48	564.95	565.39	548.65	551.39	517.63

Respecting an intended region (with a dimension of $7.0 \times 3.5\ \mathrm{mm}^2$) in the vicinity of the crack path after its tip, the opening strain contour ε_{yy} for a set of three crack measurements were acquired as indicated in Figure 3.29.

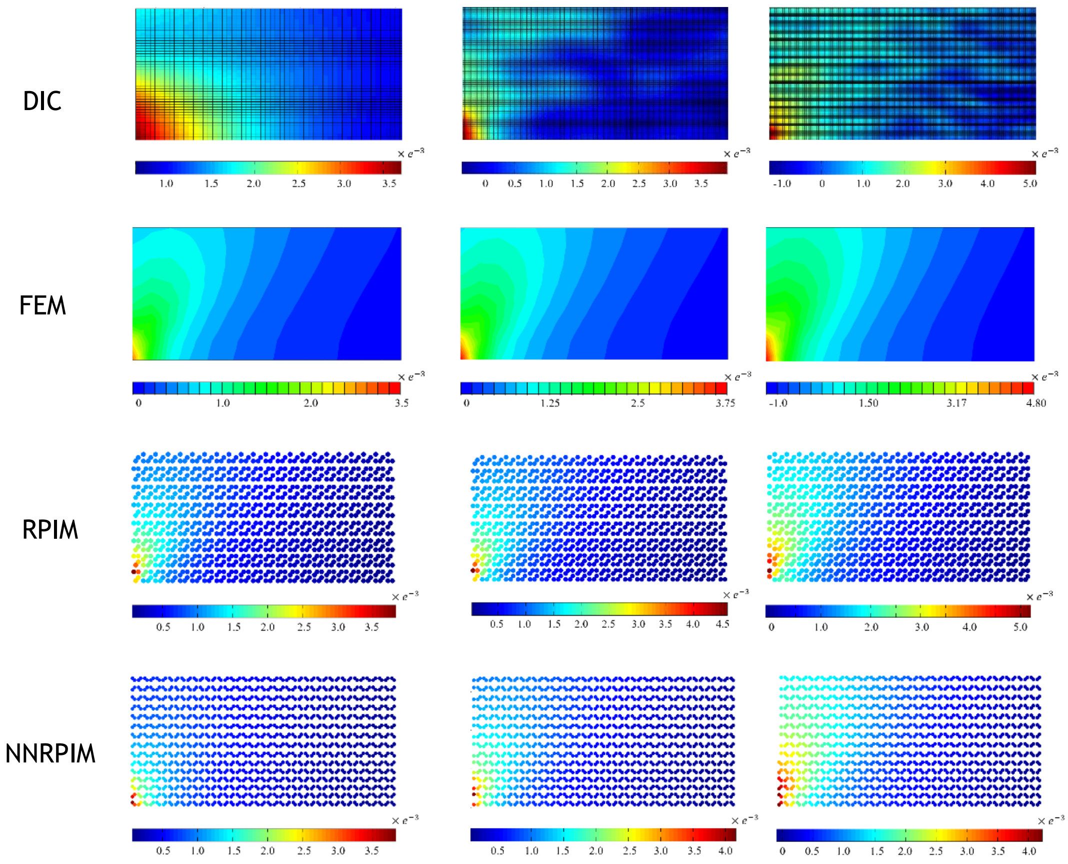

a) $a = 14.07\ \mathrm{mm}$ b) $a = 17.01\ \mathrm{mm}$ c) $a = 21.74\ \mathrm{mm}$

Figure 3.29: Opening strain distribution [161].

This study contributed to the fracture characterization, SIF and crack path, of an aluminium CT specimen subjected to a fatigue loading condition by means of the 3D DIC. The SIF range and internal fields have been experimentally documented and verified by the numerical analyses. Further results can be found in the published manuscript [161].

3.1.4 Polycarbonate middle tension specimen

In this example, a Middle Tension (MT) specimen made of polycarbonate, optical grade for elastostatic regime was designed according to ASTM E647 [162]. It aims at the assessment on stress dead zone concept and its characterization with uniaxial tensile testing a MT specimen [163]. To acquire the experimental solution, DIC, has been used. Computationally, based on the Linear Elastic Fracture Mechanics, LEFM, the problem is resolved using FE and Meshless methods. Considering a stress "dead zone" concept, the experiment intended to determine an alternative analytical solution of the SIF. Therefore, the compliance method was adopted, which was associated with the specimen's "dead zone" area, i.e., the area that had not been involved in the cracking resistance. Thus, LEFM formulations complying with SERR criterion were assumed [163]. The adopted methodology to obtain SIF using compliance and stress "dead zone" concept is extensively described in Appendix D.4. With width, $W = 30\text{ mm}$, the specimen geometry and its dimensions are shown in Figure 3.30. The specimen's thickness was considered as $e = 3\text{ mm}$.

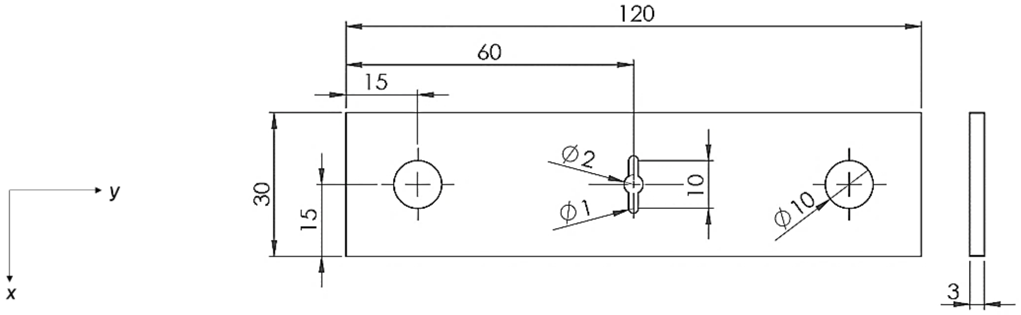

Figure 3.30: A general view of the tested polycarbonate central notch MT specimen, dimensions are in mm [163].

The standard ASTM E647-08 [162] requires that $2a_n$ should be at least $0.2\,W$ when using the compliance method to monitor the crack extension in the specimen. Hence, the central notch was designated with the following dimensions: diameter of 1.0 mm ($\text{Ø}1$) and $a_n = 6.0\text{ mm}$. In addition, a pre-crack has been machined by a coping saw on the central notch (both sides) leading to construct the crack length as $a = 7.0\text{ mm}$. Moreover, physical and mechanical properties of polycarbonate were considered as reported in Table 3.7. The experiment has been performed by an Instron® tensile testing machine (E1000) with a load capacity of 1.0 kN. The specimen was loaded at 1.0 kN, the experimental setup is shown in Figure 3.31-b).

Table 3.7: Material characteristics of Polycarbonate, Optical Grade [163].

Property	Amount
Density	$\rho = 1.20\ \text{gr/cc}$
Young's modulus	$E = 2380.00\text{ MPa}$
Poisson's ratio	$\nu = 0.37$
Yield Strength	$S_Y = 62.70\text{ MPa}$
Ultimate Tensile Strength	$UTS = 65.40\text{ MPa}$

In order to use the 2D DIC, a synchronized camera with a resolution of $2048 \times 2048\ \mathrm{pixels}^2$ was used with an operational distance of $\mathcal{L} = 700\ \mathrm{mm}$ to the specimen's surface. The camera lens was configured based on work objectives; $60\ \mathrm{mm}\ f/4$ C-Mount Rodagon lens. Two $150\ \mathrm{W}$ halogen lamps illuminated on the specimen surface, as shown in Figure 3.31-a).

Regarding DIC analysis and referring to Figure 3.32, the camera's FOV corresponds to an $55.30 \times 30.00\ \mathrm{mm}^2$ area. The examined area was gridded with a subset size of $29.00\ \mathrm{pixel}$ $(0.78\ \mathrm{mm})$ and a step size of seven pixel. Therefore, a $29.00 \times 29.00 - \mathrm{pixel}$ facet field per seven pixels is followed. The speckle size varied from 1.00 to $6.00\ \mathrm{pixels}$ $(0.03\text{–}\ 0.16\ \mathrm{mm})$.

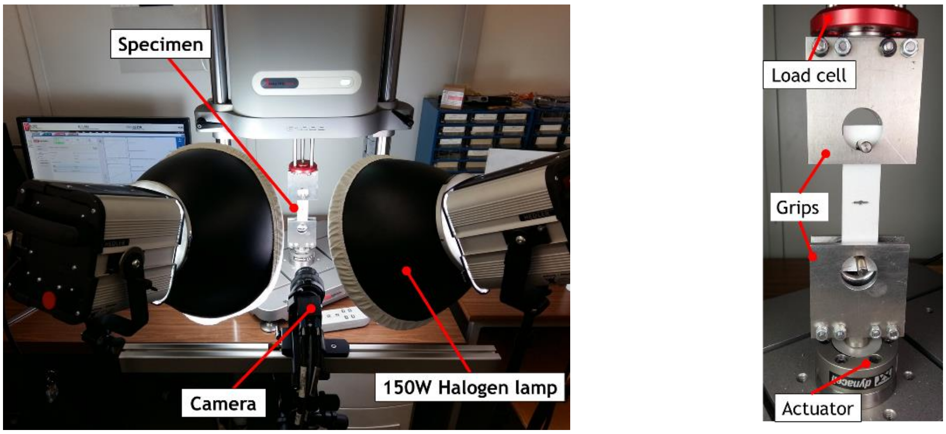

a)

b)

Figure 3.31: a) the 2D DIC standing in front of the specimen and b) experimental setup [163].

To evaluate the SIF, a numerical iterative procedure was implemented to analyse the strain field derived from the DIC processing software (VIC-2D 2009©), as the procedure described in Appendix D.3, more details available in [163]. Regarding Mode I, the dominant stress was the opening stress, σ_{yy}, the algorithm was handled using this component following Equations (D.4) and (D.6) in Appendix D.2.

Numerically, the problem was solved using FEM formulation in ABAQUS©. Linear quadrilateral elements of type S4R were adopted to build the mesh with the element size ranging from $0.10\ \mathrm{to}\ 1.00\ \mathrm{mm}$ with a total number of 12076 and 11949 nodes and elements, respectively, see Figure 3.33-a). The boundary conditions have been applied to the assigned reference points (RF1 and RF2) to meet the experimental circumstances. The SIF has been directly derived from ABAQUS© for 10 contour integrals relying on the maximum SERR criterion.

The problem has also been resolved using RPIM and NNRPIM meshless methods. The nodal discretization comprised of 7944 nodes and accordingly 46338 and 53920 gauss integration points for RPIM and NNRPIM analyses. Both first- and second-degree influence cells have been taken into account for the NNRPIM analyses. Hence, SIF was calculated throughout Williams series expansion and overdetermined algorithm as explained in Appendix D.2 and Appendix D.3.

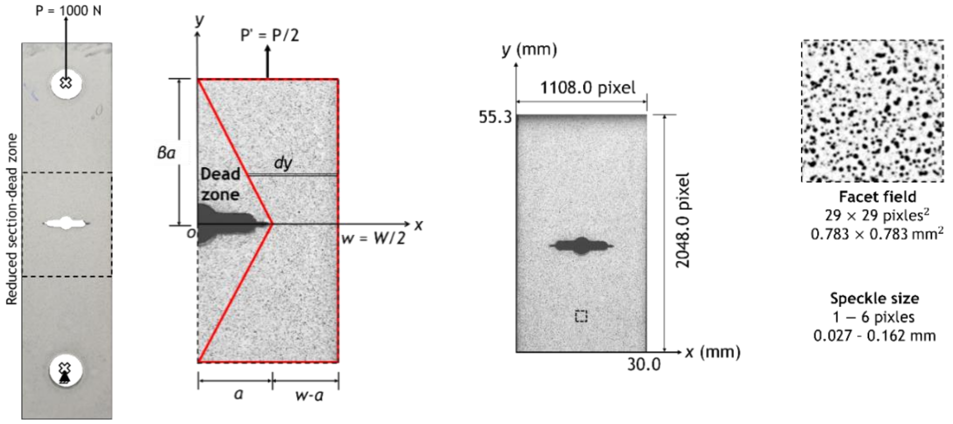

a) b) c) d)

Figure 3.32: MT specimen; a) applied boundary conditions, b) detail on anticipated dead zone, c) FOV and d) a facet field with speckle size [163].

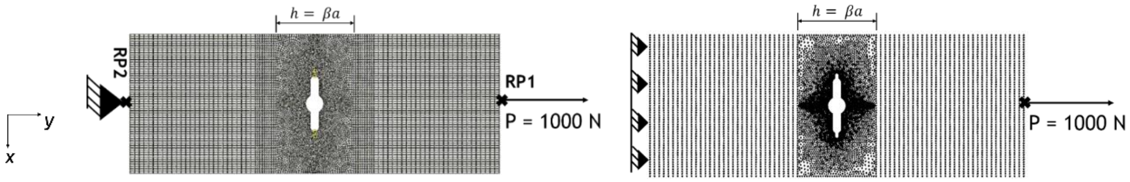

a) b)

Figure 3.33: Numerical model respecting applied boundary conditions a) FEM mesh and b) nodal discretization for meshless methods [163].

Table 3.8 presents the SIF range acquired for all methods for the proposed polycarbonate MT specimen. The ASTM solution has been calculated following Equation (D.2) in Appendix D.1. The compliance solution was derived from Equation (D.24) in Appendix D.4.

Table 3.8: Mode I SIF obtained from all methods, values are in (MPa.mm^0.5) [163].

ASTM	Compliance	DIC	FEM	RPIM	NNRPIMv1	NNRPIMv2
60.42	62.36	59.28	62.00	61.96	61.70	61.49

Regarding strain variation, Figure 3.34 presents the longitudinal strain profile (ε_{yy}) distributed on the intended region extracted from DIC, FEM and Meshless methods analyses obtained at the end of the elastostatic analysis plotted on the undeformed shape.

Concerning the “dead zone” concept implication, the proposed assumption, β must be validated. So, the interest $a \times \beta a$ “dead zone” was extracted from all acquired strain distribution, Figure 3.35. Line OA presents the dead zone height, which presumed as βa while line OB stands as the crack length a. The corresponding triangle (OAB) was marked in profiles. Points A and B were coordinated as $A = (0.0, 8.4)$, to meet the “dead zone” height (OA), and $B = (7.4, 0.0)$ to guarantee that the plastic zone was eliminated from the calculation. This meant that point B positioned ahead of the crack tip $(a = 7.0\ \mathrm{mm})$ with a gap of $0.4\ \mathrm{mm}$.

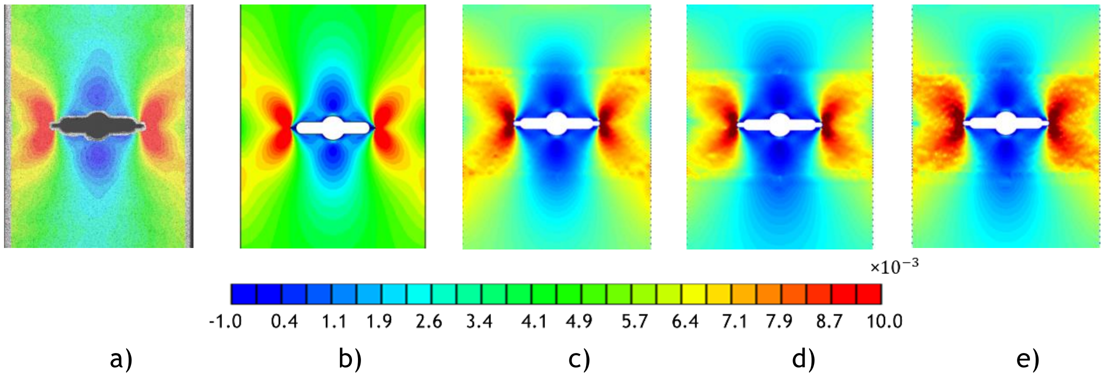

Figure 3.34: Longitudinal strain profile; a) DIC, b) FEM, c) RPIM, d) NNRPIMv1 and e) NNRPIMv2 analyses [163].

Table 3.9 reports the longitudinal strain value measured at points A and B respecting predefined coordinates. Acquired results correspond to point A imply that the vertical strain magnitude accounted for a very low value compared to amounts captured on point B, ahead of the crack tip, less than 20% [163].

Further results and detail regarding this example can be found in the published manuscript [163].

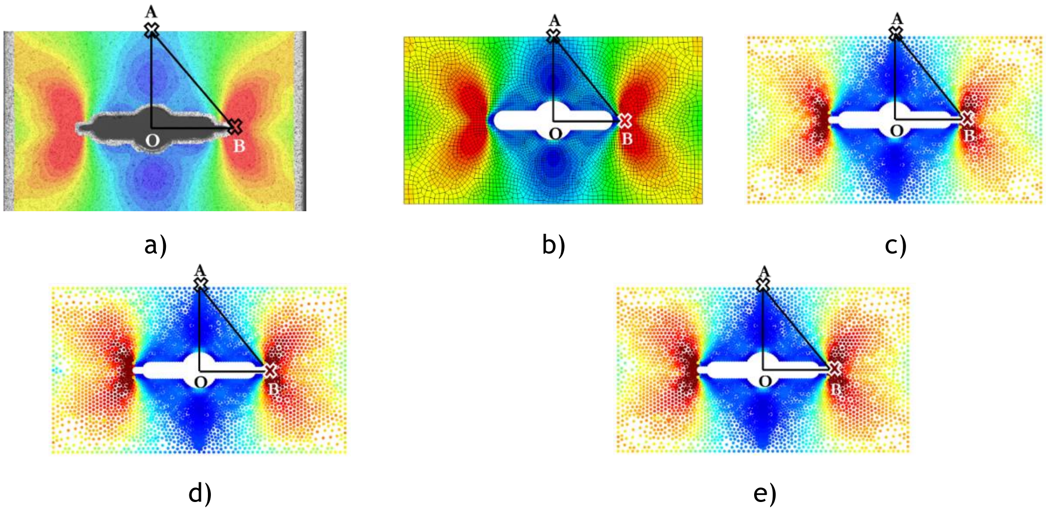

Figure 3.35: Longitudinal strain profile mapped on the dead zone for a) DIC, b) FEM, c) RPIM, d) NNRPIMv1 and e) NNRPIMv2 analyses [163].

Table 3.9: Dead zone characterizations [163].

			Point $A = (0.0, 8.4)$			
Method	**Compliance**	**DIC**	**FEM**	**RPIM**	**NNRPIMv1**	**NNRPIMv2**
ε_{yy}	0.0025	0.0024	0.0023	0.0024	0.0022	0.0023
			Point $B = (7.4, 0.0)$			
Method	**Compliance**	**DIC**	**FEM**	**RPIM**	**NNRPIMv1**	**NNRPIMv2**
ε_{yy}	0.0132	0.0131	0.0131	0.0127	0.0131	0.0130

3.2 Numerical damage analysis on concrete structures

In this section, a nonlinear continuum damage mechanics model for concrete structures is analysed using meshless method formulations. As an alternative computational solution, the employed methodology can be implemented on the damaged railway tunnels to numerically study the fracture behaviour of the railway tunnel's interior surface.

The 2D plane stress radial point interpolation meshless, RPIM formulation, fully described in Appendix B, is developed to a standard rate-independent damage model with regard to both tension and compression static states. Besides, the former local damage formulation is improved to a non-local constitutive damage criterion by means of a Helmholtz free energy potential. The complete damage formulations are presented in Appendix C. The standard local damage procedure is firstly signified, and it is thereby extended for the non-local damage models. To assess the performance and validity of the proposed damage mechanic formulations combined with RPIM, two concrete benchmarks (notched-three-point bending beam and CT specimens) are studied following experimental results available in the literature.

The presented results are part of the relevant published papers [105], [127], [164], [165]. The numerical resolution scheme follows a return-mapping damage algorithm in which the internal variational fields, local and non-local damage, are evaluated. Owing to the nonlinear nature of the model, a displacement-controlled Newton-Raphson iterative methodology is taken into account contributing to obtain the nonlinear damage solution. Overall, encouraging results infer that the RPIM meshless method is capable to successfully analyse the damage response of the concrete structures which is of interest in the inspection of railway tunnel structures.

3.2.1 Concrete three-point-bending analysis

The proposed computational methodology for the non-local damage model is validated throughout the analysis of a three-point bending single-edge notched beam experimentally conducted by Malvar et al. [119]. First, the non-local damage parameters must be calibrated (see Appendix C for the governing formulations). The geometrical properties and essential boundary conditions, as shown in Figure 3.36, were adopted in accordance with the experimental test; $L = 788\ \mathrm{mm}, D = 102\ \mathrm{mm}, a_0 = 51\ \mathrm{mm}$ and thickness $e = 102\ \mathrm{mm}$.

The material and damage properties of concrete were used as reported in [113], [166], Young's modulus: $E = 21.7 \times 10^9\ \mathrm{Pa}$, Poisson's ratio: $\nu = 0.2$, fracture energy $G_f = 30.0\ \mathrm{N/m}$, maximum uniaxial tensile and compressive strengths $f_0^+ = 2.4 \times 10^6\ \mathrm{Pa}$ and $f_0^- = 2.9 \times 10^5\ \mathrm{Pa}$, respectively. Furthermore, the tensile and compressive local damage constants were adopted as $A^+ = 1.0 \times 10^{-3}$, $A^- = 1.0$ and $B^- = 8.9 \times 10^{-1}$ [108]. The characteristic length was used as $l_{ch} = 1129.6 \times 10^{-4}\ \mathrm{mm}$ [106]. According to the algorithm presented in Appendix C, Figure C.2, an incremental/iterative procedure of pseudo-time stepping scheme was adopted (the

Newton-Raphson nonlinear solution algorithm), in which a total vertical displacement $\delta = -3.2 \times 10^{-1}$ mm is enforced in point A, see Figure 3.36-b), respecting 20 increments. As reported in [105], [127], [164], [165], three distinct RPIM nodal discretizations have been considered for this analysis. Taking advantage of the symmetrical geometry, only half of the beam was solved.

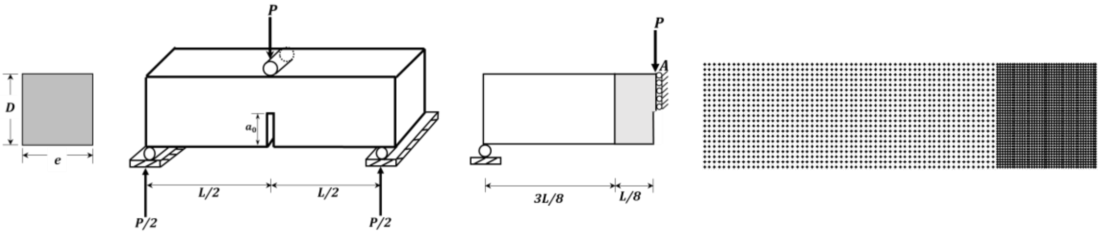

a) b)

Figure 3.36: Concrete three-point-bending beam: a) geometry and b) RPIM nodal pattern [127].

According to obtained results on the load/displacement response for distinct nodal distributions presented in [127], [164], it can be concluded that the non-local damage parameter can be calibrated as $s = 0.8$ combined with the 3rd order of weight function remained as the optimum value, see Appendix C.1 and the published papers [127], [164] for more detail.

Regarding the high-density discretization analysis, the nodal distribution presented in Figure 3.36-b) standing with 2441 nodes. Both regular and irregular nodal discretizations have been considered. The irregular nodal discretizations followed the procedure described in Appendix B.2 and the relevant published papers [127], [164]. The load *P* response vs. deflection on point *A* was captured and compared with the experimental result [119], Figure 3.37-a). The damage variation in terms of effective strain for non-local and local damage at the crack tip is shown in Figure 3.37-b).

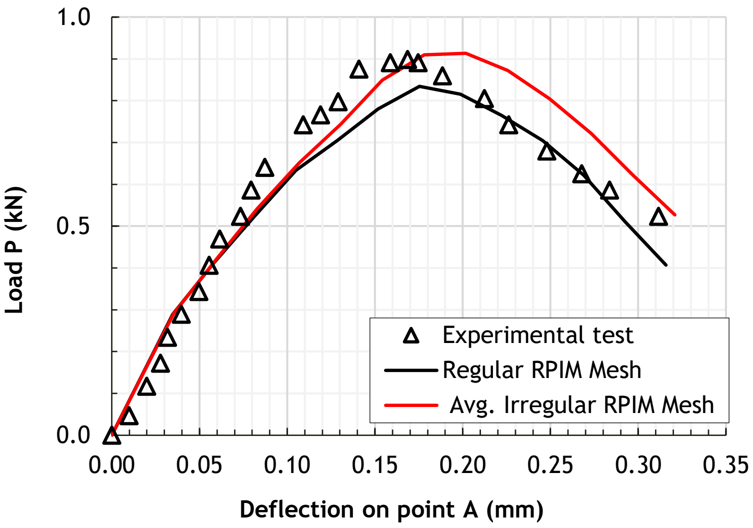

a)

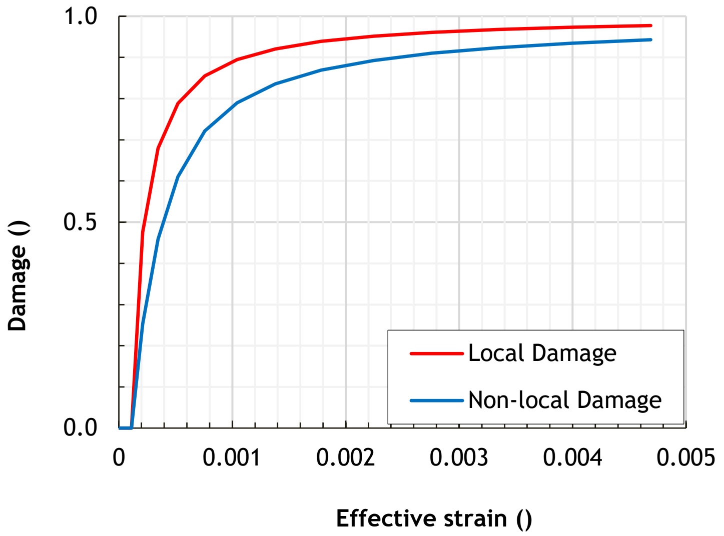

b)

Figure 3.37: The final analysis results correspond to a) force response vs. deflection on point A and b) damage variation versus effective strain at the crack tip [164].

Damage evolution for various displacement enforcements is revealed in Figure 3.38.

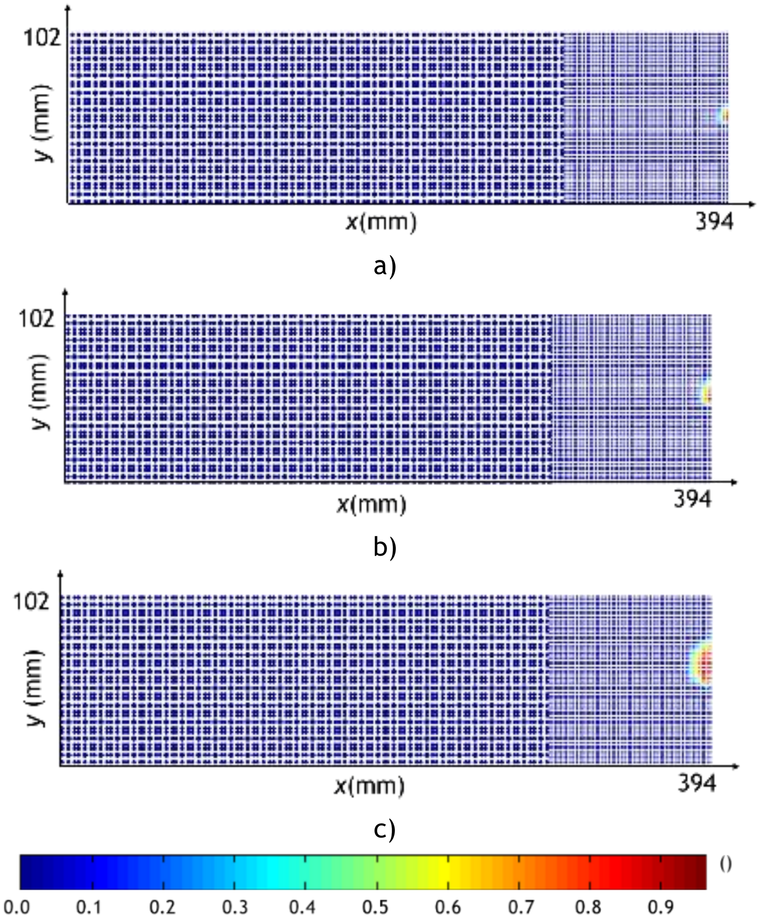

a)

b)

c)

Figure 3.38: Total damage evolution for concrete three-point-bending beam at different displacement impositions a) 1.2841E-01 mm, b) 1.7526E-01 mm and c) 3.1581E-01 mm [164].

3.2.2 *Concrete compact tension test*

The concrete CT analysis was carried out with the proposed non-local damage model combined with the RPIM (Appendix C). In the literature, it is possible to find experimental results showing the global behaviour of the structure during linear elastic damage mechanics (LEDM) and LEFM [167], [168]. The CT specimen's geometry with its dimensions is shown in Figure 3.39-a). Owing to the symmetry, half of the specimen was modelled. The regular RPIM distribution is depicted in Figure 3.39-b). The analysis relied on a displacement controlled where it was enforced at point *Q*. Moreover, the nodes positioned on the right border side were immobilized along *x* direction.

The geometrical properties were considered as: $L = 600\ \text{mm}$, $D = 750\,\text{mm}$, $b = 100\,\text{mm}$ and $g = 250\,\text{mm}$. The thickness was assumed as $e = 100\,\text{mm}$. The material properties of concrete were adopted as stated in [168]: Young's modulus $E = 34.5 \times 10^9\ \text{Pa}$; Poisson's ratio $\nu = 0.2$; maximum uniaxial tensile strength $f_0^+ = 4.2 \times 10^6\ \text{Pa}$; maximum uniaxial compressive strength $f_0^- = 29.0 \times 10^6\ \text{Pa}$; maximum uniaxial tensile strain $\varepsilon_0^+ = 12.3 \times 10^{-5}$; maximum uniaxial compressive strain $\varepsilon_0^- = 8405.8 \times 10^{-7}$ and fracture energy $G_f = 102.0\ \text{N/m}$.

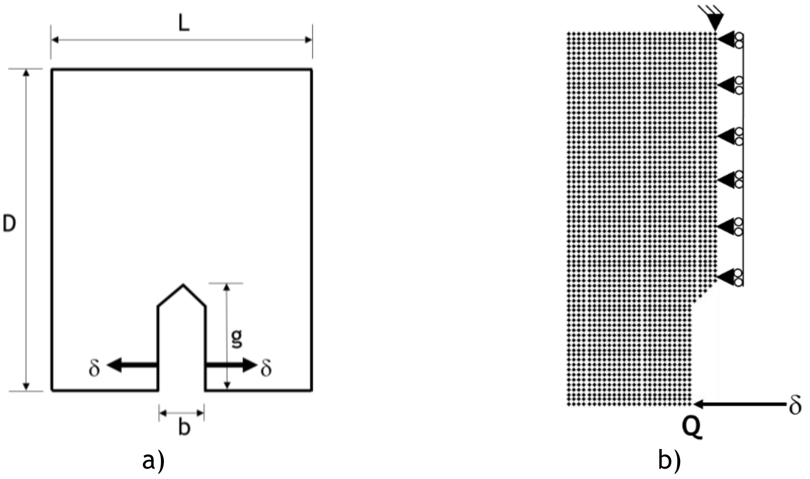

a) b)

Figure 3.39: Concrete CT specimen: a) geometry and b) RPIM nodal discretization [127].

The damage parameters were assumed as: characteristic length $l_{ch} = 30.0\ \text{mm}$ [168], $A^- = 1.0$ and $B^- = 8.9 \times 10^{-1}$ [108]. Substituting the known values, $\bar{H}^+ = 2558.6\ \times 10^{-6}\ \text{mm}^{-1}$ and $A^+ = 166.3 \times 10^{-3}$ were computed [127]. Regarding the numerical damage algorithm, a total displacement $\delta\ = 22.5 \times 10^{-2}\ \text{mm}$ was enforced throughout 15 increments (the algorithm is presented in Appendix C, Figure C.2). As reported in [105], [127], the problem was solved by several RPIM nodal distributions. Considering the optimum non-local damage factors, $s = 0.8$ and 3rd order weight function, as described in [127], the force/displacement response has been obtained for different nodal densities and compared to the experimental solution [168] as presented in Figure 3.40.

The results show that the material tolerated a linear elastic behaviour (OA curve) and then started getting softer leading to a decrease in its stiffness. It was confirmed that the concrete endured a linear damage with micro cracks while the macro cracks have not yet been formed, AB curve. At the end, it entered the linear fracture in which micro cracks evolved to macro cracks (BC curve). Hence, some parts of concrete have been already damaged, and the existing cracks propagated along Oy direction. Hence, the structural failure might be evaluated.

A closer view to the force/displacement curve, it permits to assess a point locating at the interface between LEDM and LEFM, so point B was nominated. The total damage is the maximum value at this point, $d_{total} = 1.0$. Besides, point *B* provides essential information about the damage and fracture mechanism. According to [168], point *B* is identified in the experimental force/*Q* curve with the following values: $(19.5 \times 10^{-2}\ \mathrm{mm}, 18.0\ \mathrm{kN})$. RPIM results were thereby obtained for the corresponding nodal discretizations and reported in Table 3.10. It was also possible to measure the equivalent crack length (a). Its FEM value was reported as $a = 1.3 \times 10^{-4}\ \mathrm{mm}$ [168]. Therefore, it was also calculated for RPIM studies, Table 3.10.

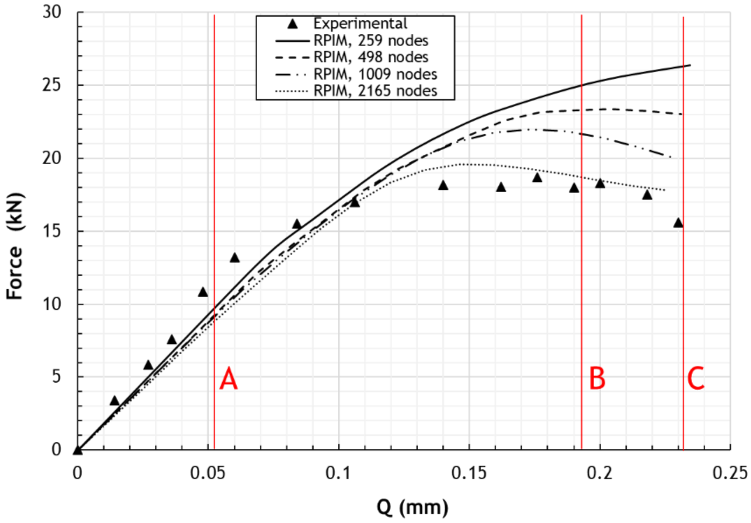

Figure 3.40: Load response versus mouth opening of the hole, *Q*, obtained for different nodal discretizations [127] compared to the experimental solution [168].

Table 3.10: Assessment on point B: RPIM [127], FEM [168] and experimental solution [167].

No. nodes	Force, *F*			Equivalent crack length, *a*		
	Experiment (kN)	RPIM (kN)	Difference * %	FEM ($\times 10^{-4}$ mm)	RPIM ($\times 10^{-4}$ mm)	Difference ** %
259	18.0	24.8	37.8	1.3	0.6	53.8
498		23.3	29.4		0.8	38.5
1009		21.6	20.0		1.0	23.1
2165		18.8	4.4		1.3	0.0

$^{*}|100 \times (F_{RPIM} - F_{\mathrm{Experiment}})/F_{\mathrm{Experiment}}|$;
$^{**}|100 \times (a_{RPIM} - a_{\mathrm{Experiment}})/a_{\mathrm{Experiment}}|$.

Furthermore, Figure 3.41 shows the evolution of total damage derived from RPIM studies. Besides, considering the denser mesh, equivalent effective von-Mises stress contours in total and damaged states are shown in Figure 3.42. Damage versus the effective strain in local and non-local states at the crack tip was acquired, see Figure 3.43. A study of irregular nodal distributions with the obtained results can be found in [105], [127]. The presented numerical damage examples on concrete structures would assist to characterise and lifetime prediction of the railway tunnel structures as an emerging tool in the future research works.

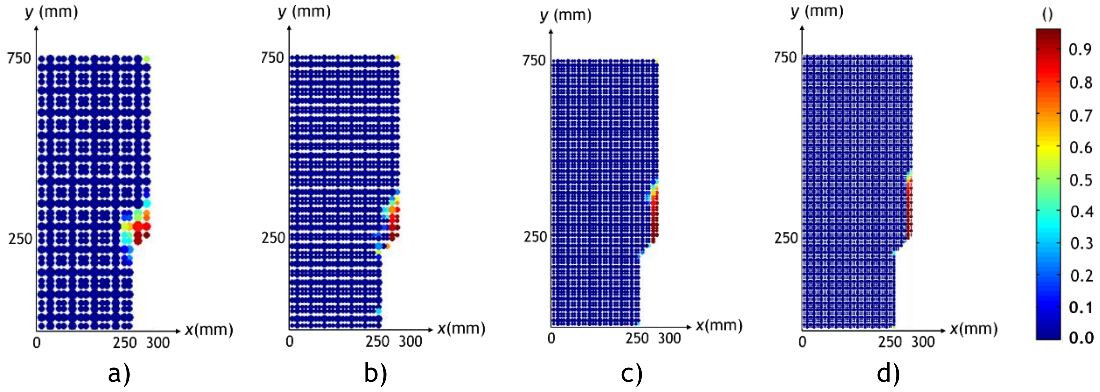

a) b) c) d)

Figure 3.41: Total damage distribution for different RPIM nodal discretizations; a) 259, b) 498, c) 1009 and d) 2165 nodes [127].

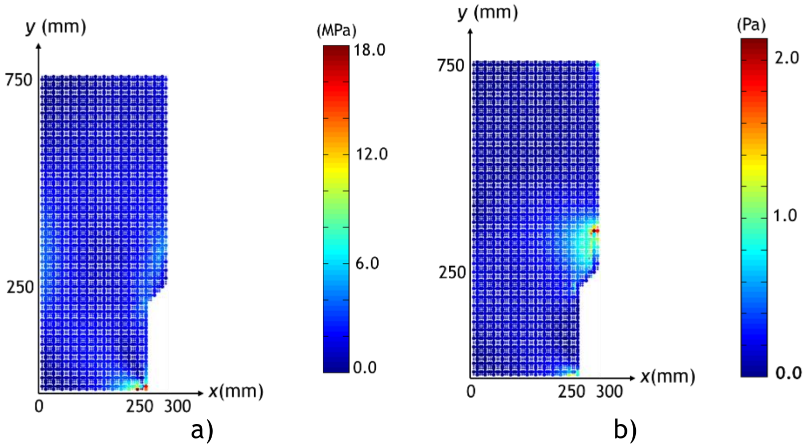

a) b)

Figure 3.42: a) Equivalent total von-Mises stress profile and b) Equivalent damaged von-Mises stress profile [127].

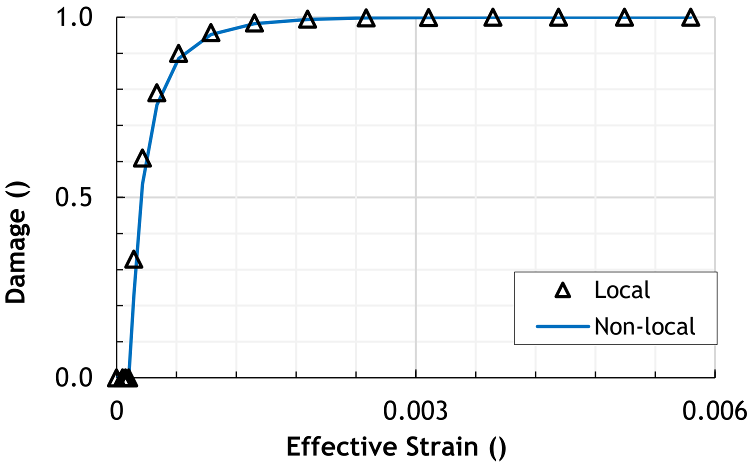

Figure 3.43: Total damage in terms of effective strain [127].

3.3 Chapter summary

In this chapter, as the second-stage inspection technologies following the development of NDI tools for SHM of the engineering components, the application of DIC in the engineering structures has been assessed by performing experimental/computational analyses. The elastostatic, elastoplastic, damage, fatigue and fracture response of various material behaviours resorting to Aluminium alloys, Steel alloys, Polycarbonate and Concrete structures have been documented.

The obtained results from the DIC were considered as a chief key to characterise the structural response and SHM of the tested materials. On the other hand, performed numerical simulations based on advanced discretization techniques, including FE and meshless methods, assisted in the analysis of complex components, and were validated by results of the experimental testing.

The experimental and computational methodologies studied in this chapter will be thereby adopted on the deployed automated inspection system leading to facilitate the implementation of the tunnel examination, an issue which is discussed in the next chapter.

Chapter 4 : Deployed Inspection System

In this chapter, the conducted work on the proposed methodology for railway tunnel inspection is rendered. Experimental tests and computational simulations were performed to examine a tunnel state relying on the deployed 3D LSS. The methodology was established in a laboratory setting intending to be applied on the real railway environment in the future.

The developed inspection system is based on the 3D image processing where a scaled tunnel (prototype) and a small-sized real tunnel are considered. To investigate the geometrical status of the tunnels, an optical system is designed consisting of a circular laser module and a high-resolution camera to capture the projected light on the tunnel interior surface. Therefore, a demonstrator was built relying on the 3D LSS. The camera and laser are mounted on a motorized slider to acquire the images as the slider went through the tunnel prototype. To control and regulate the system's motion, a belt driven linear actuator bundle is used whose power is supplied by a stepper motor. The slider moves through the tunnel with a constant velocity, V_z, ranged between 29 and $115\ \mathrm{mm/s}$. The system is calibrated using a checkerboard pattern. The captured data is processed when all images are collected. The inspection consists in the detection of cracks via computer vision algorithms programmed in MATLAB©. Therefore, it aims at determining the tunnel profile adopting the proposed technological inspection scheme. It is beneficial to identify the geometric characteristics of existing defects and features besides the full 3D tunnel profile acquisition. Furthermore, to maintain a proprietary SHM assessment for analysing the detected defects such as cracks, geometric changes and others, an optical NDI measurement technique was developed based on the 3D DIC.

Furthermore, along with the developed 3D LSS, the system was implemented in a field experiment model in which a section of a wind tower is considered. The tower's geometry has been obtained by means of the deployed 3D LSS.

Figure 4.1 presents a general view of the deployed inspection system.

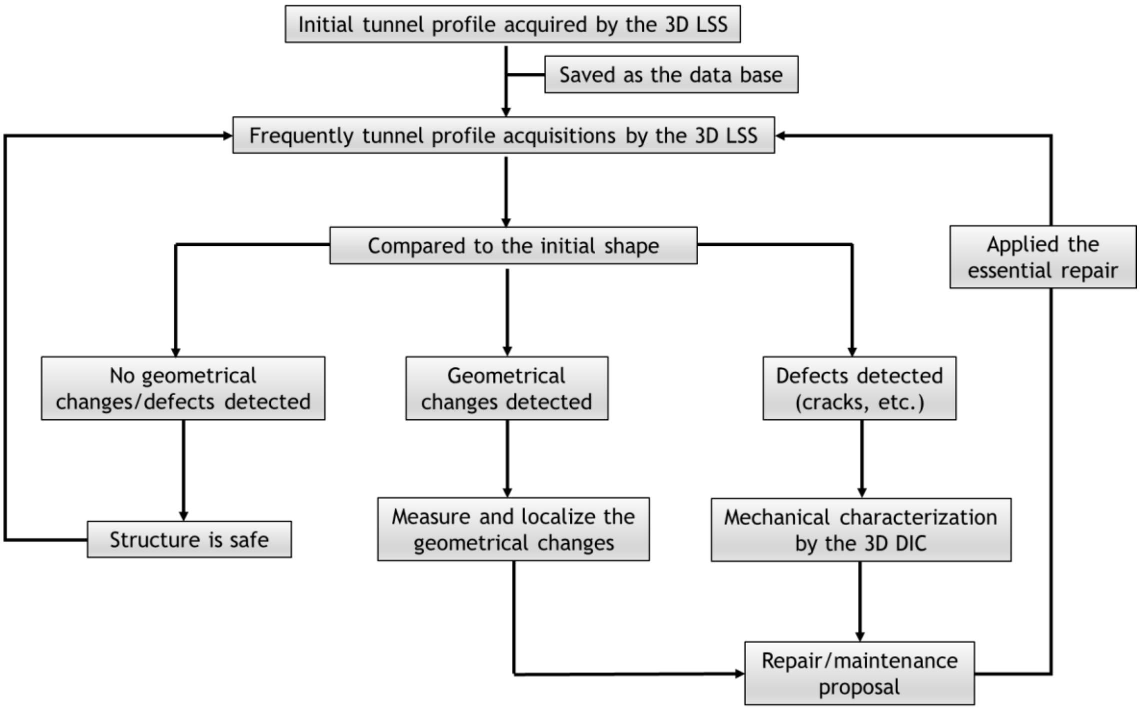

Figure 4.1: A general view of the developed inspection system.

The next section describes the essential mathematical formulations governing the deployed automated inspection system.

4.1 Mathematical formulations

In general, a machine vision system consists of a camera, a light projecting device, a laser, and a station to receive and process the attained data. The laser illuminates the object of interest. In this study, Zhang's camera calibration method [169] was pursued to determine the camera's intrinsic parameters, including radial and tangential distortions. The laser was projected on the calibration pattern during the experiments, so that coordinates of illuminated points can be used to compute the position and orientation of the laser relative to the camera. In this section, the camera and circular laser calibrations are described in detail. The 3D laser shape reconstruction used to detect the shape of the tunnel's inner wall is addressed.

4.1.1 Camera model and calibration

Initially, a 3D point and its image projection can be related as follows:

$$s\boldsymbol{x} = \boldsymbol{A}[\boldsymbol{R}|\boldsymbol{t}]\boldsymbol{X} \tag{4.1}$$

In which $\boldsymbol{x} = \{u \quad v \quad 1\}^T$ and $\boldsymbol{X} = \{X \quad Y \quad Z \quad 1\}^T$ denote the representations of a point in homogeneous image coordinates and world coordinates, respectively, s is an arbitrary scale factor. In addition, rotation matrix $\boldsymbol{R}$ and translation vector $\boldsymbol{t}$ describe a coordinate transformation, and $\boldsymbol{A}$ is the intrinsic matrix, which takes the following form:

$$\boldsymbol{A}=\begin{bmatrix}\alpha & \gamma & u_0\\ 0 & \beta & v_0\\ 0 & 0 & 1\end{bmatrix} \tag{4.2}$$

where (u_0, v_0) signifies the principal point coordinates, α and β present the scale factors correspond to *u*- and *v*- image axes and the skewness of the two image axes is defined by γ. Considering radial distortion up to the sixth order and tangential distortion, the equation system associated to the ideal (undistorted) pixel image coordinates (u, v) and the real (distorted) pixel image coordinates $(\breve{u}, \breve{v})$ can take the following form:

$$\begin{gathered}\breve{u}=u+(u-u_0)(k_1r^2+k_2r^4+k_3r^6)+p_1(r^2+2(u-u_0)^2)+2p_2(u-u_0)(v-v_0)\\ \breve{v}=v+(v-v_0)(k_1r^2+k_2r^4+k_3r^6)+2p_1(u-u_0)(v-v_0)+p_2(r^2+2(v-v_0)^2)\end{gathered} \tag{4.3}$$

If images are acquired on a planar checkerboard pattern and therefore its corners are detected in each image, the parameters of the camera can be estimated because the locations of these corners within the checkerboard's coordinate system are known.

Zhang's model [170] can be used to determine initial estimates for these values based on a linear approach, and subsequently arrive at optimal values throughout a nonlinear error minimization algorithm such as the Levenberg-Marquardt method [171] where the error, for i images of a pattern with j corners, is defined by:

$$\sum_{i=1}^{n}\sum_{j=1}^{m}\left\|\boldsymbol{x}_{ij}-\widehat{\boldsymbol{x}}(\boldsymbol{A},\boldsymbol{k},\boldsymbol{R}_i,\boldsymbol{t}_i,\boldsymbol{X}_j)\right\|^2 \tag{4.4}$$

where $\widehat{\boldsymbol{x}}(\boldsymbol{A},\boldsymbol{k},\boldsymbol{R}_i,\boldsymbol{t}_i,\boldsymbol{X}_j)$ denotes the projection of a checkerboard corner with coordinates $\boldsymbol{X}_j$ in the i^{th} image as computed by the camera model defined by intrinsic matrix $\boldsymbol{A}$, distortion parameters $\boldsymbol{k}=[k_1\ k_2\ k_3\ p_1\ p_2]$ and the rotation $\boldsymbol{R}_i$ and translation $\boldsymbol{t}_i$ of the checkerboard in each image. As a measurement of accuracy of the model, the mean re-projection error (MRE) can be calculated as:

$$\text{MRE}=\frac{1}{mn}\sum_{i=1}^{n}\sum_{j=1}^{m}\left\|\boldsymbol{x}_{ij}-\widehat{\boldsymbol{x}}(\boldsymbol{A},\boldsymbol{k},\boldsymbol{R}_i,\boldsymbol{t}_i,\boldsymbol{X}_j)\right\| \tag{4.5}$$

Appendix A describes the thorough mathematical equations associated with the camera calibration based on Zhang's method [169], [170], [172].

4.1.1.1 Laser calibration

The beams of light emitted by the laser describe a cone in three dimensions. By having the laser projecting its light on the checkerboard pattern during the calibration image acquisition, the 3D coordinates of laser points on the checkerboard could be obtained from their pixel coordinates and the acquaintance of the checkerboard's rotation and translation. The points extracted from all calibration images can then be used as data points to fit a model of a cone. The plane defined by a checkerboard with extrinsic matrix $[\boldsymbol{R}_i \mid \boldsymbol{t}_i]$ can be expressed as:

$$\boldsymbol{n}^T[x \quad y \quad z]^T - \boldsymbol{n}^T\boldsymbol{t}_i = 0 \tag{4.6}$$

where $\boldsymbol{n} = \boldsymbol{R}_i[0 \quad 0 \quad 1]^T$ is the plane normal. After correcting the acquired images for distortion and extracting the laser points $\boldsymbol{x}_{laser}$ using a specified threshold, the homogeneous coordinates of these points are given by:

$$\boldsymbol{x}_h = \frac{1}{z}[x \quad y \quad z]^T = \boldsymbol{A}^{-1}\boldsymbol{x}_{laser} \tag{4.7}$$

From Equations (4.6) and (4.7):

$$\boldsymbol{n}^T\boldsymbol{x}_h z - \boldsymbol{n}^T\boldsymbol{t}_i = 0 \tag{4.8}$$

Which leads to:

$$[x \quad y \quad z]^T = \frac{\boldsymbol{n}^T\boldsymbol{t}_i}{\boldsymbol{n}^T\boldsymbol{x}_h}\boldsymbol{x}_h \tag{4.9}$$

After determination of the 3D point coordinates, a cone, modelled by the position of its vertex $\boldsymbol{T}_L$, the axis $\boldsymbol{a}$ that defines its direction and its aperture φ, is fitted to the resulting point cloud using a nonlinear optimization method, mentioned before.

4.1.1.2 The 3D laser triangulation

The coordinate transformation between the laser's frame of reference $\boldsymbol{X}_L$ and the camera's frame of reference $\boldsymbol{X}_C$ can be formulated as:

$$\boldsymbol{X}_C = \boldsymbol{R}_L\boldsymbol{X}_L + \boldsymbol{T}_L \tag{4.10}$$

$\boldsymbol{R}_L$ being a rotation matrix such that $\boldsymbol{a} = \boldsymbol{R}_L[0 \quad 0 \quad 1]^T$. Then, the camera origin in the laser coordinates is defined by:

$$\boldsymbol{O}_L = [x_0 \quad y_0 \quad z_0]^T = -\boldsymbol{R}_L^T\boldsymbol{T}_L \tag{4.11}$$

Given a certain image point, its possible 3D location, as seen by the laser, can be defined in terms of the camera origin and the point's homogeneous coordinates $\boldsymbol{x}_h$, as;

$$\boldsymbol{X}_L = \boldsymbol{O}_L + k\boldsymbol{u}_n \tag{4.12}$$

where $\boldsymbol{u}_n = [u \quad v \quad w]^T = \boldsymbol{R}_L^T\boldsymbol{x}_h$ and k is any non-negative real number. On the other hand, the cone defined by the laser light can be expressed as:

$$\begin{bmatrix} x_L \\ y_L \\ z_L \end{bmatrix} = \begin{bmatrix} r\cos\theta \\ r\sin\theta \\ z \end{bmatrix} = \begin{bmatrix} z\tan\varphi\cos\theta \\ z\tan\varphi\sin\theta \\ z \end{bmatrix} \tag{4.13}$$

In which (r, θ, z) denotes the cylindrical coordinate of points to the laser centerline. Therefore, a point, which is viewed by the camera and illuminated by the laser, follows the relation below:

$$\begin{bmatrix} z \tan\varphi \cos\theta \\ z \tan\varphi \sin\theta \\ z \end{bmatrix} = \begin{bmatrix} x_0 \\ y_0 \\ z_0 \end{bmatrix} + k \begin{bmatrix} u \\ v \\ w \end{bmatrix} \tag{4.14}$$

The trigonometric identity gives:

$$(z \tan\varphi \cos\theta)^2 + (z \tan\varphi \sin\theta)^2 = z^2 \tan^2\varphi \tag{4.15}$$

According to Equation (4.14), the recent equation can be rewritten as:

$$(x_0 + ku)^2 + (y_0 + kv)^2 = (z_0 + kw)^2 \tan^2\varphi \tag{4.16}$$

This can then be rearranged to become a quadratic equation in terms of k:

$$(u^2 + v^2 - w^2 \tan^2\varphi)k^2 + 2(x_0 u + y_0 v - z_0 w \tan^2\varphi)k + ({x_0}^2 + {y_0}^2 - {z_0}^2 \tan^2\varphi) = 0 \tag{4.17}$$

Solving this equation will yield k such that the point's world coordinates in the camera's frame of reference are given by $\boldsymbol{X}_w = k\boldsymbol{x}_h$. The equation produces two solutions, only one of them is correct; but if it is assumed that the camera center is located behind the laser, inside a cone with the same vertex and aperture as the one defined by the laser, but facing the opposite direction, then the smallest value of k will correspond to the intersection of the light beam seen by the camera with that cone and the largest obtained value of k will be correct.

Besides, if the camera and the laser pass through the tunnel with a constant linear velocity of V_z and considering the camera framerate of f_s, it is arrived at:

$$\boldsymbol{X}_w = k\boldsymbol{x}_h + V_z(N/f_s) \tag{4.18}$$

where N is the index of the current frame. So, $\boldsymbol{X}_w$ is updated to consider the camera motion and laser through the tunnel. For any point extracted from the tunnel images by applying a threshold, Equations (4.17) and (4.18) are used to calculate the world coordinates of that point. Besides, the term V_z/f_s denotes the system resolution in z direction.

The presented mathematical formulations are valid for all presented benchmarks carried out by the developed 3D LSS, examples in Section 4.2, Section 4.3 and Section 4.4.

4.2 Scaled tunnel: model definition and experiments

In this experiment, considering a railway tunnel prototype, a polymer pipe (Ø211.0×14.8 mm) was used, longitudinally cut in half respecting the geometrical and mechanical properties reported in Table 4.1.

Table 4.1: Properties of AlfaGAS, EN 1555 SDR 17, PE100 pipe, extracted from manual.

Parameter	Value
Outer diameter	$D_o^{real} = 211.00\ \mathrm{mm}$
Inner diameter	$D_i^{real} = 181.40\ \mathrm{mm}$
Thickness	$e = 14.80\ \mathrm{mm}$
Length	$L = 630.00\ \mathrm{mm}$
Density	$\rho = 9.30 \times 10^{-10}\ \mathrm{tonne/mm^3}$
Young's Modulus	$E = 200.00\ \mathrm{MPa}$
Poisson's Ratio	$\upsilon = 0.45$

To provide a linear motion to the system, a V-Slot® Linear Actuator Belt Driven (slider) was adopted in which a Nema 17 stepper motor generated the system power. The slider moves through the tunnel with a constant velocity that may be set between $V_z = 29 - 115\ \mathrm{mm/s}$, see Figure 4.2.

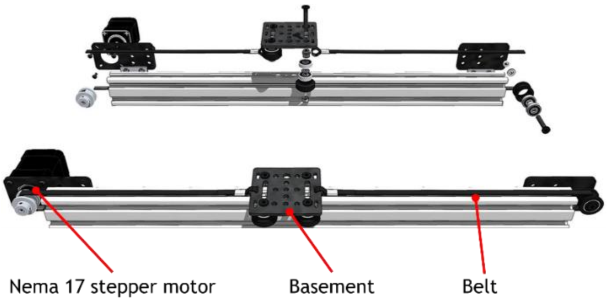

Figure 4.2: The slider adopted for the developed 3D LSS.

To mount the camera and laser, a perforated plate was used on the slider basement, see Figure 4.3-c) and -d). The stepper motor was controlled by means of an ATmega328 (Arduino Nano 3.x) with a Dual H Bridge DC Stepper Motor Controller Board. Additionally, the LSS consists of the optical instruments. Experiments were performed using a Point-Grey Gazelle $4.1\ \mathrm{MP}$ Mono, a 2048.0×2048.0 resolution camera with a Schneider Cinegon $1.8/16.0\ \mathrm{mm}$ c-mount lens. This camera can achieve a frame rate of $f_s = 150.0\ \mathrm{fps}$, which enables a high sampling rate. A green $50\ \mathrm{mW}$ circular laser module possessing an output wavelength of $520.0\ \mathrm{nm}$ was adopted, (more technical information of the optical instruments is reported in Table 4.2). A general view of the optical components of the deployed 3D LSS is shown in Figure 4.3. The tube interior surface was coated by a white powder detector to avoid the laser light reflection.

Image acquisition was accomplished by VIC-Snap 2012© vision software. To calibrate the camera relying on Zhang's algorithm [169], a checkerboard including 9×8 squares, with square size of $10.0\ \mathrm{mm}$ was used, see Figure 4.4-a). The calibration was performed, and calibration results are reported in Table 4.3. Moreover, the mean re-projection error (MRE) in pixel, which has been calculated relying on Equation (4.11), is demonstrated in Figure 4.4-b). Then, the circular laser was calibrated on the checkerboard in order to parametrize the 3D laser triangulation respecting its coordinates to the camera, see Figure 4.4-c).

Notice that it was attempted to maintain the calibration solution for all the LSS experiments performed during this work.

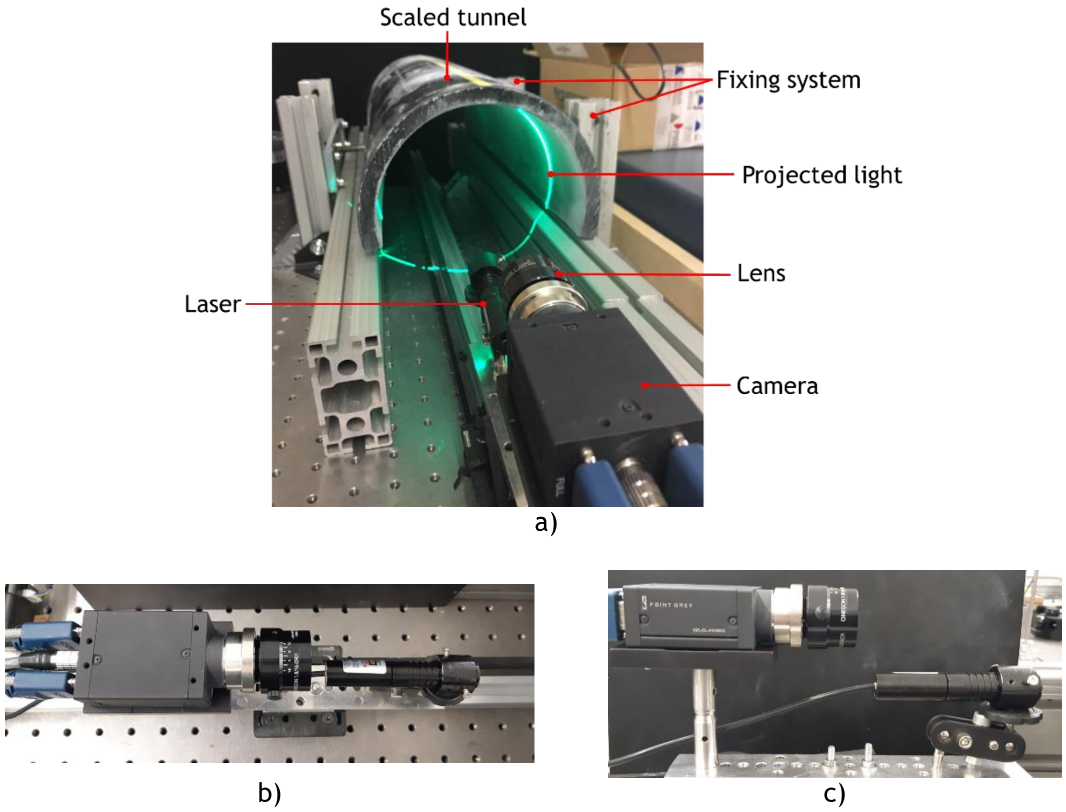

a)

b)

c)

Figure 4.3: Deployed 3D LSS; a) a general view of the system, b) top and c) side view.

Table 4.2: Optical instruments technical specification adopted for the 3D LSS.

Specification	Information
Stereo camera	
Model	PointGrey- CMOSIS CMV4000-2E5 CMOS
Resolution	2048.0 x 2048.0
Frame Rate	150.0 FPS
Sensor Format	1.0"
Pixel Size	5.5 µm
Lens Mount	C-mount
Exposure Range	74.2 µs - 54.0 s (Full 8.0-tap mode)
Interface	Camera Link
Cinegon 1.8/16 -0901 Schneider lens	
F-number	1.8
Focal length	16.4 mm
Interface	C-mount
Circular laser modulus	
Output wavelength	520.0 nm
Light	green
Laser Shape	Circle
Focus	Adjustable, the width of the laser beam (>0.8 mm)
Output power	Max 50.0 mw (Adjustable)
Operation current	<400.0 mA
Working distance	0.0~10.0 meters
Operation mode	Continuous Wave (CW)
Others	The diameter of circle and distance of the radiation is about 1.0:1.0

Table 4.3: Camera and laser calibration results, scaled tunnel experiments.

Camera calibration		
Intrinsic parameters	α	3553.19
	β	3563.26
	γ	1.69
	u_0	1005.17
	v_0	1039.33
Radial Distortion	k_1	-1.87E-01
	k_2	5.60E-01
	k_3	5.38E+00
Tangential Distortion	p_1	-5.14E-04
	p_2	-9.03E-05

Circular laser calibration			
	x (mm)	*y* (mm)	*z* (mm)
Laser position	-4.93	33.55	134.65
Laser axis	3.13E-02	2.52E-03	9.99E-01
Aperture, φ	-27.70 °		

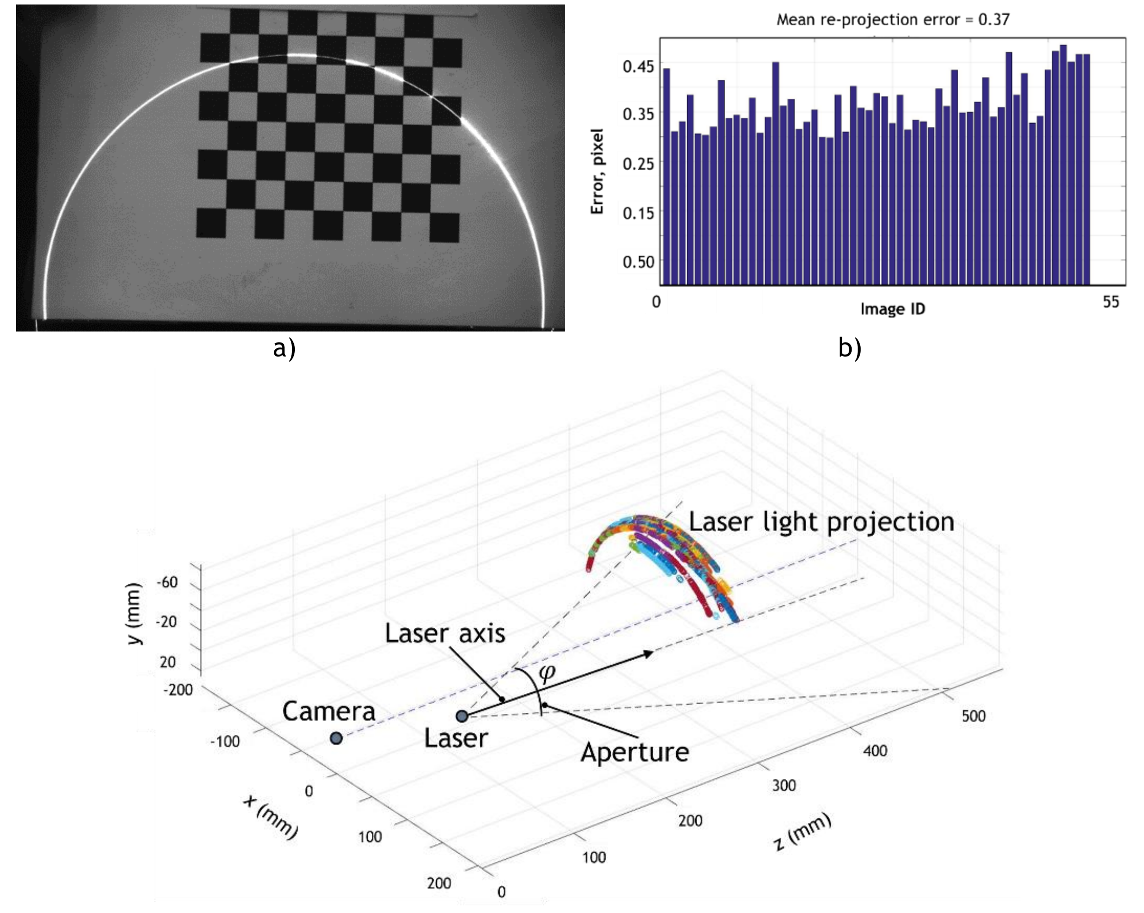

a)

b)

c)

Figure 4.4: a) A-9×8-checker board used for the calibration, laser light projection illustration, b) re-projection error in pixels acquired from calibration procedure and c) camera and laser position in the scaled tunnel experiment.

Regarding the experimental activities, several experiments were performed on the corresponding scaled tunnel to obtain its 3D point cloud and detect artificial defects placed in the tunnel interior wall, as well as the notches which were created in different locations. Several tunnel states were examined by the deployed LSS as follows:

- **Initial state**, which corresponds to tunnel with its reference geometry after cutting;
- **Feature detection**, objects attached along the tunnel's interior wall to assess the accuracy of the developed system in the presence of small objects;
- **Loaded tunnel**, with a displacement imposed to the exterior wall leading to a deformation in the interior wall;
- **Tunnel containing notches**, three linear notches were produced on the tunnel's interior wall and the change in geometry detected by the 3D LSS and then mechanically studied by the 3D DIC upon loading.

In all image acquisition experiments by the LSS, the threshold was chosen as $TH = 0.5$ for the laser point extraction. It must be noted that in the last experiment on defect detection, once the defect was detected by the LSS, a 3D DIC analysis was performed to obtain the deformation field in the notch region upon loading. Moreover, one of tunnel models containing notches was simulated with the FEM and a comparison was drawn on obtained results. Scanning parameters for all LSS experiments were adopted as follows: $V_z = 114.98\ \mathrm{mm/s}$, $f_s = 100.00\ \mathrm{fps}$ and the system resolution in z-direction was computed as $1.15\ \mathrm{mm/frame}$.

In this work, it was opted to employ DIC due to its wide applicability and accuracy in the deformation measurement as a non-contact optical technique amongst others. It can be adopted as a non-destructive inspection (NDI) technique in the structural health monitoring (SHM) of railway tunnels to monitor and characterise defects as demonstrated in [173].

4.2.1 Initial geometry

In order to acquire the tunnel initial shape, it was opted to obtain a reference solution. Hence, the tunnel was scanned by a commercial 3D scanning system that uses structured light, as shown in Figure 4.5-a). The 3D shape acquisition structured light system setup positioned in a 1000-mm-working distance to the model. The acquired point cloud characterised the geometry with $D_i^{ref.} = 181.52\ \mathrm{mm}$ as shown in Figure 4.5-b).

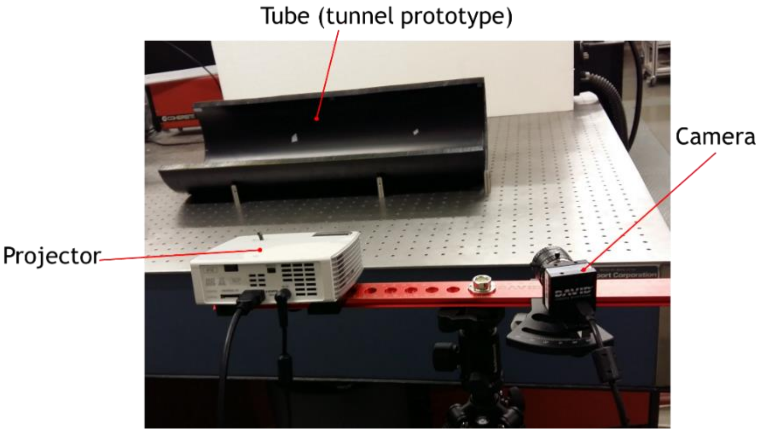

a)

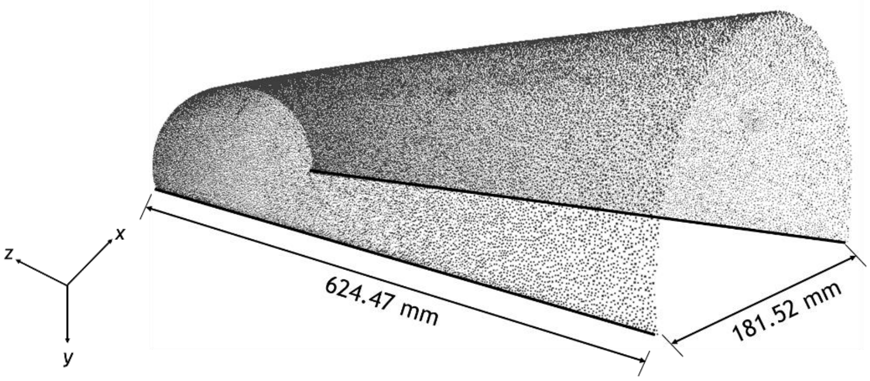

b)

Figure 4.5: the 3D structured light scanning system experiment, reference solution, a) setup and b) Initial tunnel profile.

The image acquisition of the initial tunnel state regarding the deployed LSS was then performed following the LSS system presented in Figure 4.3. The projected laser light on the interior surface of the tunnel was stable in shape and intensity as shown in Figure 4.6-a). Figure 4.6-b) displays the profile of the initial tunnel state with an inner diameter measured as $D_i^{LSS} = 181.38\,\mathrm{mm}$, which has a $0.08\,\%$ difference to the reference solution, $D_i^{ref.}$. The acquired point cloud includes 5326169 vertices and it was then simplified to 233744 vertices by means of Poisson-disk sampling [174] in a 3D mesh processing software system.

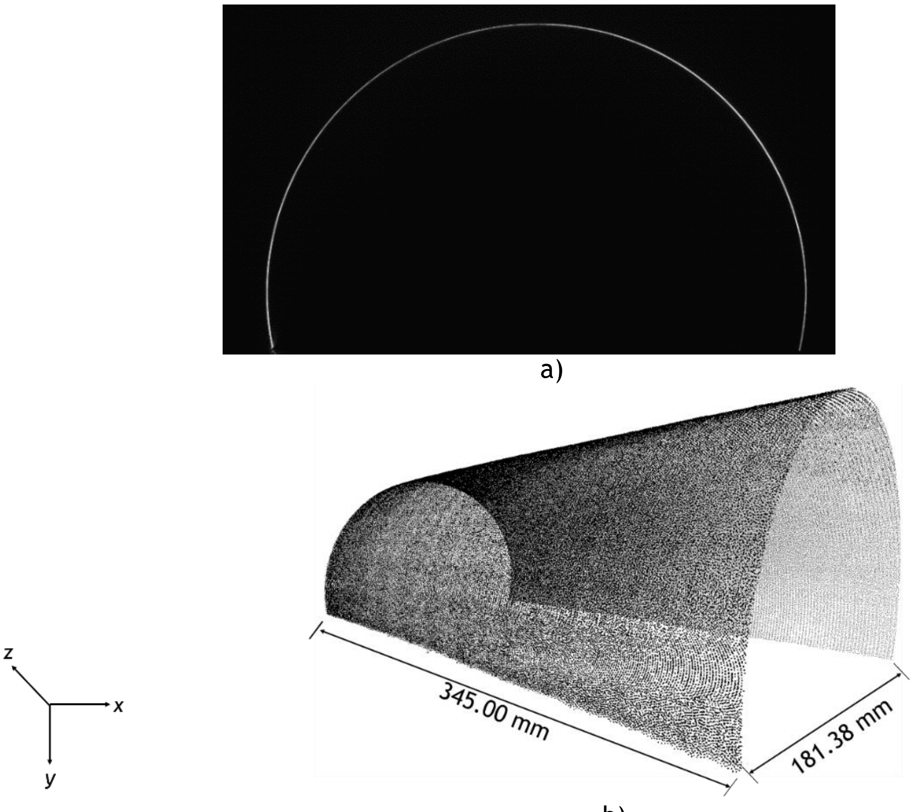

b)

Figure 4.6: Initial tunnel experiment performed by the 3D LSS a) projected laser light on the scaled tunnel interior wall and b) obtained point cloud.

Table 4.4 reports the inner diameter of the scaled tunnel in the initial state obtained from the 3D LSS and structured light scanning system. D_i^{real} denotes the tube diameter before cutting.

Table 4.4: Inner diameter measured by the 3D structured light (reference) and LSS.

D_i^{real}	$D_i^{ref.}$	D_i^{LSS}	**Deviation * (reference and real)**	**Deviation** (LSS and real)**
181.40 mm	181.52 mm	181.38 mm	0.07 %	0.01 %

$*100 \times \left|\left(D_i^{ref.} - D_i^{real}\right)/D_i^{real}\right|$;
$**100 \times \left|\left(D_i^{LSS} - D_i^{real}\right)/D_i^{real}\right|$.

Considering both methods employed to acquire the tunnel's initial geometry, it can be inferred that the experiment with the structured light commercial scanning system required a considerable image processing task. Owing to the model dimensions, the scanning procedure was performed on different tube sections and then the obtained shapes per each section were fused to acquire the full tunnel profile. Hence, it demands high computational costs in time and computer processing. On the other hand, the LSS experiment showed that the tunnel shape could be obtained with a single pass and thereby the acquired point cloud was simply processed in a vision software. Overall, it can be concluded that the developed LSS is more cost-effective and easier to implement when compared to the structured light solution.

4.2.2 Feature detection

In this experiment, four dissimilar objects have been attached on the tunnel's interior wall as identified in Figure 4.7. The experiment was carried out and re-done three times to obtain the tunnel profile respecting the feature detection. To obtain the complete geometry, the experiment has been performed in the tunnel, which was positioned in the initial place, and then the tunnel was turned around and the image acquisition repeated. The obtained point clouds were then merged and aligned.

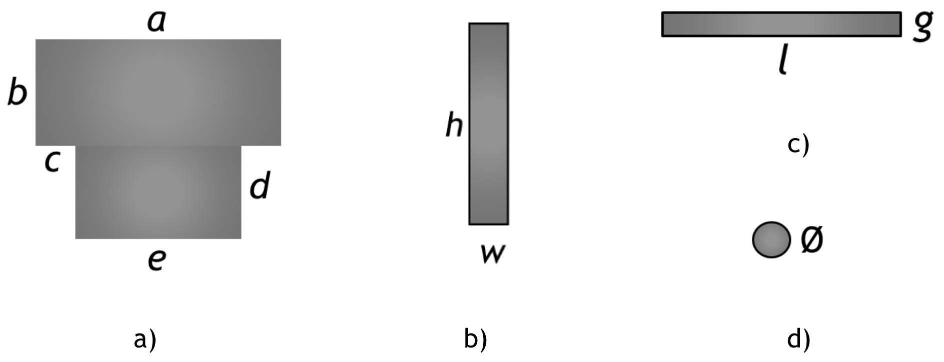

a) b) c) d)

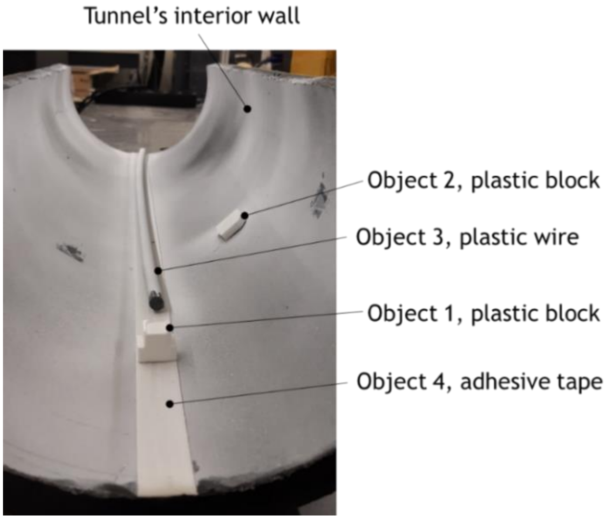

e)

Figure 4.7: Objects used for feature detection experiments with the dimension illustration: a) object 1, plastic block, b) object 2, plastic block, c) object 3, adhesive tape, d) object 4, plastic wire and e) a general view of the objects attached to the interior wall.

The mean values of the measured geometrical characteristics from LSS experiments compared to their real dimensions are reported in Table 4.5. Small deviations were verified between the LSS and real values. The obtained results put into evidence that the developed 3D LSS has the capability to detect accurately the small objects relative to the tunnel dimensions with a reasonable measurement consistency. The acquired tunnel shape regarding the detected features with detail is shown in Figure 4.8.

Table 4.5: Geometrical characteristics of the objects in the feature detection experiments measured by LSS.

	Dimension	***a***	***b***	***c***	***d***	***e***
Object 1	Real (mm)	18.50	8.00	3.00	7.00	12.50
	LSS_mean (mm)	18.63	7.97	3.07	7.07	12.56
	Deviation* (%)	0.70	0.38	2.33	1.00	0.48

	Dimension	***h***	***w***
Object 2	Real (mm)	20.00	5.00
	LSS_mean (mm)	20.16	5.05
	Deviation* (%)	0.80	1.00

	Dimension	***Ø***
Object 3	Real (mm)	8.50
	LSS_mean (mm)	8.26
	Deviation* (%)	2.82

	Dimension	***l***	***g***
Object 4	Real (mm)	20.00	1.20
	LSS_mean (mm)	19.38	1.19
	Deviation* (%)	3.10	0.83

*****$100 \times |(value^{LSS\_mean} - value^{Real})/value^{Real}|$.

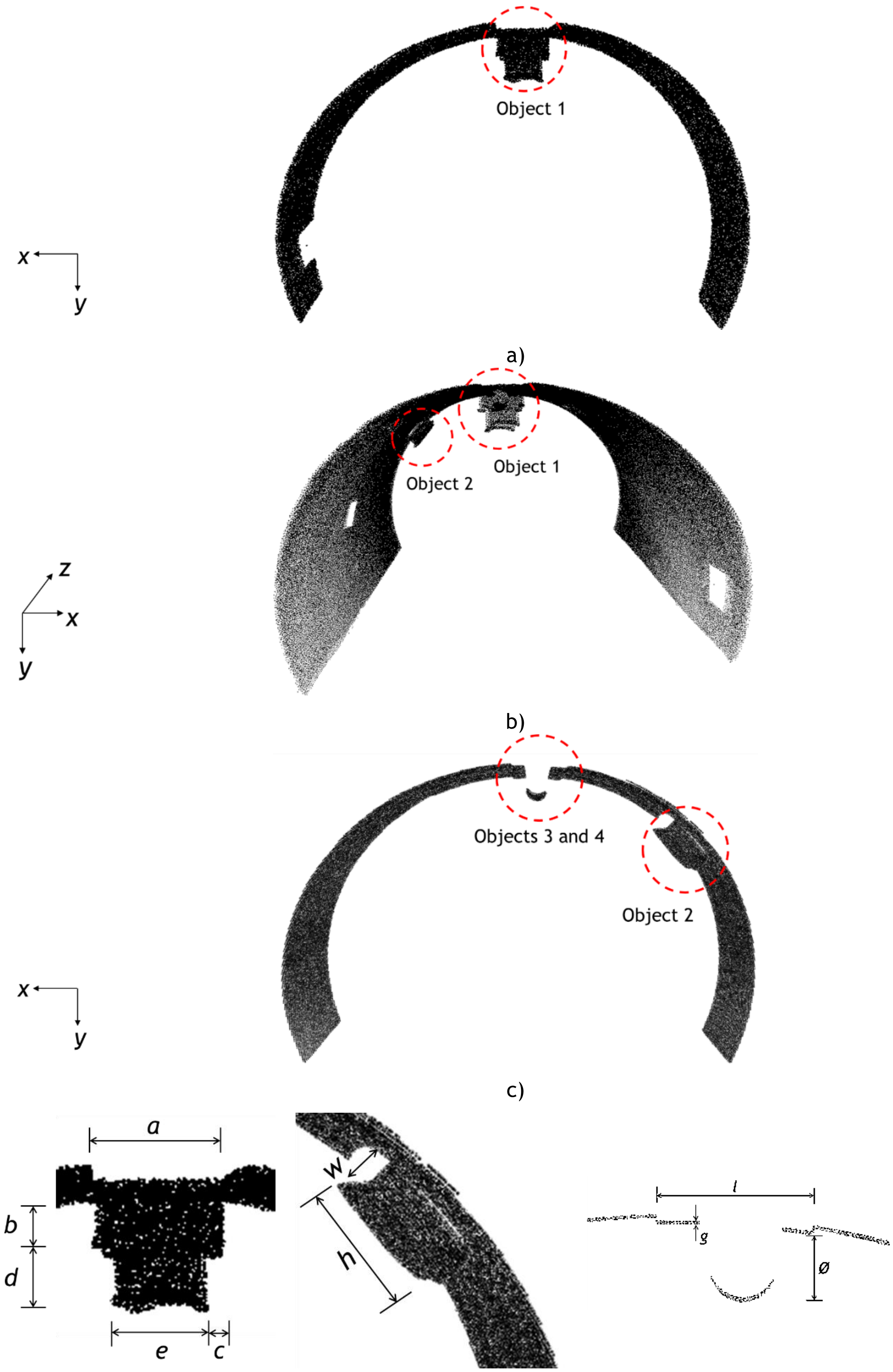

d)

Figure 4.8: Obtained results from feature detection LSS experiments: a) object 1, b) objects 1 and 2, c) objects 2, 3 and 4 and d) detail on all objects.

4.2.3 Loaded tunnel

This section focuses on the tunnel shape reconstruction when it is subjected to a compressive loading state. Considering the real case in which tunnels are loaded from the exterior wall by the surroundings, a compressive load was imposed by means of a displacement enforcement from the tunnel's exterior wall. The mechanical setup is shown in Figure 4.9-a). To enforce the displacement, a M10 bolt threaded on a fixed plate was used to impose a deformation of the tunnel wall close to the tunnel mid-section. A digital displacement sensor was used to measure the enforced displacement magnitude, Figure 4.9-a).

As shown in Figure 4.9-b), a displacement in x-direction, $u(x, y, z)$, was imposed on point P for three magnitudes: $u_1 = 5\ \mathrm{mm}$, $u_2 = 10\ \mathrm{mm}$ and $u_3 = 15\ \mathrm{mm}$. Point P is located at the tunnel mid-section, with an offset of $20\ \mathrm{mm}$ in y-direction from the tunnel base.

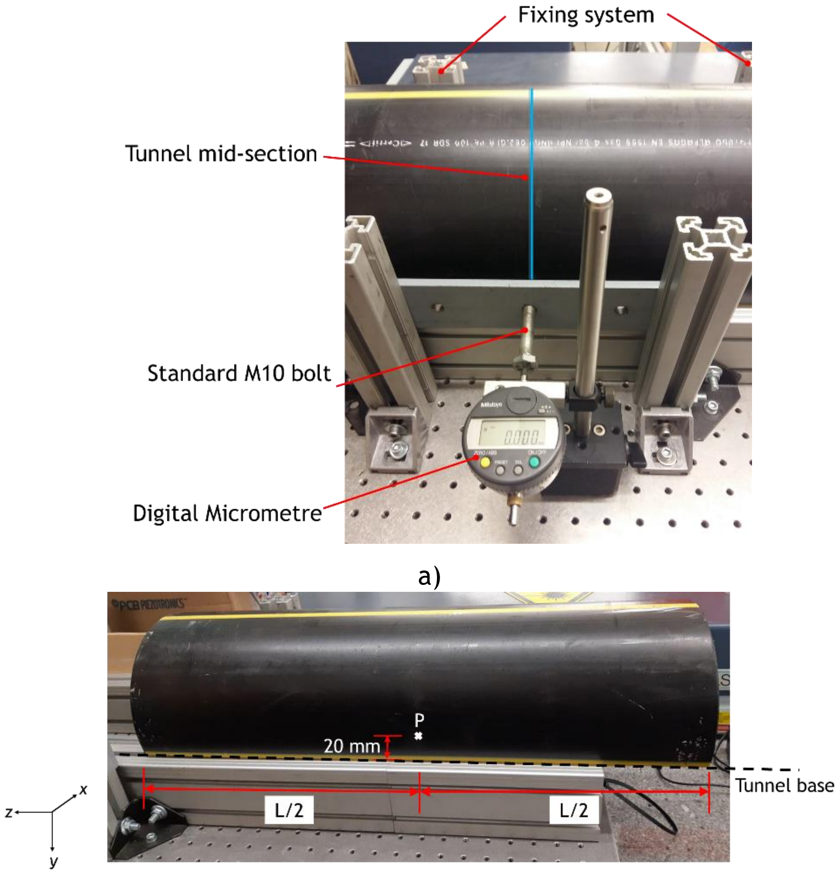

a)

b)

Figure 4.9: Loaded tunnel experiment a) mechanical setup and b) displacement imposition configuration.

4.2.3.1 The 3D LSS experiment

This experiment was carried out and point clouds associated with the initial and deformed tunnel were extracted for each displacement imposition, see Figure 4.10-a). The obtained point clouds were processed in a 3D vision software to simplify the point clouds based on the Poisson-disk sampling method [174]. Table 4.6 reports the obtained point cloud vertices and their simplified values related to the loaded tunnel experiments. Figure 4.10-b) shows one section extracted where the displacement was enforced. To assess the accuracy and validity of the proposed 3D LSS model, it is worth to draw a numeric comparison amongst all acquired deformed profiles with the initial shape. To accomplish this assessment, some auxiliary points were chosen in the initial and deformed shapes. Hence, points A, B, C and D were selected on the tunnel base and their world coordinates extracted from the resultant point clouds. On the other hand, to study the displacement variation on the location point P where the displacement was imposed, points E, F, G and H were accordingly followed through the deformed profiles: $u_1 = 5\ \mathrm{mm}$; $u_2 = 10\ \mathrm{mm}$, and $u_3 = 15\ \mathrm{mm}$. The coordinates of the chosen points are reported in Table 4.7.

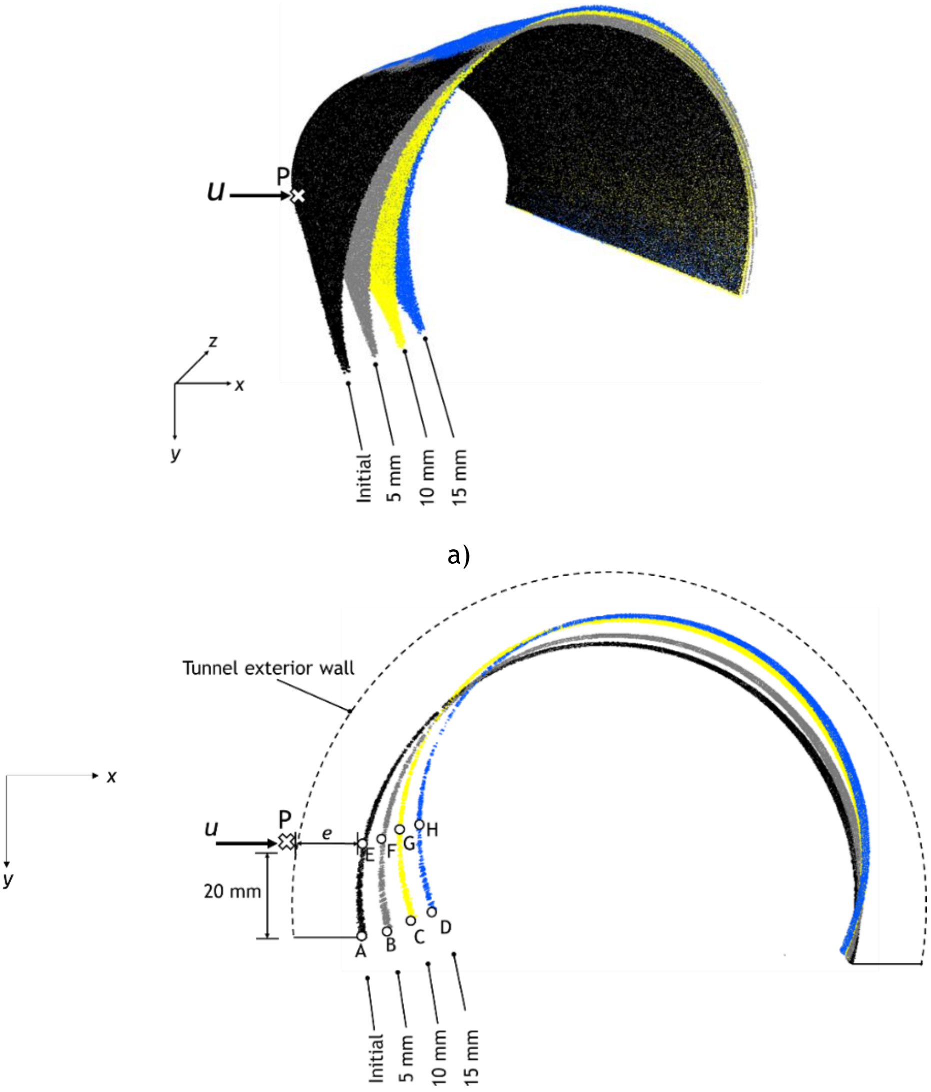

a)

b)

Figure 4.10: a) Graphical representation of acquired point clouds and b) one frame point cloud corresponding to position where the displacement was imposed, notice that the tunnel was loaded on point P.

Table 4.6: Point cloud extracted from each experiment, loaded tunnel state.

Experiment	Extracted point cloud vertices	Simplified point cloud vertices
Initial	4820515	233744
$u_1 = 5\ \text{mm}$	4823627	206994
$u_2 = 10\ \text{mm}$	4821818	213283
$u_3 = 15\ \text{mm}$	4650573	183803

Table 4.7: Point coordinates acquired for the loaded tunnel experiments.

	Initial		$u_1 = 5\ \text{mm}$		$u_2 = 10\ \text{mm}$		$u_3 = 15\ \text{mm}$	
Points	**A**	**E**	**B**	**F**	**C**	**G**	**D**	**H**
***x* (mm)**	-86.7	-88.6	-81.2	-84.2	-75.4	-79.3	-69.9	-74.1
***y* (mm)**	57.4	37.4	56.5	35.3	54.4	32.9	53.8	31.1
***z* (mm)**	297.9	295.8	286.8	286.3	274.5	276.7	263.2	266.1

For any experiment of the loaded tunnel, one frame has been extracted from the acquired point cloud. It was located on the position where the displacement has been imposed form the exterior wall. The tunnel's inner diameter has been measured as shown in Figure 4.11.

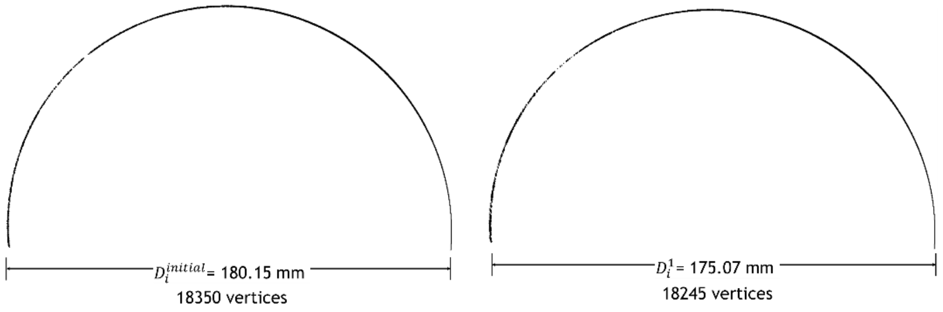

a) initial state b) $u_1 = 5\ \text{mm}$

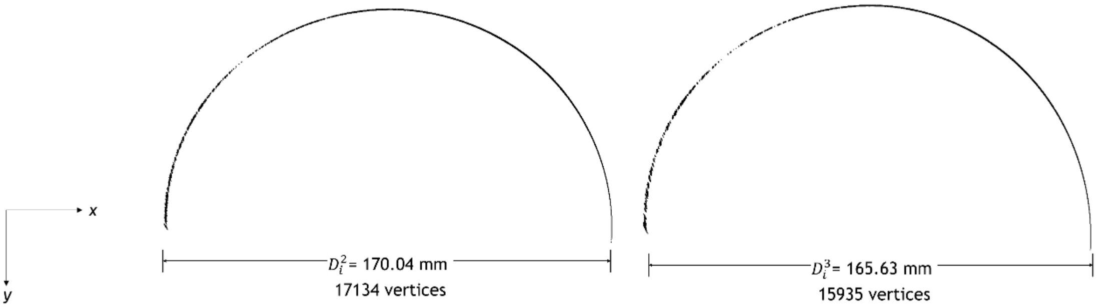

c) $u_2 = 10\ \text{mm}$ d) $u_3 = 15\ \text{mm}$

Figure 4.11: One frame extraction on tunnel mid-section where displacement imposed from exterior wall, inner diameter measurements.

4.2.3.2 The 3D DIC analysis

To obtain another alternative solution on the tunnel's deformation while it was loaded, the 3D DIC technique was implemented. The area of interest of the tunnel interior wall, on the region where the displacement had been imposed, was prepared by inserting a random speckle pattern to its surface. Since the tunnel wall was black, the random pattern had been generated by sprinkling white dots creating a speckle pattern with dot size ranging between 8 and 10 pixel, as shown in Figure 4.12-f). The DIC system was arranged and positioned inside the tunnel with a working distance of $150.0\ \mathrm{mm}$ in front of the interest region as shown in Figure 4.12-b). As seen in Figure 4.12-a), two $1.3\ \mathrm{MP}$ cameras with a resolution of $1280.0 \times 1024.0\ \mathrm{pixel}^2$ with a focal length of $F = 3.8\ \mathrm{mm}$ were adopted for the established 3D DIC analyses, technical specifications of the cameras are reported in Table 4.8. The region was illuminated using the spotlights included with the cameras, Figure 4.12-c). The acquired data was analysed through VIC-3D©-2012 software. The system has been calibrated using a 12-by-9 dots calibration pattern spaced as $5.5\ \mathrm{mm}$, as shown in Figure 4.12-d), by means of the bundle adjustment. Thus, a set of images was taken on the calibration pattern, and therefore they were processed by a stereo system calibration. The calibration results are outlined in Table 4.8. The examined region was gridded with a subset of $23\ \mathrm{pixel}$ and a step size of $5\ \mathrm{pixel}$. The 2D camera FOV and a facet field are presented in Figure 4.12-e) and -f), respectively.

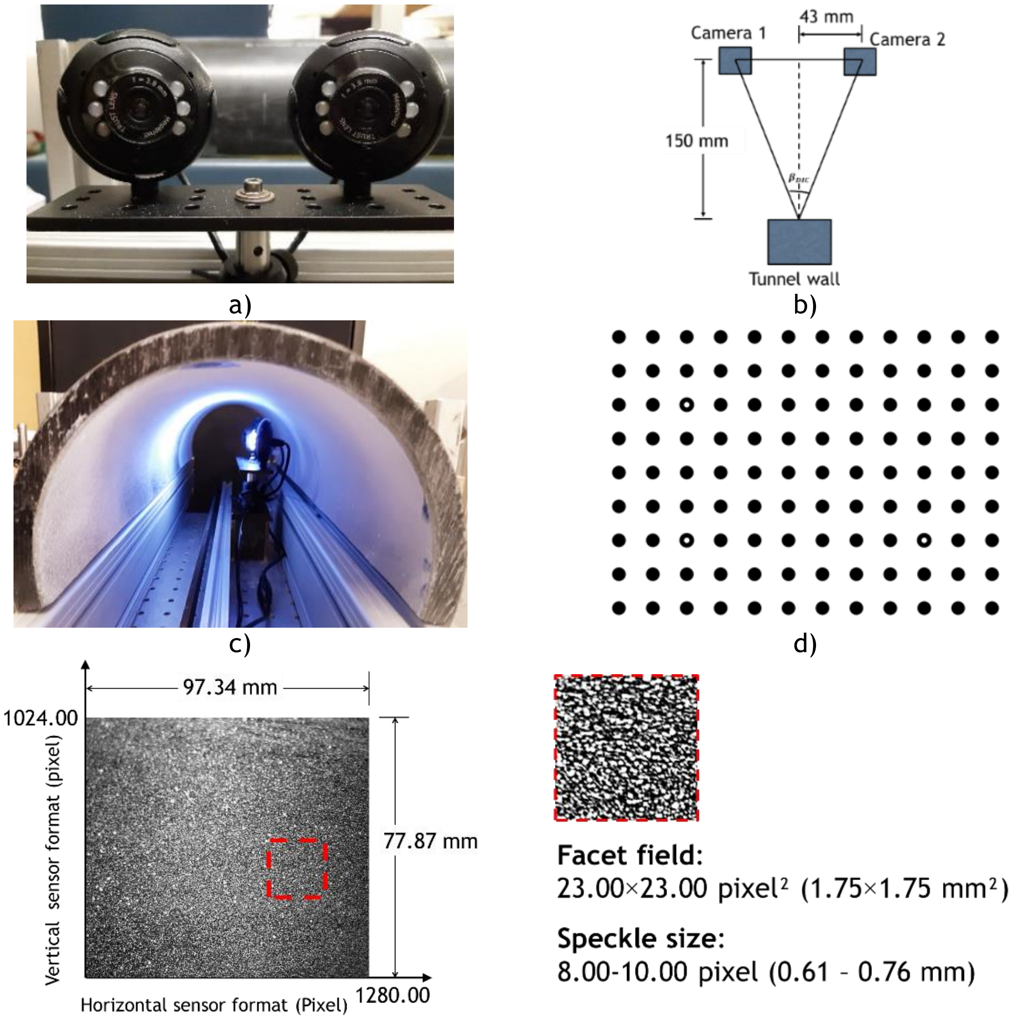

a) b) c) d) e) f)

Figure 4.12: The 3D DIC analysis: a) adopted DIC system, b) a schematic view of the system arrangement, c) cameras positioned in front of the interest region, d) calibration pattern, e) camera FOV with its dimensions and f) a facet field with the speckle pattern presentation.

Table 4.8: Key features of the webcam and the calibration solution adopted for the DIC analysis, loaded tunnel experiment.

Features	Information
Model	Trust SpotLight Pro Webcam with LED lights
Sensor resolution	1.3 megapixel (1280.0 x 1024.0 pixel^2)
Focus type	Manual
Others	Integrated dimmable LED lights for recording in low light conditions

The correctness degree of the DIC calibration

Calibration result	Camera 1	Camera 2
k_1	-0.146	-0.152
k_2	0.017	0.069
k_3	-0.093	-0.256
γ	-3.747	3.577
β_{DIC}	32.490°	

The obtained images of the initial and deformed state of the tunnel were analysed and displacement fields were monitored as depicted in Figure 4.13. Since DIC cameras were positioned in front of the interest region, so points E, F, G and H possess the same coordinates as the ones selected in the 3D LSS tests. The *x*-displacement variation on the nominated points is reported in Table 4.9 for both studies.

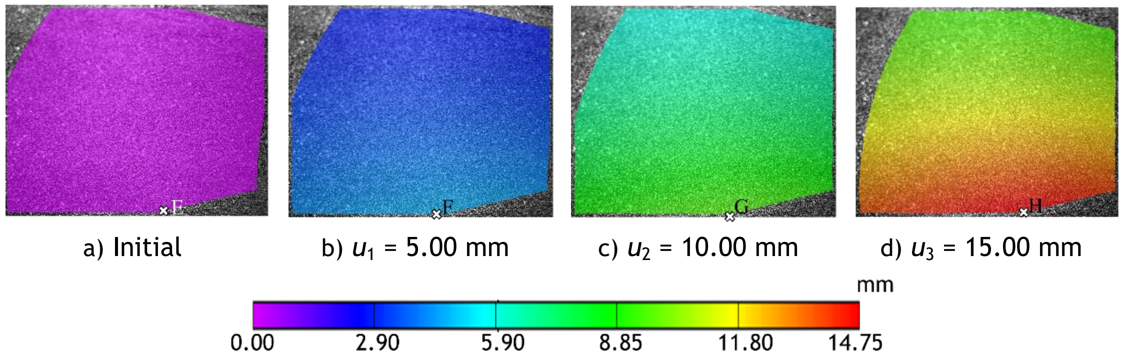
a) Initial b) u_1 = 5.00 mm c) u_2 = 10.00 mm d) u_3 = 15.00 mm

Figure 4.13: Displacement field obtained from the DIC analysis.

Table 4.9: *X*-displacement variation obtained for distinct displacement impositions, the LSS and the DIC.

Displacement	u_F	u_G	u_H
The 3D LSS (mm)	4.40	9.30	14.50
The 3D DIC (mm)	4.76	9.72	14.75
Difference* (%)	7.50	4.32	1.69

$^*100 \times |(u^{LSS} - u^{DIC})/u^{DIC}|$.

4.2.4 Tunnel containing notches

In this experiment, three distinct defects were created in different location of the tunnel. The inserted defects are shown in Figure 4.14. They have been created with a depth of $10\ \mathrm{mm}$ through the tunnel thickness. They were identified as horizontal, vertical and angled notches respecting z-direction. The latter one was oriented as 45 degree to the tunnel base. It aimed at detecting the corresponding defects where the tunnel was subjected to a compressive loading condition by means of a mechanism adopted for each experiment.

Therefore, to load the tunnel, a displacement enforcement was locally imposed in three stages. Concerning the horizontal and angled defects, it was accordingly enforced as $u_1 = 5\ \mathrm{mm}$, $u_2 = 10\ \mathrm{mm}$ and $u_3 = 15\ \mathrm{mm}$ on points P and R, see Figure 4.15-a) and -c) for the corresponding configurations. Besides, the loading mechanism for the mentioned notch experiment is shown in Figure 4.16-a). In the vertical defect case, tunnel was loaded on point Q with displacement impositions of $v_1 = 5\ \mathrm{mm}$, $v_2 = 10\ \mathrm{mm}$ and $v_3 = 15\ \mathrm{mm}$, as illustrated in Figure 4.15-b). The loading mechanism for this experiment is depicted in Figure 4.16-b).

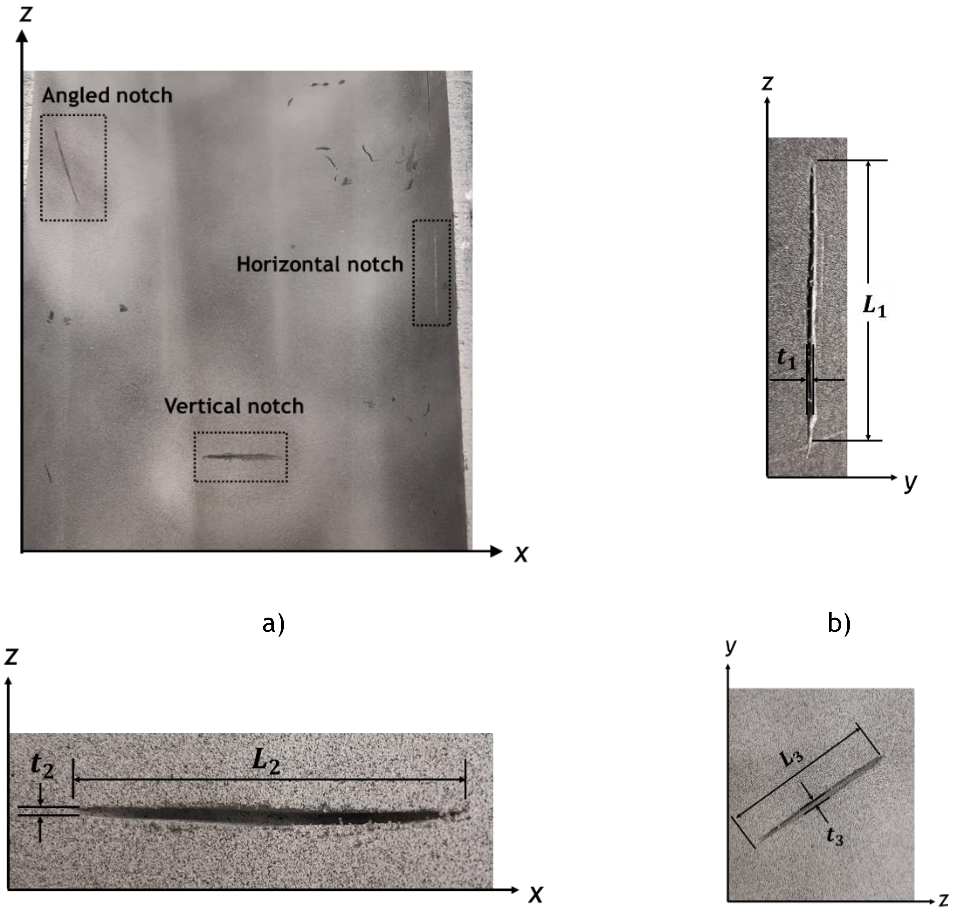

a)

b)

c)

d)

Figure 4.14: Defects built in the tunnel's interior wall, arranged respecting z-direction, a) a general 2D view of the tunnel wall with the notches, b) horizontal, c) vertical and d) angled notch.

Initially it must be checked whether geometric changes due to the presence of the defect could be detected by the system, by comparing the obtained LSS profile with the initial one, in which case it could be mechanically characterised through deformation measurement with the DIC, which was adopted to evaluate the deformation field in the reference and deformed tunnel states.

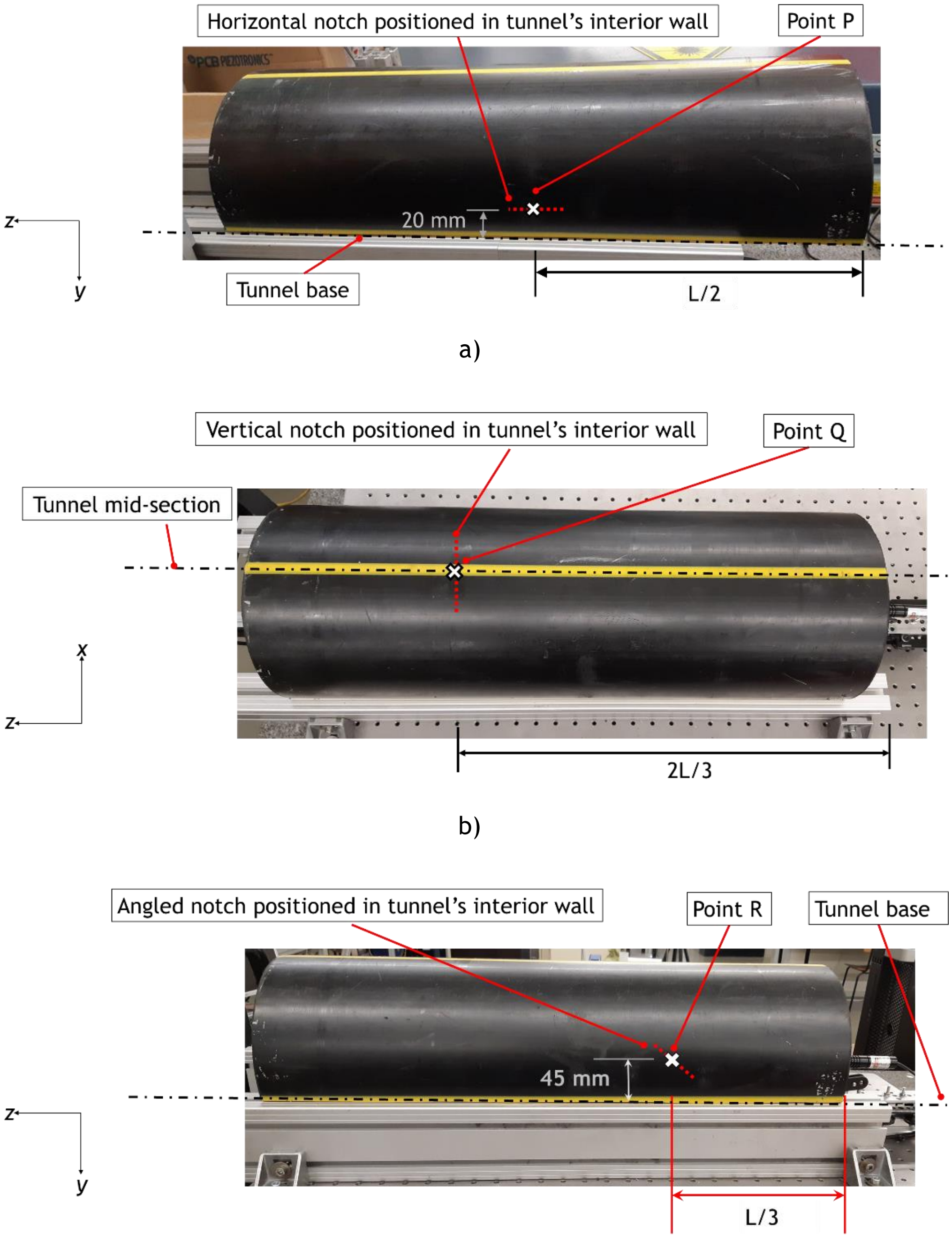

a)

b)

c)

Figure 4.15: Tunnel containing notch experiments, a) horizontal notch, b) vertical notch, c) angled notch configurations.

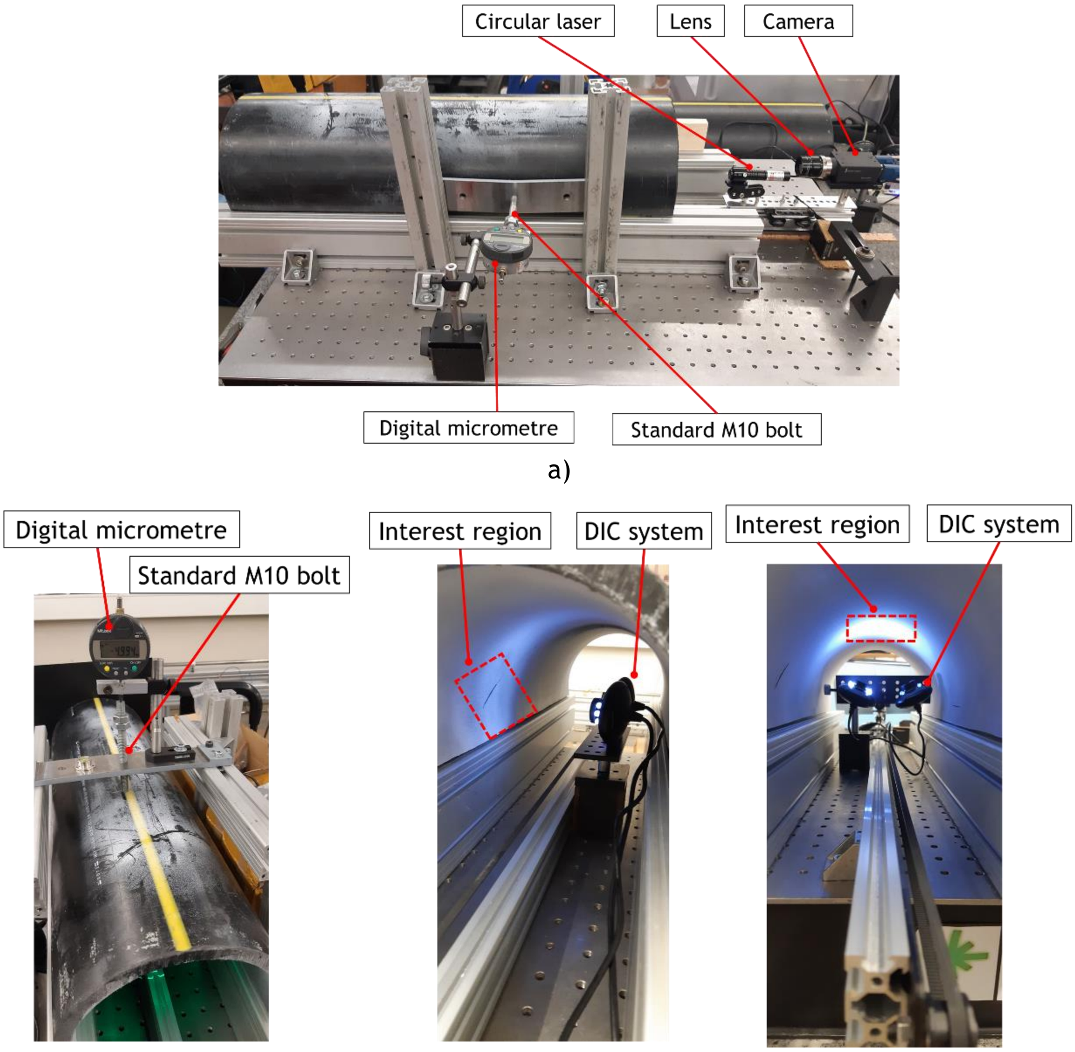

a)

b) c) d)

Figure 4.16: a) Loading mechanism adopted for horizontal and angled notches, b) loading mechanism for vertical notch, c) DIC system for horizontal and angled notches and d) DIC adopted for the vertical notch.

Experimental tests with the LSS were performed and re-done three times for each defect. Comparing the obtained profile, where the tunnel was loaded, to the original shape of the tunnel, notches were distinguished with the measured dimensions as reported in Table 4.10.

Table 4.10: Notch dimensions measured by LSS experiments compared to the real values.

Defect/dimension	***L***			***t***		
	Real (mm)	LSS_mean (mm)	Deviation * (%)	Real (mm)	LSS_mean (mm)	Deviation ** (%)
Horizontal notch	45.00	45.20	0.44	2.00	2.00	0.00
Vertical notch	50.00	49.33	1.34	3.00	2.96	1.33
Angled notch	35.00	34.95	0.14	2.00	1.99	0.50

$^{*}100 \times \left|L_{LSS\_mean} - L_{Real}\right| / L_{Real}$;
$^{**}100 \times \left|t_{LSS\_mean} - t_{Real}\right| / t_{Real}$.

Once the defects were identified and characterised, the 3D DIC analysis was performed, following the procedure explained in previous section. DIC cameras were positioned in front of the notch region of interest, to monitor the resulting deformation of the wall. For the horizontal and angled notches, the adopted 3D DIC system to monitor the deformation is shown in Figure 4.16-c). Concerning the vertical notch experiment, the system was set up as demonstrated in Figure 4.16-d). Notice that the calibration adopted for the analysis in the previous section, is still valid in this experiment, insofar as the lenses were not moved or refocused between experiments.

The DIC experiments were carried out in accordance with the loading condition previously described for each defect case. As a result for the vertical notch study, the displacement field perpendicular to the notch plane and the normal strain ε_{xx} and ε_{zz} were monitored in the interest region over the deformation period for different displacement impositions as revealed in Figure 4.17.

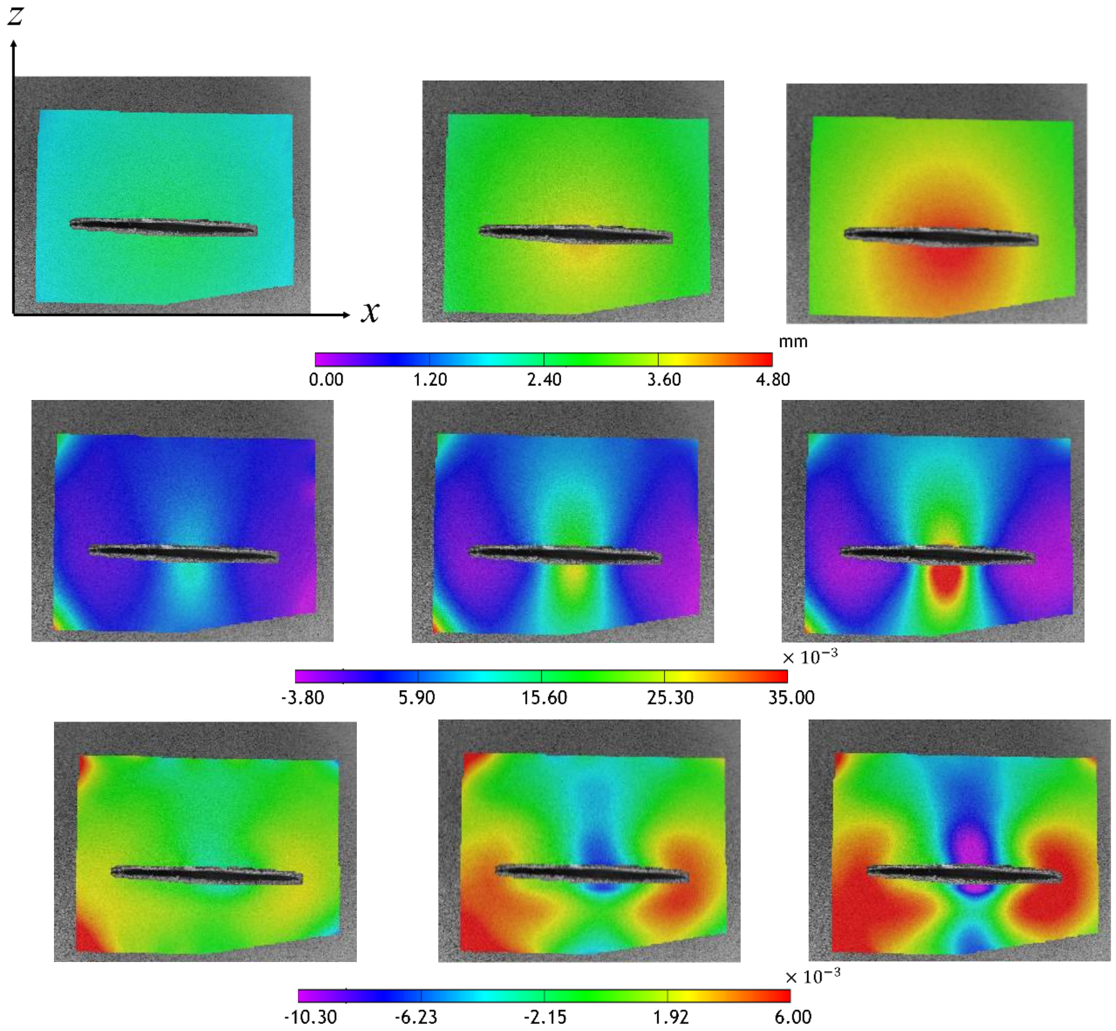

a) $v_1 = 5 \text{ mm}$ b) $v_2 = 10 \text{ mm}$ c) $v_3 = 15 \text{ mm}$

Figure 4.17: DIC results for the vertical notch loading experiment for different displacements: top row: y-displacement perpendicular to the notch plane; middle row ε_{xx}, and; bottom row ε_{zz}.

Regarding the angled notch, the *x*-displacement, normal to its plane, in addition to the strain evolution in *y*- and *z*-direction during the deformation period were extracted from the DIC analysis as exposed in Figure 4.18.

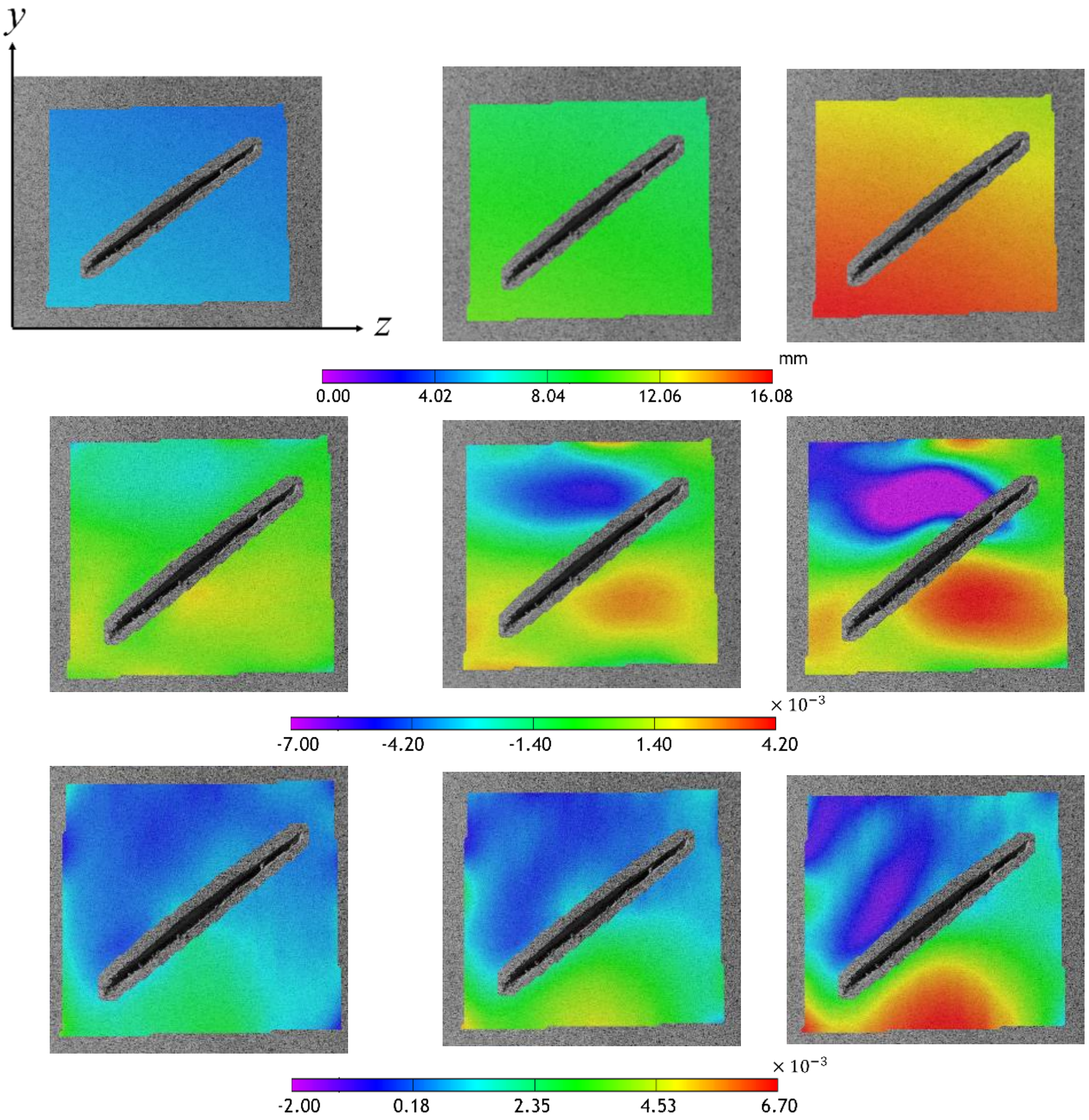

a) $u_1 = 5$ mm b) $u_2 = 10$ mm c) $u_3 = 15$ mm

Figure 4.18: DIC results obtained for the angled notch experiment measured for various displacement impositions, top row: *x*-displacement perpendicular to the notch plane; middle row ε_{yy}, and; bottom row ε_{zz}.

Concerning the horizontal notch experiment, a detail study is provided, since it is going to be considered as the example for numerical validation. From the LSS experiment, it was possible to extract the point cloud of the tunnel when loaded.

Figure 4.19 presents the tunnel profile showing the horizontal notch, and its coordinates are reported in Table 4.11.

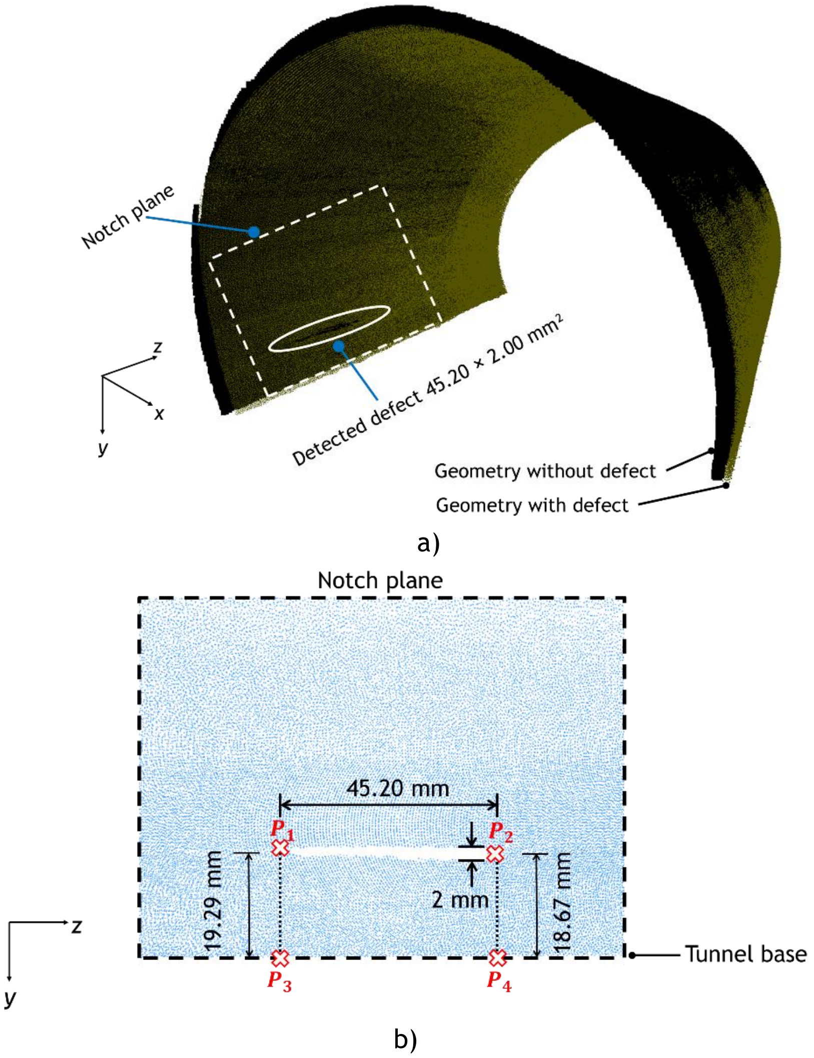

Figure 4.19: The LSS experiment extracted point cloud; a) profile with the detected horizontal defect and b) notch plane, points coordinates.

Table 4.11: Horizontal notch coordinates obtained from the LSS.

Point coordinates	P_1	P_2	P_3	P_4
x (mm)	-89.00	-89.62	-86.69	-87.62
y (mm)	38.06	39.16	57.13	57.72
z (mm)	381.92	427.11	383.73	427.46

Acquired details on the horizontal notch will be used in the numerical simulation. However, for this case study, x-displacement profiles correspond to each displacement imposition were evaluated in the notch plane by the DIC as shown in Figure 4.21 (top row profiles). Besides, it is possible to extract strain variations ε_{yy} and ε_{xx} as Figure 4.22 and Figure 4.23 show.

In order to validate the experimental results obtained from the DIC analysis, the horizontal notch experiment was considered as a potential case study. So, the obtained point cloud associated with the initial tunnel shape with defect, as presented in Figure 4.19, was transformed to a solid surface and imported to ABAQUS©. To perform a 3D analysis, the surface was extruded with the true thickness, $e = 14.80\ \mathrm{mm}$, see Figure 4.20-a). This analysis intends to obtain the numerical solution of proposed experimental methodology. Hence, the 3D deformable solid model was considered following the standard FEM formulation. Regarding the notch, it accounted for a depth of $10.00\ \mathrm{mm}$ through tunnel thickness to meet the real conditions. As Figure 4.20-a) depicts, the whole model was meshed with the 10-node quadratic tetrahedron FE elements (C3D10) respecting 601918 nodes and 428619 elements where the notch plane comprises 535348 and 380350 nodes and elements, respectively. The element size accordingly ranges between 1.25 and 20.00 mm in the notch plane and the rest of the model. The mechanical properties of the tested tunnel were used as $E = 200.00\ \mathrm{MPa}$ and $\upsilon = 0.45$.

According to the notch plane detail indicated in Figure 4.19-b), boundary conditions were defined. To satisfy the experimental and real conditions, point P was specified on the tunnel exterior wall adjacent to the notch plane with the same real position as revealed in Figure 4.20-b). The other side of the tunnel was fixed as a clamp condition, see Figure 4.20-a).

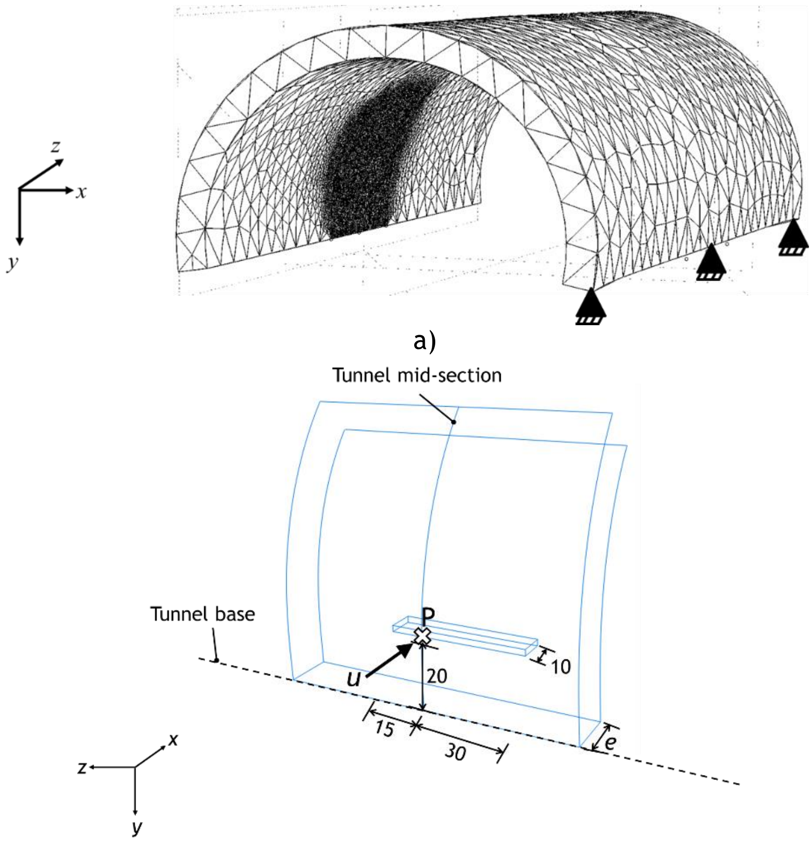

a)

b)

Figure 4.20: FE model of the horizontal notch study, a) a general view and b) displacement imposition illustration on the exterior wall adjacent to the notch plane.

Numerical simulation was performed for three distinct displacements enforced on point P and obtained displacement maps in x-direction are shown in Figure 4.21. Normal strain distributions were also extracted in the notch plane as illustrated in Figure 4.22 and Figure 4.23 for ε_{yy} and ε_{xx}, respectively.

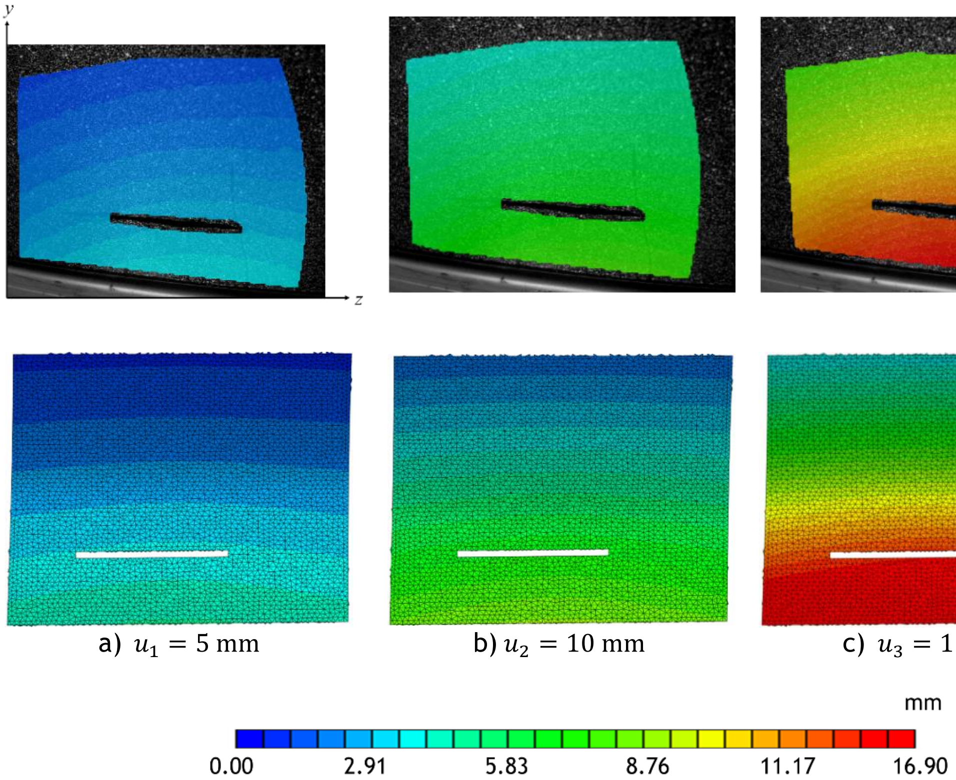

a) $u_1 = 5\ \mathrm{mm}$ b) $u_2 = 10\ \mathrm{mm}$ c) $u_3 = 15\ \mathrm{mm}$

Figure 4.21: Displacement profile in *x*-direction perpendicular to the notch plane, Top row extracted from the 3D DIC and bottom row derived from the FEM.

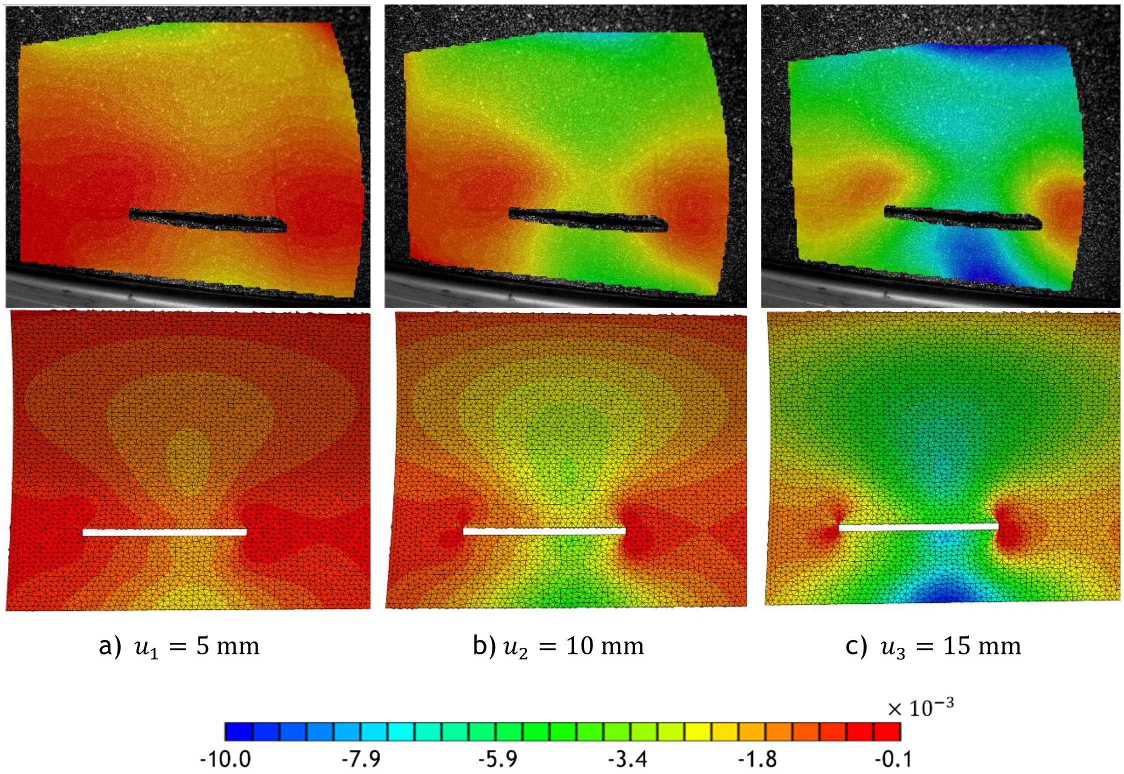

a) $u_1 = 5\ \mathrm{mm}$ b) $u_2 = 10\ \mathrm{mm}$ c) $u_3 = 15\ \mathrm{mm}$

Figure 4.22: Strain profile, ε_{yy}, evolution on the notch plane. Top row shows the deformation fields obtained with the 3D DIC and the bottom row shows the FEM results.

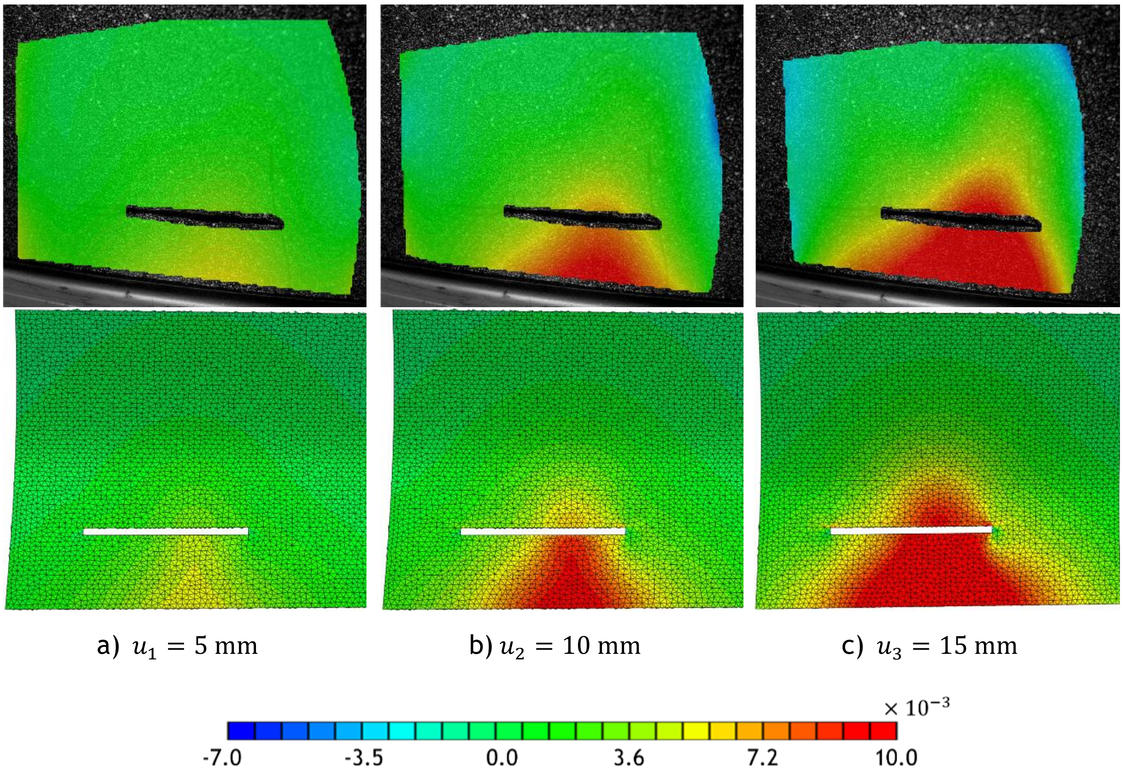

a) $u_1 = 5\ \mathrm{mm}$ b) $u_2 = 10\ \mathrm{mm}$ c) $u_3 = 15\ \mathrm{mm}$

Figure 4.23: Strain profile ε_{xx} evolution on the notch plane. Top row shows the deformation fields obtained with the 3D DIC and the bottom row shows the FEM results.

The acquired displacement profiles are smooth presenting a proper evolution of enforced displacements. Regarding the FEM results, there is an acceptable verification compared to the DIC ones. A closer view to the strain profile ε_{yy}, shows that the notch tip accounted for the maximum value, which is reasonable in accordance with the LEFM theory. Moreover, the strain profiles in *x*-direction prove that the strain distribution gets more intensive around the notch when the displacement imposition is greater. Overall, an acceptable agreement was obtained amongst the strain profiles derived from the DIC and FEM analyses in both shape and value. It can therefore be inferred that the proposed DIC solution is feasible and reliable leading to a validated numerical analysis.

It is valuable to draw a more precise numeric comparison between the results achieved from the FEM and the DIC on the tunnel model containing notch. The *x*-displacement and normal strains (ε_{xx} and ε_{yy}) were extracted on the auxiliary points P_a, P_b and P_c in the notch plane for both DIC and FEM domains, as demonstrated in Figure 4.24. Points P_a and P_b were positioned ahead of the notch tip with a gap of $g \cong 2.5\ \mathrm{mm}$ to guarantee the elimination of stress gradient effects. P_c was located nearly to the position of the displacement imposition enforced from the exterior wall.

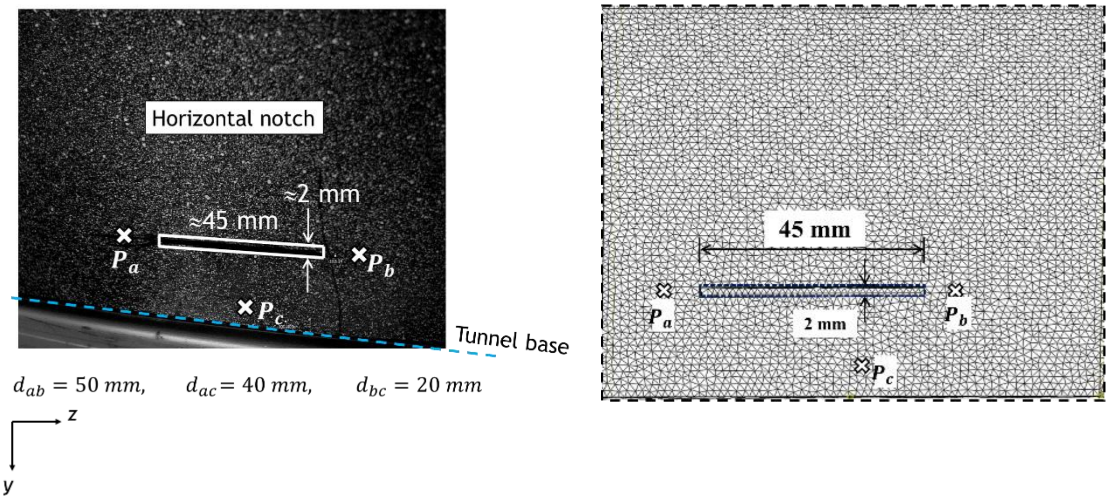

a) b)

Figure 4.24: Notch plane of the horizontal defect case study respecting the auxiliary points, a) DIC and b) FE model. These points are used to validate obtained results.

Table 4.12 reports the corresponding results gained from DIC and FEM where the tunnel subjected to various displacement impositions. Small deviations were derived amongst results.

Table 4.12: Assessment on acquired results from DIC and FEM, vertical notch experiment.

Variable	u_x			ε_{xx}			ε_{yy}		
				P_a					
	DIC (mm)	*FEM* (mm)	*Dev.* * (%)	*DIC*	*FEM*	*Dev.* § (%)	*DIC*	*FEM*	*Dev.* ¥ (%)
$u_1 = 5$ mm	4.64	4.62	0.37	7.35E-04	7.55E-04	2.80	-7.00E-04	-6.94E-04	0.81
$u_2 = 10$ mm	9.26	9.22	0.42	1.45E-03	1.49E-03	2.54	-1.16E-03	-1.15E-03	0.70
$u_3 = 15$ mm	14.53	14.57	0.29	2.41E-03	2.35E-03	2.51	-1.96E-03	-1.94E-03	1.33
				P_b					
	DIC (mm)	*FEM* (mm)	*Dev.* * (%)	*DIC*	*FEM*	*Dev.* § %	*DIC*	*FEM*	*Dev.* ¥ (%)
$u_1 = 5$ mm	4.84	4.82	0.31	7.92E-04	7.96E-04	0.52	-5.08E-04	-5.09E-04	0.14
$u_2 = 10$ mm	9.69	9.64	0.56	1.52E-03	1.53E-03	1.13	-1.21E-03	-1.21E-03	0.22
$u_3 = 15$ mm	15.18	15.16	0.18	2.55E-03	2.56E-03	0.36	-1.97E-03	-1.96E-03	0.48
				P_c					
	DIC (mm)	*FEM* (mm)	*Dev.* * (%)	*DIC*	*FEM*	*Dev.* § (%)	*DIC*	*FEM*	*Dev.* ¥ (%)
$u_1 = 5$ mm	5.31	5.33	0.44	3.79E-03	3.82E-03	0.55	-2.19E-03	-2.18E-03	0.29
$u_2 = 10$ mm	10.62	10.60	0.18	7.81E-03	7.80E-03	0.17	-4.24E-03	-4.25E-03	0.27
$u_3 = 15$ mm	16.69	16.72	0.14	9.89E-03	9.81E-03	0.62	-6.62E-03	-6.68E-03	1.04

* $100 \times |(u_x^{FEM} - u_x^{DIC})/u_x^{DIC}|$;

§ $100 \times |(\varepsilon_{xx}^{FEM} - \varepsilon_{xx}^{DIC})/\varepsilon_{xx}^{DIC}|$;

¥ $100 \times \left|(\varepsilon_{yy}^{FEM} - \varepsilon_{yy}^{DIC})/\varepsilon_{yy}^{DIC}\right|$.

In the present section, experiments were successfully conducted on several tunnel states to extract the tunnel's 3D profile: initial; feature attachment; loaded, and notch inclusion. According to acquired geometries, feature and defects were identified in addition to the deformation variation that the tunnel experienced over a loading condition. At a second-stage inspection solution, the detected defects have been mechanically characterised by means of an optical NDI tool based on the 3D DIC to measure displacement and strain fields. One of the tunnel models containing a notch has also been resolved using the FEM formulation to draw a comparison amongst internal fields.

Overall, the acquired displacement contours are smooth presenting an appropriate evolution of the enforced displacements. Regarding FEM results, there is an acceptable verification compared to the DIC solutions. A closer view to the strain profile ε_{yy}, it can be concluded that the notch tip accounted for the maximum value, which is reasonable in accordance with the LEFM theorem. Moreover, the strain profiles in x-direction put into evidence that strain distribution becomes more intensive around the notch when the displacement imposition is superior.

The next section focuses on the implementation of the deployed 3D LSS on a real case by modelling an additive manufactured tunnel. It aimed at documentation of the tunnel shape and monitor the deformation by means of the developed 3D DIC. The results have been already published in [175].

4.3 Real tunnel experiments on a scale model

This section describes the analysis of a scaled model of a shallow rock tunnel, "*Monte Seco tunnel*" in Vitoria Minas Railway in Brazil. Cacciari and Futai [176]-[178] have already studied this tunnel to characterize the rock discontinuities using a 3D Terrestrial Laser Scanning (TLS) system (Faro Focus 3D laser scanner). Several analyses were carried out on the acquired tunnel's point cloud generated by the 3D TLS led to determine the importance of the occlusion's geometries. As reported, due to the complex geometry of the irregular rock face, there might exist some occlusion zones over the scanning procedure, hence special care must be considered during orientation mapping to avoid sampling planes with limited exposures.

The obtained point cloud of the corresponding tunnel acquired by TLS, with its geometrical characteristics, is shown in Figure 4.25. The point set consists of 308620 vertices, after applying a homogenous density reduction process.

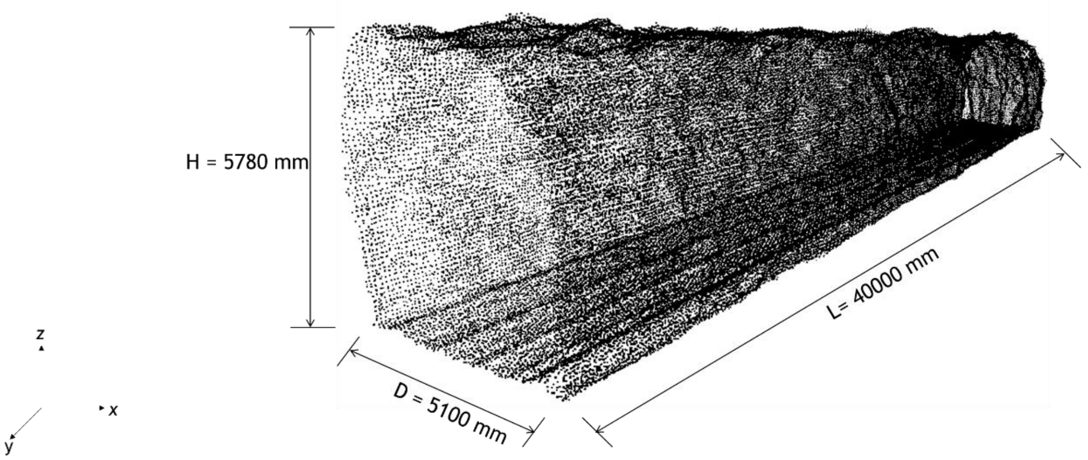

Figure 4.25: Point cloud of Monte Seco tunnel scanned by the 3D TLS technique.

Relying on the developed 3D LSS, which has been already implemented in the scaled tunnel (tunnel prototype), it would be valuable to adopt the built system to perform experiments on Monte Seco tunnel to acquire its profile. This experiment contributes to assess the performance and robustness of the deployed inspection system.

Therefore, the experiment is executed on the tunnel model to obtain its shape and then load it by way of a displacement imposition from the exterior tunnel's wall and then capture the deformation and eventually make a comparison between the reference and the deformed shapes. The 3D DIC will be also adopted to monitor the displacement field upon the deformation period.

4.3.1 Geometry acquisition by the 3D LSS

The point cloud acquired by the TLS was used to produce a 3D physical model of a part of the tunnel by means of the 3D printing. To accomplish this task, a shell surface has been initially constructed by triangulating the point cloud as shown in Figure 4.26. The tunnel was then built by additive layers in a 3D printer.

The material used to build the model was Polylactic Acid (PLA) with the material properties reported in Table 4.13. To meet the laboratory scale facilities, dimensions of Monte Seco tunnel, $L = 40000\ \mathrm{mm}$, $D = 5100\ \mathrm{mm}$ and $H = 5780\ \mathrm{mm}$, were scaled down by a factor of 34. Therefore, the fabricated model was dimensioned as $L^{real} = 200\ \mathrm{mm}$, $D^{\,real} = 150\ \mathrm{mm}$ and $H^{real} = 170\ \mathrm{mm}$ with a layer thickness (tunnel thickness) of $0.25\ \mathrm{mm}$, as shown in Figure 4.27-b), at a nominal temperature of $210\ ^{\circ}\mathrm{C}$. Notice, only a length of $6800\ \mathrm{mm}$ of the real tunnel was considered here, because this part was significant.

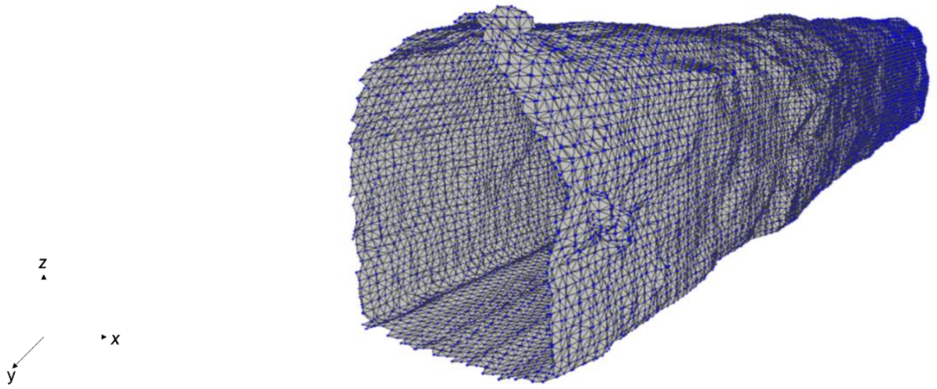

Figure 4.26: Generated 3D surface of the point cloud, Monte Seco tunnel.

Table 4.13: Material properties of the PLA used for the 3D printing.

Property	Value
Tensile strength	61 - 66 MPa
Flexural strength	48 - 110 MPa
Melt temperature	157 - 170 °C
Typical injection molding temperature	178 - 240 °C

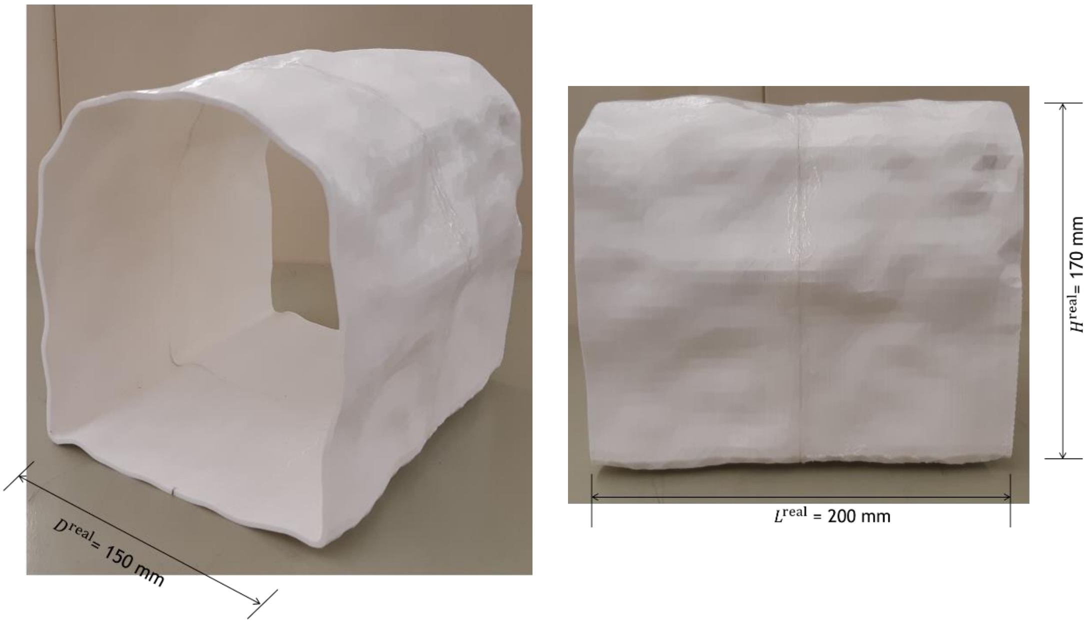

a) b)

Figure 4.27: Additive manufactured tunnel model, a) a general view of the tunnel and b) a side view with its real dimensions.

The LSS system was implemented to perform the image acquisition. In this example, the optical instruments were the same as the ones used in the scaled tunnel benchmark, (Section 4.2). The inspection system was built in the laboratory as can be seen in Figure 4.28. The system was calibrated using a checkerboard as shown in Figure 4.4-a) and then a set of images was captured. The calibration results are reported in Table 4.14.

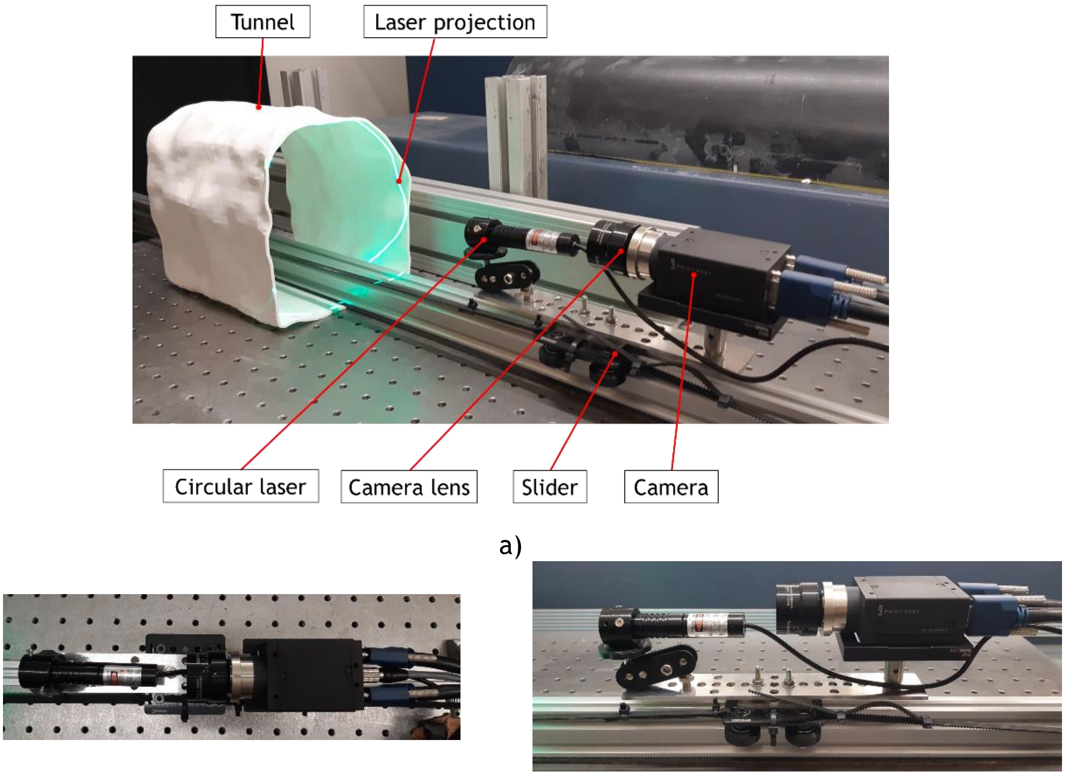

a)

b)

c)

Figure 4.28: The developed 3D LSS for the real tunnel shape acquisition, a) a general view of the components, b) top view and c) side view of the system.

Table 4.14: Calibration results for the real (additive manufactured) tunnel example.

Camera calibration			**Circular laser calibration**			
				x (mm)	y (mm)	z (mm)
Intrinsic parameters	α	3086.04	**Laser position**	5.25	17.02	124.40
	β	3089.16				
	γ	-0.61				
	u_0	1024.99				
	v_0	1064.67				
Radial Distortion	k_1	-2.52E-01	**Laser axis**	2.55E-02	9.60E-03	9.99E-01
	k_2	7.59E-01				
	k_3	-2.90E+00				
Tangential Distortion	p_1	-1.85E-06	**Aperture, φ**		-26.06 °	
	p_2	-1.09E-06				
Mean re-projection error			**MRE**		0.42 pixel	

Image acquisition to obtain the tunnel geometry has been performed with a linear velocity of $V_z = 57.49\ \mathrm{mm/s}$ with a camera framerate of $f_s = 100.00\ \mathrm{fps}$. Therefore, a total number of 350 images was captured with a system resolution equal to $0.57\ \mathrm{mm/frame}$. Due to the tunnel's complex geometry, consisting of several protruded triangles, and in order to avoid occlusions, two acquisitions have been executed: the tunnel was initially scanned in the state as shown in Figure 4.28-a), denominated status 1, and then it was turned around and another acquisition was performed, which was dubbed status 2. The full tunnel shape geometry was obtained by merging the attained point clouds from status 1 and 2. To facilitate the merging process, some pieces of cork have been attached on the tunnel exterior wall. They have been used later on the geometry fusion, see Figure 4.29-a). Moreover, Figure 4.29-b) and –c) show the obtained point clouds in both scanning states. The achieved point clouds comprise of a total number of 3640784 and 3844408 vertices for the status 1 and 2, respectively. As expected, in each acquired point cloud, there are several regions, particularly on the sidewalls, facing the occlusion phenomenon and thereby the information on the tunnel geometry has been missed on those regions. Thus, they must be aligned and fused to acquire the full tunnel geometry.

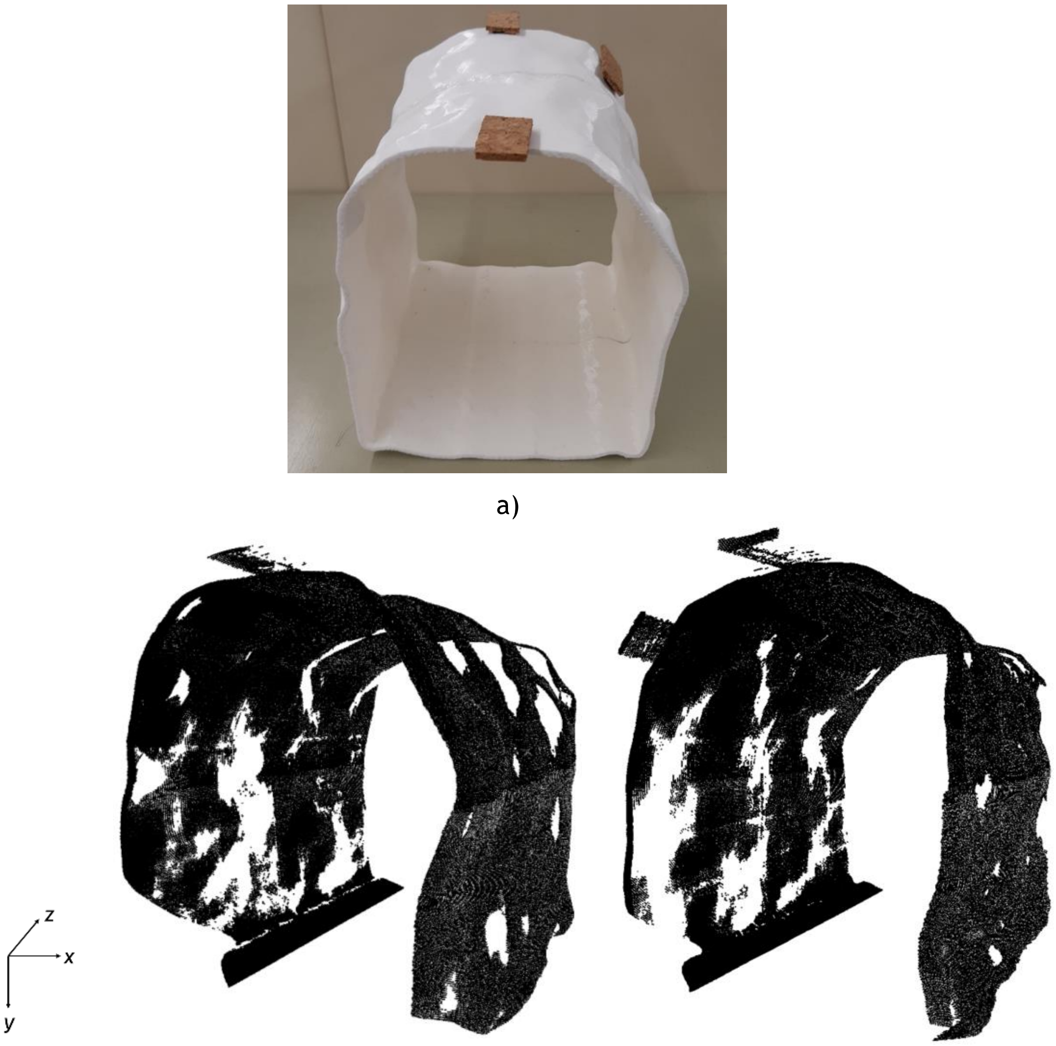

a)

b)

c)

Figure 4.29: The LSS image acquisition, a) the tunnel marked with the corks, b) the obtained point clouds in status 1 and c) status 2.

The merged point cloud of the scanned tunnel included 6919025 vertices. The cork reference objects were eliminated from the point set which was then simplified by decimating to obtain the final point cloud comprising 24841 points, as illustrated in Figure 4.30-a) and –b), respectively. The fused point cloud put into evidence that most of the missed regions have been recovered and the merged geometry includes some small regions lacking the geometrical properties.

A comparison was drawn on the tunnel dimensions between the real model (additive manufactured model) and results obtained from the 3D LSS as Table 4.15 reports. A small difference was discovered between both amounts, which supports the conclusion that the applied methodology is robust.

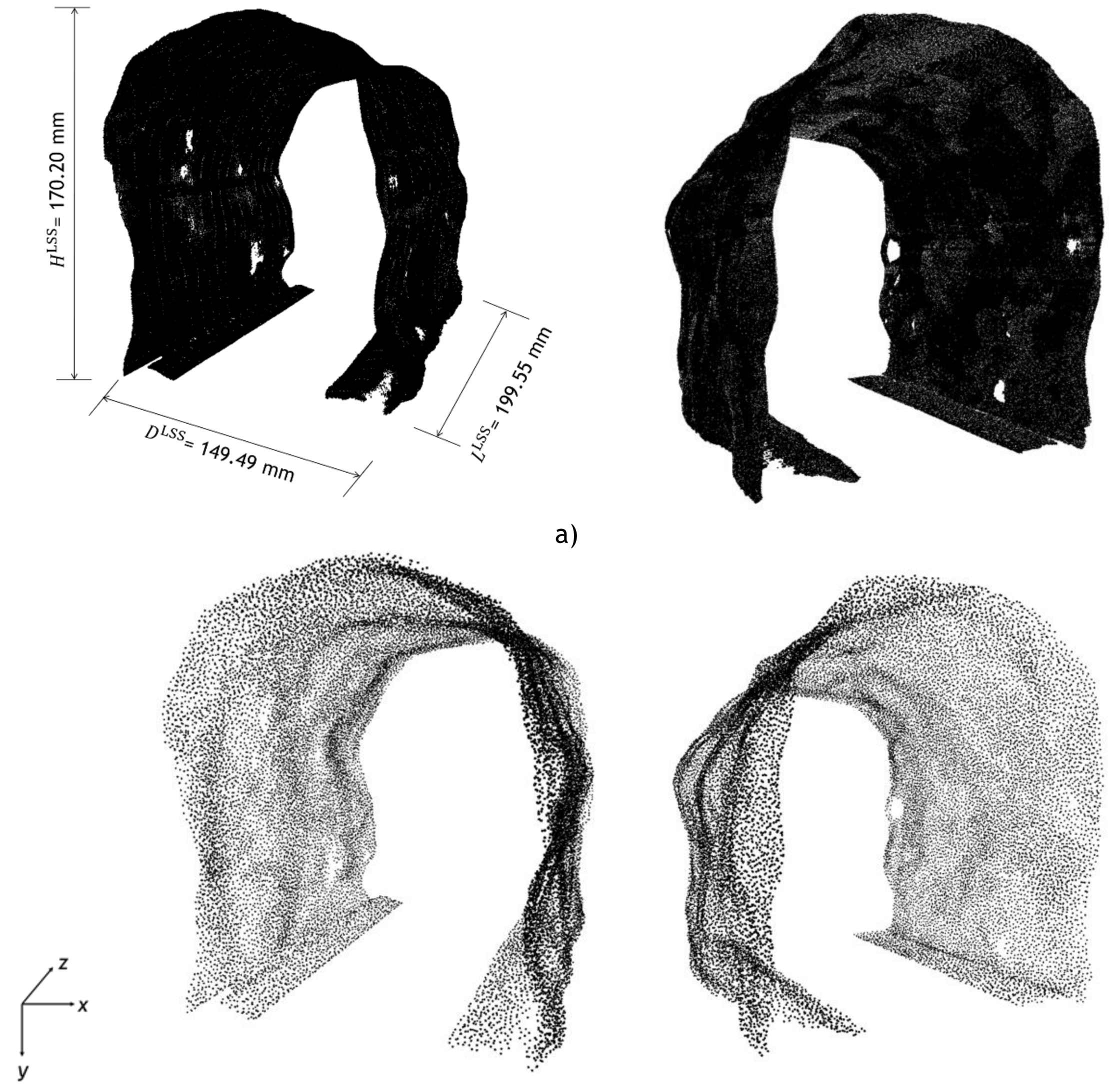

a)

b)

Figure 4.30: a) The obtained point cloud of tunnel from the LSS with its geometrical properties and b) the reduced point cloud.

Table 4.15: Comparison on tunnel dimensions, real tunnel model.

Dimension	*L* (mm)	*D* (mm)	*H* (mm)
Real (printed)	200.00	150.00	170.00
Obtained from LSS	199.55	149.49	170.20
Absolute deviation* %	0.23	0.34	0.12

$*100 \times \left|\left(value^{\text{LSS}} - value^{\text{real}}\right)/value^{\text{real}}\right|$.

Overall, the results infer that the developed 3D LSS is efficient and accurate to monitor a real rock tunnel with complex geometrical characteristics. Moreover, from the experimental point of view in the real case, it can be concluded that a 3D LSS can be installed in the train front, and another one positioned at the train end, and while the train is passing through the tunnel, both systems are scanning the tunnel simultaneously to uncover the regions with steep changes in geometry that remain occluded to the camera in a single passage. This experimental consideration contributes to minimize the number and size of occlusion areas.

4.3.2 Deformation experiment by the LSS and DIC

This section reports the results from the deformation experiment performed on the additive manufactured tunnel [175]. The loading apparatus is the same as described in Section 4.2.3, however, Figure 4.31-a) shows the mechanism employed in this experiment. As presented in this figure, a compressive displacement was imposed on point P located on the tunnel's external surface; details on point P are represented in Figure 4.31-b).

To obtain comparable solutions, a contactless measuring tool was developed relying on the 3D DIC where the displacement field was monitored during the deformation period. The DIC configuration and setup considerations followed the previously published works by the authors [3], [160], [161], [163].

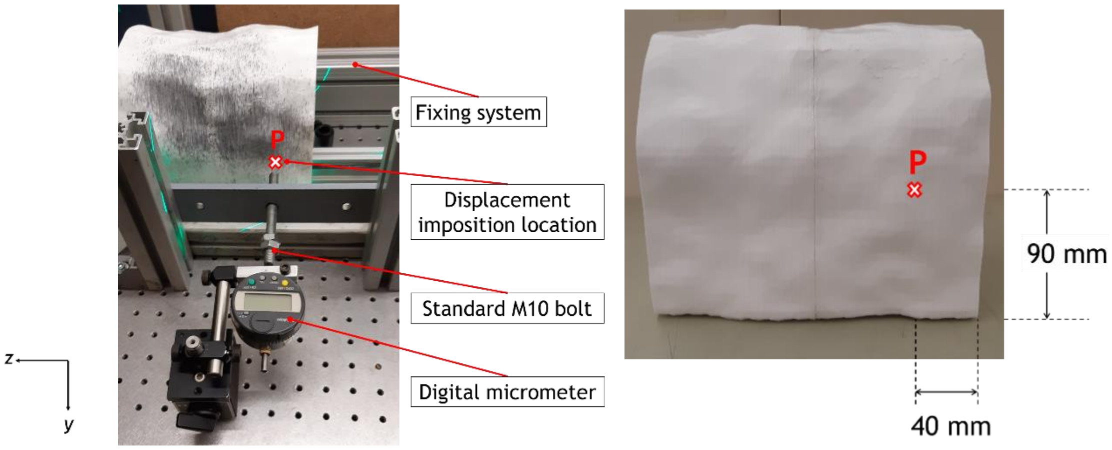

a) b)

Figure 4.31: a) Compressive loading mechanism imposed by a displacement enforcement on point P and b) details on Point P.

The developed 3D DIC system entails two $1.3\ \mathrm{MP}$ Spotlight Pro cameras with key features reported in Table 4.8. An interest region dimensioned as $90.0 \times 150.0\ \mathrm{mm}^2$ was sprinkled by black dots of adequate size, to generate an appropriate random speckle pattern for the measurement task. Figure 4.32-a) illustrates a general view of the deformation experiment performed on the tunnel including both the 3D LSS and the 3D DIC systems with the interest region sketch in Figure 4.32-d). Figure 4.32-b) represents a schematic perspective of the adopted 3D DIC system for the deformation experiment. The speckle pattern on the interest region positioned in the interior wall of the tunnel in front of the DIC camera is also shown in Figure 4.32-c). Regarding the LSS calibration, it must be noted that the previous calibration performed in section 4.3.1 is valid for the deformation test.

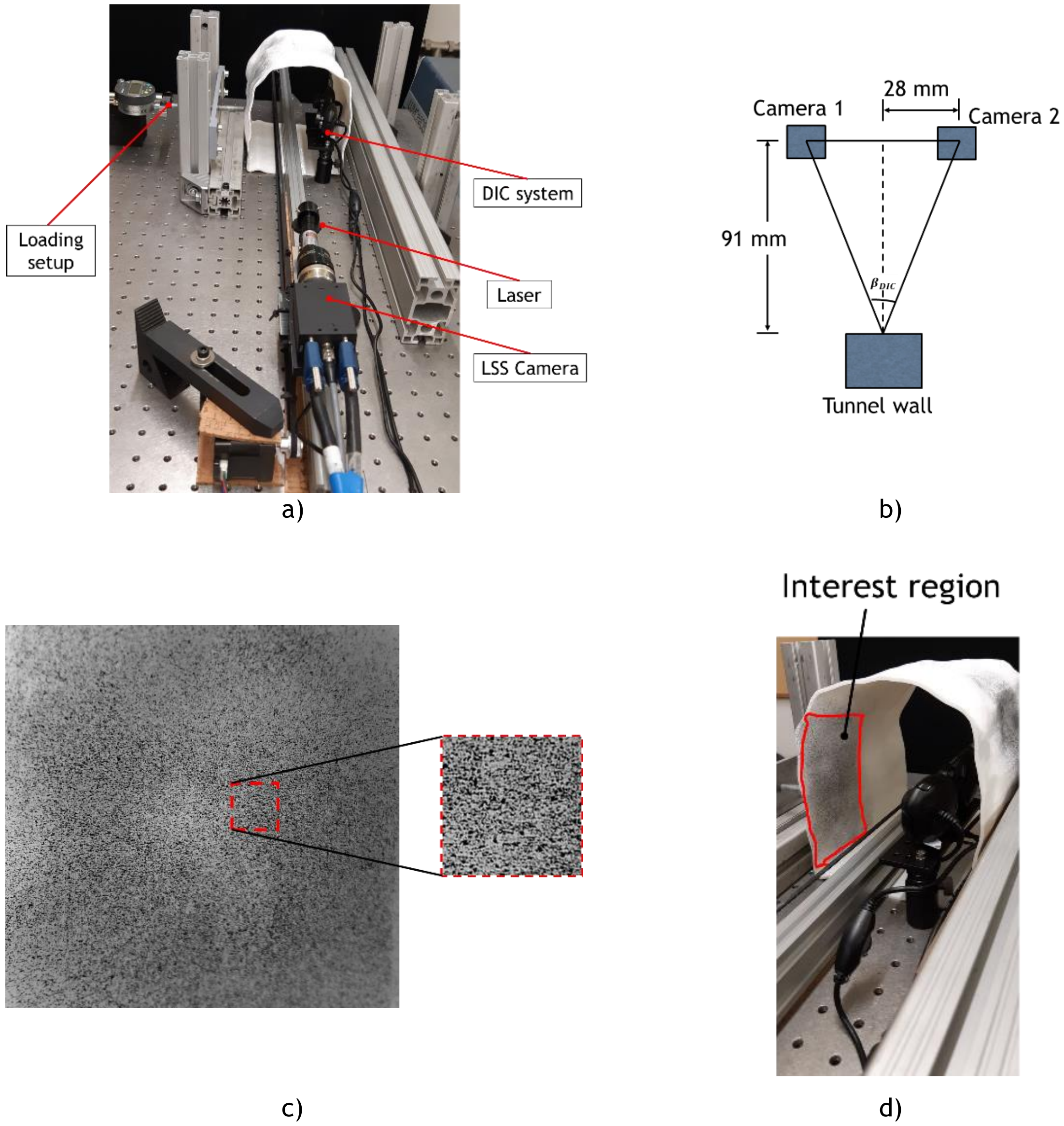

Figure 4.32: a) A general view of deformation experiment respecting the LSS and DIC systems, b) a schematic view of DIC system, c) speckle pattern respecting a-21×21-pixel^2 facet field and d) the DIC system standing in front of interest region where loading is applied.

The experiments have been performed in the following order:

a) Reference state of the tunnel acquired by the LSS to obtain the original profile;

b) Reference state of tunnel captured by the DIC to achieve reference solution;

c) Maintaining the DIC system in the tunnel, the loaded state of the tunnel was captured by the DIC to achieve the deformed solution;

d) The DIC system has been removed and the deformed state was captured by the 3D LSS.

Following the steps mentioned above, the deformation experiment has been completed. Prior to proceeding to step b), the DIC system was calibrated using a 12.0-by-9.0 dot calibration pattern spaced as $2.5\ \mathrm{mm}$ and then it was analysed in VIC-3D-2012© software considering the second order distortion and calibration results are reported in Table 4.16.

The tunnel was loaded by a displacement imposition on Point P with a magnitude of $\bar{u}(x, y, z) = 11.50\ \mathrm{mm}$. The reference and deformed profiles of the tunnels captured by the 3D LSS are demonstrated in Figure 4.33 in which both original and simplified point clouds have been presented. Since it was only possible to make the image acquisition in one direction (due to the loading mechanism), obtained tunnel profiles lacked data in some regions due to occlusions.

Table 4.16: Correctness degree of DIC calibration, real additive manufactured tunnel.

Calibration result	Camera 1	Camera 2
k_1	-0.15	-0.14
k_2	-0.00	-0.02
γ	-1.47	2.57
β_{DIC}	-34.42°	

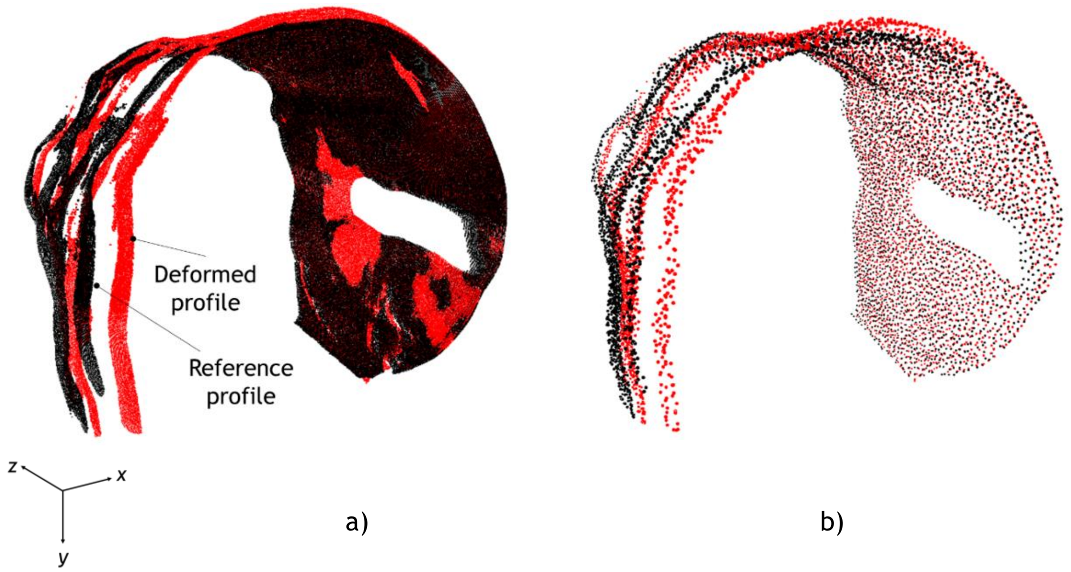

a)

b)

Figure 4.33: A 3D view of the reference and deformed profile of the tunnel obtained by the LSS, a) original and b) simplified point clouds.

Moreover, reference and deformed shapes of the tunnel have been also captured on the deformed plane by the 3D DIC, as shown in Figure 4.34. The captured images were thereby processed considering a subset and step size of 21 and 6 pixels, respectively.

Three diverse sections have been marked on the tunnel's interior wall contributing to have a comparison between the displacement fields acquired from the LSS and DIC analyses. As shown in Figure 4.34-a), points R_i were defined in the reference state on the DIC problem domain. It must be remarked that the displacement imposition ($\bar{u}$) has been applied on R_3 from the exterior wall. On the other hand, points L_i are associated with the deformed projection of former points. Table 4.17 reports coordinate of selected points in DIC domain. Also, the *x*-displacement variation captured on selected points is thus reported in Table 4.17.

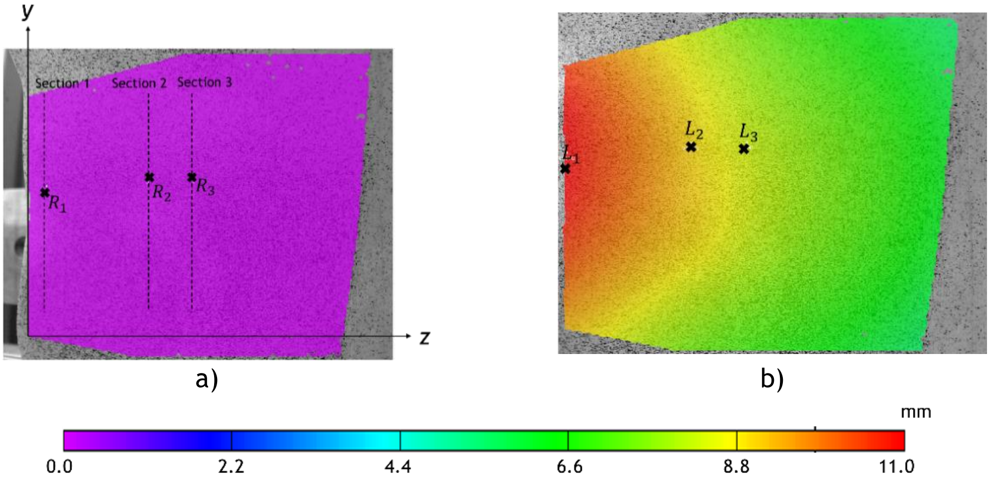

a)

b)

Figure 4.34: X-displacement field obtained from DIC analysis for a) reference, b) deformed status; $\bar{u} = 11.5\ \text{mm}$.

Table 4.17: Points coordinate related to different sections defined on DIC problem domain.

Section	Points	x (mm)	y (mm)	z (mm)
1	R_1	-6.4	34.2	4.8
2	R_2	-9.5	34.2	29.2
3	R_3	-9.6	33.5	39.7
		x-displacement variation *		
		$u_1 = 11.3\ \text{mm}$	$u_2 = 9.1\ \text{mm}$	$u_3 = 8.3\ \text{mm}$

* $u_i = x_{L_i} - x_{R_i}$.

One-frame-point cloud related to the defined sections (section 1, 2 and 3) was extracted. This aimed at evaluating the accuracy of the developed LSS by comparing displacement fields on the nominated points in different sections.

Owing to the marks attached to the tunnel’s interior wall prior to the image acquisitions, it is feasible to detect the interest points, R_i and L_i, in the corresponding one-frame-point cloud associated to each section. Figure 4.35 presents the point cloud of the reference and deformed shapes acquired by the 3D LSS in different sections. Table 4.18 reports the comparison on the *x*-displacement variation in distinct sections obtained by both studies.

Table 4.18: Comparison on the displacement variation obtained from DIC and LSS studies.

Section	Method		Deviation (%) *
	DIC	LSS	
1	$u_1 = 11.3\ \text{mm}$	$u_1 = 11.5\ \text{mm}$	1.8
2	$u_2 = 9.1\ \text{mm}$	$u_2 = 9.0\ \text{mm}$	1.1
3	$u_3 = 8.3\ \text{mm}$	$u_3 = 8.5\ \text{mm}$	2.4

$*100 \times \left|(u_i^{LSS} - u_i^{DIC})/u_i^{DIC}\right|$.

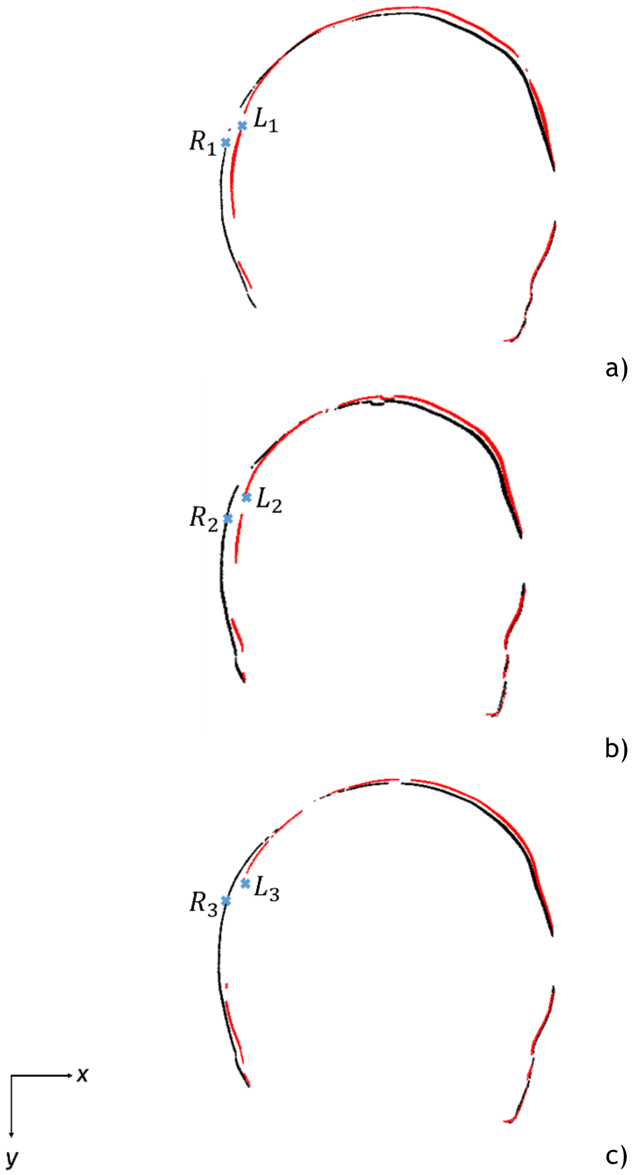

━	Reference profile
🟥	Deformed profile

	Coordinates		
	x (mm)	y (mm)	z (mm)
R_1	-55.5	-10.8	272.9
L_1	-44.0	-12.9	250.5
Deformation	$u_1 = 11.5\ \mathrm{mm}$		

	Coordinates		
	x (mm)	y (mm)	z (mm)
R_2	-53.5	-18.3	274.9
L_2	-44.5	-14.2	252.7
Deformation	$u_2 = 9.0\ \mathrm{mm}$		

	Coordinates		
	x (mm)	y (mm)	z (mm)
R_3	-49.0	-23.1	270.9
L_3	-40.5	-25.4	257.2
Deformation	$u_3 = 8.5\ \mathrm{mm}$		

Figure 4.35: One-frame-point-cloud extraction on different sections as described in the DIC analysis, a) section 1, b) section 2 and c) section 3.

According to the accomplished results from both studies, it can be inferred that the deployed LSS has the potential to produce accurate results both in the geometry reconstruction and in the deformation analysis with a robust accuracy. On the other hand, the adopted DIC system was successfully implemented to monitor deformation variations on a tunnel submitted to a compressive load. It can be concluded that both developed optical techniques were efficient and cost-effective and objectives of the present study were encouragingly fulfilled.

The coupling of the LSS and DIC has a great potential for tunnel convergence measurement and monitoring over time (Figure 4.34 and Figure 4.35). After tested in a real tunnel environment, this method can be used for monitoring tunnels of any geometry, including the acute-irregular shapes from exposed rock faces, such as tested herein in laboratory scale, smooth-irregular shapes from shotcrete, and regular shapes from structural concrete liners.

In the next section, the built 3D demonstrator associated to the LSS is used on a demanding field experiment model to acquire an interior surface shape of a wind tower section as published in [179].

4.4 Field application, Wind tower experiment

This section is devoted to the field application of the established laser scanning system. Hence, a section of a cylindrical wind tower manufactured by Tegopi Company has been considered as the testing model. The tower was made of S355J0 Steel sheets and its fabrication followed the roll bonding process of sheets and then welding the abutted rolled sheets together. It aimed at acquiring the tower interior wall profile by means of the designed demonstrator.

During fabrication, the tower might experience some plastic deformation in welded joints, which may occur due to the imperfect welding process on joints or even the tower own weight. Mechanically, this can result in a build-up of residual stress and geometrically the fabricated tower will not possess the required geometry. The LSS allows to scan the tower's interior surface, enabling detection of geometrical changes and location and plastic deformation measurement which occurred because of mentioned reasons. Thus, this deployed LSS is advantageous and would assist to tower fabrication industry to correct geometrical changes due to deformation.

4.4.1 Model Definition and system setup

A 9-meter-long section of a cylindrical tower has been considered as shown in Figure 4.36. The tower's inner diameter was reported by the company as $D_i \cong 4177\ \mathrm{mm}$. This section was constructed by three parts, with different length, joining by means of circular seam welding. In this experiment, the middle part has been inspected with a total length of $3000\ \mathrm{mm}$.

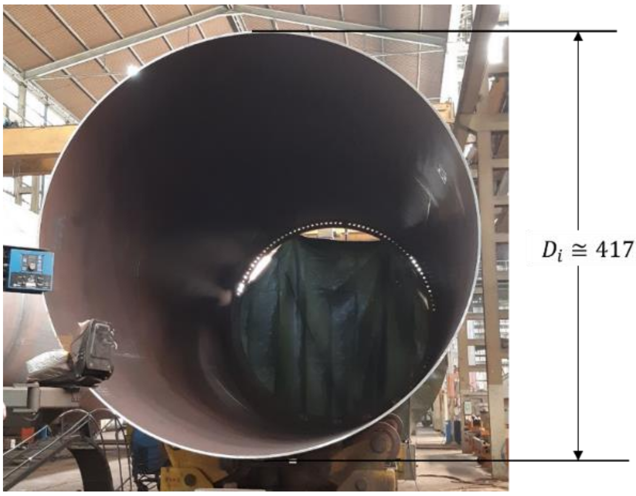

Figure 4.36: A-9-meter-long cylindrical wind tower, field experiment; Tegopi Company.

As shown in Figure 4.37-a), the LSS system equipped with a 2.0 MP CMOS camera with the technical specifications presented in Table 4.19, has been assembled on a 1000 mm long 20-by-20-mm^2 Bosch profile. It was designed to mount on the welding robot's arm moving inside the tower with an adjustable altitude, see Figure 4.37-b).

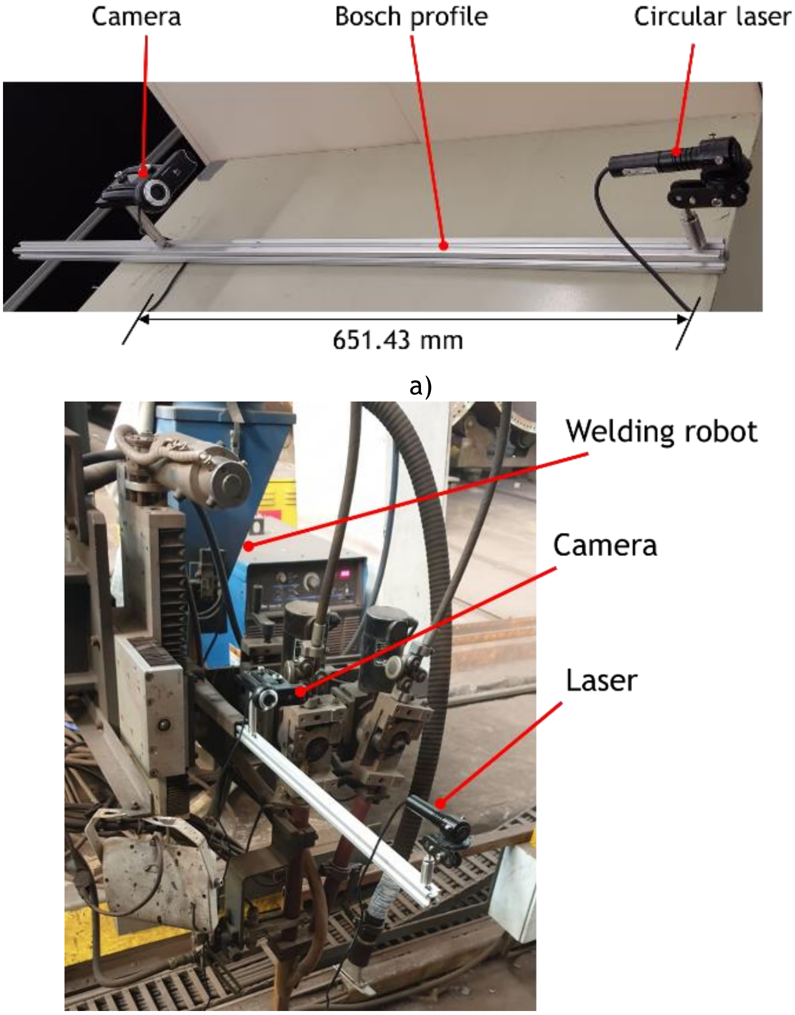

a)

b)

Figure 4.37: a) Adopted LSS for tower experiment and b) system mounted on the welding robot's arm.

The system has been calibrated based on the Zhang's formulations described in previous examples (see Appendix A for the governing formulations). A-9-by-8-calibration pattern spaced as 80 mm was used to proceed the calibration procedure. A series of images was captured on the calibration pattern with the laser projected on. Figure 4.38 depicts the calibration, laser and camera positions. Camera and laser calibration results are therefore outlined in Table 4.19.

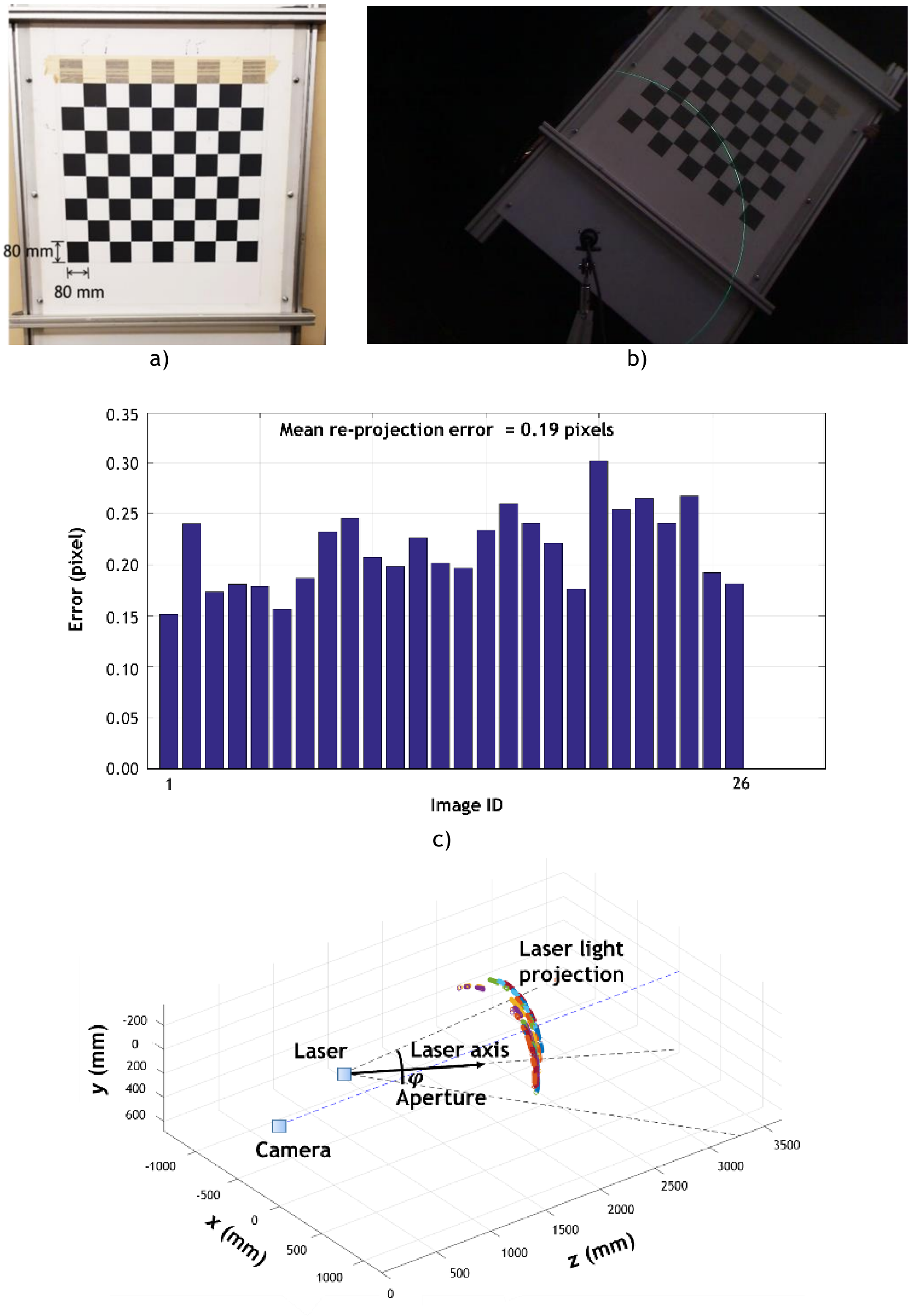

a) b) c) d)

Figure 4.38: a) A 9-by-8-square calibration pattern, b) laser projection on the calibration pattern, c) re-projection error and d) laser and camera positions.

Table 4.19: Key features of camera and calibration results used in the tower experiment.

Feature	**Detail**
Product name	Logitech QuickCam Pro 9000
Resolution	1600.0 x 1200.0 pixels^2
Image sensor	2.0 MP CMOS
Focal length	3.7 mm
Lens aperture	F/2.0
Frame rate	30.0 fps

Calibration results

Camera calibration		
Intrinsic parameters	α	1364.08
	β	3.33
	γ	1365.83
	u_0	773.86
	v_0	441.53
Radial Distortion	k_1	7.82E-02
	k_2	-2.24E-01
	k_3	0.00E00
Tangential Distortion	p_1	0.00E00
	p_2	0.00E00

Circular laser calibration	x (mm)	y (mm)	z (mm)
Laser position	-49.32	98.95	651.43
Laser axis	-6.86E-02	1.29E-01	9.99E-01
Aperture, φ	-26.56 °		

Mean re-projection error	**MRE**	0.19 pixel

After calibration, the image acquisition has been carried out as described in the next part.

4.4.2 Experiments and results

As explained in the previous chapter, the adopted LSS was mounted on the welding robot's arm and the whole system was moved through the tower section with a linear constant velocity as $V_z = 32\ \text{mm/s}$. Figure 4.39 presents a general perspective of the adopted system. One side of the tower's outlet has been covered by a curtain to avoid the environment light shining over the image acquisition.

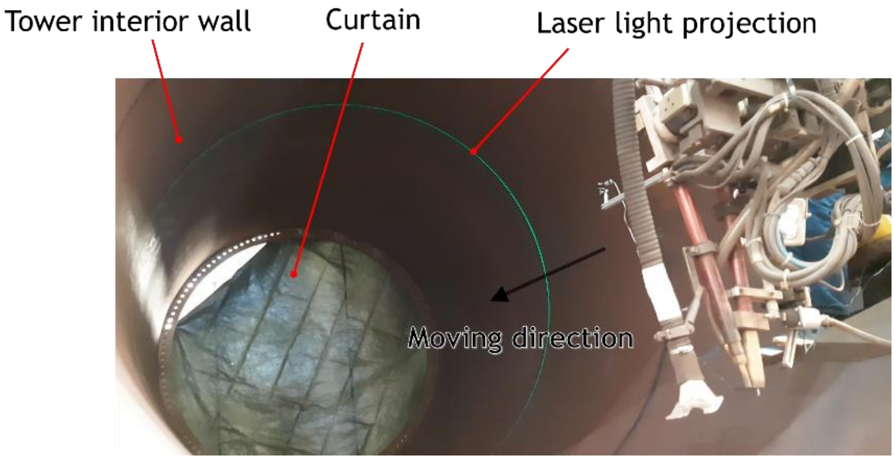

Figure 4.39: A general view of the LSS experiment in the tower model.

Due to the camera FOV, it was not conceivable to procure the complete profile by a single image acquisition, therefore, to tackle this disturbance, the experiment has been carried out in two stages. First, the image acquisition has been executed in the original status of the tower and then the tower was rotated through 180° by the rollers holding the exterior wall, see Figure 4.40-a). The experiment related to the original and rotated states of the tower were identified as *Half_one* and *Half_two*, respectively.

Prior to the experiment performance, two magnetic bases were attached on the interior wall where the second part of the tower section (it meant the Half_two experiment) initiates, as Figure 4.40-b) depicts. They played a role of auxiliary marks led to merge two point clouds acquired in the original and rotated states.

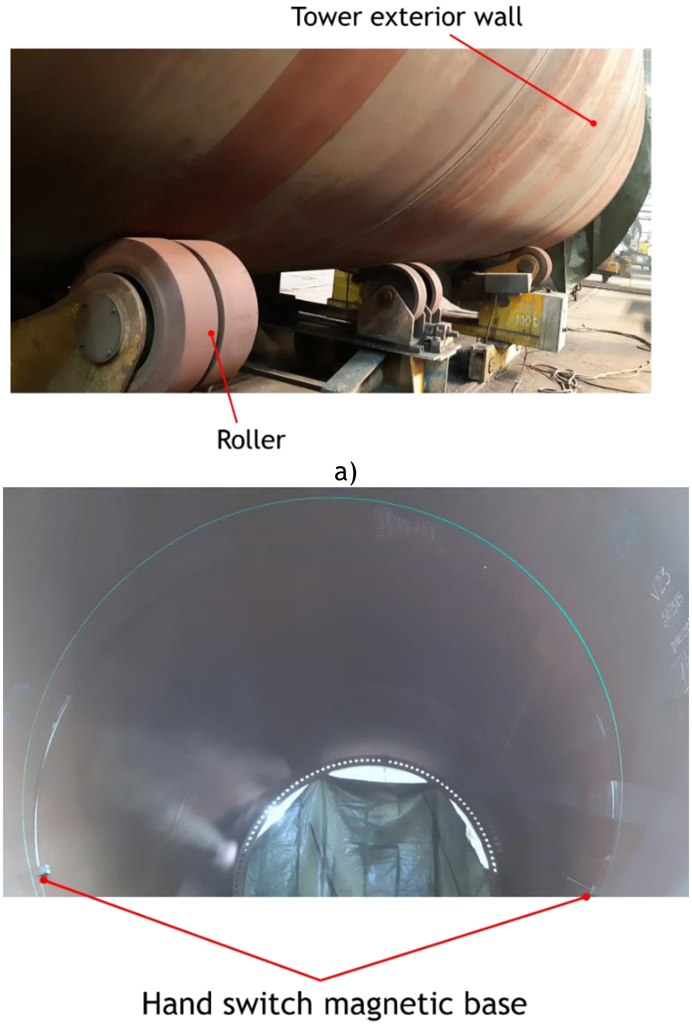

b)

Figure 4.40: Tower exterior wall with the roller presentation and b) the magnetic bases hold on the interior surface of the tower.

Experimental activities have been executed following the configurations reported in Table 4.20. Due to the limited travelling distance of the welding robot, only $2561\ \mathrm{mm}$ of the middle part has been captured.

Table 4.20: Experimental test configurations, field experiment.

Velocity in z-direction, V_z	**Frame rate, f_s**	**Total length**	**No. images**	**Resolution**
$32.00\ \mathrm{mm/s}$	$8.00\ \mathrm{fps}$	2561.00 mm	728.00	3.52 mm

Figure 4.41 presents a RGB image captured by the camera for both Half_one and Half_two experiments.

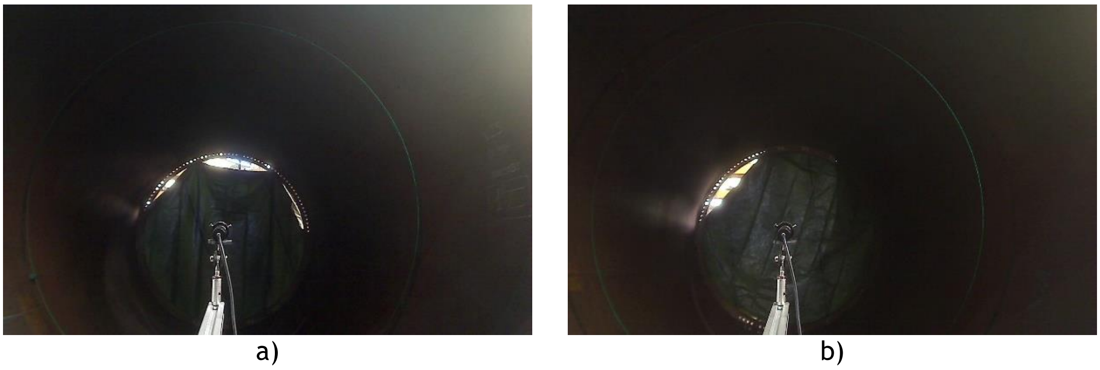
a) b)

Figure 4.41: An individual RGB image captured by the camera over the image acquisition, a) Half_one experiment and b) Half_two experiment.

The captured images must be transformed into binary images within the image processing. This task has been accomplished through converting the RGB images into CIELAB colour space ($CIE\ L^*\ a^*\ b^*$). In which the lightness value, L^*, represents the darkest black if $L^* = 0$, and the brightest white if $L^* = 100$. The colour channels, $a^*$and b^*, signify true neutral grey values at $a^* = 0$ and $b^* = 0$. Minor values of a^* denote the green colour.

Nevertheless, the points were filtered according to three conditions:

1. A region of interest (ROI) was defined. The area covering the possible locations of the laser light was manually selected.
2. The points must be green: the a^* channel on the CIELAB image shall be below a certain threshold, $0.1 \leq TH \leq 0.9$. Values for TH were defined differently for dissimilar consecutive series of images, due to inconsistent lighting throughout the performed tests.
3. The points must be significantly brighter than the background (BG). The background was obtained by applying a Gaussian filter to the RGB image's red channel, which made the laser light less visible, and the brightness was the CIELAB image's L^* channel, which emphasised the laser light. The ratio between the brightness and the background must be above a certain threshold, $0.8 \leq TH2 \leq 1.7$, $TH2$ also varied for different series of images based on the lighting conditions.

Figure 4.42 presents the transformation evolution from the RGB to binary images following above-mentioned steps.

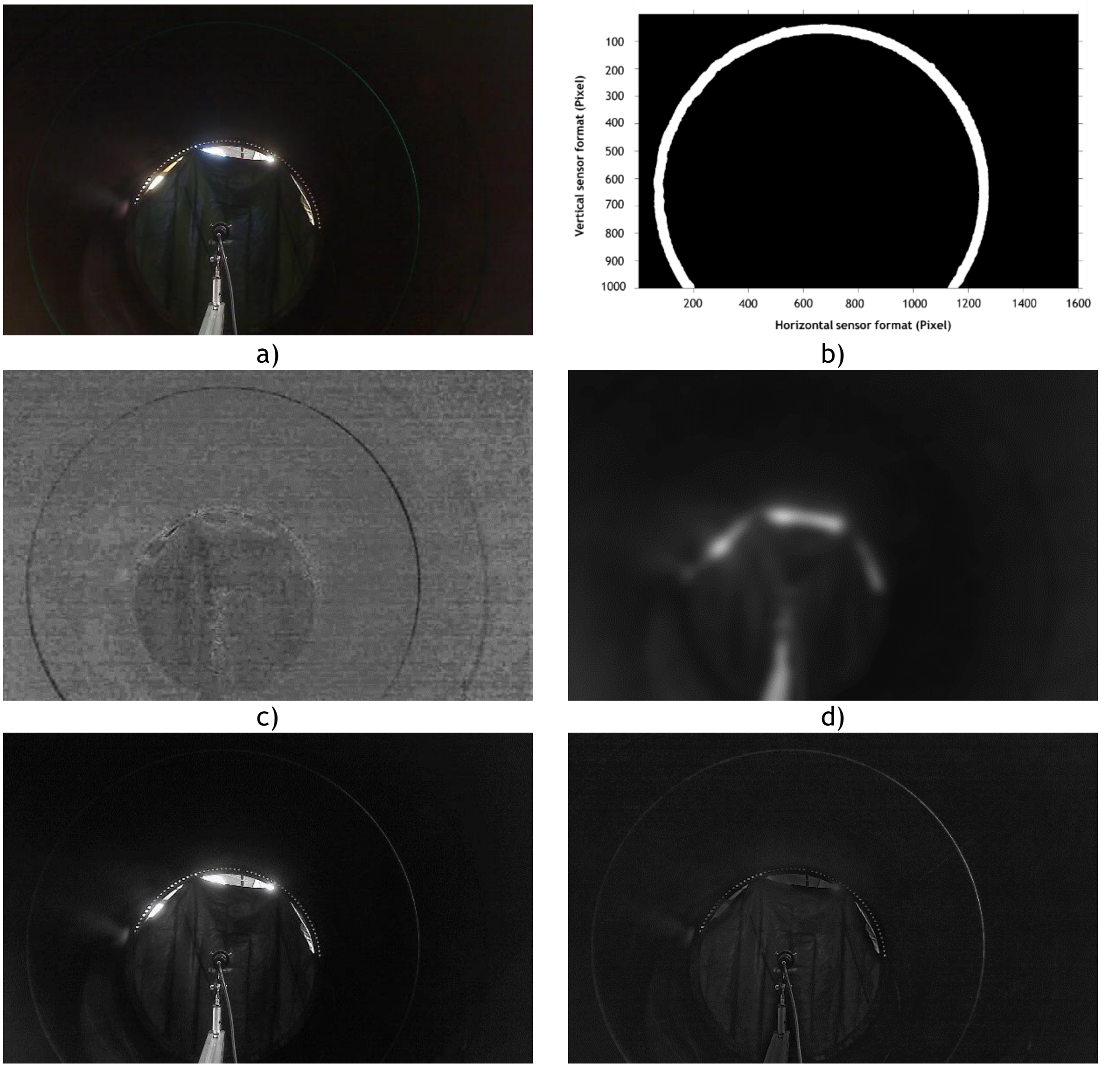

a) b)

c) d)

e) f)

Figure 4.42: Image processing steps performed to convert the RGB into binary image, a) original RGB image, b) ROI, c) CIELAB a*, d) BG, e) CIELAB L* and f) TH2 conversion.

The transformed image through the image processing algorithm is shown in Figure 4.43 for Half_one and Half_two experiments. The laser points on both acquisitions have been extracted from the marks position (which were identified by the magnetic bases held on the tower wall) and they will be fused together to construct the whole tower profile.

The Half_one experiment contributed to produce a point cloud consisting of 10241263 vertices while the other one included 5325869 vertices. After merging, simplified and aligned point cloud of the tower, including 64331 vertices, on different views is shown in Figure 4.44.

The tower's inner diameter has been measured as $D_i^{LSS} \cong 4015.77\,\mathrm{mm}$ from the LSS experiment. Comparing to the value reported by Tegopi company, $D_i \cong 4177.00\,\mathrm{mm}$, a deviation of $3.70\ \%$ has been achieved which is promising. This small difference on the obtained result strongly implied that the supporting methodology is accurate and robust in the field experiment application.

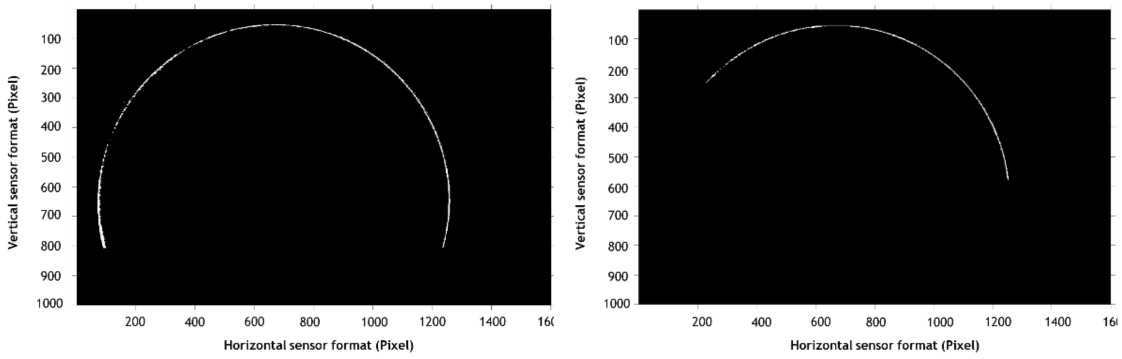

a) b)

Figure 4.43: Binary image derived from image processing for; a) Half_one experiment and b) Half_two experiment.

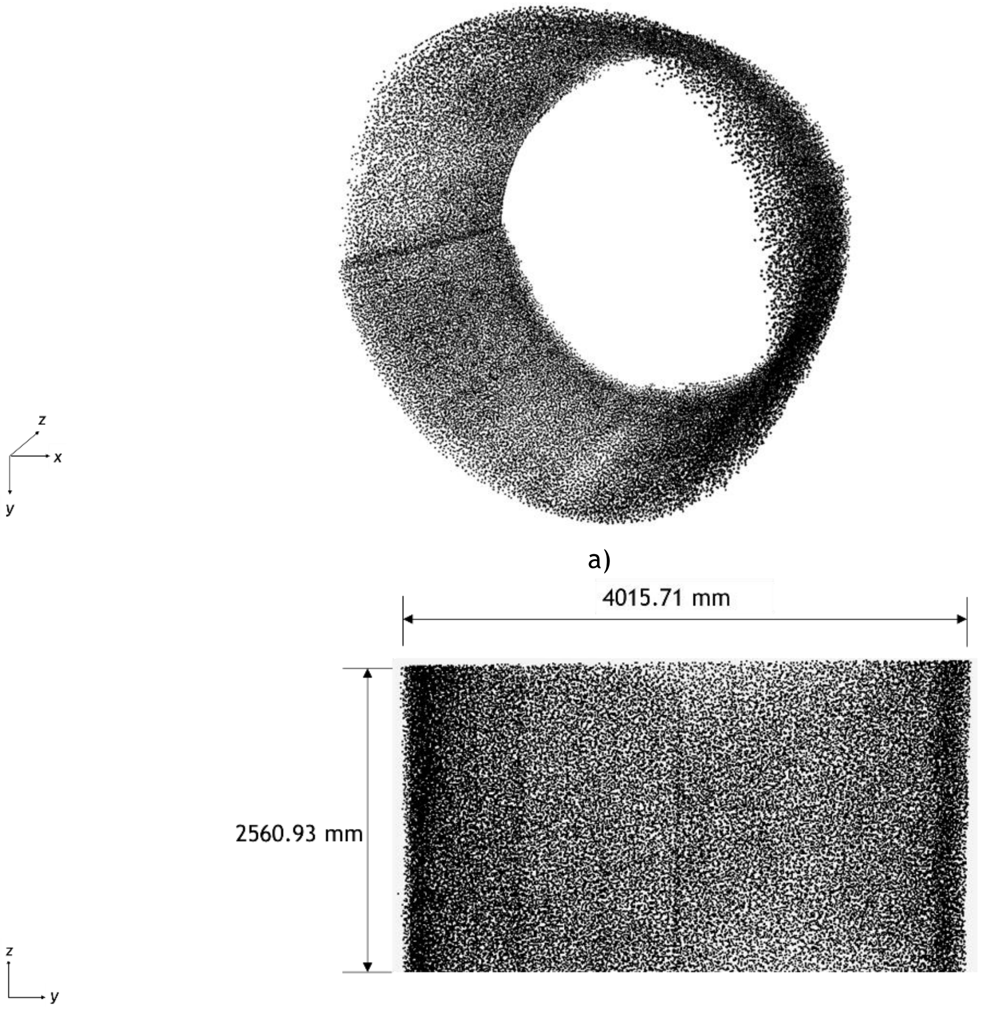

a)

b)

Figure 4.44: a) A 3D view of the tower profile and b) a top view of the tower with its dimensions obtained by the LSS.

4.5 Chapter summary

In this chapter, a new technological solution to inspect railway tunnels was designed and built. The innovated system relies on a 3D LSS consisting of a camera, a circular laser module, a slider and a station to receive and analyse the data. The deployed inspection system is capable to capture images with high resolution in various linear velocities of the system. As a tunnel scale model, half of a polymer tube was considered and analysed under different states as; initial, feature detection, loaded and defect detection. The deployed system was competent to provide the tunnel's point cloud in several conditions. Once the defect has been detected, the tunnel was mechanically studied using a non-contact optical measurement system developed based on the 3D DIC. In addition, the tunnel model with defect has been solved using FEM formulations in ABAQUS© to obtain comparable solutions.

Besides, to assess the accuracy and robustness of the deployed LSS in a real tunnel, an additive manufactured model of a shallow rock tunnel so-called "*Monte Seco tunnel*", in Vitoria Minas Railway in Brazil was built by means of a 3D printing. The tunnel was therefore scanned and its profile was achieved by the 3D LSS. Furthermore, the tunnel was compressively loaded by a displacement imposition and the deformation was monitored by comparing the deformed shape to the initial one. Moreover, the developed 3D DIC, which has been also used in the scaled tunnel experiment (tunnel prototype), was adopted to capture the deformation led to draw an evaluation amongst the deformation results.

Owing to the successful results achieved from tunnel inspection experiments, the designed 3D LSS has been used in a field application. Therefore, a section of a cylindrical wind tower was examined, and its interior surface profile has been attained. It was a demanding problem in terms of the image processing task on the captured images due to the test environments.

Overall, promising results were accomplished from all experimental activities. It would be inferred that the innovative methodology, based on the 3D LSS, in the railway tunnel inspection is robust, cost-effective and efficient. Moreover, it evolved that the deployed inspection system is capable to acquire the tunnel's geometry and to detect and characterise defects.

Chapter 5 : Conclusions

5.1 Concluding final remarks

One of the greatest challenges engineers encounter is the inspection, assessment, maintenance and safe operation of the existing civil infrastructure in particular rail structures. Railway tunnels deteriorate due to ageing, environmental factors, increased loading, and damage caused by human or natural elements, skipped maintenance, and remitted repairs. The increased perception of those problems, led by advances in analysis techniques, further demands the deployment of automated systems for structural heath monitoring (SHM). The laser scanning method has the advantage to scan underground infrastructures without illumination facilities.

In this PhD thesis, the railway tunnel structures, in addition to the potential defects in real environments, have been reviewed and technological solutions were proposed for the tunnel inspection.

Owing to the second-stage inspection solution, several engineering benchmark examples were experimentally and numerically studied to assess the SHM relying on the optical Non-Destructive Inspection (NDI) tools. The mechanical behavior of different materials that can be found on tunnels, from metal alloys to concrete, have been characterized by means of Digital Image Correlation (DIC) technique. The encouraging results contributed to signify the accuracy and robustness of the mentioned method in the structural integrity assessment.

To fulfil the objectives of the research project, an innovative automated inspection solution was proposed for railway tunnels' examination. A demonstrator was built based on the 3D laser scanning system (LSS) technology, which consists of a circular laser and a camera. The deployed LSS has been implemented in laboratory and field experiment models to examine the structural condition. Further experiments have been carried out to detect features and defects. In addition, once a defect was recognised by the system, a post-processing analysis has been performed by means of a developed non-contact optical measuring tool relying on the 3D DIC. The developed DIC solution enabled monitoring and characterisation of the defects by evaluating the acquired displacement and strain fields. The developed inspection system has been implemented in scaled tunnel models.

Future systems must be capable of both inspection and maintenance with the minimal human intervention without supervision. The aim is to devise more efficient systems, capable of performing more accurate and cost-effective inspection, maintenance and assessment of structural integrity. The deployed system has the potential to be replaced with the currently performed manual inspection and to propose appropriate solutions for efficient maintenance or changes in maintenance plans. The innovated inspection methodology enables the detection of structural defects, mainly cracks.

Concerning the research questions set in Chapter 1, it was concluded that all secondary research queries have been addressed. The first research question, “*How is it possible to comprehensively detect, measure and assess interacting geometrical changes to support integrated condition assessment of railway tunnels infrastructure?*”, was addressed by implementation of the deployed 3D LSS in the scaled tunnel models in which the geometrical changes in addition to the defect and features have been identified. As a result, the structural integrity of the tunnels has been successfully assessed. The second research question, “*How it is possible to adopt the optical NDIs for the efficient and on-demand updating of tunnels’ stability parameters in defect detection and assessment models?”,* was addressed by the development of a non-contact measuring tool developed based on the 3D DIC. Once a defect has been detected by the 3D LSS, it was monitored and characterised by the deployed DIC system and displacement variation in addition to the strain field were documented. Moreover, further experiments have been carried out where the tunnels were subjected to a compressive loading condition imposed by a displacement enforcement and the deformation was captured by the 3D DIC. The obtained results were robust and accurate, leading to the validation of the supporting methodologies. The third research question, “*What are the efficient approaches based on the image processing techniques to assess the SHM of the related engineering components?*”, was addressed by performing experiments based on optical NDI techniques, as DIC, on the relevant engineering structures in the field of civil and mechanics. Several benchmark examples ranging from metal alloys to concrete were studied by means of the supporting NDI to assess the material response in elastostatic, elastoplastic, damage, and fracture and fatigue behaviours. The performed experiments implied that the adopted NDI tool has the potential to assess the SHM of the engineering components with a great success. The last research question, “*How the numerical simulations assist to study defects and predict the structures’ lifetime?*” was addressed by conducting a numerical simulation on the defected scaled tunnel using a Finite Element Analysis, FEA. The obtained result was verified by the experimental measurements of the deformation and displacement fields. Regarding the concrete structures, several concrete models were computationally resolved using the FE and meshless method formulations to assess the damage behaviour of the corresponding structures leading to characterise the existing crack. Besides, the numerical analyses were performed on the engineering components leading to evaluate the fracture behaviour of different materials by determining the stress intensity factor (SIF) and fatigue life assessment.

The main research question was thereby addressed throughout the development of the PhD research project, but it still requires further work in a real scale railway tunnel to provide conclusive and definitive answer.

However, the research performed and documented in this thesis serves as a significant development in the attempt to solve that question. During this PhD research, the process was developed, and as such the technology was at a TRL 3, "research to prove feasibility stage in the laboratory studies", and at the conclusion of this research project the same joining technology is at a TRL 6/7 (Fully functioning prototype for testing in operational environment).

In summary, the innovation concepts proposed by the presented PhD project can be stated as follows:

- An automated inspection system has been implemented and deployed;
- A system built on highly robust technologies and fully addressing all inspection concerns;
- Deployment of a low-cost inspection system at signalled sites for defect monitoring and structural health monitoring;
- Implementation of a network of deployed systems for data gathering at different positions and global appraisal.

5.2 Future works

Considering the successfully established research work and results at laboratory TRL, the research novelty has been proven at this stage. Further study is demanded for the adaptation of the developed technological design, which would be considered as a fully functioning prototype, in operational environment.

Two main paths for future development of the proposed automated inspection system are drawn. The first should be the implementation of the 3D LSS developed on a real scale tunnel. To this end, all system components should be designed or selected considering each application. The other path is the adaptation of a thermography method to monitor and characterise leakage/moisture in a real tunnel. New design methodologies and procedures should be studied, along with physical properties relevant to this application.

Nevertheless, regarding the first path, a system has been designed to be adopted in a real scale railway tunnel. The Monte Seco railway tunnel in Brazil (which is a-single-line tunnel) is considered as the real case study. Notice that a scaled model of a section of this tunnel has been inspected by the deployed automated inspection system, as presented in Section 4.3.

Sound results have been obtained which encourage the application of the new inspection solution on a real tunnel.

The real tunnel with its geometrical properties is shown in Figure 5.1-a). Maintaining the deployed 3D LSS system arrangement, a schematic view of the designed system is depicted in Figure 5.1-b). Regarding the laser module, according to the experiments carried out in this thesis, it was inferred that a more powerful laser is required. For instance, A 100 mW or higher power circular laser line should be considered to meet the system requirements. A high-speed camera should be hired to provide a higher measurement accuracy. Also, it is suggested the use of a wider lens in order to minimise the distance between the camera and laser, however, Table 5.1 reports the technical details of the optical instruments preferable to design the system.

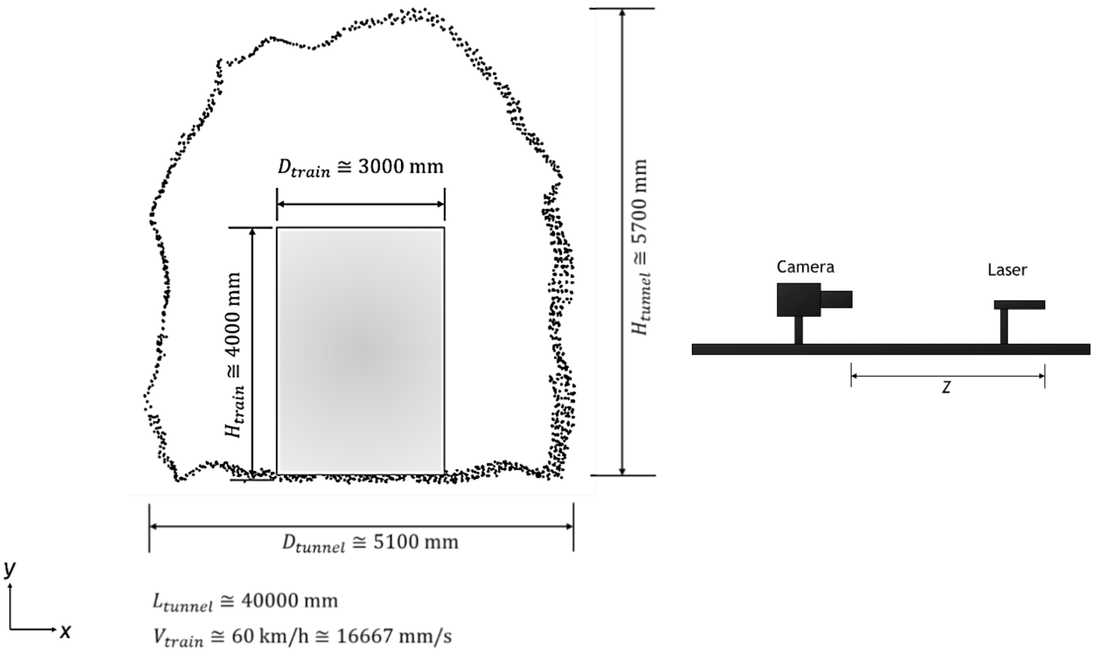

a) b)

Figure 5.1: a) The Monte Seco railway tunnel detail and b) a schematic view on the designed system.

Two elements play significant roles in the designed system; the system resolution in z direction, which can be computed as V_z/f_s (referring to Equation 4.18) in which V_z is the train velocity and f_s is the camera frame rate, and the nominal distance (Z) between camera and laser mounted on the train top roof, see Figure 5.1-b). If the instruments, proposed in Table 5.1, are adopted, it is possible to elaborate the designed system configurations. In this regard, Table 5.2 presents the detailed calculus of the designed system for the future.

Table 5.1: Technical specifications of the designed system proposed for the future plan.

Feature	Detail
Circular laser	
Core power	100.0 mW
Output wavelength	650.0 nm/520.0 nm/450.0 nm
Aperture	27.9 °
Others	500.0 mm distance: Circle diameter: 530.0 mm 1000.0 mm distance: Circle diameter: 1060.0 mm 1500.0 mm distance: Circle diameter: 1590.0 mm
Camera	
Resolution	720.0 × 540.0 pixel^2
Sensor type	CMOS
Sensor size	5.0 × 3.7 mm^2
Pixel size	6.9 µm x 6.9 µm
Framerate	525.0 fps
Interface	USB 3.0
Camera lens	
Focal length	4.0 mm
Lens mount	C-mount
Iris	F1.8-F22.0
Iris type	Manual
Max. image circle	1/2.5”
Working distance	100.0 mm

Table 5.2: Details of the designed LSS system for the future plan.

Key feature	R (mm)	r (pixel)	DL (mm)	DC (mm)	x_l'	x_l (pixel)	In-plane Resolution (mm/pixel)
x	2550	720	4811.3	5311.3	0.48	278	9.16
y	1700	540	3207.6	3707.6	0.46	266	6.39

R	Tunnel radius
r	Camera resolution
DL	Distance from laser to laser projection on the tunnel
DC	Distance from camera to laser projection on the tunnel
x_l'	Laser point in homogeneous coordinates
x_l	Laser point in image coordinate

Notice that tunnel radius in x-direction is $(D_{tunnel}/2)$ while the y-direction is the vertical distance from the train’s roof to the tunnel’s ceiling. Besides, the laser points in image coordinates must be always in a range smaller than half of the image size in the corresponding direction, because the system is dimensioned so that the laser projection at the tunnel radius must remain inside the image.

Adopting the designed system as reported with detail in Table 5.2, the distance between camera and laser was optimized as $Z = 500.0\ \text{mm}$. Considering the train velocity as $V_{train} \cong 60\ \text{km/h} \cong 16667.0\ \text{mm/s}$, the acquisition time takes $t = 2.4\ \text{s}$ for a total tunnel length of $L_{tunnel} \cong 40000.0\ \text{mm}$. The system resolution in z direction is thereby calculated as $31.8\ \text{mm/frame}$.

Concerning the computer station, adopting the mentioned system led to capture 1260 monochrome images over the test acquisition of a-40000-mm long tunnel. Hence, the required memory capacity can be approximately 490 MB respecting an acquisition rate of 204 MB/s.

Considering the designed system details, it must be mentioned that the system resolution in z direction is always a function of the train speed and in particular the camera framerate. In general, the higher framerate camera, the lower resolution is available. Since the system resolution in z direction is a very important key on the designed system, it was preferred to choose a high framerate camera with a low resolution. If a higher resolution camera is used, the system resolution in z direction may drop significantly.

Another point regarding the designed system, a very wide camera lens was selected for the system contributing to calibrate the system with a quite large calibration pattern.

One of the advantages of this system is the possibility to be mounted on both train sides, at the front and the rear ends. When the train enters the tunnel, both systems can be functioning simultaneously and scan the tunnel interior wall. This feature supports acquisition of the tunnel shape with a minimum occlusion since it is possible to merge and align both obtained point clouds afterwards. This capability is very important in rocky/mount tunnel encompassing several irregular protruded shapes that cause camera occlusions. In the experiment of the additive manufactured Monte Seco tunnel presented in section 4.3, it was shown that the full tunnel profile could be obtained only if the acquisition was performed twice; one in the original tunnel state and the other one when it turned around, which amounts to an equivalent system scanning in a single direction from both composition ends.

The described system for the real case tunnel examination has been proposed in relation to the mathematical calculations and optical products' availability in the market, it can be inferred that there will might be some unexpected issues and disturbances when this system implemented in the real environment.

Form the DIC point of view, it must be noted that once a structural defect is detected on the real tunnel's wall, the DIC system must be mounted in front of the inspected region. A special care must be devoted to the system mounting in order to avoid the disturbance of the deformation/vibration of the whole tunnel structure. Hence, it is recommended to mount the DIC system on a rigid body. Concerning the camera and lens, it must be configured in relation to the working distance to the interest region. Once the camera and lens are setup, the speckle pattern must be generated on the surface following the correlated solution. There is a possibility to generate the proper speckle pattern on the interest region (which would last for a long time) by specific inks used for the concrete, soil and rocks available from the commercial partners.

Regarding the second path, the thermography adaption to detect the moisture and leakage in the real environment, it must be mentioned that some preliminary studies have been already performed through thermography methods. A hybrid experimental/numerical work [101], [102] has been carried out on a pre-cracked Compact Tension (CT) specimen made of AA6082-T6 Aluminum alloy which was subjected to a fatigue loading condition. As a result, the Stress Intensity Factor (SIF) was calculated following the stress field monitored by a Thermoelastic Stress Analysis, TSA, which is categorized as a thermography method. The acquired results were promising and reliable. Besides, based on the lock-in thermography, the thermal fatigue behavior of the polymeric specimens have been evaluated and encouraging results were thereby accomplished [100]. Owing to the performed analyses by the thermography methods, it would be emphasized that an infrared camera and a computer station are essentially required to perform the thermography analysis. Moreover, the inspected region, which is suspected to a leakage, must be coated by a black ink with a specific thermal emissivity.

Appendix A: Camera Calibration

This section describes the camera calibration formulations based on Zhang's model [169], [170], [172]. Generally, camera calibration remains an essential stage in the 3D computer vision to extract metric information from the 2D images. If a 2D and a 3D point are defined as $\boldsymbol{m} = \{u \quad v\}^T$ and $\boldsymbol{M} = \{X \quad Y \quad Z\}^T$, respectively, it is possible to present their augmented vectors as, $\widetilde{\boldsymbol{m}} = \{u \quad v \quad 1\}^T$ and $\widetilde{\boldsymbol{M}} = \{X \quad Y \quad Z \quad 1\}^T$. Considering a pinhole camera model, it is rational to make a relationship between a 3D point and its image projection as follows:

$$s\widetilde{m} = \boldsymbol{A}[\boldsymbol{R}|\boldsymbol{t}]\widetilde{M} \tag{A.1}$$

In which *s* presents an arbitrary scale factor, the extrinsic matrix $[\boldsymbol{R}|\boldsymbol{t}]$ takes the form of a rigid transformation matrix: a 3x3-rotation matrix in the left-block, and 3x1-translation column-vector in the right as:

$$[\boldsymbol{R}|\boldsymbol{t}] = \left[\begin{array}{ccc|c} r_{1,1} & r_{1,2} & r_{1,3} & t_1 \\ r_{2,1} & r_{2,2} & r_{2,3} & t_2 \\ r_{3,1} & r_{3,2} & r_{3,3} & t_3 \end{array}\right] \tag{A.2}$$

$[\boldsymbol{R}|\boldsymbol{t}]$ is associating the world coordinate system to the camera coordinate system. In addition, the camera intrinsic matrix, ***A***, can take the following form:

$$\boldsymbol{A} = \begin{bmatrix} \alpha & \gamma & u_0 \\ 0 & \beta & v_0 \\ 0 & 0 & 1 \end{bmatrix} \tag{A.3}$$

where (u_0, v_0) is the principal point coordinates, α and β are the scale factors correspond to *u*- and *v*- image axes and the skewness of the two image axes is defined by γ.

A.1 Homography

Assuming a pinhole camera model, any two images of the same planar surface in space are related by a homography. In this section, the homography between the model plane and its image is explained. Without losing the totality, it is assumed that the model plane remains as $Z = 0$ respecting the world coordinate system. Hence, it is possible to present the i^{th} column of the rotation matrix ***R*** as $\boldsymbol{r}_i$ and rewrite Equation (A.1) as follows:

$$s\begin{bmatrix}u\\v\\1\end{bmatrix} = \boldsymbol{A}[r_1 \quad r_2 \quad r_3 \quad t]\begin{bmatrix}X\\Y\\0\\1\end{bmatrix} = \boldsymbol{A}[r_1 \quad r_2 \quad t]\begin{bmatrix}X\\Y\\1\end{bmatrix} \tag{A.4}$$

It is noticeable that vector ***M*** is used to signify a single point related to the model plane and defined as $\boldsymbol{m} = \{X \quad Y\}^T$ if $Z = 0$. Therefore, $\widetilde{\boldsymbol{M}} = \{X \quad Y \quad 1\}^T$. The homography matrix, $[\boldsymbol{H}]_{3\times3}$, between ***M*** and ***m*** can the take the following form:

$$s\widetilde{\boldsymbol{m}} = \boldsymbol{H}\widetilde{\boldsymbol{M}} \text{ if } \boldsymbol{H} = \boldsymbol{A}[r_1 \quad r_2 \quad t] \tag{A.5}$$

A.2 Intrinsic constraints

If an image is considered on the plane model, it is rational to estimate the homography as $\boldsymbol{H} = [h_1 \quad h_2 \quad h_3]$. Based on Equation (A.5), it can be arrived at;

$$[h_1 \quad h_2 \quad h_3] = \lambda\boldsymbol{A}[r_1 \quad r_2 \quad t] \tag{A.6}$$

In which λ denotes an undetermined scalar. Assuming r_1 and r_2 as orthonormal, the below relationships can be derived;

$$h_1^T\boldsymbol{A}^{-T}\boldsymbol{A}^{-1}h_2 = 0 \tag{A.7}$$

$$h_1^T\boldsymbol{A}^{-T}\boldsymbol{A}^{-1}h_1 = h_2^T\boldsymbol{A}^{-T}\boldsymbol{A}^{-1}h_2 \tag{A.8}$$

Since any homography owns 8 degrees of freedom (DOF) while only six extrinsic parameters (3 for rotation and 3 for translation) exist, a homography can be only determined by existence of two essential constraints on the intrinsic parameters. Besides, $\boldsymbol{A}^{-T}\boldsymbol{A}^{-1}$ signifies the image of the absolute conic.

A.3 Camera calibration resolution

It is feasible to solve the camera calibration problem. The resolution procedure follows an analytical solution known as the closed-form solution. This procedure is based on minimizing an algebraic distance that does not possess any physical meaning. Then, there is another solution strategy governing by a nonlinear optimization approach relying on the maximum likelihood criterion. For both resolution techniques, it concentrates on the lens distortion providing the nonlinear and analytical solutions.

Closed-form solution

The solution obtained in this section is known as the estimated results. In the perspective of the analytical solution, if matrix ***B*** defines a symmetric 6D vector as follows:

$$\boldsymbol{B} = \boldsymbol{A}^{-T}\boldsymbol{A}^{-1} \equiv \begin{bmatrix} B_{11} & B_{12} & B_{13} \\ B_{21} & B_{22} & B_{23} \\ B_{31} & B_{32} & B_{33} \end{bmatrix} = \begin{bmatrix} \frac{1}{\alpha^2} & -\frac{\gamma}{\alpha^2\beta} & -\frac{v_0\gamma-u_0\beta}{\alpha^2\beta} \\ -\frac{\gamma}{\alpha^2\beta} & \frac{\gamma}{\alpha^2\beta^2}+\frac{1}{\beta^2} & -\frac{\gamma(v_0\gamma-u_0\beta)}{\alpha^2\beta^2}-\frac{v_0}{\beta^2} \\ \frac{v_0\gamma-u_0\beta}{\alpha^2\beta} & -\frac{\gamma(v_0\gamma-u_0\beta)}{\alpha^2\beta^2}-\frac{v_0}{\beta^2} & \frac{(v_0\gamma-u_0\beta)^2}{\alpha^2\beta^2}+\frac{v_0^2}{\beta^2}+1 \end{bmatrix} \tag{A.9}$$

The vector ***b*** can be defined as;

$$\boldsymbol{b} = [B_{11}, B_{12}, B_{22}, B_{13}, B_{23}, B_{33}]^T \tag{A.10}$$

Considering the i^{th} column vector of the homography matrix, ***H*** as;

$$\boldsymbol{h}_i = [h_{i1}, h_{i2}, h_{i3}]^T \tag{A.11}$$

Then, the following relationship can be derived;

$$\boldsymbol{h}_i{}^T\boldsymbol{B}\boldsymbol{h}_j = \boldsymbol{v}_{ij}^T\boldsymbol{b} \tag{A.12}$$

With regard to;

$$v_{ij} = \left[h_{i1}h_{j1}, h_{i1}h_{j2} + h_{i2}h_{j1}, h_{i2}h_{j2}, h_{i3}h_{j1} + h_{i1}h_{j3}, h_{i3}h_{j2}, h_{i2}h_{j3}, h_{i3}h_{j3}\right]^T \tag{A.13}$$

Considering the constraints presented in Equations (4.7) and (4.8), it is possible to express two homogenous relations by vector ***b*** as follows:

$$\begin{bmatrix} v_{12}^T \\ (v_{11} - v_{22})^T \end{bmatrix} \boldsymbol{b} = 0 \tag{A.14}$$

If *n* images of the model plane are captured, it is possible to generalize the above-mentioned equation by arranging *n* where ***V*** is a-2*n*×6-matrix;

$$\boldsymbol{Vb} = \boldsymbol{0} \tag{A.15}$$

The following condition is valid for the generalized equation:

- If $n \geq 3$, a unique solution on ***b***;
- If $n = 2$, the skew constraint can be obtained as $\gamma = 0$, i.e. $[0,1,0,0,0,0]\boldsymbol{b} = 0$;
- If $n = 1$, only two camera intrinsic parameters, α, β, are determined if v_0, u_0 are known.

In general, the solution to equation system stated in Equation (A.15) is the eigenvector of $\boldsymbol{V}^T\boldsymbol{V}$ respecting the smallest eigenvalue. As vector ***b*** is determined, the camera intrinsic matrix can be calculated from matrix ***B*** by the following equations.

$$\boldsymbol{B} = \lambda\boldsymbol{A}^{-T}\boldsymbol{A} \tag{A.16}$$

$$v_0 = (B_{12}B_{13} - B_{11}B_{23})/(B_{11}B_{22} - B_{12}^2) \tag{A.17}$$

$$\lambda = B_{33} - [B_{13}^2 + v_0(B_{12}B_{13} - B_{11}B_{23})]/B_{11} \tag{A.18}$$

$$\alpha = \sqrt{\lambda/B_{11}} \tag{A.19}$$

$$\beta = \sqrt{\lambda B_{11}/(B_{11}B_{22} - B_{12}^2)} \tag{A.20}$$

$$\gamma = -B_{12}\,\alpha^2\beta/\lambda \tag{A.21}$$

$$u_0 = \gamma v_0/\beta - B_{13}\alpha^2/\lambda \tag{A.22}$$

Regarding the extrinsic parameters associated to any image, since matrix ***A*** is determined, the following resolution procedure is applicable deriving from Equation (A.5);

$$r_1 = \lambda \boldsymbol{A}^{-1}\boldsymbol{h_1}, \qquad r_2 = \lambda \boldsymbol{A}^{-1}\boldsymbol{h_2}\,, \qquad r_3 = r_1 \times r_2\,, \qquad t = \lambda \boldsymbol{A}^{-1}\boldsymbol{h_3} \tag{A.23}$$

where $\lambda = 1/\|\boldsymbol{A}^{-1}\boldsymbol{h_1}\| = 1/\|\boldsymbol{A}^{-1}\boldsymbol{h_2}\|$. The obtained matrix ***R*** does not generally meet rotation matrix properties due to the data noise. Hence, the singular value decomposition of an approximated matrix $[\boldsymbol{Q}]_{3\times 3}$ must be used to compute the best rotation matrix, ***R***. The best solution is referring the smallest Frobenius norm of the difference ***R***-***Q***.

A.4 Radial and tangential distortion

Radial distortion is mostly detectible when images are captured on vertical objects owning straight lines and then they appear as a curve. This distortion appears most noticeably when the widest angle (shortest focal length) is nominated rather than with a fixed or a zoom lens. Radial distortion is symmetric where ideal image points are distorted along radial directions from the distortion centre. It is due to the lens shape imperfection. Tangential distortion occurred due to the physical elements in a lens not being perfectly aligned, i.e. an improper lens assembly. In general, ideal image points are distorted in both radial and tangential directions. The following equations are involving in the lens distortion determination. Considering $(\breve{x}, \breve{y})$ as distorted or true (real) normalized image coordinate and $(\delta x, \delta y)$ as the distortions applied to the ideal image coordinate (x, y), the below relation is valid;

$$\breve{x} = x + \delta x\,, \breve{y} = y + \delta y \tag{A.24}$$

The distortion can be stated as power series in the radial distance of $r = \sqrt{x^2 + y^2}$ as follows;

$$\begin{aligned} \delta x &= x(k_1r^2 + k_2r^4 + k_3r^6 + \cdots) + [p_1(r^2 + 2x^2) + 2p_2xy](1 + p_3r^2 + \cdots), \\ \delta y &= y(k_1r^2 + k_2r^4 + k_3r^6 + \cdots) + [2p_1xy + p_2(r^2 + 2y^2)](1 + p_3r^2 + \cdots). \end{aligned} \tag{A.25}$$

In which the radial and tangential distortions coefficients are k_i and p_j, respectively. Besides, the correlated transformation from true image coordinates $(\breve{x}, \breve{y})$ to the frame buffer (pixel) image coordinates $(\breve{u}, \breve{v})$ can be formulated as;

$$\breve{u} = u_0 + \alpha\, \breve{x} + \gamma\, \breve{x} \quad , \quad \breve{v} = v_0 + \beta\, \breve{y} \tag{A.26}$$

where (u_0, v_0) denotes the principal point coordinates. Then, (u, v) and $(\breve{u}, \breve{v})$ present the undistorted (ideal) and corresponding real image coordinates in pixel. Assuming the distortion centre being the same as the principal point in addition to $\gamma = 0$ in Equation (A.26), in relation to Equation (A.25), if $i = 3$ and $j = 2$ are chosen, hence the system of equation associated to the ideal (undistorted) pixel image coordinates (u, v) and the real (distorted) pixel image coordinates $(\breve{u}, \breve{v})$ can take the following form;

$$\begin{gathered}\breve{u} = u + (u - u_0)(k_1 r^2 + k_2 r^4 + k_3 r^6) + p_1(r^2 + 2(u - u_0)^2) + 2p_2(u - u_0)(v - v_0),\\ \breve{v} = v + (v - v_0)(k_1 r^2 + k_2 r^4 + k_3 r^6) + 2p_1(u - u_0)(v - v_0) + p_2(r^2 + 2(v - v_0)^2).\end{gathered} \tag{A.27}$$

Hence;

$$\begin{bmatrix} r^2(u - u_0) & r^4(u - u_0) & r^6(u - u_0) & r^2 + (u - u_0)^2 & 2(u - u_0)(v - v_0) \\ r^2(v - v_0) & r^4(v - v_0) & r^6(v - v_0) & 2(u - u_0)(v - v_0) & r^2 + (v - v_0)^2 \end{bmatrix} \begin{Bmatrix} k_1 \\ k_2 \\ k_3 \\ p_1 \\ p_2 \end{Bmatrix} = \begin{Bmatrix} \breve{u} - u \\ \breve{v} - v \end{Bmatrix} \tag{A.28}$$

The presented system of equation can be considered for *m* points in a total number of *n* images together with a total number of $2mn$ equations in a matrix form of $\boldsymbol{Dk} = \boldsymbol{d}$, hence the linear least-squares solution can be expressed as;

$$\boldsymbol{k} = (\boldsymbol{D^T D})^{-1} \boldsymbol{D^T d} \tag{A.29}$$

Thus, the estimated radial and tangential distortion coefficients, $[k_1, k_2, k_3]^T$ and $[p_1, p_2]^T$, can be computed.

Nonlinear solution MLE

The obtained results from the closed-from resolution procedure can be refined through the maximum likelihood estimation, (MLE). Considering a total number of *n* images respecting *m* points on the model plane, it is possible to state that these image points were taken through independent and similarly distributed noise; hence, the MLE solution can be achieved through a minimization of the series function as;

$$\sum_{i=1}^{n} \sum_{j=1}^{m} \left\| m_{ij} - \hat{\boldsymbol{m}}(\boldsymbol{A}, \boldsymbol{R}_i, \boldsymbol{t}_i, M_j) \right\|^2 \tag{A.30}$$

In which $\widehat{\boldsymbol{m}}(\boldsymbol{A}, \boldsymbol{R}_i, \boldsymbol{t}_i, M_i)$ denotes the projection of point M_j associated to the i^{th} image following Equation (A.5). Besides, rotation element ***R*** is characterised by a-3-pararmeter-vector, ***r***. this vector is defined parallel to the rotation axis which its magnitude is the same as the rotation angle. Moreover, ***R*** and ***r*** are connected together through the Rodrigues formulation [180]. To minimize the presented function in Equation (A.30), it is essential to employ a nonlinear minimization proposed by Levenberg-Marquardt’s routine implemented by Minpack [181].

Appendix B : Meshless Method

Meshless methods discretize the problem domain and respective boundaries using a nodal distribution. This nodal set cannot be classified as a mesh, because no previous information regarding the relation between each node is required to build the interpolation functions for the unknown variational fields [182]. The meshless method concepts and mathematical relationships including Radial Point Interpolation method (RPIM) and its Natural Neighbour version (NNRPIM) are fully described in this section.

B.1 Nodal connectivity

Meshless methods are discrete computational approaches, similar to the Finite Element Method (FEM). On the other hand, instead of discretizing the problem domain in elements and nodes, meshless methods discretize the problem domain only using nodes. The predefined FEM mesh assures the nodal connectivity in the FEM. The nodes belonging to the same element directly interact between each other and with the boundary nodes of neighbour finite elements. In opposition, since there is no predefined nodal interdependency, in meshless method formulation, the nodal connectivity is determined after the nodal discretization [183], being obtained by the overlap of the influence-domain of each interest point. In the RPIM, these influence-domains can be determined by searching radially enough nodes inside a fixed area or a fixed volume, respectively for the 2D problems and for the 3D problems. Due to its mathematical simplicity, the concept of influence-domain is widely applied on several meshless methods versions [183]-[187]. Moreover, in RPIM, the nodal set is identified in the 2D space by $\boldsymbol{X} = \{x_1, x_2, \dots, x_N\} \wedge x_i \in \mathbb{R}^2$, where n is the number of nodes in the influence-domain of x_I. The density of $\boldsymbol{X}$ is identified by h,

$$h = \boldsymbol{min}\left\| x_j - x_i \right\|, \forall \{i, j\} \in N : \{i, j\} \leq N \wedge i \neq j \tag{B.1}$$

In which $||\cdot||$ is the Euclidean norm. A previous research work regarding the RPIM formulation recommends that each 2D influence-domain should possess 20 nodes [182]. Thus, here, the problem was analysed considering 20 nodes in each influence-domain. Figure B.1 schematically indicates a 13-node influence-domain illustration.

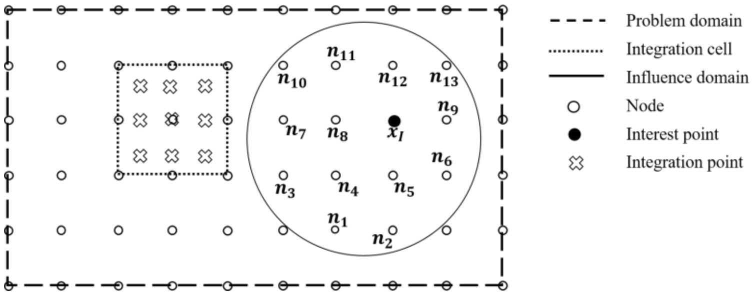

Figure B.1: A RPIM problem domain and its influence domain with regard to the interest point and an integration cell with 3×3 integration points in the discrete model illustration [157].

Alternatively, in order to impose the nodal connectivity, the NNRPIM uses the natural neighbours concept, that was released in 1980 by Sibson [188]. This mathematical concept can be characterized by the Voronoï diagram of the discretized domain. In the NNRPIM the problem domain $\Omega \in \mathbb{R}^d$, bounded by a physical boundary $\Gamma \subset \Omega$, is discretized in several randomly distributed nodes $\boldsymbol{N} = \{n_0, n_1, \dots, n_N\}$ scattered in the space domain: $\boldsymbol{X} = \{x_1, x_2, \dots, x_N\} \in \Omega$. The Voronoï diagram of $\boldsymbol{N}$ is the partition of the domain defined by Ω in sub-regions $\boldsymbol{V}_i$, closed and convex where any sub-region $\boldsymbol{V}_i$ is associated with the node n_i, in a way that any point in the interior of the $\boldsymbol{V}_i$ is closer to n_i than any other node n_j, where $n_j \in \boldsymbol{N} \wedge j \neq i, \boldsymbol{x}_I \in \Omega$.

$$\mathbf{V}_{\mathrm{i}} := \left\{ \mathrm{x}_I \in \Omega \subset \Re^{\mathrm{d}} : \left\| \mathrm{x}_I - \mathrm{x}_i \right\| < \left\| \mathrm{x}_I - \mathrm{x}_j \right\|, \forall i \neq j \right\} \tag{B.2}$$

The set of Voronoï cells, $\boldsymbol{V}$, defines the Voronoï diagram, $\boldsymbol{V} = \{V_1, V_2, \dots, V_N\}$. A Voronoï diagram is shown in Figure B.2-a. In the literature, it is possible to find several works properly addressing the Voronoï construction procedure [183], [189], [190].

Concerning the nodal connectivity in NNRPIM formulation, it is formed by a set of nodes in the neighbourhood of an interest point $\boldsymbol{x}_i \in \boldsymbol{X}$, the NNRPIM “influence-cell” concept contributes to establish the nodal connectivity [189], allowing to organically determine the influence domain of an interest node $\boldsymbol{x}_i$. Since it is simpler to represent, only the determination of the 2D influence-cell is given, although this concept is applicable to a d-dimensional space. Two types of influence-cells including the first degree influence-cell, and the second degree influence-cell are shown in Figure B.2-a). The first-degree influence cell is composed by the first natural neighbours of the interest node $\boldsymbol{x}_i$ while the second-degree influence cell, in addition to the first natural neighbours of the interest node $\boldsymbol{x}_i$, contains the natural neighbours of the nodes belonging to the first degree influence-cell of node $\boldsymbol{x}_i$. This procedure is well described in detail in the works of Belinha et al. [183], [189], [190].

It is also visible in Figure B.2-a) that the second degree influence-cell enforces a higher nodal connectivity when compared with the first degree influence-cell. The literature [189],

[191]–[196] states that regardless the studied phenomenon, higher degree influence-cells permit to achieve more accurate solutions.

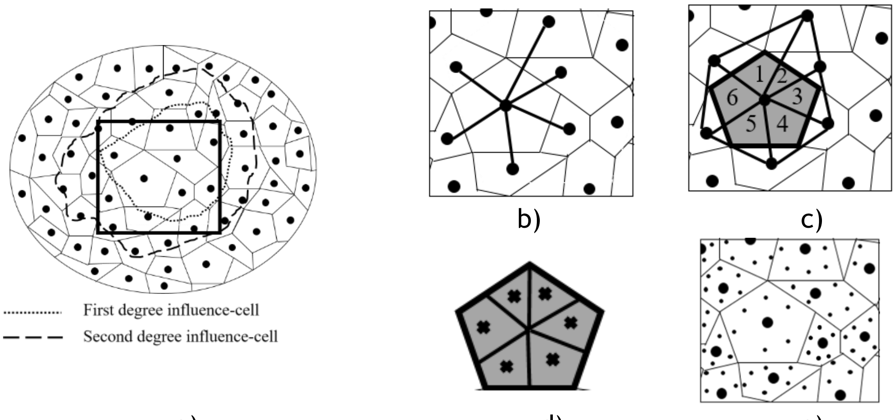

b) c)

a) d) e)

Figure B.2: a) Voronoï Diagram, b) Natural neighbours, c) Sub-cells obtained by the overlap of a cell of the Voronoï diagram and the Delaunay tessellation of that cell, d) Application of the quadrature points (one in each sub-cell) following the Gauss-Legendre integration scheme and e) Mesh of the integration points [157].

B.2 RPI behaviour with irregular nodal distribution

In order to generate an irregular mesh the following procedure is considered [182]. First, a regular mesh is constructed, with all nodes equally spaced and aligned as the mesh example in Figure B.3-a, afterwards all the nodes $x \in \Omega\backslash\Gamma$ are affected with,

$$x_i^{new} = x_i + \frac{\tilde{r}_1.h}{\lambda} cos(2\tilde{r}_2.\pi),\ y_i^{new} = y_i + \frac{\tilde{r}_2.h}{\lambda} sin(2\tilde{r}_2.\pi) \tag{B.3}$$

Being x_i the initial coordinates of node n_i, x_i^{new} the new coordinates obtained for node n_i and h is the inter-nodal distance shown in Figure B.3-a). The random coefficient is defined by $\tilde{r} \approx N(0,1)$ and λ is a parameter that controls the irregularity level of the mesh. The effect of irregularity parameter λ is shown in Figure B.3. Notice, if $\lambda = \infty$ the mesh is perfectly regular, Figure B.3-a), and with decrease of λ, mesh becomes more irregular, Figure B.3-b) and –c).

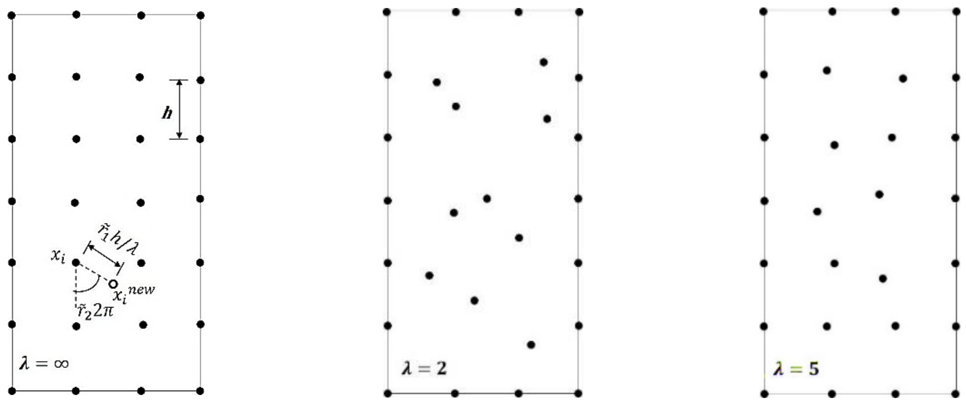

a) b) c)

Figure B.3: a) a 7×4 regular nodal discretization, b) irregular arrangement with λ=2 and c) irregular arrangement with λ=5 [182].

B.3 Integration scheme

In discrete numerical methods using a variational formulation, such as the Galerkin weak formulation, a numerical integration process is required in order to determine the system of equations. In the FEM, the integration mesh is coincident with the element mesh. Since the FEM shape functions are known polynomial functions, the number of integration points per integration cell can be pre-determined using accurate well-known relations [197], [198]. However, in RPIM meshless methods, the shape function degree is generally unknown. Thus, it is not possible to accurately define a priori the background integration mesh.

The numerical integration scheme used in this work follows the recommendation of previous RPIM works [182], [187], [199], [200]. The solid domain is divided in a regular grid forming quadrilateral integration cells. Then, as Figure B.1 illustrates, each grid-cell is filled with 3×3 integration points, respecting the Gauss-Legendre quadrature rule [183]. As previous work [182] showed, this integration scheme is highly efficient.

In the perspective of the numerical integration scheme used in NNRPIM formulation, after the definition of the Voronoï Diagram, Figure B.3-a), it is built the integration mesh required to numerically integrate the differential equation ruling the studied physical phenomenon. One of the numerical advantages of the NNRPIM is the complete dependency of the integration mesh on the nodal discretization, i.e., the integration mesh is constructed using only the information from the nodal spatial field $\boldsymbol{X}$ and from the subsequent Voronoï diagram $\boldsymbol{V}$. Thus, in opposition to the majority of the meshless methods, the NNRPIM only requires the nodal spatial field $\boldsymbol{X}$ in order to determine: the nodal connectivity; the integration mesh; and the interpolation functions. Thus, the NNRPIM formulation can be considered as a truly meshless method.

To obtain the integration mesh, first the area of each Voronoï cell must be subdivided in several sub-areas. In order to perform this subdivision, the Delaunay triangulation [201] is applied, which can be determined by connecting the nodes whose Voronoï cells have common boundaries, as shown in Figure B.3-b).

The Delaunay triangulation permits to divide the original Voronoï cell area, A^{V_j}, of an interest node $\boldsymbol{x}_j$ in k sub-areas $A_k^{V_j}$, being $A^{V_j} = \sum_{i=1}^{k} A_i^{V_j}$, Figure B.3-c). The distribution of integration points inside each sub-area $A_k^{V_j}$, Figure B.3-d), permits to obtain the integration mesh for the Voronoï cell V_j.

Repeating the process for the N Voronoï cells discretizing the problem domain, it is possible to obtain the integration mesh of the entire domain, Figure B.3-e), being $A^{\Omega} = \sum_{j=1}^{n} \sum_{i=1}^{k} A_i^{V_j}$, as suggested in previous NNRPIM works [183], [189]. The distribution of the integration point inside each sub-area $A_k^{V_j}$ follows the Gauss-Legendre quadrature rule. In Figure B.3-d), only one quadrature point was applied in each one of the sub-areas, which is sufficient for the used NNRPIM formulation [183], [189].

B.4 Radial Point Interpolators

The RPIM shape functions are obtained using the Radial Point Interpolators (RPI), which combine radial basis functions with polynomial basis functions. Here, only simplified two-dimensional domains $\Omega \subset \mathbb{R}^2$ are studied, therefore it considers an interpolation function $u^h(\boldsymbol{x})$ defined in an influence-domain $\Omega_I \subset \Omega$ of an interest point $\boldsymbol{x}_I \in \mathbb{R}^2$. The nodal set of the domain is defined in the two-dimensional space by $\boldsymbol{X} = \{\boldsymbol{x}_1, \boldsymbol{x}_2, \dots, \boldsymbol{x}_N\} \wedge \boldsymbol{x}_i \in \mathbb{R}^2$. Thus, the influence domain of an interest point $\boldsymbol{x}_I$ is defined by $\{\boldsymbol{x}_1, \boldsymbol{x}_2, \dots, \boldsymbol{x}_n\} \subset \boldsymbol{X}$, where n is the number of nodes in the influence-domain of $\boldsymbol{x}_I$. The RPI constructs the interpolation function $u^h(\boldsymbol{x})$ capable to pass through all nodes within the influence-domain, meaning that since the nodal function value is assumed to be u_i at the node $\boldsymbol{x}_i$, $u_i = u(\boldsymbol{x}_i)$, consequently $u^h(\boldsymbol{x}_i) = u(\boldsymbol{x}_i)$. Using a radial basis function $r(\boldsymbol{x})$ and polynomial basis function $p(\boldsymbol{x})$, the interpolation function $u^h(\boldsymbol{x})$ can be defined at the interest point $\boldsymbol{x}_I \in \boldsymbol{Q}$ (not necessarily coincident with any $\boldsymbol{x}_i \in \boldsymbol{X}$),

$$u^h(\boldsymbol{x}_I) = \sum_{i=1}^{n} r_i(\boldsymbol{x}_I) a_i + \sum_{j=1}^{m} p_j(\boldsymbol{x}_I) b_j = \boldsymbol{r}(\boldsymbol{x}_I)^T \boldsymbol{a} + \boldsymbol{p}(\boldsymbol{x}_I)^T \boldsymbol{b} = u(\boldsymbol{x}_I) \tag{B.4}$$

Notice that a_i is the non-constant coefficient of $r_i(\boldsymbol{x}_I)$ and b_j is the non-constant coefficient for $p_j(\boldsymbol{x}_I)$. The integers n and m are the number of nodes inside the influence-domain of the interest point $\boldsymbol{x}_I$. The vectors are defined as $\boldsymbol{a}^T = \{a_1, a_2, \dots, a_n\}$, $\boldsymbol{b}^T = \{b_1, b_2, \dots, b_m\}$, $\boldsymbol{r}(\boldsymbol{x})^T = \{r_1(\boldsymbol{x}), r_2(\boldsymbol{x}), \dots, r_n(\boldsymbol{x})\}$ and $\boldsymbol{p}(\boldsymbol{x})^T = \{p_1(\boldsymbol{x}), p_2(\boldsymbol{x}), \dots, p_m(\boldsymbol{x})\}$, in which $\boldsymbol{x}_i = (x_i, y_i)$. This work uses the Multiquadrics Radial Basis Function (MQ-RBF) [183], [202], [203], which can be defined by $r_i(\boldsymbol{x}_I) = s(d_{iI}) = (d_{iI}^2 + c^2)^p$, where d_{iI} is a distance between the interest point $\boldsymbol{x}_I = (x_I, y_I)$ and the node $\boldsymbol{x}_i = (x_i, y_i)$, where $d_{iI} = \sqrt{(x_i - x_I)^2 + (y_i - y_I)^2}$. The parameters c and p are the MQ-RBF shape parameters, which are fixed parameters determined in previous works [183], [191], [204]. The variation of these parameters can affect the performance of the MQ-RBFs. In the work of Wang and Liu [187], [199], it was shown that the optimal values are $c = 1.42$ and $p = 1.03$, which are the values used in this work. The original RPI formulation requires a complete polynomial basis function, following the Pascal's triangle. For instances, for the 2D space the quadratic polynomial basis is defined as $\boldsymbol{p}(\boldsymbol{x}_i)^T = \{1, x_i, y_i, x_i^2, x_i y_i, y_i^2, \dots\}$.

However, it was shown in previous RPI research works [183], [191], [204] that using a simple constant basis increases the RPI formulation efficiency. Thus, in this work only the constant basis is considered $\boldsymbol{p}(\boldsymbol{x}_i) = \{1\}$, for which the number of monomial terms is defined by $m = 1$. The coefficients a_i and b_j in Equation (B.4) are determined by enforcing the interpolation to pass through all n nodes within the influence-domain [183]. The interpolation at the k^{th} node is defined by,

$$u^h(x_k, y_k) = \sum_{i=1}^{n} r_i(x_k, y_k) a_i + \sum_{j=1}^{m} p_j(x_k, y_k) b_j = u_k \quad , \qquad k = 1,2, \dots, n \tag{B.5}$$

The inclusion of the following polynomial term is an extra-requirement that guarantees unique approximation, $\sum_{i=1}^{n} p_j(x_i, y_i)a_i = 0$, $j = 1,2,\dots,m$ [183], [191]. Thus, the computation of the shape functions can be written in a matrix form as

$$\begin{bmatrix} \mathbf{R} & \mathbf{P} \\ \mathbf{P}^T & \mathbf{Z} \end{bmatrix} \begin{Bmatrix} \mathbf{a} \\ \mathbf{b} \end{Bmatrix} = \begin{Bmatrix} \mathbf{u} \\ \mathbf{z} \end{Bmatrix} \Leftrightarrow \mathbf{G} \begin{Bmatrix} \mathbf{a} \\ \mathbf{b} \end{Bmatrix} = \begin{Bmatrix} \mathbf{u} \\ \mathbf{z} \end{Bmatrix} \tag{B.6}$$

Matrix $\mathbf{G}$ is the complete moment matrix, matrix $\mathbf{Z}$ is a null matrix defined as $Z_{ij} = 0, \forall\{\{i,j\} \in \mathbb{N}: \{i,j\} \leq m\}$ and the null vector $\mathbf{z}$ can be represented by $z_i = 0, \forall\{i \in \mathbb{N}: i \leq m\}$, being $\mathbb{N}$ the set of natural numbers. The vector for function values is defined as $u_i = u(\mathbf{x}_i), \forall\{i \in \mathbb{N}: i \leq n\}$. The radial moment matrix $\mathbf{R}$ is represented as $R_{ij} = r_i(\mathbf{x}_j) = \left(d_{ij}^2 + c^2\right)^p$ and the polynomial moment matrix $\mathbf{P}$ is defined $P_{ki} = p_k(\mathbf{x}_i)$. Since the distance is directionless, $r_i(x_j, y_j) = r_j(x_i, y_i)$, i.e. $R_{ij} = R_{ji}$, matrix $\mathbf{R}$ is symmetric. A unique solution is obtained if the inverse of the radial moment matrix $\mathbf{R}$ exists, $\{\mathbf{a} \quad \mathbf{b}\}^T = \mathbf{G}^{-1}\{\mathbf{u} \quad \mathbf{z}\}^T$. The solvability of this system is usually guaranteed by the requirements $rank(p) = m \leq n$ [205]. In this study, the influence-domain will always possess enough nodes to largely satisfy the previously mentioned condition. It is possible to obtain the interpolation with;

$$u^h(\mathbf{x}_I) = \{\mathbf{r}(\mathbf{x}_I)^T; \mathbf{p}(\mathbf{x}_I)^T\}\mathbf{G}^{-1} \begin{Bmatrix} \mathbf{u} \\ \mathbf{z} \end{Bmatrix} = \{\mathbf{\Phi}(\mathbf{x}_I)^T; \mathbf{\Psi}(\mathbf{x}_I)^T\} \begin{Bmatrix} \mathbf{u} \\ \mathbf{z} \end{Bmatrix} \tag{B.7}$$

where the interpolation function vector $\mathbf{\Phi}(\mathbf{x}_I)$ is identified by $\mathbf{\Phi}(\mathbf{x}_I) = \{\varphi_1(\mathbf{x}_I) \quad \varphi_2(\mathbf{x}_I) \quad \dots \quad \varphi_n(\mathbf{x}_I)\}$ and the residual vector $\mathbf{\Psi}(\mathbf{x}_I)$, with no relevant physical meaning, is expressed as: $\mathbf{\Psi}(\mathbf{x}_I) = \{\psi_1(\mathbf{x}_I) \quad \psi_2(\mathbf{x}_I) \quad \dots \quad \psi_n(\mathbf{x}_I)\}$. The RPI test functions $\mathbf{\Phi}(\mathbf{x}_I)$ depend uniquely on the distribution of scattered nodes [183]. Previous works [183], [187], [204] show that RPI test functions possess the Kronecker delta property. Since the acquired RPI test functions have a local compact support it is possible to assemble a well-conditioned and a banded stiffness matrix. If a polynomial basis is included, the RPI test functions have reproducing properties and possess the partition of unity property [183].

B.5 Deformation theory, equation system

If plane stress deformation theory is assumed, a simplified 2D theory suited to analyse the 3D thin plates only submitted to in-plane loads, as Figure B.4 shows. This theory assumed that all displacement and stress components along zz axis can be neglected [105].

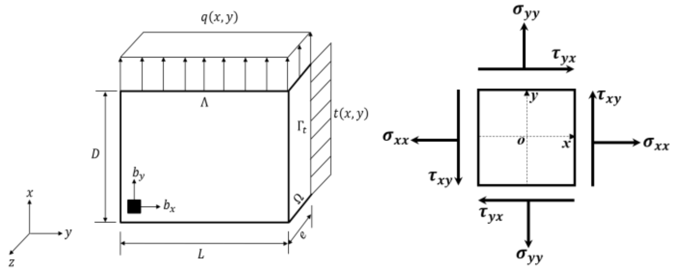

a) b)

Figure B.4: The 3D thin plates and b) stress components in plane stress state [105].

The discrete equation system is obtained using the Galerkin weak-form, which can be expressed as,

$$\int_{\Omega} \delta\boldsymbol{\varepsilon}^T \boldsymbol{\sigma}\, d\Omega = \int_{\Omega} \delta\boldsymbol{u}^T \boldsymbol{b}\, d\Omega + \int_{\Gamma} \delta\boldsymbol{u}^T \boldsymbol{t}\, d\Gamma + \delta\boldsymbol{u}^T \boldsymbol{q} \tag{B.8}$$

Vector $\boldsymbol{b}$ is the body force vector, $\boldsymbol{t}$ is the external traction force vector applied on a natural surface boundary Γ and $\boldsymbol{q}$ represents the external force vector applied locally. The infinitesimal domain $d\Omega$ is defined as $d\Omega = dx.dy.dz$.

In the RPI, the weak form has local support, which means that the discrete system of equations is developed firstly for every influence-domain. After that, the local system of equations is assembled to form the global system of equations, which is solved afterwards. The RPIM trial function is given by Equation (B.7), thus for each degree of freedom, it is possible to write: $u_x^h(\boldsymbol{x_I}) = \sum_{i=1}^{n} \varphi_i\,(\boldsymbol{x_I}) u_x(\boldsymbol{x}_i)$ and $u_y^h(\boldsymbol{x_I}) = \sum_{i=1}^{n} \varphi_i\,(\boldsymbol{x_I}) u_y(\boldsymbol{x}_i)$.

In the abovementioned equations, $\varphi_i(\boldsymbol{x}_I)$ represents the RPIM interpolation function while $u_x(\boldsymbol{x}_i)$ and $u_y(\boldsymbol{x}_i)$ are the nodal parameters of the i^{th} node belonging to the nodal set defined in the influence domain of the interest point $\boldsymbol{x}_I$. Subsequently, it is reasonable to generate a more general equation:

$$\boldsymbol{u}^h(\boldsymbol{x}_I) = \begin{Bmatrix} u_x(\boldsymbol{x}_I) \\ u_y(\boldsymbol{x}_I) \end{Bmatrix} = \sum_{i=1}^{n} \begin{bmatrix} \varphi_i(\boldsymbol{x}_I) & 0 \\ 0 & \varphi_i(\boldsymbol{x}_I) \end{bmatrix} \begin{Bmatrix} u(\boldsymbol{x}_i) \\ v(\boldsymbol{x}_i) \end{Bmatrix} = \sum_{i=1}^{n} \boldsymbol{H}_i\,(\boldsymbol{x}_I)\boldsymbol{u}(\boldsymbol{x}_i) \tag{B.9}$$

Besides, as a result of Equation (B.9), it is possible to develop the strain field equation:

$$\boldsymbol{\varepsilon}(\boldsymbol{x}_I) = \begin{bmatrix} \frac{\partial}{\partial x} & 0 \\ 0 & \frac{\partial}{\partial y} \\ \frac{\partial}{\partial y} & \frac{\partial}{\partial x} \end{bmatrix} \boldsymbol{u}^h(\boldsymbol{x}_I) = \boldsymbol{L}\boldsymbol{u}^h(\boldsymbol{x}_I) = \boldsymbol{L} \textstyle\sum_{i=1}^{n} \boldsymbol{H}_i\,(\boldsymbol{x}_I)\boldsymbol{u}(\boldsymbol{x}_i) \tag{B.10}$$

$$\boldsymbol{\varepsilon}(\boldsymbol{x}_I) = \textstyle\sum_{i=1}^{n} \boldsymbol{B}_i\,(\boldsymbol{x}_I)\boldsymbol{u}(\boldsymbol{x}_i) = \sum_{i=1}^{n} \begin{bmatrix} \frac{\partial \varphi_i(x_I)}{\partial x} & 0 \\ 0 & \frac{\partial \varphi_i(x_I)}{\partial y} \\ \frac{\partial \varphi_i(x_I)}{\partial y} & \frac{\partial \varphi_i(x_I)}{\partial x} \end{bmatrix} \begin{Bmatrix} u_x(\boldsymbol{x}_i) \\ u_y(\boldsymbol{x}_i) \end{Bmatrix} \tag{B.11}$$

The matrix $\boldsymbol{B}$ is the deformation matrix, $\boldsymbol{B} = \boldsymbol{LH}$. As mentioned before, the stress field is a function of the strain vector. Thus, the developed relation of the stress vector for an interest point $(\boldsymbol{x}_I)$ could be written, using the matrix notation, as $\boldsymbol{\sigma}(\boldsymbol{x}_I) = \boldsymbol{C}\,\boldsymbol{\varepsilon}(\boldsymbol{x}_I)$. The material constitutive matrix $\boldsymbol{C}$ is defined as,

$$\boldsymbol{C} = \frac{E}{(1+\nu)(1-\nu)} \begin{bmatrix} 1 & \nu & 0 \\ \nu & 1 & 0 \\ 0 & 0 & \frac{1-\nu}{2} \end{bmatrix} \tag{B.12}$$

The Young's modulus and Poisson's ratio are defined by E and ν, respectively, and e the plate thickness. To evaluate the stiffness matrix, first it is necessary to present the general integration of the weak formulation for any interest point ($\boldsymbol{x}_I$):

$$\delta\boldsymbol{u}^T \int_{\mathrm{A}} e\boldsymbol{B}^T\boldsymbol{C}\boldsymbol{B}\, d\mathrm{A}\, \boldsymbol{u} = \delta\boldsymbol{u}^T \int_{\mathrm{A}} e\boldsymbol{H}^T \begin{Bmatrix} b_x \\ b_y \end{Bmatrix} dA \; + \delta\boldsymbol{u}^T \int_{\Gamma_C} e\boldsymbol{H}^T \begin{Bmatrix} t_x \\ t_y \end{Bmatrix} d\Gamma_C \; + \delta\boldsymbol{u}^T \begin{Bmatrix} q_x \\ q_y \end{Bmatrix} \tag{B.13}$$

Being A the domain area and Γ_C the curve in which $\boldsymbol{t}$ is applied. The linear system of equations based on Equation (B.13) is represented as, $\delta\boldsymbol{u}^T(\boldsymbol{K}\boldsymbol{u} - \boldsymbol{f}_b - \boldsymbol{f}_t - \boldsymbol{f}_q) = 0$, leading to: $\boldsymbol{u} = \boldsymbol{K}^{-1}(\boldsymbol{f}_b + \boldsymbol{f}_t + \boldsymbol{f}_q)$. Since the RPI test functions possess the delta Kronecker property, the essential boundary conditions are directly imposed in the global stiffness matrix.

B.6 Constitutive elastoplastic model

This section focuses on the nonlinear elastoplastic response of materials; therefore, a constitutive law for the plastic components in accordance with deformation fields is described [159]. Hence, the following aspects are essentially noticeable: a yield criterion, counting on the stress proportion correlated with the stress tensor authorising to examine the initiation of the plasticity, a flow rule, it focuses on the affiliation among stress and deformation variation in the plastic routine; and a hardening law, justifying the conditions that the yield surface progressed with the plastic deformation [206].

Generally, a yield criterion can be fashioned by $F(\boldsymbol{\sigma},\kappa) = f(\boldsymbol{\sigma}) - \sigma_Y(\kappa) = 0$ in which κ denotes the hardening coefficient. Besides, $f(\boldsymbol{\sigma})$ presents the yield function recognized as a scalar. Considering $\sigma_Y(\kappa)$ as the yield strength, at a given node, if the stress propels to $f(\boldsymbol{\sigma}) < \sigma_Y(\kappa)$, it implies that this node undergoes an elastostatic behaviour [207], otherwise, it concludes that it enters the plastic state $f(\boldsymbol{\sigma}) = \sigma_Y(\kappa)$, bearing a loading/unloading situation contingent on the flow vector direction [157].

The plasticitification occurs if the second invariant of deviatoric stress overtakes its acute amount in accordance with the isotropic von Mises plasticity criterion. However, it is adopted here for an isotropic material [208]. With the 2D plane stress deformation consideration, von Mises criterion signifies that yielding is experienced if the principal stresses fulfil the yield function;

$$f(\boldsymbol{\sigma}) = \bar{\sigma} = \sqrt{\sigma_{xx}^2 + \sigma_{yy}^2 + \sigma_{xx}\sigma_{yy} + 3\tau_{xy}^2} \tag{B.14}$$

Meanwhile, the plastic flow stands accompanying by yield criterion and associative Prandtl-Reuss flow rule outlines the plastic strain by the below expression,

$$d\boldsymbol{\varepsilon}_p = d\lambda \frac{\partial f}{\partial \boldsymbol{\sigma}} = d\lambda \boldsymbol{a} \tag{B.15}$$

Accordingly, being $d\boldsymbol{\varepsilon}_p$ and $d\lambda$ the plastic strain rate and its multiplier. The flow vector is described by $\boldsymbol{a}$ which is perpendicular to the implemented $f(\boldsymbol{\sigma})$, formulated by Equation (B.14).

The flow vector, $\boldsymbol{a}$, takes the following relationship, $\boldsymbol{a} = \partial f / \partial \boldsymbol{\sigma}$. Following the elastostatic Hooke's law, $\partial \boldsymbol{\sigma}$ and $d\boldsymbol{\varepsilon}_e$ are correlated as,

$$d\boldsymbol{\sigma} = \boldsymbol{c}\, d\boldsymbol{\varepsilon}_e = \boldsymbol{c}\left(d\boldsymbol{\varepsilon} - d\boldsymbol{\varepsilon}_p\right) \tag{B.16}$$

In the mentioned equation, $d\boldsymbol{\varepsilon}_e$ and $d\boldsymbol{\varepsilon}$ are the elastic and total strain rate, respectively while $\boldsymbol{c}$ is the elasticity matrix. In relation to Equation (B.15), and presuming that the yield surface, $F(\boldsymbol{\sigma}, \kappa)$, solely depends on the applied principal stresses magnitude and a hardening parameter κ, $F(\boldsymbol{\sigma}, \kappa) = f(\boldsymbol{\sigma}) - \sigma_Y(\kappa) = 0$, Equation (B.16) would be rearranged as:

$$d\boldsymbol{\sigma} = \boldsymbol{c}(d\boldsymbol{\varepsilon} - d\lambda \boldsymbol{a}) \tag{B.17}$$

It is noticeable that the stress must maintain on yield surface forcing to occur plastic flow. Hence, Equation (B.18) is valid if $A = \frac{1}{d\lambda} \frac{\partial \sigma_Y}{\partial \kappa} d\kappa$ defining an hardening parameter (it mainly relies on the hardening rule [206]). Combining Equations (B.17) and (B.18), $d\lambda$ can be computed as expressed in Equation (B.19). Finally, the stress rate can be established, referring to Equation (B.20).

$$dF = \frac{\partial f}{\partial \boldsymbol{\sigma}} d\boldsymbol{\sigma} - \frac{\partial \sigma_Y}{\partial \kappa} d\kappa = 0, \qquad \text{or} \quad dF = \boldsymbol{a}^T d\boldsymbol{\sigma} - A d\lambda = 0 \tag{B.18}$$

$$d\lambda = \frac{\boldsymbol{a}^T \boldsymbol{c} d\boldsymbol{\varepsilon}}{\boldsymbol{a}^T \boldsymbol{c} \boldsymbol{a} + A} \tag{B.19}$$

$$d\boldsymbol{\sigma} = \boldsymbol{c} d\boldsymbol{\varepsilon} - \frac{\boldsymbol{a}^T \boldsymbol{c} d\boldsymbol{\varepsilon}}{\boldsymbol{a}^T \boldsymbol{c} \boldsymbol{a} + A} \boldsymbol{c} \boldsymbol{a} = \left(\boldsymbol{c} - \frac{\boldsymbol{c} \boldsymbol{a} \boldsymbol{a}^T \boldsymbol{c}}{\boldsymbol{a}^T \boldsymbol{c} \boldsymbol{a} + A}\right) d\boldsymbol{\varepsilon} = \boldsymbol{c}_t d\boldsymbol{\varepsilon} \tag{B.20}$$

Taking into account that $\boldsymbol{c}_t$ is the tangential constitutive matrix. So as for explicitly gaining the hardening term, A, work hardening supposition must be considered [206] with regard to the accompanying flow rule. Due to the linear elastic-linear plastic response, A can be defined as $A = E_{T_0}/[1 - (E_{T_0}/E)]$ [206] where E and E_{T_0} represent the elastic (Young's) and tangential modulus in the reference direction. In addition, the equivalent strain, $\tilde{\varepsilon}$, can take the following form:

$$\tilde{\varepsilon} = \frac{2}{3} \sqrt{\frac{3}{2}\left(e_{xx}^2 + e_{yy}^2 + e_{zz}^2\right) + \frac{3}{4}\left(\gamma_{xy}^2 + \gamma_{yz}^2 + \gamma_{zx}^2\right)} \tag{B.21}$$

where deviatoric strains are;

$$\begin{Bmatrix} e_{xx} \\ e_{yy} \\ e_{zz} \end{Bmatrix} = \frac{1}{3} \begin{bmatrix} 2 & -1 & -1 \\ -1 & 2 & -1 \\ -1 & -1 & 2 \end{bmatrix} \begin{Bmatrix} \varepsilon_{xx} \\ \varepsilon_{yy} \\ \varepsilon_{zz} \end{Bmatrix}, \quad \gamma_{ij} = 2\varepsilon_{ij} \tag{B.22}$$

In numerical analyses, an incremental association for the incremental stress and strain increment can model material characteristics. To oblige stresses rebounding to yield surface, a backward Euler procedure [209] must be involved. Owing to this methodology, the stiffness matrix can be computed straight off in the first iteration of the first load increment due to the displacement enforcement. Figure B.5 schematically depicts the nonlinear solution algorithm associated with K_{T0}. Notice that input data is made up of $\boldsymbol{K}_0$, $\boldsymbol{f}$ referring to Equation (B.13), and an assumed tolerance, *toler*. In accordance with Figure B.5, the proposed formulation reflects the elastoplastic deformation subject, the incremental form associated with the discretized system ($\boldsymbol{Ku} = \boldsymbol{f}$) within an incremental load stated as, $\boldsymbol{K}_T\Delta\boldsymbol{u} - \Delta\boldsymbol{f} = \boldsymbol{f}^{res}$. So, $\boldsymbol{K}_T$ denotes the tangent stiffness matrix, the incremental displacement field stands for $\Delta\boldsymbol{u}$ and $\Delta\boldsymbol{f}$ presents the incremental load vector. Besides, the residual force vector is recognised as $\boldsymbol{f}^{res}$. This procedure follows the Newton-Raphson nonlinear solution method - initial stiffness method combined with an incremental solution (K_{T0}) - to solve the nonlinear equations as described in the former works [157], [209].

```
Input:                 Initial Stiffness matrix: $\boldsymbol{K}_0$
                       Force vector: $\boldsymbol{f}$
                       Tolerance value: $toler$

Increment : i          Displacement increment

      Iteration: n
      Appendix         $\boldsymbol{u^i} = \boldsymbol{K}_0^{-1}\boldsymbol{f}^i$                          Displacement field

        Appendi        $\boldsymbol{\sigma}^i = \boldsymbol{CBu}^i$                              Stress field

                       $f(\boldsymbol{\sigma}) \leq \boldsymbol{\sigma}_Y^0 \xrightarrow{so} \Delta\boldsymbol{\sigma} = \boldsymbol{\sigma}^i$
                                                                  Check the yield
        Appendi        $f(\boldsymbol{\sigma}) > \boldsymbol{\sigma}_Y^0$                              function
                       $\xrightarrow{\text{Stress returning algorithm}} \Delta\boldsymbol{\sigma} = \boldsymbol{\sigma}_r^i$      $\boldsymbol{\sigma}_t^i = \boldsymbol{\sigma}_t^{i-1}\Delta\boldsymbol{\sigma}$

        Appendi        $\boldsymbol{f}_{res}^i = \boldsymbol{f}^i - \int_{\Omega} \boldsymbol{B}^T \Delta\boldsymbol{\sigma} d\,\Omega$                  Residual force

                       Check the residual force:

                       $\frac{(\boldsymbol{f}_{res}^i)^T \boldsymbol{f}_{res}^i}{(\boldsymbol{f}^i)^T \boldsymbol{f}^i} \geq toler \xrightarrow{so} \boldsymbol{f}^i$      Go to the next
        Appendi                    $= \boldsymbol{f}_{res}^i$                     iteration n+1

                       $\frac{(\boldsymbol{f}_{res}^i)^T \boldsymbol{f}_{res}^i}{(\boldsymbol{f}^i)^T \boldsymbol{f}^i} < toler$                   Go to the next
                                                                  increment i+1
  End.
```

Figure B.5: Nonlinear K_{T0} algorithm, it is based on the incremental displacement imposition and stress returning mapping scheme [159].

Appendix C : Damage Formulation

The continuum damage mechanics theory relies on the definition of the effective stress concept associated to the equivalent effective strain. It indicates the strain value related to the damage state, when the stress $\boldsymbol{\sigma}$ applied, is equivalent to the strain obtained from the undamaged state under the effective stress $\overline{\boldsymbol{\sigma}}$.

$$\overline{\boldsymbol{\sigma}} = \boldsymbol{C} : \boldsymbol{\varepsilon} \tag{C.1}$$

Subsequently, effective stress tensor, $\overline{\boldsymbol{\sigma}}$, must be split into tensile and compressive components; $\overline{\boldsymbol{\sigma}} = \overline{\boldsymbol{\sigma}}^{+} + \overline{\boldsymbol{\sigma}}^{-}$ [108]. Equation (C.2) is applicable to split the effective stress tensor through the Macaulay bracket operator $\langle . \rangle$, for more detail see e.g. [107], [110], [210], [211].

$$\overline{\boldsymbol{\sigma}}^{+} = \langle \overline{\boldsymbol{\sigma}} \rangle = \textstyle\sum_{i=1}^{3} \langle \overline{\boldsymbol{\sigma}}_i \rangle \, p_i \otimes p_i \ , \qquad \overline{\boldsymbol{\sigma}}^{-} = \ \rangle \overline{\boldsymbol{\sigma}} \langle \ = \textstyle\sum_{i=1}^{3} \rangle \overline{\boldsymbol{\sigma}}_i \langle \ p_i \otimes p_i \tag{C.2}$$

Considering $\langle \overline{\boldsymbol{\sigma}} \rangle + \rangle \overline{\boldsymbol{\sigma}} \langle = \overline{\boldsymbol{\sigma}}$, it is possible to acquire equivalent effective tensile and compressive norms, which are defined as,

$$\bar{\tau}^{+} = \sqrt{\overline{\boldsymbol{\sigma}}^{+} : \boldsymbol{C}^{-1} : \overline{\boldsymbol{\sigma}}^{+}}, \qquad \bar{\tau}^{-} = \sqrt{\sqrt{3}(\varkappa \bar{\sigma}_{oct}^{-} + \bar{\tau}_{oct}^{-})} \tag{C.3}$$

where $\boldsymbol{C}$ is undamaged fourth order linear elastic constitutive tensor, $\bar{\sigma}_{oct}^{-}$ and $\bar{\tau}_{oct}^{-}$ are the octahedral normal and shear stress terms and $\varkappa$ is a material property depending on the ratio between the biaxial and uniaxial compressive strengths, for concrete materials, the literature recommends $\varkappa = 0.17$ [211]. Moreover, Simo et al. [212] proposed the damage criterion for tensile and compressive states, being the latter known as Drucker-Prager cone for compression. r^{+} and r^{-} present damage thresholds for tension and compression, respectively. Damaged surface expansion must be controlled by mentioned parameters according to:

$$g^{\pm}(\bar{\tau}^{\pm}, r^{\pm}) = \bar{\tau}^{\pm} - r^{\pm} \leq 0 \tag{C.4}$$

Then, the uniaxial tensile and compressive strengths are considered as f_0^{+} and f_0^{-}, respectively and can be used to attain the following initial thresholds,

$$r_0^+ = \sqrt{f_0^+ \frac{1}{E} f_0^+} = \frac{f_0^+}{\sqrt{E}}, \qquad r_0^- = \sqrt{\frac{\sqrt{3}}{3}\left(K - \sqrt{2}\right) f_0^-} \tag{C.5}$$

Notice that damage grows if $\bar{\tau}^+ = r^+$ or $\bar{\tau}^- = r^-$ with regard to the initial conditions: $r_0^\pm = \bar{\tau}^\pm$. Thus, damage is a function of damage thresholds in tensile and compressive states, leading to a rate-independent model [108].

$$r^\pm = \max\left(r_0^\pm, max(\bar{\tau}^\pm)\right), \quad d^\pm = G^\pm(r^\pm) \tag{C.6}$$

Therefore, it is possible to establish the corresponding relations for local damage in both tension d^+ and compression d^- states.

$$d_{local}^+ = G^+(r^+) = 1 - \frac{r_0^+}{r^+}\exp\left(A^+(1 - r^+/r_0^+)\right) \qquad if \qquad r^+ \geq r_0^+ \tag{C.7}$$

$$d_{local}^- = G^-(r^-) = 1 - \frac{r_0^-}{r^-}(1 - A^-) - A^-\exp\left(B^-(1 - r^-/r_0^-)\right) \qquad if \quad r^- \geq r_0^- \tag{C.8}$$

Where A^+, A^- and B^- are the local tensile and compressive damage coefficients, respectively. Regarding A^+, there exists a parameter, so-called "*characteristic length, l_{ch}*" , playing a substantial role in its determination. In the literature, it is possible to find semi-empirical equations to determine the characteristic length [213]-[215]. Precisely, Faria et al. [107], [110], [211] reported that the characteristic length could be defined as follows:

$$l_{ch} = \frac{A^+}{\bar{H}^+(2 + A^+)} \tag{C.9}$$

Notice that $\bar{H}^+$is dependent on the material properties obtained within the following equation:

$$\bar{H}^+ = \frac{(r_0^+)^2}{2G_f^+} = \frac{(f_0^+)^2}{2EG_f^+} \tag{C.10}$$

Therefore, that G_f^+represents the tensile fracture energy per unit area and f_0^+ is the uniaxial tensile strength available for the material in the literature. The corresponding conditions must be satisfied in the problem analysis: $A^+ \geq 0$ and $l_{ch} \leq \frac{1}{\bar{H}^+}$. The importance of l_{ch} is to control the maximum size of the finite elements (in the FEM) or influence domain (in meshless methods). It means that if the size of elements in FEM or discretization in meshless method increases, the softening branch of the response undergoes an almost vertical slope and perhaps the fracture procedure is more brittle [105], [164].

C.1 Non-local damage extension

So far, the standard local constitutive model has been formalized to include damage phenomenon. The non-local damage methodology adopted for this work is here described. Consider an interest point $\boldsymbol{x}_i \in \Omega$. First, a circle with a definite radius, μ, and centred in the interest integration, is assigned covering a certain number of integration points (neighbour points). Then, these neighbour points are picked out to take part in damage localization process, Figure C.1.

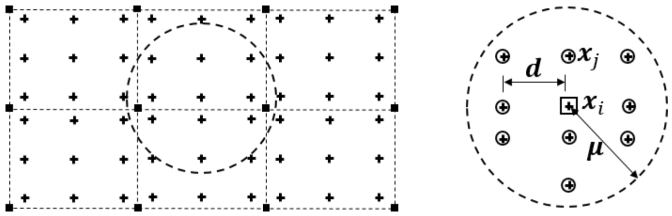

Figure C.1: Arrangement of the interest point and accepted neighbour points for non-local damage process [165].

The radius of this circle is calculated from $\mu = s.h$, therefore, it is dependent on the average distance between nodes, *h*. Assuming that nodes discretizing the problem domain Ω are distributed respecting specific divisions along *x* and *y* directions, *h* is calculated based on the following relation: $h = L/(\text{divisions along}\,x) = D/(\text{divisions along}\,y)$, being L and *D* the dimensions of the specimen along *x* and *y* directions. Furthermore, s is the normalization parameter controlling the corresponding radius varying between 0.5 and 2.1 [216]. Afterwards, the distance between the *i*th interest point $\boldsymbol{x}_i = \begin{Bmatrix} x_i \\ y_i \end{Bmatrix}$ and its *j*th neighbours $\boldsymbol{x}_j = \begin{Bmatrix} x_j \\ y_j \end{Bmatrix}$ must be calculated within the following relation $d_{ij} = \left[(x_i - x_j)^2 + (y_i - y_j)^2 \right]^{0.5}$.This condition must be satisfied as a requirement of proposed non-local damage technique; $d_{ij} < \mu$.

The non-local damage concept requires a weight function, in order to smooth the damage variables in the vicinity of the analysed interest point $\boldsymbol{x}_i$. Here, three weight functions were tested, Table C.1. After defining the neighbour points contributing to the non-local damage value of $\boldsymbol{x}_i$, their weight must be added based on the following relation:

$$w_{total}^{+/-} = \sum_{j=1}^{n} w_j \tag{C.11}$$

Notice that w_j is acquired with the weight functions presented in Table C.1 using the spatial position with respect to $\boldsymbol{x}_i$. It is remarkable that only neighbour point satisfying $d_{ij} < \mu$ will be included in the operation, called accepted neighbour points.

Table C.1: Weight function for non-local damage analysis [165].

Order	Weight Function
0	$w = 1$
2nd	$w = -\frac{(d_{ij})^2}{\mu^2} + 1$
3rd	$w = 2\frac{(d_{ij})^3}{\mu^3} - 3\frac{(d_{ij})^2}{\mu^2} + 1$

Then, the final weighted non-local damage $(w_d^{+/-})$ related to the interest point $\boldsymbol{x}_i$ is acquired by multiplying the local damage of each accepted neighbour point, $d_{local}^{+/-}$, by the corresponding $w_{total}^{+/-}$:

$$\left(w_d^{\pm}\right)_i = \sum_{j=1}^{n}\left(d_{local}^{\pm}\right)_j \times w_{total}^{\pm} \tag{C.12}$$

where n is the number of accepted neighbours within the vicinity of $\boldsymbol{x}_i$. In the end, it is possible to evaluate the non-local damage value for $\boldsymbol{x}_i$ in both tensile and compressive states as follows:

$$d_{\text{non-local}}^{\pm} = \frac{w_d^{\pm}}{w_{total}^{\pm}} \tag{C.13}$$

Considering all presented calculations, it is reasonable to obtain the new Cauchy stress tensor based on the following relation [217]:

$$\boldsymbol{\sigma}_{new} = (1 - d_{non-local}^{+})\overline{\boldsymbol{\sigma}}^{+} + (1 - d_{non-local}^{-})\overline{\boldsymbol{\sigma}}^{-} \tag{C.14}$$

In Equation (C.1), $\overline{\boldsymbol{\sigma}}^{+}$ and $\overline{\boldsymbol{\sigma}}^{-}$ represent the effective stress tensor in tensile and compressive state respectively, calculated from Equation (C.2). To obtain the total damage scalar variable, d_{total}, the equivalent von-Mises stress, $\tilde{\sigma}$, of new Cauchy stress tensor $\boldsymbol{\sigma}_{new}$ must be used. Furthermore, $\tilde{\overline{\sigma}}$ is the equivalent von-Mises effective stress derived from Equation (C.1).

$$d_{total} = 1 - \left(\tilde{\overline{\sigma}}/\tilde{\sigma}\right) \tag{C.15}$$

Since the continuum damage mechanic is an irreversible process in the sense of thermodynamics, the defined constitutive model should be related to a free energy potential such as Helmholtz free energy. The current damage model is based on the uncoupled elasticity theory proposed by Faria and Oliver [211]. The schematic representation of the methodology here presented is shown in Figure C.2.

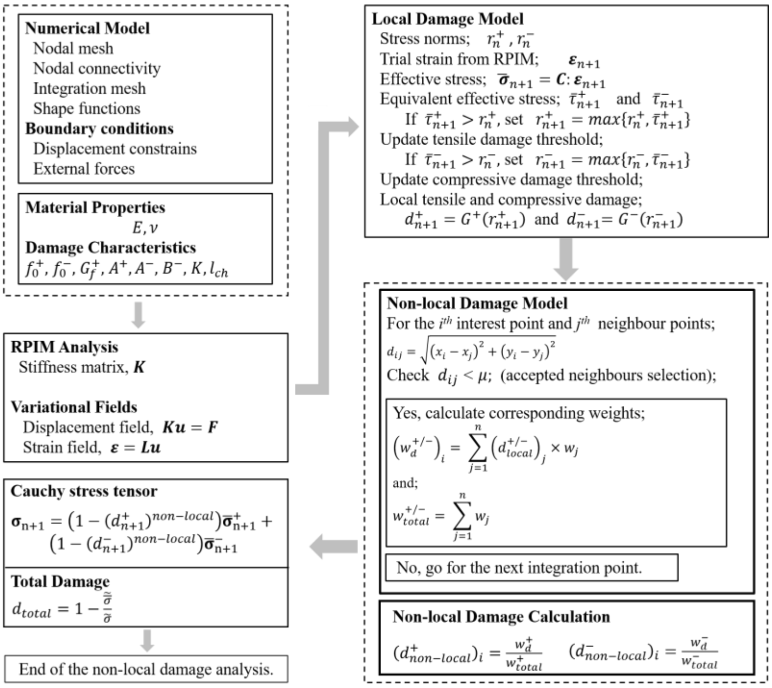

Figure C.2: Numerical algorithm of non-local damage model [165].

Appendix D : SIF Calculation

This part describes different apparoaaches to evaluate the mode I SIF range. It aimed at detemrining the SIF range for the intended fracture specimens tested in this PhD thesis reserch.

D.1 Reference solution, ASTM

According to the ASTM E647 International [162] (Standard Test Method for Measurement of Fatigue Crack Growth Rates), the equation to calculte the SIF range (ΔK_{ASTM}) for CT and MT specimens is given by:

$$\Delta K_{ASTM}^{CT} = \frac{\Delta P}{B\sqrt{W}} \frac{2+\alpha}{(1-\alpha)^{3/2}} (0.886 + 4.64\alpha - 13.32\alpha^2 + 14.72\alpha^3 - 5.6\alpha^4) \qquad \text{(D.1)}$$

$$\Delta K_{ASTM}^{MT} = \frac{\Delta P}{B} \sqrt{\frac{\pi\alpha}{2W} sec \frac{\pi\alpha}{2}} \qquad \text{(D.2)}$$

where $\Delta P = P_{max} - P_{min}$ presents the load range, W is the specimen width, B is the thickness and a is considered as the crack size satisfying the following condition; $\alpha = \frac{a}{W} \geq 0.2$ [162]. The foregoing relationships are valid for the material with linear elastic, isotropic and homogeneous behaviour. The initial crack size and maximum crack extension have been determined where the uncracked ligament (*W*-*a*) was greater than the maximum acceptable SIF [162].

D.2 Williams series expansion

To evaluate the SIF within experiments, a numerical iterative algorithm can be adopted to process the stress field extracted from experimental or numerical analyses, i.e. DIC, FEM and Meshless methods. This function joins the overdeterministic SIF calculation algorithm and the stress computation based on the principal stresses in the vicinity of a straight line in front of the crack under mode I condition. For the plane problem of a homogeneous isotropic solid, Williams series expansion for plane stress state were applicable as demonstrated in the following equations where the implication of K_{I} is represented in Equation (D.3), [218].

$$\sigma_{xx} = \sum_{n=1}^{\infty} \left(A_{\mathrm{I}n} \frac{n}{2}\right) r^{\frac{n}{2}-1} \left\{\left[2 + (-1)^n + \frac{n}{2}\right] cos\left(\frac{n}{2} - 1\right)\theta - \left(\frac{n}{2} - 1\right) cos\left(\frac{n}{2} - 3\right)\theta\right\} \tag{D.3}$$

$$\sigma_{yy} = \sum_{n=1}^{\infty} \left(A_{\mathrm{I}n} \frac{n}{2}\right) r^{\frac{n}{2}-1} \left\{\left[2 - (-1)^n - \frac{n}{2}\right] cos\left(\frac{n}{2} - 1\right)\theta + \left(\frac{n}{2} - 1\right) cos\left(\frac{n}{2} - 3\right)\theta\right\} \tag{D.4}$$

$$\tau_{xy} = \sum_{n=1}^{\infty} \left(A_{\mathrm{I}n} \frac{n}{2}\right) r^{\frac{n}{2}-1} \left\{-\left[(-1)^n + \frac{n}{2}\right] sin\left(\frac{n}{2} - 1\right)\theta + \left(\frac{n}{2} - 1\right) sin\left(\frac{n}{2} - 3\right)\theta\right\} \tag{D.5}$$

$$A_{\mathrm{I}1} = \frac{K_{\mathrm{I}}}{\sqrt{2\pi}} \tag{D.6}$$

D.3 Nonlinear overdeterministic algorithm

The nonlinear overdeterministic algorithm is applicable to compute SIFs. Any numerical and experimental analysis can produce stress/strain fields as a result. Considering one such a result Φ which is a function of some unknowns $A_{\mathrm{I}1}, A_{\mathrm{I}2}, \dots A_{\mathrm{I}n}$, it can be expressed as: $\Phi = f(A_{\mathrm{I}1}, A_{\mathrm{I}2}, \dots A_{\mathrm{I}n})$. This equation could be linear or nonlinear in the unknowns. If the dependence is nonlinear, hence the equation could be solved with an iterative procedure based on the Newton-Raphson method [219]. Considering one as g_k;

$$\mathrm{g}_k(A_{\mathrm{I}1}, A_{\mathrm{I}2}, \dots A_{\mathrm{I}n}) = f(A_{\mathrm{I}1}, A_{\mathrm{I}2}, \dots A_{\mathrm{I}n}) - \Phi \tag{D.7}$$

Taylor’s series expansion of Equation (D.7) gives:

$$(\mathrm{g}_k)_{i+1} = (\mathrm{g}_k)_i + \left(\frac{\partial \mathrm{g}_k}{\partial \mathrm{A}_{\mathrm{I}1}}\right)\Delta\mathrm{A}_{\mathrm{I}1} + \left(\frac{\partial \mathrm{g}_k}{\partial \mathrm{A}_{\mathrm{I}2}}\right)\Delta\mathrm{A}_{\mathrm{I}2} + \cdots + \left(\frac{\partial \mathrm{g}_k}{\partial \mathrm{A}_{\mathrm{I}n}}\right)\Delta\mathrm{A}_{\mathrm{I}n} \tag{D.8}$$

where *i* is the iteration step and $\Delta\mathrm{A}_{\mathrm{I}n}$ are the corrections to the previous estimates of $\mathrm{A}_{\mathrm{I}n}$. Since the desired result is obtained if $= 0$, an iterative equation is presented in the following form:

$$\left(\frac{\partial \mathrm{g}_k}{\partial \mathrm{A}_{\mathrm{I}1}}\right)\Delta\mathrm{A}_{\mathrm{I}1} + \left(\frac{\partial \mathrm{g}_k}{\partial \mathrm{A}_{\mathrm{I}2}}\right)\Delta\mathrm{A}_{\mathrm{I}2} + \cdots + \left(\frac{\partial \mathrm{g}_k}{\partial \mathrm{A}_{\mathrm{I}n}}\right)\Delta\mathrm{A}_{\mathrm{I}n} = -(\mathrm{g}_k)_i \tag{D.9}$$

If the Φ results obtained from M various points, thus M functions $\mathrm{g}_k(k = 1, \dots M)$ are obtained. Hence, the matrix from of Equation (D.9) is: $[\Delta] = \{[B]^T . [B]\}^{-1} . [B]^T . [\mathrm{g}]$. In which;

$$[\Delta] = \begin{Bmatrix} \Delta\mathrm{A}_{\mathrm{I}1} \\ \Delta\mathrm{A}_{\mathrm{I}2} \\ \cdot \\ \cdot \\ \cdot \\ \Delta\mathrm{A}_{\mathrm{I}n} \end{Bmatrix}; [\mathrm{g}] = \begin{Bmatrix} \mathrm{g}_1 \\ \mathrm{g}_2 \\ \cdot \\ \cdot \\ \cdot \\ \mathrm{g}_M \end{Bmatrix}; B = \begin{bmatrix} \partial\mathrm{g}_1/\partial\mathrm{A}_{\mathrm{I}1} & \partial\mathrm{g}_1/\partial\mathrm{A}_{\mathrm{I}2} & \dots & \partial\mathrm{g}_1/\partial\mathrm{A}_{\mathrm{I}n} \\ \partial\mathrm{g}_2/\partial\mathrm{A}_{\mathrm{I}1} & \partial\mathrm{g}_2/\partial\mathrm{A}_{\mathrm{I}2} & & \partial\mathrm{g}_2/\partial\mathrm{A}_{\mathrm{I}n} \\ & \vdots & & \vdots \\ \partial\mathrm{g}_M/\partial\mathrm{A}_{\mathrm{I}1} & \partial\mathrm{g}_M/\partial\mathrm{A}_{\mathrm{I}2} & \cdots & \partial\mathrm{g}_M/\partial\mathrm{A}_{\mathrm{I}n} \end{bmatrix} \tag{D.10}$$

The solution of the matrix equation yields the correction terms for the prior estimated coefficients. Therefore, the estimates of the unknowns are revised as:

$$(\Delta\mathrm{A}_{\mathrm{I}n})_{i+1} = (\mathrm{A}_{\mathrm{I}n})_i + \Delta\mathrm{A}_{\mathrm{I}n} \tag{D.11}$$

D.4 Stress-free dead zone and compliance method

Concerning the practically stress-free or dead zone, on removing it from a finite element mesh of a plate carrying a singularity, as for example, a side edge crack; it is possible to use alternative tools for SIF evaluation, as is the case of the Compliance Method. Griffith [220] employed an energy-balance approach that has become one of the most famous developments in material science. The strain energy per unit volume of stressed material is:

$$U^* = \frac{1}{V}\int P dx = \int \frac{P}{A}\frac{dx}{L} = \int \boldsymbol{\sigma} d\varepsilon \tag{D.12}$$

Assuming linear elastic material behavior, $\boldsymbol{\sigma} = E\boldsymbol{\varepsilon}$, hence, strain energy per unit volume is;

$$U^* = \frac{E\varepsilon^2}{2} = \frac{\sigma^2}{2E} \tag{D.13}$$

A simple manner to visualize the corresponding strain energy release, as shown by the red line in Figure D.1-a) is to regard two triangular regions near the crack flanks, of width a up to the crack length and height βa, as being completely unloaded, while the remaining material continues to experience the full stress $\boldsymbol{\sigma}$. The parameter β can be selected so that the method in discussion could compatibilize with the Griffith's solution, and it turns out that for MT specimens in plane stress state, $\beta \cong 1.2$ an assumption only. Considering the plate thickness as unity, the total strain energy U released is then the strain energy per unit volume times the volume in both triangular regions as follows;

$$U = -\frac{\sigma^2}{2E}\beta a^2 \tag{D.14}$$

Furthermore, in accordance with LEFM theory, the dead stress zone does not contribute to the cracking resistance and is accountable for a minimum deformation field during fatigue crack growth, which can be neglected for fracture growth.

From the theoretical point of view, the compliance method follows the Irwin-Kies' relation [221]. Irwin [222] presented an energy-based methodology for fracture mechanics which is fundamentally equivalent to Griffith's model [220], except that Irwin's method is in a more convenient form for solving engineering problems. Irwin defined a parameter G as the *Strain Energy Release Rate*, which is the amount of the energy available for a crack extension's increment. It is the rate of change in potential energy with the crack area. Since G is obtained from the partial derivative of a potential. It is also called the crack extension force or the crack driving force. It is convenient at this point to introduce the compliance (C), which is the inverse of the plate stiffness given by;

$$C = \Delta/P \tag{D.15}$$

where P is the load applied at a point of the cracked plate such that the crack opens a displacement $\varDelta$ measured at the load P application point. Hence, G for a wide plate in plane stress with a crack of length $2a$ can take the following form [223]:

$$G = \frac{P^2}{2B}\frac{dC}{da} \tag{D.16}$$

Based on the LEFM theory, it is possible to acquire the mode I SIF for the cracked specimen in the plane stress state as follows [224].

$$K_I^2 = EG \tag{D.17}$$

As illustrated in Figure D.1-c), referring to the trapezoid region (redline area, ahead of the dead zone), it is considered that $w = W/2 = 15.0\ \mathrm{mm}$. Due to the symmetry assumption, only half of the model is considered, which accounts for one side of the crack, thus, the dominant applied force should be considered as $P' = P/2$. Therefore, the displacement variation is dependent on the uncrakced ligament $(w - a)$ and by a simple computation, it can be achieved with the integral contribution of an element of dy where: $w(y) = w - a + y/\beta$.

Consequently, it is conceivable to obtain the intended stress field in the trapezoid area (uncracked ligament) as follows;

$$\sigma(y) = \frac{P'}{w(y)B} = \frac{P}{2B(w - a + y/\beta)} \tag{D.18}$$

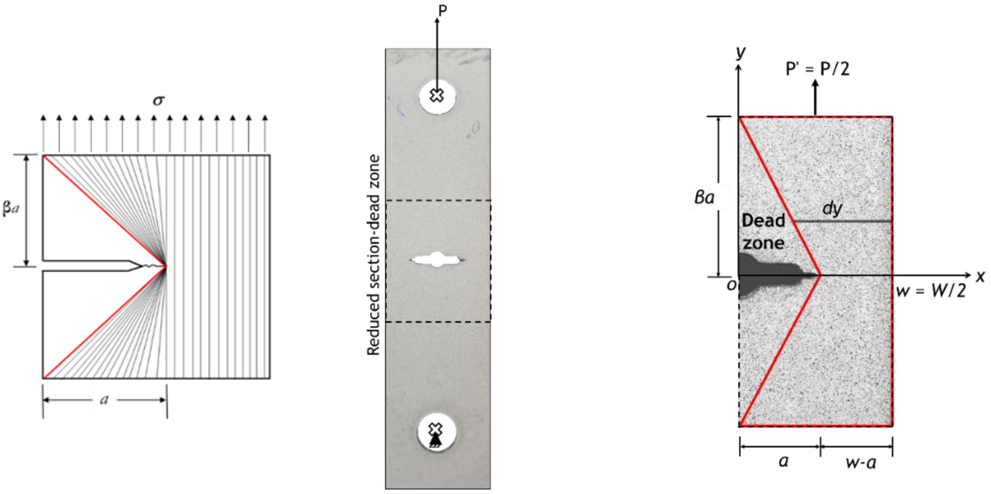

a) b) c)

Figure D.1: a) Ideal unloaded region, the red highlighted region depicts the stress dead zone, b) central notch MT specimen and c) dead zone characteristics [163].

In relation to Equation (D.15);

$$\varepsilon(y) = \frac{P}{2EB(w - a + y/\beta)} \tag{D.19}$$

and the v-displacement over y-axis, normal to crack line, can be evaluated by the expression below:

$$v(x,y) = \frac{P}{2EB}\int_0^{\beta a} \frac{dy}{(w-a+y/\beta)} \tag{D.20}$$

In relation to Equation (D.15), compliance function can be computed as $C = v/P' = 2v/P$. Partial derivatives related to crack length evolution can be calculated as:

$$C = \frac{2v(x,y)}{P} = \frac{1}{EB}\int_0^{\beta a} \frac{dy}{(w-a+y/\beta)} \tag{D.21}$$

$$\frac{\partial C}{\partial a} = \frac{1}{EB}\int_0^{\beta a} \frac{dy}{(w-a+y/\beta)^2} = \frac{1}{EB}\frac{\beta a}{w(w-a)} \tag{D.22}$$

It must be noted that a is a variable in the integrand while it is assumed as a fixed and geometric characteristic of the structure (the crack length) in the integral limits. Substituting Equation (D.22) into Equation (D.16), G can be reformulated as,

$$G = \frac{P^2}{2B}\frac{\partial C}{\partial a} = \frac{P^2}{2EB^2}\int_0^{\beta a} \frac{dy}{(w-a+y/\beta)^2} = \frac{P^2}{2EB^2}\frac{\beta a}{w(w-a)} \tag{D.23}$$

Afterward, mode I SIF (K_I^{CMP}) for the MT specimen is obtained following Equation (D.17) through the compliance function associated to the dead zone;

$$K_I^{CMP} = \sqrt{EG} = \frac{P}{B}\sqrt{\frac{\beta a}{2w(w-a)}} \tag{D.24}$$

Appendix E : Gurson- Tvergaard-Needleman Damage Criterion

Fundamentally, in damage mechanics, the simplest criteria assume that the fracture takes place if the equivalent plastic strain $\bar{\varepsilon}^p$ reaches a critical value $\bar{\varepsilon}_f^p$, where the equivalent plastic strain is defined as the integral of the equivalent plastic strain rate expressed as;

$$\bar{\varepsilon}^p = \int_0^t \dot{\bar{\varepsilon}}^p dt \tag{E.1}$$

where $\dot{\bar{\varepsilon}}^p$ is the plastic strain rate tensor can be calculated as;

$$\dot{\bar{\varepsilon}}^p = \sqrt{\frac{2}{3}\dot{\varepsilon}^p : \dot{\varepsilon}^p} \tag{E.2}$$

Although many commercial programs comprise this alternative as a failure criterion, it is an old criterion, and lacks the generality necessary for nonlinear analyses. In the fracture and failure mechanics, it is possible to find some essential failure criteria such as Cockcroft-Latham [225]; Wilkins [226]; Johnson-Cook [227] and Xue-Wierzbicki [228]. Microscopic voids in ductile materials play a crucial role in various fracture mechanisms. In some cases, fracture is a direct consequence of the continued growth of voids with stretching, since finally the voids coalesce. Amongst others and based on an analysis of a void in a rigid – plastic matrix, Gurson [229] established a model of porous plastic material. Nevertheless, the material softening could be modelled relying on the void volume fraction (VVF). Likewise, micro-structural criterion of ductile materials accounted for a significant task to analyse the material degradation. As an extensively implemented coupled model, the GTN model was projected by Gurson [229]. Afterwards, new parameters were introduced and the model was modified by Tvergaard [230]. However, the constitutive model was defined relying on the following equation:

$$\Phi = \left(\frac{\tilde{\sigma}}{\sigma_m}\right)^2 + 2q_1 f^* cosh\left(-\frac{3}{2}\frac{q_2\sigma_h}{\sigma_m}\right) - \left(1 + q_3 {f^*}^2\right) = 0 \tag{E.3}$$

where $\tilde{\sigma} = \left(\frac{3}{2}S_{ij}S_{ij}\right)^{0.5}$ and $\sigma_h = \frac{1}{3}\sigma_{ii}$ are accordingly the equivalent von Mises and hydrostatic stress terms. Besides, $S_{ij} = \sigma_{ij} - 1/3\,\sigma_{kk}\delta_{ij}$ presents the deviatoric elements of Cauchy stress and the Kronecker delta denotes δ_{ij}. Moreover, the equivalent stress associated with the matrix material is identified as $\boldsymbol{\sigma_m}$. Concerning other parameters, Tvergaard and Needleman [230], [231] proposed the total effective void volume fraction as f^*. Three supplementary fitting material coefficients, being calibration parameters, were considered as q_1, q_2 and q_3 demonstrating void interaction impacts. In numerous cases, it was found that $q_1 \times q_2 = 1.5$, and $q_3 = q_1^2$. Here, these have been adopted as proposed in the former study [230]. The matrix equivalent plastic strain can take the following form in accordance with the plastic work principle,

$$(1-f)\sigma_m \mathrm{d}\tilde{\varepsilon}_m^p = \boldsymbol{\sigma}\colon \mathrm{d}\boldsymbol{\varepsilon^p} \tag{E.4}$$

In which, $\mathrm{d}\tilde{\varepsilon}_m^p$ and $\mathrm{d}\boldsymbol{\varepsilon^p}$ denote the increment of equivalent plastic strain associated to the matrix material and the plastic strain, respectively. From Equation (E.3), f^* stands as a function of the VVF, f; so, f^* accounted for zero if the material is undamaged. The modified porosity function can be defined as,

$$f^* = f \quad if \quad f \le f_c \quad \text{and} \quad f^* = f_c + \kappa(f - f_c) \quad if \quad f > f_c \tag{E.5}$$

Where the initiation of the void nucleation is characterized by f_c and it thereby describes the critical VVF at the onset of voids coalescence when f starts to diverge from f^*. Parameter κ, can be computed as $\kappa = \frac{f_u - f_c}{f_f - f_c}$, is an acceleration factor related to the void propagation. In which, $f_u = 1/q_1$ corresponds to the ultimate value of VVF as the stress carrying capability leads to zero. Moreover, f_f is the total VVF at the final failure. Notice that the critical VVF at which void coalescence first occurs that is when the damage value reaches its critical value f_c, fracture begins to propagate [232], [233]. Besides, it must be remarked that f_c and f_f properties can be found in the literature for the selected material.

The change in the void volume fraction (df) during an increment of deformation consists of two parts; one due to the growth of existing voids, df_{growth}, and the other due to the nucleation of new voids, $df_{nucleation}$, referring to Equation (E.6). Owing the incompressible state of matrix material, df_{growth} which is related to the existing voids' growth, can be connected to the hydrostatic term of $\boldsymbol{\varepsilon^p}$, as Equation (E.6) demonstrates.

$$df = df_{growth} + df_{nucleation} \text{ where } df_{growth} = (1-f)\mathbf{d}\boldsymbol{\varepsilon^p}\colon \boldsymbol{I} \tag{E.6}$$

In which $\boldsymbol{I}$ denotes the second order unit tensor. Besides, the void nucleation might be either strain or stress persuaded. In the current analysis, plastic strain controlled nucleation rule is taken into account. Hence, the nucleation VVF variation can take the following form [234]:

$$df_{nucleation} = \mathcal{A}\mathrm{d}\tilde{\varepsilon}_m^p \text{ where } \mathcal{A} = \frac{f_N}{S_N\sqrt{2\pi}}\exp\left\{-\frac{1}{2}\left[\frac{\tilde{\varepsilon}_m^p-\varepsilon_N}{S_N}\right]\right\}^2 \tag{E.7}$$

In the above equation, $\mathcal{A}$ represents the nucleation ratio of VVFs, and $\mathrm{d}\tilde{\varepsilon}_m^p$ denotes the plastic strain rate. Besides, f_N is the volume fraction of particles existing for void nucleation, in which the mean void nucleation strain is presented as ε_N and the standard deviation is defined as S_N [3]. These parameters are known as the void nucleation criteria that can be found in the literature for the corresponding material.

In order to evaluate the stress triaxiality factor (TF) which is the ratio of hydrostatic pressure, or mean stress, to the von Mises equivalent stress, the following equation can be used to compute TF,

$$TF = \frac{\sigma_h}{\tilde{\sigma}} = \frac{{}^1\!/_3(\sigma_1+\sigma_2+\sigma_3)}{\frac{1}{\sqrt{2}}\sqrt{(\sigma_1-\sigma_2)^2+(\sigma_2-\sigma_3)^2+(\sigma_3-\sigma_1)^2}} \tag{E.8}$$

where σ_1, σ_2 and σ_3 are principal stresses. The equivalent von Mises strain ($\tilde{\varepsilon}$) can be derived throughout the simplified formulation for the 2D plane stress state as follows [160]:

$$\tilde{\varepsilon} = \frac{2}{3}\sqrt{\frac{3}{2}\left(e_{xx}^2 + e_{yy}^2 + e_{zz}^2\right) + \frac{3}{4}\left(\gamma_{xy}^2\right)} \tag{E.9}$$

Where deviatoric strains are;

$$\begin{Bmatrix} e_{xx} \\ e_{yy} \\ e_{zz} \end{Bmatrix} = \frac{1}{3}\begin{bmatrix} 2 & -1 & -1 \\ -1 & 2 & -1 \\ -1 & -1 & 2 \end{bmatrix}\begin{Bmatrix} \varepsilon_{xx} \\ \varepsilon_{yy} \\ \varepsilon_{zz} \end{Bmatrix}, \quad \gamma_{ij} = 2\varepsilon_{ij} \tag{E.10}$$

References

[1] V. A. Cristino, J. P. Magrinho, G. Centeno, M. B. Silva, and P. A. Martins, “A digital image correlation based methodology to characterize formability in tube forming,” *The Journal of Strain Analysis for Engineering Design*, vol. 54, no. 2, pp. 139–148, Feb. 2019.

[2] T. M. Fayyad and J. M. Lees, “Application of Digital Image Correlation to reinforced concrete fracture,” *Procedia Materials Science*, vol. 3, pp. 1585–1590, 2014.

[3] B. V. Farahani, J. Belinha, R. Amaral, P. J. Tavares, and P. Moreira, “A digital image correlation analysis on a sheet AA6061-T6 bi-failure specimen to predict static failure,” *Engineering Failure Analysis*, vol. 90, pp. 179–196, 2018.

[4] A. H. Salmanpour and N. Mojsilović, “Application of Digital Image Correlation for strain measurements of large masonry walls,” 2013.

[5] S. Bagavathiappan, B. B. Lahiri, T. Saravanan, J. Philip, and T. Jayakumar, “Infrared thermography for condition monitoring - A review,” 2013.

[6] J. B. Rauch and R. E. Rowlands, “Thermoelastic Stress Analysis,” in *Springer Handbook of Experimental Solid Mechanics (A.S. Kobayashi, Ed.)*, 2008, pp. 743–767.

[7] P. Brémond, “New developments in Thermo Elastic Stress Analysis by Infrared Thermography,” in *IV Conferencia Panamericana de END*, 2007.

[8] N. Rajic, A. K. Wong, and Y. C. Lam, “A Thermomechanical Technique for Measuring Residual Stress,” *Experimental Techniques*, vol. 20, no. 2, pp. 25–27, Mar. 1996.

[9] R. House, L. Holness, I. Taraschuk, and R. Nisenbaum, “Infrared thermography in the hands and feet of hand-arm vibration syndrome (HAVS) cases and controls,” *International Journal of Industrial Ergonomics*, vol. 62, pp. 70–76, 2017.

[10] D. Wu and C. Busse, “Lock-in thermography for nondestructive evaluation of materials,” *Revue générale de thermique*, vol. 37, no. 8, pp. 693–703, 1998.

[11] C. Balaguer and J. G. Victores, “Robotic tunnel inspection and repair,” in *Technology Innovation in Underground Construction*, CRC Press, 2010, pp. 445–460.

[12] J. H. Wang, “Lifecycle cost and performance analysis for repair of concrete tunnels,” *Eco-efficient Repair and Rehabilitation of Concrete Infrastructures*, pp. 637–672, 2018.

[13] P. H. Emmons and B. W. Emmons, *Concrete repair and maintenance illustrated : problem analysis, repair strategy, techniques*. R.S. Means Co, 1993.

[14] A. M. Lateef, “Analysis of the Common Defects on In-Service Urban Tunnels and Repairing Effects,” Chongqing University, 2011.

[15] T. Asakura, Y. Kojima, and S. Onoda, “Developmentof reinforcement and repair methods for railway tunnel,” *Q. Rep. RTRI*, vol. 32, no. 3, pp. 163–172, 1991.

[16] J. A. Richards, “Inspection, Maintenance and Repair of Tunnels: International Lessons and Practice,” *Tunnelling and Underground Space Technology*, vol. 13, no. 4, pp. 369–375, 1998.

[17] J. A. Richards, “Inspection, maintenance and repair of tunnels: International lessons and practice,” *Tunnelling and Underground Space Technology*, vol. 13, no. 4, pp. 369–375, 1998.

[18] G. Mays, *Durability of concrete structures : investigation, repair, protection*. E & FN Spon, 1992.

[19] Federal Highway Administration (FHWA) and Federal Transit Administration, “Highway and Rail Transit Tunnel Inspection Manual, U.S. Department of Transportation,” 2005.

[20] B. Maidl, M. Thewes, and U. Maidl, *Handbook of tunnel engineering*, 1st ed. Wiley, 2013.

[21] O. Büyüköztürk, “Imaging of concrete structures,” *NDT & E International*, vol. 31, no. 4, pp. 233–243, 1998.

[22] P. Ferreira, M. S. Martins, and L. R. e Sousa, “Rehabilitation of Lapa tunnel, Metro do Porto,” *Underground Works under Special Conditions*, vol. 1, pp. 63–70, 2007.

[23] L. R. Sousa, C. Jorge, and A. Vieira, “Inspection and safety control of Portuguese railway tunnels. Trindade, São Bento, Seminário II, China II, Tamel, Caminha, Régua and Bagaúste tunnels,” Lisbon, Portugal, 2003.

[24] L. R. Sousa, M. Oliveira, L. N. Lamas, and C. Silva, “Maintenance and repair of

underground structures: Case studies in Portugal," in *Symposium EUROCK*, 2004, pp. 355–360.

[25] C. Silva, L. R. Sousa, and E. Portela, "Behaviour analysis of the São Bento tunnel: application of a knwledge based system," in *Symposium NARMS-TAC*, 2002, pp. 1507–1513.

[26] Federal Highway Administration:, "Tunnel Operations, Maintenance, Inspection and Evaluation (TOMIE)," 2010.

[27] L. P. Hsu and S. L. Weng, "The geological treatment for railway tunnel after seismic damage – a case study of Sanyi no. 1 railway tunnel," *Treatment Technology of Engineering Geology on Tunnel*, pp. 125–153, 2000.

[28] X. Zhang, Y. Jiang, and S. Sugimoto, "Seismic damage assessment of mountain tunnel: A case study on the Tawarayama tunnel due to the 2016 Kumamoto Earthquake," *Tunnelling and Underground Space Technology*, vol. 71, pp. 138–148, 2018.

[29] T. Asakura and Y. Kojima, "Tunnel maintenance in Japan," *Tunnelling and Underground Space Technology*, vol. 18, pp. 161–169, 2003.

[30] H. Mashimo, "State of the road tunnel safety technology in Japan," *Tunnelling and Underground Space Technology*, vol. 17, no. 2, pp. 145–152, 2002.

[31] T. Cronvall, "Laser Scanning of Railway Tunnels," Helsinki, 2014.

[32] C. H. Dowding and A. Rozan, "Damage to Rock Tunnels from Earthquake Shaking," *Journal of the Geotechnical Engineering Division*, vol. 104, no. 2, pp. 175–191, 1978.

[33] S. Sharma and W. R. Judd, "Underground opening damage from earthquakes," *Engineering Geology*, vol. 30, no. 3–4, pp. 263–276, 1991.

[34] T. Asakura and Y. Sato, "Damage to mountain tunnels in hazard area," *International journal of soils and foundations*, vol. 36, pp. 301–310, 1996.

[35] H. Yu, J. Chen, A. Bobet, and Y. Yuan, "Damage observation and assessment of the Longxi tunnel during the Wenchuan earthquake," *Tunnelling and Underground Space Technology incorporating Trenchless Technology Research*, vol. 54, pp. 102–116, 2016.

[36] H.-M. Chen, C. Ulianov, and R. Shaltout, "3D Laser Scanning Technique for the Inspection and Monitoring of Railway Tunnels," *Transport Problems*, vol. 10, no. SE, pp. 73–84, 2015.

[37] F. Railroad Administration and N. Jersey Transit, "Chapter 3: Construction Methods and Activities," 2017.

[38] L. Higgs, "New Hudson River rail tunnels needed so old tunnels can be repaired," *NJ.com*, 2014. [Online]. Available: https://www.nj.com/news/index.ssf/2014/10/new_hudson_river_rail_tunnels_needed_so_old_tunnels_can_be_repaired.html.

[39] L. Hengna, "Haflong Times: Crack In Tunnel No.10 of Newly Conversed B.G. Railway," *Haflong Times*, 2016. [Online]. Available: https://haflongtimes.blogspot.com/2016/05/crack-in-tunnel-no10-of-newly-conversed.html.

[40] R. Montero, J. G. Victores, S. Martínez, A. Jardón, and C. Balaguer, "Past, present and future of robotic tunnel inspection," *Automation in Construction*, vol. 59, pp. 99–112, 2015.

[41] International Atomic Energy Agency, *Guidebook on Non-destructive Testing of Concrete Structures*, 1st ed., no. 17. Vienna, 2002.

[42] A. Basu and A. Aydin, "A method for normalization of Schmidt hammer rebound values," *International Journal of Rock Mechanics and Mining Sciences*, vol. 41, no. 7, pp. 1211–1214, 2004.

[43] V. M. Malhotra, "Evaluation of the Windsor probe test for estimating compressive strength of concrete," *Matériaux et Construction*, vol. 7, no. 1, pp. 3–15, 1974.

[44] L. Binda and C. Tiraboschi, "Flat-Jack Test: A slightly destructive technique for the diagnosis of brick and stone masonry structures," *International Journal for Restoration of Buildings and Monuments*, vol. 5, no. 5, pp. 449–472, 1999.

[45] P. Lourenço and P. Gregorczyk, "Review on Flat-Jack Testing," *Engenharia Civil*, vol. 9, pp. 35–50, 2000.

[46] K. Mori, A. Spagnoli, Y. Murakami, G. Kondo, and I. Torigoe, "A new non-contacting non-destructive testing method for defect detection in concrete," *NDT & E International*, vol. 35, no. 6, pp. 399–406, 2002.

[47] M. Sansalone and N. J. Carino, “Detecting Delaminations in Concrete Slabs With and Without Overlays Using the Impact-Echo Method,” *ACI Materials Journal*, vol. 86, no. 2, pp. 175–184, 1989.

[48] M. J. Sansalone and W. B. Streett, *Impact-echo. Nondestructive evaluation of concrete and masonry*. Bullbrier Press, 1997.

[49] N. J. Carino, “The Impact-Echo Method: An Overview,” in *the 2001 Structures Congress & Exposition. Washington, DC, American Society of Civil Engineers*, 2001, p. 18.

[50] T. C. Powers, “Measuring Young’s modulus of elasticity by means of sonic vibrations,” *Proceedings American Society for Testing and MaterialsAmerican Society for Testing and Materials*, vol. 38, no. Part II, p. 460, 1938.

[51] L. Obert, “Sonic method of determining the modulus of elasticity of building materials under pressure,” *Proc. ASTM*, vol. 39, p. 987, 1939.

[52] H. Toutanji, “Ultrasonic wave velocity signal interpretation of simulated concrete bridge decks,” *Materials and Structures*, vol. 33, no. 3, pp. 207–215, 2000.

[53] J. Blitz and G. Simpson, *Ultrasonic methods of non-destructive testing*. Chapman & Hall, 1996.

[54] J. Makar and R. Desnoyers, “Magnetic field techniques for the inspection of steel under concrete cover,” *NDT & E International*, vol. 34, no. 7, pp. 445–456, 2001.

[55] G. Sawade and H.-J. Krause, “Inspection of Prestressed Concrete Members using the Magnetic Leakage Flux Measurement Method — Estimation of Detection Limit,” *Advances in Construction Materials*, pp. 639–649, 2007.

[56] R. B. Polder, “Test methods for on site measurement of resistivity of concrete — a RILEM TC-154 technical recommendation,” *Construction and Building Materials*, vol. 15, no. 2–3, pp. 125–131, 2001.

[57] J. F. Lataste, C. Sirieix, D. Breysse, and M. Frappa, “Electrical resistivity measurement applied to cracking assessment on reinforced concrete structures in civil engineering,” *NDT & E International*, vol. 36, no. 6, pp. 383–394, 2003.

[58] W. J. McCarter and Ø. Vennesland, “Sensor systems for use in reinforced concrete structures,” *Construction and Building Materials*, vol. 18, no. 6, pp. 351–358, 2004.

[59] E. Nakamura, H. Watanabe, H. Koga, M. Nakamura, and K. Ikawa, “Half-Cell Potential Measurements to Assess Corrosion Risk of Reinforcement Steels in a PC Bridge,” in *RILEM Symposium on On Site Assessment of Concrete, Masonry and Timber Structures - SACoMaTiS*, 2008, pp. 109–117.

[60] N. P. Avdelidis and A. Moropoulou, “Applications of infrared thermography for the investigation of historic structures,” *Journal of Cultural Heritage*, vol. 5, no. 1, pp. 119–127, 2004.

[61] G. Parkinson and C. Ékes, “Ground penetrating radar evaluation of concrete tunnel linings,” in *12th International Conference on Ground Penetrating Radar-Birmingham, UK*, 2008, p. 11.

[62] X. Xie and C. Zeng, “Non-destructive evaluation of shield tunnel condition using GPR and 3D laser scanning. In: Ground Penetrating Radar (GPR),” in *14th International Conference on IEEE*, 2012, pp. 479–484.

[63] J. Hugenschmidt and R. Mastrangelo, “GPR inspection of concrete bridges,” *Cement and Concrete Composites*, vol. 28, no. 4, pp. 384–392, 2006.

[64] D. . McCann and M. . Forde, “Review of NDT methods in the assessment of concrete and masonry structures,” *NDT & E International*, vol. 34, no. 2, pp. 71–84, 2001.

[65] O. Büyüköztürk, “Imaging of concrete structures,” *NDT & E International*, vol. 31, no. 4, pp. 233–243, Aug. 1998.

[66] Y.-K. Zhu, G.-Y. Tian, R.-S. Lu, and H. Zhang, “A review of optical NDT technologies,” *Sensors*, vol. 11, no. 8, pp. 7773–7798, 2011.

[67] C. Colla, M. Krause, C. Maierhofer, H.-J. Höhberger, and H. Sommer, “Combination of NDT techniques for site investigation of non-ballasted railway tracks,” *NDT & E International*, vol. 35, no. 2, pp. 95–105, 2002.

[68] R. Medina, J. Llamas, J. Gómez-García-Bermejo, E. Zalama, and M. J. Segarra, “Crack Detection in Concrete Tunnels Using a Gabor Filter Invariant to Rotation.,” *Sensors (Basel, Switzerland)*, vol. 17, no. 7, 2017.

[69] E. Protopapadakis *et al.*, “Autonomous Robotic Inspection in Tunnels,” *ISPRS Annals of*

Photogrammetry, Remote Sensing and Spatial Information Sciences, vol. III–5, pp. 167–174, 2016.

[70] K. Loupos *et al.*, "Robotic intelligent vision and control for tunnel inspection and evaluation - The ROBINSPECT EC project," in *2014 IEEE International Symposium on Robotic and Sensors Environments (ROSE) Proceedings*, 2014, pp. 72–77.

[71] C. Balaguer, R. Montero, J. G. Victores, S. Martínez, and A. Jardón, "Towards Fully Automated Tunnel Inspection: A Survey and Future Trends," 2014.

[72] A. Mohan and S. Poobal, "Crack detection using image processing: A critical review and analysis," *Alexandria Engineering Journal*, vol. 57, no. 2, pp. 787–798, 2018.

[73] S.-N. Yu, J.-H. Jang, and C.-S. Han, "Auto inspection system using a mobile robot for detecting concrete cracks in a tunnel," *Automation in Construction*, vol. 16, no. 3, pp. 255–261, 2007.

[74] M. Ukai, "Technology for Measurement and Diagnosis. Development of Image Processing Technique for Detection of Tunnel Wall Deformation Using Continuously Scanned Image," *Quarterly Report of RTRI*, vol. 41, no. 3, pp. 120–126, 2000.

[75] H. Huang, Q. Li, and D. Zhang, "Deep learning based image recognition for crack and leakage defects of metro shield tunnel," *Tunnelling and Underground Space Technology*, vol. 77, pp. 166–176, 2018.

[76] T. Xu, L. Xu, X. Li, and J. Yao, "Detection of Water Leakage in Underground Tunnels Using Corrected Intensity Data and 3D Point Cloud of Terrestrial Laser Scanning," *IEEE Access*, vol. 6, pp. 32471–32480, 2018.

[77] R. Klette, *Concise Computer Vision*. London: Springer London, 2014.

[78] Pedro de Deus Vieira Buschinelli, "Desenvolvimento de um sistema óptico por triangulação cônica para inspeção do perfil interno de dutos," Federal De de Santa Catarina, 2007.

[79] A. Albertazzi, M. R. Viotti, P. Buschinelli, A. Hoffmann, and W. Kapp, "Residual stresses measurement and inner geometry inspection of pipelines by optical methods," in *SEM Annual Conference on Experimental and Applied Mechanics*, 2011, vol. 8, pp. 1–12.

[80] P. D. V Buschinelli, G. A. B. Landeira, C. Kohler, A. Albertazzi, and G. B. Teixeira Da Silva, "A GPU based real-time image processing for an axis-symmetrical optical laser triangulation system," in *SPIE - The International Society for Optical Engineering*, 2012, vol. 8498.

[81] P. D. V Buschinelli, J. R. C. Melo, A. Albertazzi, J. M. C. Santos, and C. S. Camerini, "Optical profilometer using laser based conical triangulation for inspection of inner geometry of corroded pipes in cylindrical coordinates," in *SPIE - The International Society for Optical Engineering*, 2013, vol. 8788.

[82] P. Buschinelli, T. Pinto, F. Silva, J. Santos, and A. Albertazzi, "Laser Triangulation Profilometer for Inner Surface Inspection of 100 millimeters (4″) Nominal Diameter," in *Physics: Conference Series*, 2015, vol. 648, no. 1.

[83] S. Fekete, M. Diederichs, and M. Lato, "Geotechnical and operational applications for 3-dimensional laser scanning in drill and blast tunnels," *Tunnelling and Underground Space Technology*, vol. 25, no. 5, pp. 614-628, 2010.

[84] C. Stentoumis, K. Loupos, A. Doulamis, and A. Amditis, "A Computer Vision System for Tunnel Inspection," in *SEE Tunnel:Promoting Tunneling in SEE Region*, 2015.

[85] M. Pejić, "Design and optimisation of laser scanning for tunnels geometry inspection," *Tunnelling and Underground Space Technology*, vol. 37, pp. 199–206, 2013.

[86] J. Laurent, R. Fox-Ivey, F. Sanchez Dominguez, J. Antonio, and R. Garcia, "Use of 3D Scanning Technology for Automated Inspection of Tunnels," in *the World Tunnel Congress*, 2014, pp. 1–10.

[87] W. Qiu and Y.-J. Cheng, "High-Resolution DEM Generation of Railway Tunnel Surface Using Terrestrial Laser Scanning Data for Clearance Inspection," *Journal of Computing in Civil Engineering*, vol. 31, no. 1, pp. 1–13, 2017.

[88] M. Xiao, Z. Qi, and H. Shi, "The Surface Flattening based on Mechanics Revision of the Tunnel 3D Point Cloud Data from Laser Scanner," *Procedia Computer Science*, vol. 131, pp. 1229–1237, 2018.

[89] A. Haack, J. Schreyer, and G. Jackel, "State-of-the-art of non-destructive testing methods for determining the state of a tunnel lining," *Tunnelling and Underground Space Technology*, vol. 10, no. 4, pp. 413–431, 1995.

[90] B. V. Farahani, P. J. Sousa, F. Barros, P. J. Tavares, and P. M. G. P. Moreira, "Advanced image based methods for structural integrity monitoring: Review and prospects," in *AIP Conference Proceedings*, 2018, vol. 1932.

[91] M. A. Sutton, S. R. McNeill, J. D. Helm, and Y. J. Chao, "Advances in Two-Dimensional and Three-Dimensional Computer Vision," in *Photomechanics*, Berlin, Heidelberg: Springer Berlin Heidelberg, 2000, pp. 323-372.

[92] T. Ramos *et al.*, "2D and 3D Digital Image Correlation in Civil Engineering – Measurements in a Masonry Wall," *Procedia Engineering*, vol. 114, pp. 215–222, 2015.

[93] L. Areias, S. Iliopoulos, L. Pyl, and J. Gu, "Recent experience with the use of DIC and AE to monitor surface cracking in a cylindrical concrete buffer," 2013.

[94] J.-F. Destrebecq, E. Toussaint, and E. Ferrier, "Analysis of Cracks and Deformations in a Full Scale Reinforced Concrete Beam Using a Digital Image Correlation Technique," *Experimental Mechanics*, vol. 51, pp. 879–890, 2011.

[95] D. Lei, Z. Huang, P. Bai, and F. Zhu, "Experimental research on impact damage of Xiaowan arch dam model by digital image correlation," *Construction and Building Materials*, vol. 147, pp. 168–173, 2017.

[96] S. Gali and K. V. L. Subramaniam, "Investigation of the dilatant behavior of cracks in the shear response of steel fiber reinforced concrete beams," *Engineering Structures*, vol. 152, pp. 832–842, 2017.

[97] A. Rimkus, A. Podviezko, and V. Gribniak, "Processing Digital Images for Crack Localization in Reinforced Concrete Members," *Procedia Engineering*, vol. 122, pp. 239–243, 2015.

[98] M. Nahant, S. Paez, and J. Van Leeuwen, "DEFBETIR Detection by infrared thermography of the heat signature of diseases and defects in concrete structures of civil engineering," in *QIRT 2010 - 10th International Conference on Quantitative InfraRed Thermography*, 2010.

[99] F. Weritz, R. W. Arndt, M. Röllig, and H. Maierhofer, C., Wiggenhauser, "Investigation of concrete structures with pulse phase thermography," *Materials and Structures,* vol. 38, pp. 843–849, 2010.

[100] S. Eslami, B. V. Farahani, P. J. Tavares, and P. M. G. P. Moreira, "Fatigue behaviour evaluation of dissimilar polymer joints: Friction stir welded, single and double-rivets," *International Journal of Fatigue*, vol. 113, pp. 351–358, 2018.

[101] B. V. Farahani, P. J. Tavares, P. M. G. P. Moreira, and J. Belinha, "Stress intensity factor calculation through thermoelastic stress analysis, finite element and RPIM meshless method," *Engineering Fracture Mechanics*, vol. 183, pp. 66–78, 2017.

[102] B. V. Farahani, P. J. Tavares, and P. M. G. P. Moreira, "SIF Determination with Thermoelastic Stress Analysis," in *Procedia Structural Integrity*, 2016, vol. 2, pp. 2148–2155.

[103] P. Yu, H. Wu, C. Liu, and Z. Xu, "Water Leakage Diagnosis in Metro Tunnels by Integration of Laser Point Cloud and Infrared Thermal Imaging," *ISPRS - International Archives of the Photogrammetry, Remote Sensing and Spatial Information Sciences*, vol. XLII-3, pp. 2167–2171, 2018.

[104] C. Shufei and H. Hongwei, "Monitoring Methods of Long-term Water Seepage in Shield Tunnel," *Chinese Journal of Underground Space and Engineering*, vol. 10, no. 3, pp. 733–738, 2014.

[105] B. V. Farahani, J. Belinha, F. M. Andrade Pires, and P. M. G. P. Moreira, "The Simulation of Concrete Materials Using a Damage Model Combined with an Advanced Discretization Meshless Technique," in *Material Modelling: Applications, Challenges and Research; Series in Mechanical Engineering Theory and Applications*, 1st ed., André Ferreira Costa Vieira, Ed. New York: Nova Science Publishers, Inc, 2017, pp. 249-303.

[106] G. Voyiadjis and Z. Taqieddin, "Elastic Plastic and Damage Model for Concrete Materials: Part I-Theoretical Formulation," *International Journal of Structural Changes in Solids*, vol. 1, no. 1, pp. 31–59, 2009.

[107] R. Faria, J. Oliver, and M. Cervera, "A strain-based plastic viscous-damage model for massive concrete structures," *International Journal of Solids and Structures*, vol. 35, no. 14. pp. 1533–1558, 1998.

[108] M. Cervera, J. Oliver, and O. Manzoli, "A Rate-dependent Isotrpic Damage Model for

Seismic Analysis of Concrete Dams," *Earthquake Engineering and Structural Dynamics*, vol. 25, pp. 987–1010, 1996.

[109] J. Oliver, M. Cervera, S. Oller, and J. Lubliner, "Isotropic Damage Models and Smeared Crack Analysis of Concrete," in *the 2nd Conference on Computer Aided Analysis and Design of Concrete Structures*, pp. 945–957.

[110] M. Cervera, J. Oliver, and R. Faria, "Seismic evaluation of concrete dams via continuum damage models," *Earthquake Engineering & Structural Dynamics*, vol. 24, no. 9, pp. 1225–1245, 1995.

[111] W. He, Y.-F. Wu, K. M. Liew, and Z. Wu, "A 2D total strain based constitutive model for predicting the behaviors of concrete structures," *International Journal of Engineering Science*, vol. 44, no. 18-19, pp. 1280–1303, 2006.

[112] R. C. Yu, G. Ruiz, and E. W. V Chaves, "A comparative study between discrete and continuum models to simulate concrete fracture," *Engineering Fracture Mechanics*, vol. 75, no. 1, pp. 117–127, 2008.

[113] J. Lee and G. L. Fenves, "A return-mapping algorithm for plastic-damage models: 3-D and plane stress formulation," *International Journal for Numerical Methods in Engineering*, vol. 50, no. 2, pp. 487–506, 2001.

[114] X. Tao and D. V. Phillips, "A simplified isotropic damage model for concrete under bi-axial stress states," *Cement and Concrete Composites*, vol. 27, no. 6, pp. 716–726, 2005.

[115] J. Y. Wu, J. Li, and R. Faria, "An energy release rate-based plastic-damage model for concrete," *International Journal of Solids and Structures*, vol. 43, no. 3–4, pp. 583–612, 2006.

[116] V. S. Gopalaratnam and S. P. Shah, "Softening response of plain concrete in direct tension," *Journal Proceedings*, vol. 82, no. 3, pp. 310–323, 1985.

[117] I. D. Karsan and J. O. Jirsan, "Behavior of Concrete Under Compressive Loadings," *Journal of the Structural Devision*, vol. 95, no. ST12, pp. 2543–2563, 1969.

[118] H. Kupfer, H. K. Hilsdorf, and H. Rusch, "Behavior of Concrete Under Biaxial Stresses," *Journal of the American Concrete Institute*, vol. 66, no. 8, pp. 656–666, 1969.

[119] J. Malvar and G. Warren, "Fracture Energy for Three-Point Bend Tests on Single-Edge Notched Beams," *Naval Civil Engineering Laboratory*, no. March, pp. 1–28, 1988.

[120] A. R. Khan, A. H. Al-Gadhib, and M. H. H. Baluch, "Elasto-damage Model for High Strength Concrete Subjected to Multiaxial Loading," *International Journal of Damage Mechanics*, vol. 16, no. 3, pp. 361–398, 2007.

[121] J. Mazars and G. Pijaudier-Cabot, "Continuum Damage Theory —Application to Concrete," *Journal of Engineering Mechanics*, vol. 115, no. 2, pp. 345–365, 1989.

[122] K. Willam, I. Rhee, and G. Beylkin, "Multiresolution analysis of elastic degradation in heterogeneous materials," *Meccanica*, vol. 36, no. 1, pp. 131–150, 2001.

[123] C. Comi and U. Perego, "Fracture energy based bi-dissipative damage model for concrete," *International Journal Of Solids And Structures*, vol. 38, no. 36–37, pp. 6427–6454, 2001.

[124] Y. Labadi and N. E. Hannachi, "Numerical Simulation of Brittle Damage in Concrete," *Strength of Materials*, pp. 268–281, 2005.

[125] S.-N. Roth, P. Léger, and A. Soulaïmani, "A combined XFEM–damage mechanics approach for concrete crack propagation," *Computer Methods in Applied Mechanics and Engineering*, vol. 283, pp. 923–955, 2015.

[126] B. V. Farahani, J. Belinha, F. M. A. Pires, and A. J. M. Ferreira, "A radial point interpolation meshless method extended with an elastic rate-independent continuum damage model for concrete materials," *Mechanics of Advanced Materials and Structures*, vol. 25, no. 10, pp. 855–867, 2018.

[127] B. V. Farahani, J. Belinha, F. M. Andrade Pires, A. J. M. Ferreira, and P. M. G. P. Moreira, "Extending a radial point interpolation meshless method to non-local constitutive damage models," *Theoretical and Applied Fracture Mechanics*, vol. 85, no. Part (A), pp. 84–98, 2016.

[128] T. Kamel, C. Silvani, and P. Breul, "Numerical modelling of the deterioration of the Parisian metro infrastructures based on a new auscultation method," *Structure and Infrastructure Engineering*, vol. 13, no. 10, pp. 1284–1293, 2017.

[129] G. Kampas, J. A. Knappett, M. J. Brown, I. Anastasopoulos, N. Nikitas, and R. Fuentes, "The effect of tunnel lining modelling approaches on the seismic response of sprayed

concrete tunnels in coarse-grained soils," *Soil Dynamics and Earthquake Engineering*, vol. 117, pp. 122–137, 2019.

[130] S. Kiryu, Y. Murono, and H. Morikawa, "Seismic response of a cut-and-cover tunnel isolated by polymer material," *Earthquake Engineering & Structural Dynamics*, vol. 41, no. 14, pp. 2043–2057, 2012.

[131] J. H. A. Rocha and Y. V Póvoas, "Infrared thermography as a non-destructive test for the inspection of reinforced concrete bridges: A review of the state of the art," *Revista ALCONPAT*, vol. 7, no. 3, pp. 200–214, 2017.

[132] C.-C. Lu and J.-H. Hwang, "Damage analysis of the new Sanyi railway tunnel in the 1999 Chi-Chi earthquake: Necessity of second lining reinforcement," *Tunnelling and Underground Space Technology*, vol. 73, pp. 48–59, 2018.

[133] Q. Yang and Z. Wang, "Information-Based Construction of High-Speed Railway Tunnel," *Shock and Vibration*, vol. 2017, pp. 1–11, 2017.

[134] S. Saloustros, M. Cervera, and L. Pelà, "Challenges, Tools and Applications of Tracking Algorithms in the Numerical Modelling of Cracks in Concrete and Masonry Structures," *Archives of Computational Methods in Engineering*, pp. 1–45, 2018.

[135] M. Varma, V. B. Maji, and A. Boominathan, "Numerical modeling of a tunnel in jointed rocks subjected to seismic loading," *Underground Space*, 2018.

[136] A. Bobet and H. Yu, "Seismic distortions of a deep circular tunnel in elastic slightly anisotropic ground," *Underground Space*, vol. 2, no. 2, pp. 134–147, 2017.

[137] D. Park, M. Sagong, D.-Y. Kwak, and C.-G. Jeong, "Simulation of tunnel response under spatially varying ground motion," *Soil Dynamics and Earthquake Engineering*, vol. 29, no. 11–12, pp. 1417–1424, 2009.

[138] P. Chaimahawan, C. Hansapinyo, P. Phuriwarangkhakul, and P. Phuriwarangkhakul, "Test and Finite Element Analysis of Gravity Load Designed Precast Concrete Wall Under Reversed Cyclic Loads," *Engineering Journal*, vol. 22, no. 2, pp. 185–200, 2018.

[139] S. Fabozzi, V. Licata, S. Autuori, E. Bilotta, G. Russo, and F. Silvestri, "Prediction of the seismic behavior of an underground railway station and a tunnel in Napoli (Italy)," *Underground Space*, vol. 2, no. 2, pp. 88–105, 2017.

[140] T. Cronvall, "Maintenance of railway tunnels in Finland," Helsinki, 2014.

[141] Railway Technical Research Institute (RTRI), "Design Manual of countermeasure to deteriorated tunnel," 2000.

[142] J. L. Clarke and P. Waldron, *The reinforcement of concrete structures with advanced composites*, vol. 74, no. 17. Institution of Structural Engineers, 1996.

[143] G. Tiberti, F. Minelli, and G. Plizzari, "Reinforcement optimization of fiber reinforced concrete linings for conventional tunnels," *Composites Part B: Engineering*, vol. 58, pp. 199–207, 2014.

[144] K. Kiriyama *et al.*, "Structure and Construction Examples of Tunnel Reinforcement Method Using Thin Steel Panels," 2005.

[145] Z. Wu, H. Yuan, Y. Kojima, and E. Ahmed, "Experimental and analytical studies on peeling and spalling resistance of unidirectional FRP sheets bonded to concrete," *Composites Science and Technology*, vol. 65, no. 7–8, pp. 1088–1097, 2005.

[146] I. Puente, B. Akinci, H. González-Jorge, L. Díaz-Vilariño, and P. Arias, "A semi-automated method for extracting vertical clearance and cross sections in tunnels using mobile LiDAR data," *Tunnelling and Underground Space Technology*, vol. 59, pp. 48–54, 2016.

[147] A. Caratelli, A. Meda, Z. Rinaldi, S. Spagnuolo, and G. Maddaluno, "Optimization of GFRP reinforcement in precast segments for metro tunnel lining," *Composite Structures*, vol. 181, pp. 336–346, 2017.

[148] B. V. Farahani, J. Berardo, J. Belinha, A. J. M. Ferreira, P. J. Tavares, and P. Moreira, "An Optimized RBF Analysis of an Isotropic Mindlin Plate in Bending," *Procedia Structural Integrity*, vol. 5, pp. 584–591, 2017.

[149] B. V. Farahani, J. Berardo, J. Belinha, A. J. M. Ferreira, P. J. Tavares, and P. M. G. P. Moreira, "On the optimal shape parameters of distinct versions of RBF meshless methods for the bending analysis of plates," *Engineering Analysis with Boundary Elements*, vol. 84, pp. 77–86, 2017.

[150] M. A. Sutton, J. J. Orteu, and H. Schreier, *Image Correlation for Shape, Motion and*

Deformation Measurements; Basic Concepts,Theory and Applications. 2009.

[151] W. Dong, Z. Wu, X. Zhou, L. Dong, and G. Kastiukas, "FPZ evolution of mixed mode fracture in concrete: Experimental and numerical," *Engineering Failure Analysis*, vol. 75, pp. 54–70, 2017.

[152] L. Marsavina, D. M. Constantinescu, E. Linul, T. Voiconi, and D. A. Apostol, "Shear and mode II fracture of PUR foams," *Engineering Failure Analysis*, vol. 58, pp. 465–476, 2015.

[153] B. V. Farahani, R. Amaral, J. Belinha, P. J. Tavares, and P. Moreira, "A GTN Failure Analysis of an AA6061-T6 Bi-Failure Specimen," *Procedia Structural Integrity*, vol. 5, pp. 981–988, 2017.

[154] B. V. Farahani, J. Belinha, P. J. Tavares, and P. M. G. P. Moreira, "An Elasto-plastic Analysis of a DP600 Bi-Failure Specimen: Digital Image Correlation, Finite Element and Meshless Methods," *Procedia Structural Integrity*, vol. 5, pp. 1237–1244, 2017.

[155] B. V. Farahani, J. Belinha, P. J. Tavares, and P. M. G. P. Moreira, "On the Non-linear Elasto-Plastic Behavior of AA6061-T6: Experimental and Numerical Implementations," *Procedia Structural Integrity*, vol. 5, pp. 468–475, 2017.

[156] ASTM International, *ASTM E8M-04 Standard Test Methods for Tension Testing of Metallic Materials*. United States, ASTM International, 2008.

[157] B. V. Farahani, J. Belinha, R. Amaral, P. J. Tavares, and P. M. P. G. Moreira, "Extending radial point interpolating meshless methods to the elasto-plastic analysis of aluminium alloys," *Engineering Analysis with Boundary Elements*, vol. 100, pp. 101–117, 2019.

[158] E. Voce, "The relationship between stress and strain for homogeneous deformations," *Journal of the Institute of Metals*, vol. 74, pp. 537–562, 1948.

[159] B. V Farahani, J. Belinha, P. J. Tavares, and P. M. Moreira, "A nonlinear simulation of a bi-failure specimen through improved discretisation methods: A validation study," *The Journal of Strain Analysis for Engineering Design*, vol. 53, no. 8, pp. 616–629, 2018.

[160] B. V. Farahani, J. Belinha, P. J. Tavares, and P. M. G. P. Moreira, "Elastoplastic response and failure assessment of steel alloys: Empirical and computational analyses," *Fatigue & Fracture of Engineering Materials & Structures*, vol. 42, no. 6, pp. 1247–1261, 2019.

[161] B. V. Farahani, P. J. Tavares, J. Belinha, and P. Moreira, "Compact tension fracture specimen: Experimental and computational implementations on stress intensity factor," *The Journal of Strain Analysis for Engineering Design*, vol. 53, no. 8, pp. 630–647, 2018.

[162] ASTM International, *ASTM E647 - 15 Standard Test Method for Measurement of Fatigue Crack Growth Rates*. United States: ASTM International, 2015.

[163] B. V. Farahani, S. Eslami, F. Q. de Melo, P. J. Tavares, and P. M. G. P. Moreira, "Concept of Stress Dead Zone in Cracked Plates: Theoretical, Experimental and Computational Studies," *Fatigue & Fracture of Engineering Materials & Structures*, vol. In Press, 2019.

[164] B. V. Farahani, J. Belinha, F. M. A. Pires, A. J. M. Ferreira, and P. M. G. P. Moreira, "A meshless approach to non-local damage modelling of concrete," *Engineering Analysis with Boundary Elements*, vol. 79, pp. 62–74, 2017.

[165] B. V. Farahani, F. M. Andrade Pires, P. M. G. P. Moreira, and J. Belinha, "A meshless method in the non-local constitutive damage models," *Procedia Structural Integrity*, vol. 1, pp. 226–233, 2016.

[166] L. N. Lowes, "Finite Element Modeling of Reinforced Concrete Beam-Column Bridge Connections_Chapter 5," University of California, Berkeley, 1999.

[167] J. Legendre, "Prevision de la ruine des structures en beton par une approche combinee : mecanique de l'endommagement-mecanique de la rupture.," Universite Paris 6 - LMT Cachan, 1984.

[168] J. Mazars and G. Pijaudier-Cabot, "From damage to fracture mechanics and conversely: A combined approach," *International Journal of Solids and Structures*, vol. 33, no. 20–22, pp. 3327–3342, 1996.

[169] Z. Zhang, "Camera Calibration," in *Emerging Topics in Computer Vision*, G. Medioni and S. Bing Kang, Eds. 2005, p. 653.

[170] Z. Zhang, "A Flexible New Technique for Camera Calibration," *IEEE Transactions on Pattern Analysis and Machine Intelligence*, vol. 10, no. 2211, pp. 1330–1334, 1998.

[171] J. J. More, "Levenberg--Marquardt algorithm: implementation and theory," in *Conference on numerical analysis*, 1977.

[172] Zhengyou Zhang, "Flexible camera calibration by viewing a plane from unknown

orientations," in *Proceedings of the Seventh IEEE International Conference on Computer Vision*, 1999, pp. 666–673 vol.1.

[173] Y. Zhu, Z. Zhang, Y. Zhu, X. Huang, and Q. Zhuang, "Capturing the cracking characteristics of concrete lining during prototype tests of a special-shaped tunnel using 3D DIC photogrammetry," *European Journal of Environmental and Civil Engineering*, vol. 22, no. sup1, pp. s179–s199, 2018.

[174] M. Corsini, P. Cignoni, and R. Scopigno, "Efficient and Flexible Sampling with Blue Noise Properties of Triangular Meshes," *IEEE Transactions on visualization and computer graphics*, vol. 18, no. 6, pp. 914–926, 2012.

[175] B. V. Farahani *et al.*, "A coupled 3D laser scanning and digital image correlation system for geometry acquisition and deformation monitoring of a railway tunnel," *Tunnelling and Underground Space Technology*, vol. 91, p. 102995, 2019.

[176] P. P. Cacciari and M. M. Futai, "Mapeamento de Descontinuidades Geológicas em Túneis Utilizando Imagens Geradas por Scanner a Laser 3D," in *Mecânica das Rochas para Recursos Naturais e Infraestrutura SBMR 2014 – Conferência Especializada ISRM*, 2014, pp. 1–8.

[177] P. P. Cacciari and M. M. Futai, "Modeling a Shallow Rock Tunnel Using Terrestrial Laser Scanning and Discrete Fracture Networks," *Rock Mechanics and Rock Engineering*, vol. 50, no. 5, pp. 1217–1242, 2017.

[178] P. P. Cacciari and M. M. Futai, "Mapping and characterization of rock discontinuities in a tunnel using 3D terrestrial laser scanning," *Bulletin of Engineering Geology and the Environment*, vol. 75, no. 1, pp. 223–237, 2016.

[179] B. V. Farahani, F. Barros, M. A. Popescu, P. J. Sousa, P. J. Tavares, and P. Moreira, "Geometry Acquisition and 3D Modelling of a Wind Tower using a 3D Laser Scanning Technology," *Procedia Structural Integrity*, vol. 17, pp. 712–717, 2019.

[180] O. Faugeras, *Three-dimensional computer vision : a geometric viewpoint*. MIT Press, 1993.

[181] J. J. Moré, "The Levenberg-Marquardt algorithm: Implementation and theory," in *Lecture Notes in Mathematics 630*, G. A. Waston, Ed. Springer, Berlin, Heidelberg, 1978, pp. 105–116.

[182] B. V. Farahani, J. Manuel Berardo, R. Drgas, J. M.A. César de Sá, A. J. M. Ferreira, and J. Belinha, "The Axisymmetric Analysis of Circular Plates Using the Radial Point Interpolation Method," *International Journal for Computational Methods in Engineering Science and Mechanics*, vol. 16, no. 6, pp. 336–353, 2015.

[183] J. Belinha, *Meshless Methods in Biomechanics: Bone Tissue Remodelling Analysis*, Vol. 16. Springer Netherlands, 2014.

[184] V. P. Nguyen, T. Rabczuk, S. Bordas, and M. Duflot, "Meshless methods: A review and computer implementation aspects," *Math. Comput. Simul.*, vol. 79, no. 3, pp. 763–813, 2008.

[185] T. Belytschko, Y. Y. Lu, and L. Gu, "Element-free Galerkin methods," *International Journal for Numerical Methods in Engineering*, vol. 37, no. 2, pp. 229–256, 1994.

[186] S. N. Atluri and T. Zhu, "A new Meshless Local Petrov-Galerkin (MLPG) approach in computational mechanics," *Computational Mechanics*, vol. 22, no. 2. pp. 117–127, 1998.

[187] J. G. Wang and G. R. Liu, "A point interpolation meshless method based on radial basis functions," *International Journal for Numerical Methods in Engineering*, vol. 54, no. 11, pp. 1623–1648, Aug. 2002.

[188] R. Sibson, "A vector identity for the Dirichlet tessellation," *Mathematical Proceedings of the Cambridge Philosophical Society*, vol. 87, no. 01, pp. 151–155, Oct. 1980.

[189] L. M. J. S. Dinis, R. M. Natal Jorge, and J. Belinha, "Analysis of 3D solids using the natural neighbour radial point interpolation method," *Computer Methods in Applied Mechanics and Engineering*, vol. 196, no. 13–16, pp. 2009–2028, 2007.

[190] J. Belinha, L. M. J. S. Dinis, and R. M. Natal Jorge, "The natural radial element method," *Int. J. Numer. Methods Eng*, vol. 93, no. 12, pp. 1286–1313, 2013.

[191] L. M. J. S. Dinis, R. M. Natal Jorge, and J. Belinha, "Analysis of plates and laminates using the natural neighbour radial point interpolation method," *Engineering Analysis with Boundary Elements*, vol. 32, no. 3, pp. 267–279, 2008.

[192] J. Belinha, R. M. Natal Jorge, and L. M. J. S. Dinis, "Bone tissue remodelling analysis

considering a radial point interpolator meshless method," *Engineering Analysis with Boundary Elements*, vol. 36, no. 11, pp. 1660–1670, Nov. 2012.

[193] L. M. J. S. Dinis, R. M. N. Jorge, and J. Belinha, "The natural neighbour radial point interpolation method: dynamic applications," *Engineering Computations*, vol. 26, no. 8, pp. 911–949, 2009.

[194] L. M. J. S. Dinis, R. M. Natal Jorge, and J. Belinha, "Static and dynamic analysis of laminated plates based on an unconstrained third order theory and using a radial point interpolator meshless method," *Computers & Structures*, vol. 89, no. 19–20, pp. 1771–1784, Oct. 2011.

[195] J. M. C. Azevedo, J. Belinha, L. M. J. S. Dinis, and R. M. Natal Jorge, "Crack path prediction using the natural neighbour radial point interpolation method," *Engineering Analysis with Boundary Elements*, vol. 59, pp. 144–158, Oct. 2015.

[196] J. Belinha, J. M. C. Azevedo, L. M. J. S. Dinis, and R. M. Natal Jorge, "The Natural Neighbor Radial Point Interpolation Method Extended to the Crack Growth Simulation," *International Journal of Applied Mechanics*, vol. 08, no. 01, p. Article ID: 1650006, 2016.

[197] O. C. Zienkiewicz and R. L. Taylor, *The Finite Element Method*, 4th ed. London: McGraw-Hill Book, 1994.

[198] K. Bathe, *Finite Element Procedures in Engineering Analysis*. New Jersey: Prentice-Hall, Inc., 1982.

[199] J. G. Wang and G. R. Liu, "On the optimal shape parameters of radial basis functions used for 2-D meshless methods," *Computer Methods in Applied Mechanics and Engineering*, vol. 191, no. 23–24, pp. 2611–2630, 2002.

[200] B. V. Farahani, J. Belinha, F. M. Andrade Pires, and A. J. . M. Ferreira, "A radial point interpolation meshless method extended with an elastic rate-independent continuum damage model for concrete materials," *Mechanics of Advanced Materials and Structures*, vol. In Press, pp. 1–13, 2017.

[201] B. Delaunay, "Sur la sphère vide. A la mémoire de Georges Voronoï," *Bulletin de l'Académie des Sciences de l'URSS*, vol. 6, pp. 793–800, 1934.

[202] J. Belinha, L. M. J. S. Dinis, and R. M. Natal Jorge, "Analysis of thick plates by the natural radial element method," *International Journal of Mechanical Sciences*, vol. 76, pp. 33–48, 2013.

[203] J. Belinha, L. M. J. S. Dinis, and R. M. N. Jorge, "Composite laminated plate analysis using the natural radial element method," *Composite Structures*, vol. 103, pp. 50–67, 2013.

[204] L. M. J. S. Dinis, R. M. N. Jorge, and J. Belinha, "Analysis of 3D solids using the natural neighbour radial point interpolation method," *Comput. Methods Appl. Mech. Eng.*, vol. 196, no. 13–16, pp. 2009–2028, 2007.

[205] J. G. Wang, G. R. Liu, and Y. G. Wu, "A point interpolation method for simulating dissipation process of consolidation," *Computer Methods in Applied Mechanics and Engineering*, vol. 190, no. 45, pp. 5907–5922, 2001.

[206] D. R. J. Owen and E. Hinton, *Finite elements in plasticity: theory and practice*. Pineridge Press, 1980.

[207] S. Timoshenko, *Theory of Elasticity*. New York: McGraw-Hill, 1934.

[208] R. Hill, *The mathematical theory of plasticity*. The Oxford Engineering Science Series. Vol.11, New York: Oxford University Press, 1998.

[209] M. A. Crisfield, *Non-Linear Finite Element Analysis of Solids and Structures, Essentials*. London: John Wiley & Sons Ltd, 1991.

[210] R. M. C. M. de Faria, "Avaliação do comportamento sísmico de barragens de betão através de um modelo de dano contínuo," Porto, 1994.

[211] R. Faria and J. Oliver, *A rate dependent plastic-damage constitutive model for large scale computations in concrete structures*. Barcelona, Spain, 1993.

[212] J. C. Simo and J. W. Ju, "Strain- and stress-based continuum damage models - I. Formulation," *International Journal of Solids and Structures*, vol. 23, no. 7, pp. 821–840, 1987.

[213] H. Ghaffarzadeh and A. Mansouri, "Numerical Modeling of Wave Propagation using RBF-based Meshless Method," in *Future Trends in Structural, Civil, Environmental and Mechanical Engineering*, 2013.

[214] C. T. Wu, W. Hu, and Y. Guo, “the Recent Update of LS-DYNA Meshfree and Advanced FEM for Manufacturing Application,” *Livermore Software Technology Corporation, LS-DYNA Forum, Bamberg,* 2014.

[215] H. Ghaffarzadeh, “Assessment of Effective Parameters on Rbf-BASED Meshfree Method for Wave Propagation Modeling,” in *the Latest Trends in Engineering Mechanics, Structures, Engineering Geology*, 2014.

[216] B. V. Farahani, “The Radial Point Interpolation Meshless Method Extended to Axisymmetric Plates and Non-linear Continuum Damage Mechanics,” University of Porto, 2015.

[217] M. A. A. Crisfield, *Non-linear Finite Element Analysis of Solids and Structures; Advanced Topics*, Vol. 2. London: John Wiley & Sons Ltd, 1996.

[218] M. L. Williams and C. Pasadena, “On the Stress Distribution at the Base of a Stationary Crack,” *APPLIED MECHANICS*, pp. 109–114, 1957.

[219] R. J. Sanford, “Application of the least-squares method to photoelastic analysis,” *Experimental Mechanics*, vol. 20, no. 6, pp. 192–197, Jun. 1980.

[220] A. A. Griffith, “Philosophical Transactions,” *Series A*, vol. 221, pp. 163–198, 1920.

[221] J. J. L. Morais *et al.*, “The double cantilever beam test applied to mode I fracture characterization of cortical bone tissue,” *Journal of the Mechanical Behavior of Biomedical Materials*, vol. 3, no. 6, pp. 446–453, Aug. 2010.

[222] G. R. Irwin, “Onset of Fast Crack Propagation in High Strength Steel and Aluminum Alloys,” *Sagamore Research Conference Proceedings*, vol. 2, pp. 289–305, 1956.

[223] F. C. Edde and Y. Verreman, “Nominally constant strain energy release rate specimen for the study of Mode II fracture and fatigue in adhesively bonded joints,” *International Journal of Adhesion and Adhesives*, vol. 15, no. 1, pp. 29–32, Jan. 1995.

[224] T. V. Duggan, M. W. Proctor, and L. J. Spence, “Stress intensity calibrations and compliance functions for fracture toughness and crack propagation test specimens,” *International Journal of Fatigue*, vol. 1, no. 1, pp. 37–47, Jan. 1979.

[225] M. G. Cockcroft and D. J. Latham, “Ductility and the workability of metals,” *J. Inst. Metals*, vol. 96, pp. 33–39, 1968.

[226] M. L. Wilkins, R. D. Streit, and J. E. Reaugh, “Cumulative-strain-damage Model of Ductile Fracture: Simulation and Prediction of Engineering Fracture Test,” *Tech. rep., UCRL- 53058, Lawrence Livermore National Laboratory*, 1980.

[227] G. R. Johnson and W. H. Cook, “Fracture characteristics of three metals subjected to various strains, strain rates, temperatures and pressures,” *Engineering Fracture Mechanics*, vol. 21, no. 1, pp. 31–48, Jan. 1985.

[228] T. Wierzbicki and L. Xue, “On the Effect of the Third Invaraint of the Stress Deviator on Ductile Fracture,” *Tech. Rep. 136. MIT Impact and Crashworthiness.*, 2005.

[229] A. L. Gurson, “Continuum Theory of Ductile Rupture by Void Nucleation and Growth: Part I—Yield Criteria and Flow Rules for Porous Ductile Media,” *Journal of Engineering Materials and Technology*, vol. 99, no. 1, pp. 2–15, 1977.

[230] V. Tvergaard and A. Needleman, “Analysis of the cup-cone fracture in a round tensile bar,” *Acta Metallurgica*, vol. 32, no. 1, pp. 157–169, 1984.

[231] A. Needleman, “Material rate dependence and mesh sensitivity in localization problems,” *Computer Methods in Applied Mechanics and Engineering*, vol. 67, no. 1, pp. 69–85, Mar. 1988.

[232] N. Benseddiq and A. Imad, “A ductile fracture analysis using a local damage model,” *International Journal of Pressure Vessels and Piping*, vol. 85, no. 4, pp. 219–227, 2008.

[233] Z. L. Zhang, C. Thaulow, and J. Ødegård, “A complete Gurson model approach for ductile fracture,” *Engineering Fracture Mechanics*, vol. 67, no. 2, pp. 155–168, 2000.

[234] C. C. Chu and A. Needleman, “Void Nucleation Effects in Biaxially Stretched Sheets,” *Journal of Engineering Materials and Technology*, vol. 102, no. 3, pp. 249–256, 1980.